Monolayers of Cationic Surfactants at the Air-Water and Oil-Water Interfaces

A thesis submitted in partial fulfillment of the requirements for the degree of Doctor of Philosophy in the University of Oxford, by

Mona Marie Knock

Magdalen College and Physical and Theoretical Chemistry Laboratory
University of Oxford

Trinity 2002

Monolayers of Cationic Surfactants at the Air-Water and Oil-Water Interfaces

A thesis submitted in partial fulfillment of the requirements for the degree of Doctor of Philosophy in the University of Oxford, by

Mona Marie Knock

Magdalen College,
Trinity 2002.

Monolayers of the cationic surfactant hexadecyltrimethylammonium halide (CTAX, where X = F^-, Cl^-, Br^-, and I^-) have been studied at the air-water and oil-water interfaces. At the air-water interface, the effects of the halide counterion and the addition of counterion were investigated. Sum-frequency spectroscopy (SFS), ellipsometry, and surface tensiometry indicated that the counterion changed the efficiency and effectiveness of the surfactant, both decreasing in the order of $Br^- > Cl^- > F^-$. The addition of salt in the form of 0.1 M KX was found to reduce the cmc but had little effect on the limiting area per molecule attained at the cmc, which increased from 44 $Å^2$ for CTAB to 65 $Å^2$ for CTAC and ca. 94 $Å^2$ for CTAF. Neither SFS nor ellipsometry provided any firm evidence for specific effects of the halide ions on the structure of the surfactant monolayers. For CTAB monolayers in the absence of excess electrolyte, the effect of area per molecule on the sum-frequency (SF) spectra was studied.

Mixed monolayers of CTAB and tetradecane at the air-water interface exhibit a first-order phase transition from a conformationally disordered to a conformationally ordered state as the temperature is lowered. The phase transition occurs ca. 11 °C above the bulk melting point of tetradecane.

A new experimental arrangement is described for acquiring SF spectra from surfactants at the oil-water interface. The key features of this approach are the stabilisation of a thin oil film between a sapphire prism and an aqueous phase, and the use of total internal reflection to enhance the total signal and discriminate against signals from other interfaces in the system. With this new methodology, the first SF vibrational spectra of surfactant monolayers at an alkane-water interface were obtained. Surface tensiometry was used to characterise the monolayers further. The structure of CTAB monolayers at the hexadecane-water interface was determined by SFS and compared with monolayers of CTAB at the air-water interface. At low concentrations, CTAB/hexadecane showed the expected features in the C–H stretching region, characteristic of a conformationally disordered monolayer. As the bulk concentration approached the critical micelle concentration, the spectra changed to one characteristic of a more ordered, upright conformation. Ellipsometric measurements supported this conclusion. This qualitative structural change is not observed in analogous monolayers at the air-water interface or CCl_4-water interface, or in surfactant solutions in contact with a hydrophobic solid surface.

Acknowledgements

In particular, I would like to give special thanks to my supervisor, Dr. Colin D. Bain, for his enthusiastic guidance, support, patience, and good humour. I am also grateful to my teachers, past and present, whose inspiration and thoughts have shaped my time at Oxford. I have benefited from the helpful advice and encouragement of many people whose research at Oxford has overlapped with mine: Dr. David Beattie, Dr. Christopher Williams, Dr. Brian Casson, Dr. Samantha Manning-Benson, Dr. Lei Qunfang, Dr. Robert Jacobs, Sarah Haydock, Richard Campbell, Katherine Wilkinson, Christopher Mellor, and indeed, all members of the Bain lab. This work would not have been possible without the help of the PTCL staff, and I extend special thanks to Mervyn Rees and John Crews in Stores, for their consistently cheerful assistance. Of course, I am very grateful to friends and family in Oxford and abroad, whose genuine concern has been invaluable.

My studies at Oxford were financially supported by scholarships from the British Marshall Commemoration Commission and the National Science Foundation Graduate Research Fellowship Program.

Publications Arising from Work Described in this Thesis

Effect of Counterion on Monolayers of Hexadecyltrimethylammonium Halides at the Air-Water Interface

Mona Marie Knock and Colin D. Bain

Langmuir **2000**, *16*, 2857.

First-Order Phase Transition in Mixed Monolayers of Hexadecyltrimethylammonium Bromide and Tetradecane at the Air-Water Interface

Caroline E. McKenna, Mona Marie Knock, and Colin D. Bain

Langmuir **2000**, *16*, 5853.

Sum-Frequency Spectroscopy of Surfactant Monolayers at the Oil-Water Interface

Mona Marie Knock, Graham R. Bell, Elisabeth K. Hill, Hannah J. Turner, Colin D. Bain.

Submitted to *Journal of Physical Chemistry B*.

Contents

Chapter 1 Introduction

1.1 Surfactants at Wet Interfaces ……...…..……...2

1.1.1 Surfactants: Background, History, and Applications ……..2

1.1.2 Surfactant Monolayers at Wet Interfaces: Air-Water, Oil-Water, and Solid-Water Interfaces ...…….…….9

1.2 Characterisation of Surfactant Monolayers at Wet Interfaces ……...11

1.2.1 Infrared Spectroscopy ……12

1.2.2 Surface-Enhanced Raman Spectroscopy ……...13

1.2.3 X-Ray Scattering ……...13

1.2.4 Neutron Scattering ……..…….……..14

1.2.5 Brewster Angle Microscopy ……..……15

1.2.6 Fluorescence Microscopy ……..15

1.2.7 Atomic Force Microscopy and Scanning Tunnelling Microscopy .16

1.2.8 Ellipsometry ……...16

1.2.9 Surface Tensiometry ……..17

1.3 Introduction to Sum-Frequency Spectroscopy at Interfaces ….……18

1.4 Literature Review for Surfactant Monolayers at the Oil-Water Interface ..20

1.4.1 Surface Tensiometry ……..21

1.4.2 Neutron Reflection and Scattering …..…….…….21

1.4.3 X-Ray Reflectivity ……...…..….22

1.4.4 Optical Microscopy ……...23

1.4.5 Ellipsometry ……...24

1.4.6 Second Harmonic Generation ……24

1.4.7 Sum-Frequency Spectroscopy ……...25

1.4.8 Mixed Monolayers of Surfactant and Oil at the Air-Water Interface ……26

1.5 Outline ……...28

Chapter 2 Theory

2.1 Interaction of Light with Matter: Linear and Non-linear Optics ……...36

2.2 Sum-Frequency Spectroscopy ……...41

2.2.1 Foundations ..……..41

2.2.2 Effects of Symmetry within the Molecule and Aggregate …….46

2.2.3 Electric Fields at an Interface……..51

2.2.3.1 Effect of Polarisation on SF Emission ……..51

2.2.3.2 Fresnel Coefficients ……..52

2.2.4 Lineshapes of SF Spectra ……..55

2.3 Ellipsometry ……..56

2.3.1 Surface Roughness and Interfacial Profile……..60

2.3.2 Optical Properties of Monolayers ……63

2.3.3 Establishing Molecular Contributions through Ellipsometry ……65

Chapter 3 Experimental

3.1 The Sum-Frequency Spectrometer ……70

3.1.1 Laser System ……...70

3.1.2 Raman Cell ……..74

3.1.3 Optical Path ……77

3.1.3.1 Herriot Cell and 532 nm Optical Path ……...77

3.1.3.2 IR Optical Path ……..78

3.1.4 Detection and Optimisation of SF Signal ……78

3.1.5 Setup for the Air-Water Interface ……...80

3.1.5.1 Experimental Design of the Air-Water Setup ……...80

3.1.5.2 Acquisition of SF Spectra at the Air-Water Interface …83

3.1.6 Setup for the Oil-Water Interface ……87

3.1.6.1 Experimental Design of the Oil-Water Setup ……...87

3.1.6.2 Alignment with Gold ……88

3.1.6.3 Acquisition of Spectrum from Gold ……..88

3.1.6.4 Acquisition of SF Spectra at the Oil-Water Interface …89

3.1.6.5 Acquisition of IR Transmission Spectrum of Oil Film ..90

3.1.7 Fitting SF Spectra ……91

3.2 The Ellipsometer ……92

3.3 Surface Tensiometry ……...94

3.3.1 du Noüy Ring Method ……..…...94

3.3.2 Drop Shape Analysis ……..95

3.4 Sample Preparation ……...102

3.4.1 Materials, Cleanliness, and Purity ……102

3.4.2 Hexadecyltrimethylammonium Halide Surfactants and Halide Salts ……..103

3.4.3 Mixed Monolayers of Surfactant and Alkane at the Air-Water Interface ……103

3.4.4 Hydrophobing the Sapphire Prism …….……..104

Appendix: Protocol for CCD Tracking at the Air-Water Interface ……...107

Appendix: Protocol for CCD Tracking at the Oil-Water Interface ……...109

Chapter 4 CTAB Monolayers at the Air-Water Interface

4.1 Rationale for Experiment ……..……113

4.2 Sum-Frequency Spectroscopy ……..113

4.3 Surface Tensiometry and the Determination of Area per Molecule via Ellipsometric Calibration …….116

4.4 SFS Line Strength and Surface Excess ……....118

4.5 Comparison with Other Experiments ……120

4.6 Conclusion ……123

Chapter 5 Effect of Halide Counterion on CTAX Monolayers

5.1 Rationale for Experiment ……127

5.2 Known Effects of Salt in the Bulk and at the Interface ……127

5.3 Effect of the Nature of the Counterion on Saturated CTAX Monolayers ...…….130

5.4 Effect of Added Electrolyte on the Structure of CTAX Monolayers at Limiting Coverage ……134

5.5 Specific Effects of Halide Counterions ……....139

5.6 Conclusion ……143

Chapter 6 Mixed Monolayers of CTAB and Alkanes

6.1 Rationale for Experiment ……149

6.1.1 Phase Transitions in Monolayers ……..149

6.1.2 Surface Freezing ……155

6.2 Mixed Monolayers of CTAB and Alkanes at the Air-Water Interface ……155

6.2.1 Ellipsometry ……..157

6.2.1.1 CTAB + Tetradecane ……...157

6.2.1.1.1 The Liquid Phase ……158

6.2.1.1.2 The Solid Phase ……..160

6.2.1.2 CTAB + Dodecane ……...163

6.2.1.3 CTAB + C_{13}, C_{15}, C_{16}, C_{17}, or C_{18} ……163

6.2.2 Sum-Frequency Spectroscopy ……...166

6.2.2.1 CTAB + Tetradecane ……...167

6.2.2.2 CTAB + Dodecane ……...172

6.3 Conclusion ……174

Chapter 7 Design of the Oil-Water SFS Experiment

7.1 Rationale for Experiment ……181

7.2 Design of Oil-Water Setup ……...182

7.2.1 Transparency of Bulk Phases ……182

7.2.2 Total Internal Reflection ……...183

7.2.2.1 C–H Stretching Region ……185

7.2.2.2 C–D Stretching Region ……186

7.2.3 The Oil-Water Setup ……187

7.3 Fresnel Coefficients ……..187

7.4 Establishing the Submerged Oil-Water Interface ……192

7.4.1 Stability of the Oil Film: the Importance of Contact Angle …..192

7.4.2 Overview of Experimental Attempts to Achieve Stability …...193

Chapter 8 CTAB Monolayers at the Hexadecane-D_2O Interface

8.1 Normalisation of SF Spectra ……201

8.1.1 Fresnel Coefficients ……..202

8.1.2 Laser Output ……..203

8.1.3 Absorption of IR by Oil ……205

8.2 Thickness of the Oil Layer ……...207

8.3 SF Spectrum of a CTAB Monolayer at the Oil-Water Interface …..208

8.4 Effect of Concentration on SF Spectra ……210

8.5 Effect of Area per Molecule on the SF Spectra of CTAB Monolayers ……211

8.5.1 Supplementary Results from Ellipsometry ……...213

8.5.2 Calculation of Coefficient of Ellipticity for CTAB Monolayers at the Oil-Water Interface ……216

8.6 Comparison with Monolayers at Other Interfaces ……...218

8.6.1 CTAB at the Oil-Water and Air-Water Interfaces …….218

8.6.2 Mixed Monolayers of Surfactants and Alkanes at the Air-Water Interface …….219

8.6.3 Surfactant Monolayers at the CCl_4-Water Interface …….220

8.6.4 Surfactant Monolayers at the Hydrophobic Solid-Liquid Interface …….221

8.7 Conclusion ……222

Chapter 9 Conclusion

9.1 Monolayers at the Air-Water and Oil-Water Interfaces ……228

9.2 Effect of Oil on the Conformation of Surfactant Monolayers ……..229

9.3 Implications for Further Research ……231

CHAPTER 1

Introduction

Chapter 1: Introduction

1.1 Surfactants at Wet Interfaces

Surfactants concentrate at interfaces, but are also present in bulk solutions as free molecules, or in the form of micelles or other mesophases. Wet interfaces generally take one of three forms: gas-liquid, liquid-liquid, or liquid-solid. Emulsions constitute a special case of the liquid-liquid interface, but can also form from liquid-solid interfacial systems. All three wet interfaces are modified by surfactants and are relevant to the science and industry of colloids and interfaces. In this thesis, I have focused on a particular model system in its gas-liquid and liquid-liquid forms, namely, monolayers of the cationic surfactant hexadecyltrimethylammonium bromide at the air-water and oil-water interfaces. I have also investigated the transitional state between the air-water and oil-water interface: that of mixed monolayers of the surfactant with oil at the air-water interface. The effect of the halide counterion and added electrolyte was also studied for surfactant monolayers at the air-water interface.

1.1.1 Surfactants: Background, History, and Applications. The role of surfactants as modifiers of interfacial phenomena is enhanced under two conditions:

(i) when interfacial area is very large relative to the volume of the bulk system;

(ii) when the interfacial phenomena caused by surfactants are so unusual relative to normative bulk behaviour that the system's behaviour as a whole is governed by interfacial processes.

(i) is the case in emulsions, foams, and solid dispersions, which are not the focus of this thesis. (ii) occurs in processes relating to corrosion, catalysis, lubrication, detergency, or flotation. The research described in this thesis is relevant to processes

in (ii). Our work is motivated by the need to establish an informed structure-function relationship between the surfactant molecule and its action at interfaces.

Surface-active molecules exhibit structural diversity that reflects their long history of use in human endeavours. Their unifying feature, however, is their amphiphilic structure,[*] which consist of a lyophobic group and a lyophilic group. The former has little attraction for the solvent, whereas the latter is strongly attracted to the solvent. In an aqueous surfactant solution, this distinction becomes one of hydrophobicity and hydrophilicity, respectively. From this molecular duality arise distinctions in the thermodynamic favorability of various molecular arrangements. To reduce the free energy of the system by limiting distortions in the solvent liquid structure, surfactants align with their lyophilic group in the solvent, and their lyophobic group away from the solvent. The lyophobic group can end up in a variety of different locations: in air, on a surface, in a different solvent, or in micellular or vesicular arrangements that collectively isolate the lyophobic group from the solvent.

The chemical groups that suitably form the lyophilic and lyophobic components of surfactant molecules vary with respect to the nature of the solvent and the conditions of use. For surfactants used in aqueous environments, the hydrophobic group is typically a long-chain hydrocarbon, but occasionally is a fluorinated or oxygenated hydrocarbon or siloxane chain. The hydrophilic group is either ionic (cationic or anionic) or highly polar (zwitterionic or nonionic). The interfacial properties of the surfactant are modified by changes in the hydrophilic head group or in the hydrocarbon chain. Figure 1.1 lists the functional features most commonly found in surfactants.

[*] The word amphiphilic arises from the Greek root of "amphi", or αμφι, which means 'on both sides.'

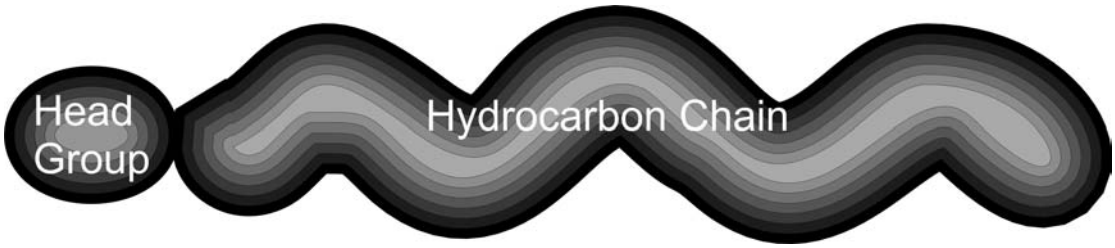

Hydrophilic Head Group	**Hydrophobic Hydrocarbon Chain***
<u>*Cationics*</u>:	
o quaternary ammonium salts	Straight-chain, long alkyl groups (C_8-C_{20})
o long-chain amines and their salts	
o diamines and polyamines and their salts	
o polyoxyethylated long-chain amines	Branched-chain, long alkyl groups (C_8-C_{20})
o quaternized polyoxyethylenated long-chain amines	
<u>*Anionics*</u>:	Long-chain (C_8-C_{15}) alkylbenzene residues
o salts of carboxylic acid, sulfonic acid, and sulfuric acid ester; alkyl benzene sulphonates	
o phospholipids, phosphoric and polyphosphoric acid ester	Alkylnaphthalene residues (C_3 and longer-chain alkyl groups)
o perfluorinated anionics.	
<u>*Nonionics*</u>:	High molecular weight propylene oxide polymers (polyoxypropylene glycol derivatives)
o alcohols	
o polyoxyethylenated alkylphenols or straight-chain alcohols, alcohol or alkylphenol ethoxylates	
o mono-, di-, or triglycerides	
o polyoxyethylenated polyoxypropylene glycols	Long-chain perfluoroalkyl groups
o polyoxyethylenated mercaptans	
o long-chain carboxylic acid esters	
o alkanolamine condensates, alkanolamides	Polysiloxane groups
o tertiary acetylenic glycols	
o polyoxyethylenated silicones	Lignin derivatives
o n-alkylpyrrolidones	
o alkylpolyglycosides	Rosin acid (abietic acid) derivatives
<u>*Amphoterics / Zwitterionics*</u>:	
o β-n-alkylaminopropionic acids	
o n-alkyl-β-iminodipropionic acids	
o imidazoline carboxylates	
o n-alkylbetaines	
o sulfobetaines, sultaines	
o n-alkyldimethylamine oxides	* *listed in no particular order*

Figure 1.1 *Common functional features in surfactant molecules.*

Anionic surfactants are used in laundry and hand dishwashing detergents, household cleaners, and personal cleansing products. They have excellent cleaning properties and generally are high sudsing. Linear alkylbenzene sulfonate, alcohol ethoxysulfates, alkyl sulfates and soap are the most common anionic surfactants. Nonionic surfactants are low sudsing and are typically used in laundry detergents, dishwasher detergents, and rinse aids. Because they do not ionize in solution, they are resistant to water hardness and clean well on most soils. The most widely used nonionic surfactants are alcohol ethoxylates. Amphoteric surfactants are used in personal cleansing and household cleaning products for their mildness, sudsing and stability. They have the ability to be anionic, cationic, or nonionic in solution, depending on the pH of the water. Imidazolines and betaines are the most common amphoteric surfactants.

The work in this thesis focuses on cationic alkyltrimethylammonium halide surfactants. Cationic surfactants easily adsorb to solid surfaces, which typically carry a negative charge. Some cationic surfactants are sensitive to changes in pH, which allows them to serve as semi-permanent surface coatings for use in corrosion inhibition and surface lubrication. Cationic amines, diamines, and polyamines are used in ore flotation, pigment coating, anticaking of fertilizers, and as adhesion promoters in surface painting. Quaternary ammonium salt surfactants, like the one studied in this thesis, are unaffected by pH changes, and remain water soluble across the pH range. This solubility can prevent them from strongly adsorbing to some hard surfaces, but enables them to be used as emulsifying agents in acidic environments. Quaternary ammonium salt surfactants are also germicidal, which makes them a popular component of detergent mixtures and certain antiseptic preparations, such as mouthwashes. Double-chained quaternary ammonium salt surfactants adsorb onto

fabric fibers with the hydrophobic groups orientated away from the fiber surface, leaving the fabric with a softer hand. When *N*-benzyl-*n*-alkyldimethylammonium halides are incorporated into hair conditioner preparations, they have a similar effect on hair.

The aggregation of cationic (and anionic) surfactants is affected by the charge on the head group. Ionic surfactants typically have critical micelle concentrations (cmc's; the bulk concentration at which micelles form) that are high in comparison to nonionic surfactants. This difference can be eliminated by working in the presence of swamping electrolyte. Electrolytes screen the electrostatic repulsive forces between the charged surfactant head groups. The presence of electrolyte in solution also changes the number of kinetically active components in the solutions and modifies the stoichiometric coefficient of the Gibbs adsorption isotherm, which describes the self-assembly of surfactant monolayers at the interface.

The first surfactants expressly prepared for cleansing purposes[†] were undoubtedly soaps. Soaps are sodium or potassium salts of long-chain carboxylic acids. Traditional saponification, or soap formation, was carried out by boiling animal or vegetable fats with wood ash (lye). This process, which likely predates the written word, stood the test of time until the industrial revolution. Written records of the use of soap exist from as early as 2800 B.C.[1] Inscriptions on ancient Babylonian clay cylinders state that fats were boiled with ashes, but do not

[†] Instead of emulsification or lubrication. Of course, ancient examples of these uses also exist. Over 4500 years ago, Egyptians made "instant" ink for writing on papyrus by dispersing coated fine carbon particles in water. The particles of carbon (lamp black, or soot) were coated with biological surfactants, such as the resin from the acacia tree (gum Arabic), casein from milk, or egg albumin. The addition of these molecules created a stable emulsion and prevented the coagulation and sedimentation of the carbon particles. The carbon black was then moulded into a pencil-like shape and dried. When ink was needed, a chip of the writing stick was broken off and dipped into water. The stabilised carbon black particles spontaneously redispersed to form a colloidal solution of ink. [Tabor, D. In *Gases, liquids, and solids*, 3rd Ed. Cambridge: Cambridge University Press, 1991.]

refer to the purpose of the 'soap.' Some believe that at that time, soap was used as a hair dressing or wound antiseptic. Written records in Egypt indicate that the ancient Egyptians bathed regularly. The Ebers Papyrus, a medical document from about 1500 B.C., describes combining animal and vegetable oils with alkaline salts to form a soap-like substance used for treating skin diseases and for washing. Although the ancient Greeks did not use soap, they used its components in sequence or in tandem. They cleaned their bodies with blocks of clay, sand, pumice and ashes, anointed themselves with oil, and then scraped off the oil and dirt with a metal instrument known as a strigil. According to an ancient Roman legend, soap got its name from Mount Sapo, a site of animal sacrifice. A mixture of melted animal fat (tallow) and wood ashes were washed down into the clay soil along the Tiber River after rainfall. Women washing in the river found that this clay mixture cleaned their washing more easily.

It is thought that the use of soap developed in both the Fertile Crescent and in Europe. Isolated tribes of Vikings and Celts discovered soap independently, and the Celts are credited with introducing soap to England around 1000 A.D. This predates the technological exchanges that occurred at the end of the Middle Ages, and during the Ottoman invasions of Europe.

Progress towards commercial soapmaking on an industrial scale occurred in 1791 when a French chemist, Nicholas Leblanc, patented a process for making soda ash (sodium carbonate) from common salt. The Leblanc process yielded quantities of good quality, inexpensive soda ash. Twenty years later, the French chemist Michel Eugene Chevreul discovered the chemical nature and relationship of fats, glycerine, and fatty acids. The invention of the ammonia process by the Belgian chemist Ernest Solvay in the mid-1800s was also important to the development of soap technology.

The ammonia process used table salt (NaCl) to make soda ash. Solvay's process further reduced the cost of obtaining this alkali, and increased both the quality and quantity of the soda ash available for manufacturing soap. Figure 1.2 illustrates the process of saponification, which yields soap.

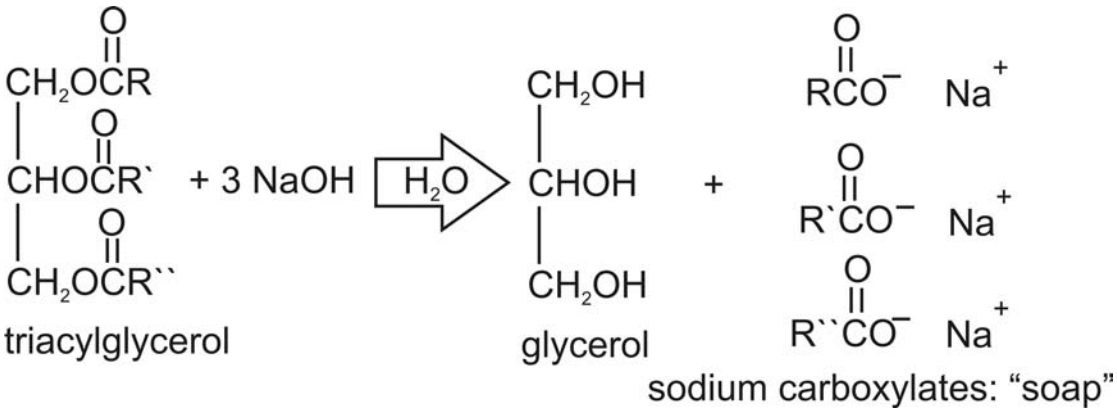

Figure 1.2 *Saponification, or alkaline hydrolysis, of triacylglycerols to produce glycerol and a mixture of salts of long-chain carboxylic acids, or soaps.*

Soaps, or surfactants, solubilise soil (oily or fatty deposits that often incorporate grime) in aqueous solution such that it can be washed away. This solubilisation occurs through micelles, which surround soil such that it separates from the surface being cleansed. This process is illustrated in Figure 1.3.

The commercial transition from soaps to detergents[‡] was made in response to the economic constraints imposed by the first and second World Wars. WWI and II led to a shortage of animal and vegetable fats and oils. In 1916, the first synthetic detergent was developed in Germany in response to this shortage. At that time, petroleum presented itself as a plentiful source for the manufacture of these detergent surfactants. An additional motivation for the transition from soaps to detergents was the problem of insoluble soap scum (or soap curd) formation in the presence of hard water, which diminishes the cleaning efficacy of soap surfactants. Today, detergents

are made from a variety of petrochemicals and/or oleochemicals, which are derived from fats and oils.

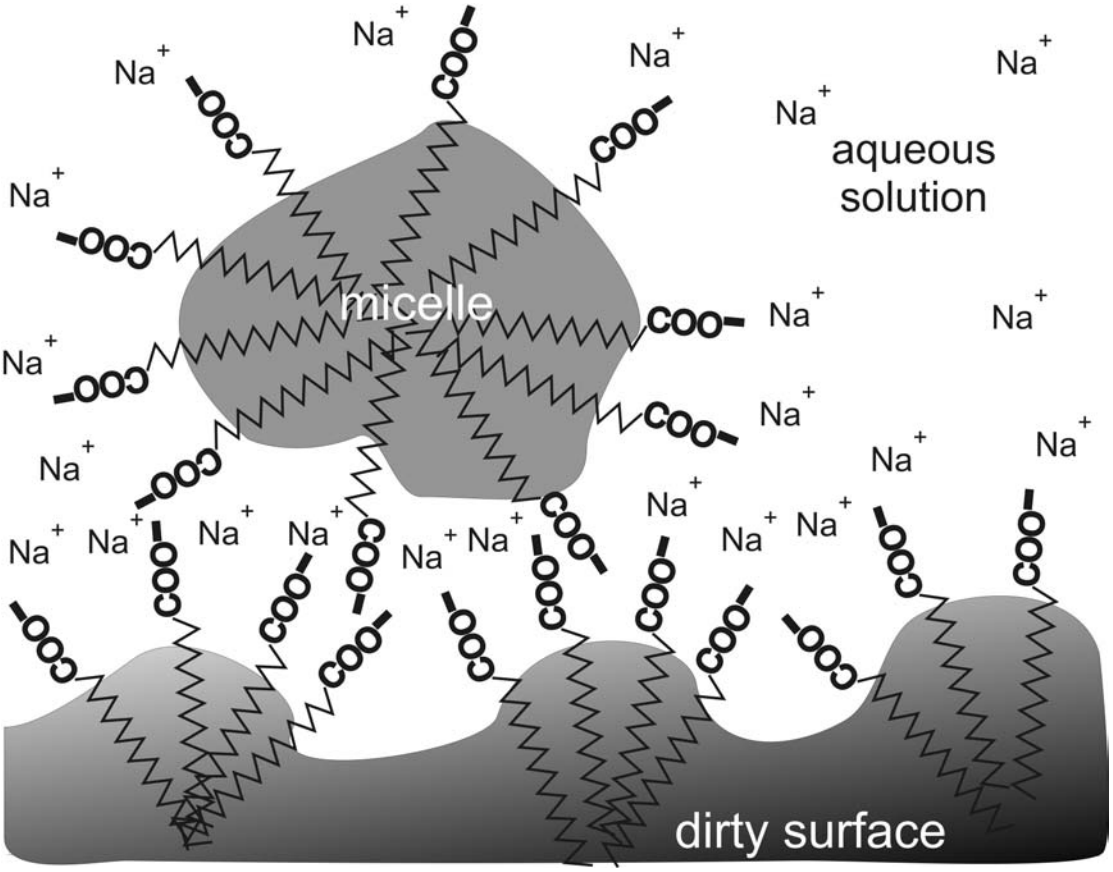

Figure 1.3 *Solubilisation of (oily) dirt on a surface by a soap. The soap illustrated here is stearic acid.*

1.1.2 Surfactant Monolayers at Wet Interfaces: Air-Water, Oil-Water, and Solid-Water Interfaces. Surfactants adsorb to interfaces in accordance with their affinity for the solvent and for the interface. At the air-water interface, surfactants adsorb with their head groups in the water and their hydrocarbon chains above the water. At this interface, air provides a suitably hydrophobic environment for the surfactant chains – at least in comparison to the water below. The level of disorder within the

‡ Detergents are synthetic surfactants that remain soluble in hard water, i.e. water containing Ca^{2+}, Fe^{2+}, Fe^{3+}, and Mg^{2+} ions.

monolayer, as well as the extent of adsorption, depends on the molecular identity of the surfactant.

At the oil-water interface, surfactants adsorb with their chains in the oil and their head groups in the water. This is understood in light of the non-polar, hydrocarbon environment of the oil matching that of the surfactant's hydrocarbon chains. The degree of ordering within this monolayer, however, is far from obvious. Though surfactants are used to solubilise oil within water through their reduction in oil-water interfacial tension, it is not implicit that this solubilisation occurs through the formation of a conformationally ordered, surfactant-bridged boundary between the oil and the water. Indeed, one could imagine that the process of solubilisation increases entropic disorder, instead of increasing order through the formation of an ordered oil-surfactant-water interfacial layer. As will be discussed further in chapters 6-8, the interfacial plane nevertheless gives rise to a wide range of fascinating ordering phenomena, in many pure substances (liquid or solid) and in mixtures or solutions. It is conceivable that under equilibrium conditions,[§] surfactant-controlled phase transitions can occur at the interface between oil and water.

At the solid-water interface, the orientation of adsorption depends upon the nature of the solid in comparison to the solvent. Hydrophilic surfaces such as those of many (clean) minerals, metals, and glasses[**] favor adsorption of the surfactant head group in the presence of a non-polar solvent (or in air, in the absence of solvent). In water, one could envision the formation of a bilayer with opposing hydrophilic headgroups facing the hydrophilic solid surface and at the interface with water. For

[§] In contrast to the kinetically intense, agitated conditions that prevail in many dynamic surfactant applications, such as cleaning, flushing, separations, etc.

[**] Hydrophilic surfaces include glass, quartz, aluminium, chromium, tin, all their oxide forms, silicon wafers, gold, silver, gallium arsenide, and freshly cleaved mica. [Ulman, A. In *An Introduction to Ultrathin Organic Films: From Langmuir-Blodgett to Self-Assembly*. San Diego: Academic Press, Inc., 1991.]

hydrophobic surfaces, such as those modified by the application of self-assembled monolayers like alkylsiloxanes or alkanethiols, the surfactants would preferentially adsorb with their chains oriented towards the hydrophobic surface, and their head groups oriented towards the aqueous phase.

1.2 Characterisation of Surfactant Monolayers at Wet Interfaces

Techniques developed for characterisation of the molecular structure of surfactant monolayers comprise a relatively new area of physical interfacial chemistry. These techniques are distinct from traditional interfacial methods, such as surface tensiometry and contact angle measurement, which study surfactant behaviour on a macroscopic scale. Current imaging microscopy techniques such as atomic force microscopy (AFM), scanning tunnelling microscopy (STM), Brewster angle microscopy (BAM), and cryo-transmission electron microscopy (cryo-TEM), are relatively new but provide exciting, pseudo-visual pictures of molecular structure. Optical techniques such as surface light scattering and reflection, ellipsometry, and fluorescence spectroscopy now also exist. Non-linear optical techniques of second-harmonic generation (SHG) and sum-frequency spectroscopy (SFS) have been developed and the latter is the primary technique employed in this thesis. Scattering techniques such as X-ray and neutron reflectivity and grazing incidence diffraction have been developed extensively to probe the molecular detail of a wide range of interfaces. The wavelengths of X-rays and neutrons, at 1.5 Å and 1-10 Å, respectively, are smaller than those of light, and can provide the details of interfacial monolayers on a molecular scale.

1.2.1 Infrared Spectroscopy. Improvements in sensitivity obtained through Fourier transform procedures have enabled traditional infrared spectroscopy to be applied to interfacial studies. The two primary methods are external reflection infrared spectroscopy (ER-IRS), which can be used at the air-solid and air-liquid interfaces,[2,3,4] and attenuated total internal reflection infrared spectroscopy (ATR, or internal reflection spectroscopy), which can be used at the air-solid and liquid-solid interfaces. Both of these techniques provide information on molecular orientation and conformational order within monolayers, and are performed as extensions to conventional Fourier transform infrared spectrometers.

In ER-IRS, an infrared beam is reflected by an interfacial monolayer, and the intensity of the reflected infrared beam is detected and referenced to that from a clean (monolayer-free) surface. Quantitative information is obtainable when polarised spectra are taken at different incident angles. Data is then fit to optical models, which are adaptations of the Fresnel equations for reflected light, and take into account contributions from both the monolayer and the subphase to the infrared absorbance. ER-IRS is thus more complicated than conventional IR transmission/absorption spectroscopy. The strength of peaks and dips in ER-IRS spectra is a function of infrared incident angle and molecular orientation, as well as the extinction coefficient for that particular vibration. The appearance of spectra is governed by both the properties of reflection and the absorption of infrared radiation.

ATR infrared spectroscopy measures the change in infrared intensity of an infrared beam as it goes through multiple total internal reflections through an infrared-transparent crystal, such as silicon, germanium, or thallium bromide (KRS-5). The evanescent field of the infrared radiation interacts with the environment adjacent to the crystal surface, giving rise to a spectrum. Because of this, ATR infrared

spectroscopy is particularly suited to the solid-liquid interface. Quantitative results from ATR infrared spectra are obtainable through the use of polarised beams and varied incident angles, employing optical theory similar to that used in ER-IRS.

At interfaces with water, the primary disadvantage of these two modified infrared spectroscopies is the strong absorption band of water in the infrared region, which overlaps the C–H stretching region. Sample spectra are referenced to spectra of clean water, but due to the strength of absorption, even the humidity above samples must be regulated. This drawback is mitigated by the development of polarisation modulation ER-IRS,[5] where the polarisation of the infrared beam is periodically oscillated in the p-polarised direction using a photoelastic modulator. Polarisation-modulated reflectivity is not influenced by isotropic molecules, and the effect of water is thus diminished.

1.2.2 Surface-Enhanced Raman Spectroscopy. Raman spectroscopy is another form of vibrational spectroscopy that can be applied to monolayers. Raman spectra are substantially enhanced by metal surfaces. This allows the sensitive detection of sub-monolayer quantities on metal surfaces in Raman spectra. Metal-substrate vibrations are also detectable. This technique is thus well-suited to investigations of metal catalysis, and the spectra can yield information on molecular orientation at metal surfaces. The use of confocal Raman microscopes allows the application of unenhanced Raman spectroscopy to be applied to monolayers on non-metallic substrates.

1.2.3 X-Ray Scattering. Well-collimated, high-intensity X-ray beams from synchrotron sources in the 1980s enabled the structural determination of crystalline

monolayers, similar to what X-ray diffraction enabled for three-dimensional (3-D) crystal structure determination in the bulk. Grazing incidence X-ray diffraction and X-ray reflection have been applied to monolayers at the air-water interface.[6] Measurements of X-ray reflection as a function of incident angle allows the determination of electron density distribution along the surface normal.[7] Accurate measurements of the absolute surface coverage, monolayer thickness, and capillary wave roughness can then be determined for crystalline or disordered monolayers.[8] In grazing incidence X-ray diffraction, the X-ray evanescent wave is diffracted by lateral two-dimensional order in the monolayer. If the monolayer possesses quasi-long-range translational order, the evanescent wave is Bragg scattered. Whereas for a 3-D crystal, Bragg points are detected, there is no restriction in the *z*-component normal to the interface in grazing incidence X-ray diffraction, resulting in the detection of Bragg rods rather than Bragg points. Angular separation of Bragg rods in the plane of the surface provides the lattice spacing for the crystal surface. The Bragg rod profile and the intensity distribution along the rod's *z*-axis provide the tilt angle and tilt direction for the molecules within the monolayer. X-ray diffraction is suitable for insoluble monolayers with quasi-long-range translational order. This technique does not provide information on liquid monolayers.

1.2.4 Neutron Scattering. Neutron scattering relies upon the same principles as X-ray scattering, except that the neutrons are scattered by the atomic nuclei of the interfacial molecules, rather than by the electrons. Each nuclear isotope has its own characteristic scattering interaction with a neutron. Protons carry a small, negative coherent scattering length, while deuterium carries a far greater and more positive scattering length. A mixture of 8% D_2O in H_2O has the same scattering length density

as air and is known as null reflecting water (nrw). Neutron reflectivity experiments can provide absolute measurements of surface coverage, as well as information on monolayer thickness and interfacial roughness.[9] Partial deuteration of surfactant molecules allows the determination of more detailed structural information from their monolayers. Surfactant molecules that are selectively and systematically deuterated in blocks enable cross-sections of the surfactant monolayer to be individually traced. Unlike X-ray diffraction, neutron reflectivity can provide information on disordered monolayers.

1.2.5 Brewster Angle Microscopy. BAM allows the direct observation of phase domains in monolayers at the air-water interface.[7] BAM is essentially an imaging form of ellipsometry, a technique detailed in chapter 2. Changes in the refractive index profile at an interface, as well as at an interface with a monolayer, are observed by BAM. The reflected spot from a laser beam incident on a surface at the Brewster angle is passed through a microscope and detected with a video camera. A narrow strip of the image is in focus; small movements in the lens change the focus to obtain an image of the adjacent strip. The image of a surface can thus be obtained in seconds with a lateral resolution of 1 μm.[10] BAM provides for the observation of phase transitions in monolayers by monitoring the growth of phase domains. Different textures within a monolayer phase can also be observed.[11]

1.2.6 Fluorescence Microscopy. Fluorescence microscopy is another imaging technique, but is reliant on doping the observed monolayer with fluorescent probe molecules. The solubilities of probe molecules differ in various monolayer phases, enabling the phase behaviour of surfactant monolayers to be observed.[12] This

technique suffers from the introduction of impurities into the monolayer, which has a detrimental effect on observing the original monolayer of interest.

1.2.7 Atomic Force Microscopy and Scanning Tunnelling Microscopy. AFM and STM allow surface imaging of nm resolution.[13] AFM measures the force between a tip and the surface as the tip is scanned across the surface. STM measures the electric current between the tip and the surface as the tip is scanned across the surface, thus requiring that the surface be conducting, but also provides better image resolution than AFM. Certain molecules can be imaged on an atomic scale.[14] AFM has been used to study aggregation at the solid-liquid interface[15] but to date, has not been used to image soluble surfactants at the air-water or oil-water interfaces successfully.

1.2.8 Ellipsometry. The theory behind ellipsometry has existed for over a century,[16] and ellipsometers have been used for interfacial analysis since 1945.[17] Ellipsometry is an optical technique that measures the change in amplitude and phase of light reflected from an interface.[18,19,20,21] Fresnel's equations[22] describe the theory of reflection and transmission at an interface between two media. The reflection properties are altered slightly by the presence of a thin film, which substantially complicates the theory. For a thin film, a single ellipsometric measurement depends upon both the thickness and refractive index of the film.[16] With improvements in the technology and design of ellipsometers, the technique has become highly sensitive to the optical properties of thin films, and surfactant solutions can be measured with a precision of less than 1% of a monolayer. The primary drawback to ellipsometry is the difficulty involved in quantitative data interpretation, since a single ellipsometric reading depends upon more than one unknown. The refractive index of a monolayer

is frequently estimated, or calculated by other methods, in order to obtain a thickness for the monolayer through ellipsometry.

1.2.9 Surface Tensiometry. There are several methods used to measure the surface tension of a liquid interface:

The *force method* is commonly used, by either the du Noüy ring or Wilhemy plate techniques, which both measure the static maximum pulling force prior to detachment of the ring or plate from the interface. Obviously, measurement of arbitrary brute force is not useful, so the pull on the ring or plate is very gradually increased and the maximum force preceding the point of incipient detachment is measured. In this thesis, surface tensiometry at the air-water interface was accomplished by the du Noüy ring technique.[23]

The *pressure method* involves measurement of the pressure inside a bubble of solution or a bubble of gas within solution. The small bubble surfactometer and the maximum bubble pressure (MBP) method both measure the pressure in order to determine the surface tension using the Laplace equation, $\Delta P = \gamma(1/R_1 + 1/R_2)$, where R_1 and R_2 are the two radii of curvature for the bubble, and γ is the surface tension of the solution. The MBP method measures the maximum pressure required to blow a bubble of inert gas from the tip of a small tube into a liquid.[24] The pressure within the tube is increased until a small bubble emerges at the tip of the tube orifice. This method can be applied to measurements of dynamic surface tension if P is kept constant and the interval between successive bubbles is measured, yielding the surface age and the surface tension. The growing drop technique is a similar approach and measures the surface tension of expanding gas-liquid and liquid-liquid interfaces. A drop grown from the end of a capillary tip into another liquid or gaseous medium is

monitored for its expanding size and the pressure difference across the interface, which is measured by a sensitive pressure transducer.

The *shape method*, or drop shape analysis, is a method by which the drop's shape is optically assessed, and the two radii of curvature are measured. The Laplace equation (above) is then used to calculate the surface tension. This technique has several variants, including formation of a bubble, a sessile drop, a pendant drop, a rising captive drop, or a spinning drop. The bubbles or drops are non-spherical due to the force of gravity and/or centrifugal forces (in the case of the spinning drop). In this thesis, drop shape analysis of bubbles and captive rising drops provided interfacial tension results for the oil-water interface.

The *capillary wave method* measures the frequency of thermally excited capillary waves on the liquid surface. The wavelength and frequency of capillary waves is used to calculate the surface tension. Surface light scattering measures scattered light from thermally excited capillary waves. The scattering can be specular or non-specular. Capillary waves depend on thermal excitations, the interfacial and bulk properties of the liquid, and are independent of gravity. The frequency of the waves depends on the surface tension and viscosity of the liquid.[25]

1.3 Introduction to Sum-Frequency Spectroscopy at Interfaces

Sum-frequency spectroscopy arises from the physics of non-linear optics, a discipline first studied in the 1960's. In 1960, Maiman irradiated ruby crystals and demonstrated the first laser,[26] which lead to the observation of non-linear optical (NLO) effects arising from the unusually strong electric fields in a laser beam.[27] In the early 1960s, Bloembergen developed the theory of non-linear optics,[28] and was awarded the Nobel Prize in 1981 for this work. Bulk NLO effects captured initial

research enthusiasm, followed by surface studies, and the first surface second-harmonic generation signal was detected from the surface of silver in 1974.[29] Bulk sum-frequency generation (SFG) was first discovered in 1962 in a crystal of triglycine sulfate,[30] but was only observed at a surface as late as 1986 by Shen for a monolayer of coumarin dye on glass.[31] The greater feat of detecting molecules that do not absorb in the visible or near-UV was accomplished by Shen and coworkers in 1987, when they obtained SF spectra from methanol on glass and pentadecanoic acid on glass and water.[32] Spectra of Langmuir-Blodgett films of cadmium arachidate on silver and germanium and of octadecanethiol on gold were also published that year by Harris and coworkers.[33] Since that time, SF spectrometers have been developed by other laboratories to study a range of interfacial systems for various purposes. Substantial developments in the application of SFS to different systems have not changed the theory behind the SFG experiment.

In SFS, a tunable infrared laser beam is overlapped (in space and time) with a fixed frequency visible laser beam at an interface, and light emitted at the sum of these two frequencies is detected. The SF signal is enhanced when a molecular vibration is in resonance with the infrared frequency; scanning the infrared frequency yields a vibrational spectrum. SFS provides information on the structure and orientation of interfacial molecules and is particularly sensitive to conformational disorder in hydrocarbon chains.[34] The C–H stretching region is frequently studied since this region is accessible to commercial laser systems and the vibrations in this region are well understood and are sensitive to molecular orientation.[35,36]

SFS has been applied extensively to study surfactant monolayers at the air-water interface. Insoluble[37,38] and soluble[34] monolayers have been characterised, and a wide range of hydrocarbon chains and head groups have been studied. Many

systems have also been investigated at the solid-liquid interface.[39] At this interface, both the solid substrate and the liquid can be varied, which enables the study of surfactant adsorption at hydrophobic and hydrophilic surfaces, as well as at electrodes.

Obtaining sum-frequency vibrational spectra from surfactant monolayers at the oil-water interface has been a long-standing challenge. The various difficulties associated with this experiment are detailed in chapter 7. To set my work in context, I have summarised existing experimental studies of the oil-water interface in section 1.4.

1.4 Literature Review for Surfactant Monolayers at the Oil-Water Interface

Surfactants at the o-w interface present particular difficulties for most surface-analytical techniques for several reasons. First, in the presence of adsorbed surfactants the surface tension, γ, of the o-w interface is greatly lowered, reaching a value of 4 mN m^{-1} at the critical micelle concentration (cmc) of CTAB. The amplitude of thermally excited capillary waves scales as $\gamma^{-½}$ and the o-w interface is therefore much rougher than the a-w interface (γ > 35 mN m^{-1} for CTAB).[40] The effect of roughness is to wash out the fine structure of the interface in scattering experiments. Second, one of the bulk phases needs to be transparent to the incoming light or particle beam. Third, surfactants adsorbed at the interface need to be distinguished from those in the bulk phases. Finally, like most liquid interfaces, the o-w interface is highly sensitive to surface-active impurities.

1.4.1 Surface Tensiometry. Surface tensiometry has long been used to study the adsorption of surfactants at the o-w interface. A good recent study is that of Goebel and Lunkenheimer who examined the neat o-w interface with a modified ring method and pendant drop technique.[41] They measured the effect of impurities in the alkane phase on the o-w interfacial tension and achieved surface tension measurements to a high standard of interfacial purity. Even-odd effects from the length of the alkane chain were observed in the surface tension of the o-w interface. Although surface tensiometry can provide thermodynamic parameters, such as surface excess or surface entropy, it provides no direct information on the structure of the interface on a molecular length scale.

1.4.2 Neutron Reflection and Scattering. Neutron scattering techniques, such as neutron reflectivity (NR) and small angle neutron scattering (SANS), provide information on density distributions and adsorbed amounts at interfaces. The ability to vary the refractive index (and hence the 'contrast' between the monolayer and the bulk phases) by deuterium substitution compensates for the inherently weak scattering of neutrons by matter. Interfacial roughness can dominate the results of NR, which also suffers from significant attenuation of the neutron beam during transmission through a liquid medium (especially one that contains hydrogen atoms). NR has been used to study polymer adsorption at a planar hexane-water interface.[42] SANS has been used to study adsorption of mixed surfactant layers at the o-w interface of a hexadecane-in-water emulsion.[43] Early NR studies of the liquid-liquid interface restricted one phase to volatile oils such as hexane which were condensed onto an aqueous liquid phase to form a thin film 1-4 μm in thickness, while the adsorbed layer was comprised of oil-insoluble molecules.[44] A newer method employs a spin-freeze-

thaw sequence to generate a thin oil layer between a silicon block and an aqueous solution. This method was used to study the adsorption of linear diblock copolymers at the hexadecane-water interface.[45]

1.4.3 X-Ray Reflectivity. X-ray reflectivity has the advantage that X-ray transmission through the sample is less difficult than for neutron reflection and scattering. In hydrocarbon surfactants, however, the lack of refractive index contrast between the surfactant and the solvents limits its applicability to the oil-water interface. Grazing-incidence X-ray surface-scattering was used to study a phospholipid monolayer at the hexadecane-water interface.[46] The study was hindered by scattering by the bulk alkane, by fluctuations in the height of the interface, and by the superposition of scattered X-rays from different boundaries within the interfacial layer (hexadecane/chain, chain/head, and head/water) though a basic description of a densely packed monolayer with all-trans chains was determined. Schlossman *et al* developed a method of flattening the hexane-water interface to reduce the interfacial roughness.[47] Solid-gas phase transitions in monolayers of partially fluorinated alcohols were later observed at the hexane-water interface.[48] This transition was observed to take place via the formation or destruction of small solid domains. This is in contrast to Langmuir layers, which do not exhibit favorable domain formation or destruction during a change of phase.[49] A recent study by Schlossman and coworkers on long-chain (n = 20, 22, 24, 30) alcohols at the hexane-water interface by X-ray reflectivity showed alcohol monolayers with (nearly) all-trans chains normal to the interface undergo a phase transition at higher temperatures in which the surfactants desorb and dissolve into the hexane phase.[50]

1.4.4 Optical Microscopy. Optical techniques such as Brewster angle microscopy (BAM) and fluorescence have been used to study the o-w interface. BAM is sensitive to changes in density or orientation on a macroscopic length scale and is therefore of particular value in the study of domains of coexisting phases. Findenegg and coworkers used BAM to study temperature-induced phase transitions in monolayers of long-chain partially fluorinated alkanols at the hexane-water interface.[51] Fluorescence anisotropy measurements provide information on molecular reorientation. Most surfactants do not fluoresce, but fluorescent dyes doped into surfactant monolayers can be used to probe the structure of monolayers on the assumption that the probe does not interfere with the local structure and dynamics of the film. Fluorescence is also not surface-specific, so amphiphilic dyes, such as acridine orange, are needed. Wirth and coworkers studied monolayers of the anionic surfactant sodium dodecyl sulfate (SDS) containing acridine orange at the water-hexadecane interface in order to establish parallels between the behaviour of the dye molecule in monolayers and micelles.[52] Attempts to repeat the experiment with a cationic surfactant, cetyltrimethylammonium chloride, failed due to charge repulsions between the cationic acridine orange dye and the surfactant. Fluorescence was also used to study the reorientation of acridine orange at an alcohol-modified hexadecane-water interface.[53] Gajraj and Ofoli have designed a total internal reflection fluorescence microscope (TIRFM) to study adsorption and interactions of labeled macromolecules (such as enzymatic proteins) at the oil-water interface.[54] Similarly, Radke, *et al* designed a total internal reflection fluorescence spectrometer (TIRFS) to follow dynamic adsorption and desorption of fluorescent macromolecules (labeled β-casein).[55]

1.4.5 Ellipsometry. Ellipsometry is a sensitive optical technique that measures the change in the polarisation of light upon reflection from a planar interface.[56] It is convenient, non-destructive, and sensitive to variations in molecular adsorption at fluid interfaces. In contrast to surface tensiometry or neutron reflection, however, ellipsometry does not allow the unambiguous determination of the surface excess of surfactants at the o-w interface. Findenegg, *et al* studied the liquid-liquid interface between colloid-rich (colloidal liquid) and polymer-rich (colloidal gas) suspensions of silica colloids, poly(dimethylsiloxane) polymers, and cyclohexane, as well as weakly and strongly amphiphilic nonionic surfactants at various liquid-liquid interfaces.[57] Russev *et al* studied the adsorption kinetics for β-casein at the a-w and o-w interfaces by ellipsometry[58] while Beaglehole and coworkers studied the amino acid tryptophan, the peptide tryptophan-leucine, and the protein bovine serum albumin at the buffered water-oleyl alcohol interface.[59] In general contrast to the behaviour of monomeric surfactants, protein adsorption at the a-w and o-w interfaces was found to be very similar.

1.4.6 Second Harmonic Generation. Second-order nonlinear optical effects are forbidden in centrosymmetric media and are therefore intrinsically surface-sensitive.[60] Second harmonic generation (SHG) is a widely used nonlinear optical technique.[61] Analysis of polarisation-dependent SHG measurements yields information on interfacial symmetry, and the orientation and number density of an amphiphile within an adsorbed layer. From SHG one can also infer the local dielectric properties of an interface[62] and, if the electronic spectrum is changed by protonation, determine the extent of ionization of adsorbed molecules and hence the surface pKa.[63] SHG is a weak effect which relies on resonant enhancement of the molecular

hyperpolarisability by electronic transitions. SHG is therefore restricted to the few surfactants with chromophores in accessible regions of the electromagnetic spectrum. Grubb, *et al* compared SHG from the surfactant sodium 1-dodecyl-naphthalene 4-sulphonate (SDNS) at the a-w, decane-water, and CCl_4-water interfaces.[64] A significant difference in tilt (21° vs 38°) for the naphthalene-sulphonate moiety was found in saturated monolayers at the decane-water and carbon tetrachloride-water interfaces, indicating that the CCl_4-water interface is not necessarily a good model for the oil-water interface. A comparison of phenol, p-nitrophenol, and p-propylphenol at the a-w and hexane-water interfaces showed that the mean tilt was higher at the a-w than o-w interfaces, with the difference being greatest for phenols with a more hydrophilic substituent in the para-position.[65] Interfacial liquid structure at the neat alkane-water interface has been studied by non-resonant total internal reflection SHG.[66] The alkane-water interfaces examined, particularly those with even-numbered alkane carbon chains, were highly ordered. The chain length had a significant effect on the degree of ordering in both the alkane and aqueous interfacial regions. The water–1,2-dichloroethane interface is popular for electrochemical studies. At this interface, SHG has been used to study an azobenzene surfactant and mixed monolayers of multiply-charged polypeptides with charged surfactants.[67]

1.4.7 Sum-Frequency Spectroscopy. Most surfactants lack chromophores in the visible or near-UV, with the result that SHG is very weak and difficult to interpret in terms of chemical structure at the interface. A related nonlinear optical technique is infrared-visible sum-frequency generation (SFG), in which enhancement arises from vibrational transitions in resonance with the IR laser.[68] A visible laser is used to upconvert the IR laser into a readily detectable region of the spectrum. Since all

surfactants have vibrations, sum-frequency spectroscopy (SFS) can be used to study any surfactant that forms an oriented film at an interface. Consequently, SFS has been widely used to study monolayers adsorbed at the solid-air,[69] solid-liquid[69(a),70] (where the solid is either hydrophilic or hydrophobic), and air-water[71] interfaces.

The major drawback of SFG compared to SHG for studying liquid-liquid interfaces is the opacity of liquid phases to the IR laser. For selected liquids, such as carbon tetrachloride, the window of transmission in the IR is wide and absorption of the IR laser by the bulk phase is inconsequential. Richmond and coworkers conducted a number of studies on surfactants at the CCl_4-water interface, which will be discussed in more detail in chapter 8.[72] The neat alkane-water interface has also been studied by SFS in the O–H stretching region where the alkane is transparent.[73] Until now, studies of surfactants at the interface between water and hydrocarbon oils have been frustrated by the fact that both phases are significantly adsorbing in the regions of the mid-IR where the surfactant vibrations occur. I will show in chapters 7 and 8 that SFS of surfactants at the o-w interface is possible if one uses deuterated oil, D_2O, and a protonated surfactant. Commercial deuterated alkanes and D_2O absorb quite strongly in the C–H stretching region, however, and thin liquid films have to be used.

1.4.8 Mixed Monolayers of Surfactant and Oil at the Air-Water Interface. It is worth mentioning briefly the body of literature on mixed monolayers of surfactants and oils at the a-w interface. When small drops of medium-chain alkanes ($n > 8$) are placed on the surface of an aqueous surfactant solution, the oil initially spreads quickly, resulting in an equilibrium between a mixed film of surfactant and oil coexisting with a macroscopic oil lens (or lenses) – a regime known as pseudo-partial

wetting.[74] These mixed monolayers are likely to have similarities to monolayers at the bulk o-w interface, but the absence of the bulk oil phase makes experimental measurements much easier. We have previously looked at mixed monolayers of alkanes and surfactants by SFS, ellipsometry, and surface tensiometry.[75] Two-dimensional solid-liquid phase transitions were observed in the monolayer at temperatures that are very sensitive to the difference in chain length between the surfactant and the alkane. Thomas and coworkers carried out NR and surface tensiometry on mixed monolayers of dodecane with C_{14}TAB,[76] with C_{16}TAB and C_{12}TAB,[77] and with pentaethylene glycol monododecyl ether.[78] Mixed monolayers of phospholipids with dodecane, hexadecane, or bicyclohexyl have been examined by ellipsometry and X-ray reflectivity.[79] The presence of oil in the mixed monolayer has a significant influence on the conformation of the surfactants. Through NR and surface tensiometry, Thomas and coworkers found that the surfactant chains are more extended and upright in the mixed monolayer than in the pure surfactant monolayer, as shown by the thickness of the alkyl chain region of the surfactant in the mixed monolayer. This increased thickness was accompanied by a slightly increased area per molecule of surfactant, which is in contrast to the usual decrease in monolayer thickness as the surface coverage decreases. In the presence of oil, Riegler, Möhwald and coworkers observed a reduction in tilt of the aliphatic chains of phospholipids, an increase in the thickness of the monolayer, and incorporation of alkane chains into the aliphatic chains of the phospholipid monolayer. It is worth noting that phase transition temperatures are not the same for monolayers at the a-w interface and at bulk liquid-liquid interfaces, demonstrating that care must be taken when extrapolating from mixed monolayers to the bulk o-w interface.[80]

1.5 Outline

This thesis presents my investigation of structure and conformational order within monolayers of cationic surfactants at the air-water and oil-water interfaces. I have focused on hexadecyltrimethylammonium halide (CTAX) surfactants, with particular emphasis placed on hexadecyltrimethylammonium bromide (CTAB), since the bromide counterion remains the most popular choice for this surfactant. The transitional system of mixed monolayers of surfactant and alkane at the air-water interface was studied to clarify its similarities with and differences from monolayers of pure surfactant at the air-water and oil-water interfaces. The air-water, mixed monolayer, and oil-water systems were studied through a synergistic combination of surface-sensitive techniques: sum-frequency vibrational spectroscopy, ellipsometry, and surface tensiometry.

Chapter 2 presents the theory behind the experiments presented in this thesis, while chapter 3 details the experimental procedures. Chapter 4 represents the foundation for all my results on CTAB monolayers, and describes the effect of area per molecule on the structure of CTAB monolayers at the air-water interface. Chapter 5 investigates the effect of halide counterion and added electrolyte on CTAX monolayers at the air-water interface for fluoride, chloride, bromide, and iodide counterions. Chapter 6 presents results for mixed monolayers of CTAB and alkanes (with an emphasis on tetradecane) at the air-water interface. Chapter 7 explains the challenge of designing the oil-water interface sum-frequency spectroscopy experiment, and serves as the background to chapter 8, which presents sum-frequency vibrational spectra for CTAB monolayers at the interface between hexadecane and water.

References

(1) The Surfactants and Detergents Association Homepage, http://www.sdahq.org

(2) Dluhy, R. A.; Cornell, D. G. *J. Phys. Chem.* **1985**, *89*, 3195.

(3) Mendelsohn, R.; Brauner, J. W.; Gericke, A. *Annu. Rev. Phys. Chem.* **1995**, *46*, 305.

(4) Dluhy, R. A.; Stephens, S. M.; Widayati, S.; Williams, A. D. *Spectrochim. Acta, Part A* **1995**, *51*, 1413.

(5) Blaudez, D.; Buffeteau, T.; Cornut, J. C.; Desbat, B.; Escarfre, N. *Appl. Spectrosc.* **1993**, *47*, 869.

(6) Als-Nielson, J.; Jacquemain, D.; Kjaer, K.; Leveiller, F.; Lahav, M.; Leiserowitz, L. *Physics Reports* **1994**, *246*, 251.

(7) Möhwald, H. *Rep. Prog. Phys.* **1993**, *56*, 653.

(8) Rieu, J. P.; Legrand, J. F.; Renault, A.; Berge, B.; Ocko, B. M.; Wu, X. Z.; Deutsch, M. *J. Phys. II France* **1995**, *5*, 607.

(9) Lee, E. M.; Thomas, R. K.; Penfold, J.; Ward, R. C. *J. Phys. Chem.* **1989**, *93*, 381.

(10) Hénon, S.; Meunier, J. *Rev. Sci. Instrum.* **1991**, *62*, 4,

(11) Weidemann, G.; Brezesinski, G.; Vollhardt, D.; Möhwald, H. *J. Phys. Chem. B* **1998**, *102*, 1224.

(12) Rondelez, F.; Suresh, K. A. In *Physics of Amphiphilic Layers*; Meunier, J., Langevin, D., Boccara, N., Eds.; Berlin: Springer, 1987, p. 20.

(13) Heckl, W. M. *Thin Solid Films* **1992**, *210/211*, 640.

(14) Cyr, D. M.; Venkatarataman, B.; Flynn, G. W.; Black, A.; Whitesides, G. M. *J. Phys. Chem.* **1996**, *100*, 13747.

(15) Wanless, E. J.; Davey, T. W.; Ducker, W. A. *Langmuir* **1997**, *13*, 4223.

(16) Drude, P. *Ann. Phys. Chem. (Leipzig)* **1891**, *43*, 126.

(17) Rothen, A. *Rev. Sci. Instr.* **1945**, *16*, 26.

(18) Beaglehole, D. In *Fluid Interfacial Phenomena*; Croxton, C. A., Ed. Wiley: New York, 1986, p. 523.

(19) Meunier, J. In *Light Scattering by Liquid Surfaces and Complementary Techniques*; Langevin, D., Ed. Marcel Dekker: New York, 1992, chapter 17.

(20) Azzam, R. M.; Bashara, N. M. *Ellipsometry and Polarized Light.* North Holland: New York, 1987.

(21) Lekner, J. *Theory of Reflection.* Nijhoff: Dordrecht, 1987.

(22) Hecht, E. *Optics*. Addison-Wesley: Massachusetts, 1987.

(23) (a) Harkins, W. D.; Jordan, H. F. *J. Am. Chem. Soc.* **1930**, *52*, 1751. (b) Freud, B. B.; Freud, H. F. *J. Am. Chem. Soc.* **1930**, *52*, 1772. (c) Zuidema, H. H.; Waters, G. W. *Ind. Eng. Chem. Anal. Ed.* **1941**, *13*, 312.

(24) (a) Hirt, E. D.; Prud'Homme, R. K.; Miller, B.; Rebenfeld, L. *Coll. And Surf.* **1990**, *44*, 101. (b) Mysels, J. K. *Langmuir* **1986**, *2*, 428. (c) Mysels, J. K. *Coll. And Surf.* **1990**, *43*, 241.

(25) (a) Schmoluchowski, M. *Ann. Physik* **1908**, *25*, 275. (b) Earnshaw, J.; McGivern, R. C. *J. Phys. D. Appl. Phys.* **1987**, *20*, 82. (c) Earnshaw, J. C.; McGivern. R. C. *J. Coll. Interface Sci.* **1988**, *123*, 37. (d) Earnshaw, J. C.; McGivern, R. C.; McLaughlin, A. C.; Winch, P. J. *Langmuir* **1990**, *6*, 649.

(26) Maiman, T. H. *Nature* **1960**, *187*, 493.

(27) Franken, P. A.; Hill, A. E.; Peters, C. W.; Weinreich, G. *Phys. Rev. Lett.* **1961**, *7*, 118.

(28) Bloembergen, N. *Nonlinear Optics*; World Scientific: Singapore, 1996.

(29) Simon, H. J.; Mitchell, D. E.; Watson, J. G. *Phys. Rev. Lett.* **1974**, *33*, 1531.

(30) Bass, M.; Franken, P. A.; Hill, A. E.; Peters, C. W.; Weinrich, G. *Phys. Rev. Lett.* **1962**, *8*, 18.

(31) Zhu, X. D.; Suhr, H. Shen, Y. R. *Phys. Rev. B* **1987**, *35*, 3047.

(32) Hunt, J. H.; Guyot-Sionnest, P.; Shen, Y. R. *Chem. Phys. Lett.* **1987**, *133*, 189.

(33) Harris, A. L.; Chidsey, C. E. D.; Levinos, N. J.; Loiacono, D. N. *Chem. Phys. Lett.* **1987**, *141*, 350.

(34) Bell, G. R.; Bain, C. D.; Ward, R. N. *J. Chem. Soc. Faraday Trans.* **1996**, *92*, 515.

(35) Snyder, R. G.; Strauss, H. L.; Elliger, C. A. *J. Phys. Chem.* **1982**, *86*, 5145.

(36) MacPhail, R. A.; Strauss, H. L.; Snyder, R. G.; Elliger, C. A. *J. Phys. Chem.* **1984**, *88*, 334.

(37) Guyot-Sionnest, P.; Hunt, J. H.; Shen, Y. R. *Phys. Rev. Lett.* **1987**, *59*, 1597.

(38) Zhang, D.; Gutow, J.; Eisenthal, K. B. *J. Phys. Chem.* **1994**, *98*, 13729.

(39) Bain, C. D. *J. Chem. Soc. Faraday Trans.* **1995**, *91*, 1281.

(40) Buff, F. P.; Lovett, R. A.; Stillinger, F. H. *Phys. Rev. Lett.* **1965**, *15*, 621.

(41) Goebel, A.; Lunkenheimer, K. *Langmuir* **1997**, *13*, 369.

(42) (a) Cosgrove, T.; Phipps, J. S.; and Richardson, R. M. *Colloids Surf.* **1992**, *62*, 199. (b) Cosgrove, T.; Phipps, J. S.; and Richardson, R. M. *Langmuir* **1994**, *9*, 3530.

(43) Staples, E.; Penfold, J.; and Tucker, I. *J. Phys. Chem. B* **2000**, *104*, 606.

(44) (a) Cosgrove, T.; Phipps, J. S.; Richardson, R. M. *Colloids Surf.* **1992**, *62*, 199. (b) Phipps, J. S.; Richardson, R. M.; Cosgrove, T.; Eaglesham, A. *Langmuir* **1993**, *9*, 3530.

(45) Bowers, J.; Zarbakhsh, A.; Webster, J. R. P.; Hutchings, L. R.; Richards, R. W. *Langmuir* **2001**, *17*, 140.

(46) Fradin, C.; Luzet, A.; Braslau, A.; Alba, M.; Muller, F.; and Daillant, J. *Langmuir* **1998**, *14*, 7327.

(47) Mitrinovic, D. M.; Zhang, Z.; Williams, S. M.; Huang, Z.; Schlossman, M. L. *J. Phys. Chem. B* **1999**, *103* (*11)*, 1779.

(48) Tikhonov, A. M.; Li, M.; Schlossman, M. L. *J. Phys. Chem. B* **2001**, *105 (34)*, 8065.

(49) McConnell, H. M.; DeKoker, R. *Langmuir* **1996**, *12*, 4897.

(50) (a) Tikhonov, A. M.; Li, M.; Schlossman, M L. *BNL National Synchrotron Light Source Activity Report 2001*, **2002**, *2.73*, in press. (b) Schlossman, M. L. *Curr. Opinion in Coll. and Interface Sci.* **2002**, *7*, 235.

(51) Uredat, S. and Findenegg, G. H. *Langmuir* **1999**, *15*, 1108.

(52) Piasecki, D. A.; Wirth, M. J. *J. Phys. Chem.* **1993**, *97*, 7700.

(53) Sassaman, J. L.; Wirth, M. J. *Colloids. Surfaces A: Physicochem. Eng. Aspects* **1994**, *93*, 49.

(54) Gajraj, A.; Ofoli, R. Y. *Langmuir* **2000**, *16*, 4279.

(55) Tupy, M. J.; Blanch, H. W.; Radke, C. J. *Ind. Eng. Chem. Res.* **1998**, *37*, 3159.

(56) Keddie, J. L. *Curr. Opinion in Coll. & Interface Sci.* **2001**, *6*, 102.

(57) (a) de Hoog; E. H. A.; Lekkerkerker, H. N. W.; Schulz, J.; Findenegg, G. H. *J. Phys. Chem. B* **1999**, *103*, 10657. (b) Schultz, J.; Hirtz, A.; Findenegg, G. H. *Physica A* **1997**, *244*, 334.

(58) Russev, S. C.; Arguirov, T. V.; Gurkov, T. D. *Colloids & Surfaces B: Biointerfaces* **2000**, *19*, 89.

(59) Beaglehole, D.; Lawson, F.; Harper, G.; Hossain, M. *J. Coll. Interface Sci.* **1997**, *192*, 266.

(60) Bloembergen, N. *App. Phys. B* **1999**, *68*, 289.

(61) (a) Shen, Y. R. *Surface Science* **1994**, *299/300*, 551. (b) Corn, R. M.; Higgins, D. A. *Chem. Rev.* **1994**, *94*, 107.

(62) Wang, H. F.; Borguet, E.; Eisenthal, K. B. *J. Phys. Chem. A* **1997**, *101*, 713.

(63) Tamburello-Luca, A. A.; Hebert, P.; Antoine, R.; Brevet, P. F.; Girault, H. H. *Langmuir* **1997**, *13*, 4428.

(64) Grubb, S. G.; Kim, M. W.; Rasing, T.; Shen, Y. R. *Langmuir* **1988**, *4*, 452.

(65) Tamburello-Luca, A. A.; Hebert, P.; Brevet, P. F.; Girault, H. H. *J. Chem. Soc. Faraday Trans.* **1996**, *92*, 3079.

(66) Conboy, J. C.; Daschbach, J. L.; Richmond, G. L. *J. Phys. Chem.* **1994**, *98*, 9688.

(67) (a) Naujok, R. R.; Paul, H. J.; Corn, R. M. *J. Phys. Chem.* **1996**, *100 (25)*, 10498. (b) Paul, H. J. and Corn, R. M. *J. Phys. Chem. B* **1997**, *101*, 4494.

(68) (a) Hunt, J. H.; Guyot-Sionnest, P.; Shen, Y. R. *Chem. Phys. Lett.* **1987**, *133*, 189. (b) Shen, Y. R. *Nature* **1989**, *333*, 519.

(69) (a) Ong, T. H.; Davies, P. B.; Bain, C. D. *Langmuir* **1993**, *9*, 1836. (b) Braun, R.; Casson, B. D.; Bain, C. D.; van der Ham, E. W. M.; Vrehen, Q. H. F.; Eliel, E. R.; Briggs, A. M.; Davies, P. B. *J. Chem. Phys.* **1999**, *110 (9)*, 4634. (c) Williams, C. T.; Yang, Y.; Bain, C. D. *Langmuir* **2000**, *16 (5)*, 2343.

(70) Bain, C. D. *J. Chem. Soc. Faraday Trans.* **1995**, *91 (9)*, 1281.

(71) (a) Bell, G. R.; Bain, C. D.; Ward, R. N. *J. Chem. Soc., Faraday Trans.* **1996**, *92 (4)*, 515. (b) Bell, G. R.; Manning-Benson, S.; Bain, C. D. *J. Phys. Chem. B*

1998, *102*, 218. (c) Bell, G. R.; Li, Z. X.; Bain, C. D.; Fischer, P.; Duffy, D. C. *J. Phys. Chem. B* **1998**, *102*, 9461. (d) Goates, S. R.; Schofield, D. A.; Bain, C. D. *Langmuir* **1999**, *15 (4)*, 1400.

(72) (a) Messmer, M. C.; Conboy, J. C.; Richmond, G. L. *J. Am. Chem. Soc.* **1995**, *117*, 8039. (b) Conboy, J. C.; Messmer, M. C.; Richmond, G. L. *J. Phys. Chem.* **1996**, *100*, 7617. (c) Conboy, J. C.; Messmer, M. C.; Richmond, G. L. *Langmuir* **1998**, *14*, 6722. (d) Gragson, D. E. and Richmond, G. L. *J. Phys. Chem. B* **1998**, *102*, 569.

(73) Du, Q.; Freysz, E.; Shen, Y. R. *Science* **1994**, *264*, 826.

(74) Brochard-Wyart, F.; Di Meglio, J. M.; Quéré, D.; De Gennes, P.G. *Langmuir* **1991**, *7*, 335.

(75) (a) Lei, Q.; Bain, C. D. unpublished results. (b) McKenna, C. E.; Knock, M. M.; Bain, C. D. *Langmuir* **2000**, *16*, 5853.

(76) Lu, J. R.; Thomas, R. K.; Aveyard, R.; Binks, B. P.; Cooper, P.; Fletcher, P. D. I.; Sokolowski, A.; Penfold, J. *J. Phys. Chem.* **1992**, *96*, 10971.

(77) Lu, J. R.; Thomas, R. K.; Binks, B. P.; Fletcher, P. D. I.; Penfold, J. *J. Phys. Chem.* **1995**, *99*, 4113.

(78) (a) Lu, J. R.; Thomas, Li, Z. X.; Thomas, R. K.; Binks, B. P.; Crichton, D.; Fletcher, P. D. I.; McNab, J. R.; Penfold, J. *J. Phys. Chem. B* **1998**, *102*, 5785. (b) Binks, B. P.; Crichton, D.; Fletcher, P. D. I.; MacNab, J. R.; Li, Z. X.; Thomas, R. K.; Penfold, J. *Colloids and Surfaces A: Physicochem. Eng. Aspects* **1999**, *146*, 299.

(79) Thoma, M.; Schwendler, M.; Baltes, H.; Helm, C. A.; Pfohl, T.; Riegler, H.; Möhwald, H. *Langmuir* **1996**, *12*, 1722.

(80) Lei, Q.; Bain, C. D. unpublished results.

CHAPTER 2

Theory

Chapter 2: Theory

2.1 Interaction of Light with Matter: Linear and Non-Linear Optics

Non-linear optical phenomena are understood through defining the interaction between a material and the electric field of an incident electromagnetic beam. Common optical phenomena are governed by linear optics. In linear optics, the electric field, **E**, is weak in comparison to the field that binds an electron to a nucleus. The induced dipole within a molecule placed in this field responds proportionately to the strength of **E**. In the presence of **E**, the dipole is given by

$$\boldsymbol{\mu} = \boldsymbol{\mu}^{\mathbf{0}} + \alpha\mathbf{E} \tag{2.1}$$

where $\boldsymbol{\mu}^{\mathbf{0}}$ is the static dipole and α is the polarisability. The static dipole is zero in highly symmetric molecules that possess a centre of symmetry or belong to a cubic symmetry group. The induced dipole is usually not in the same direction as the electric field and thus α is represented by a 3×3 tensor.

In condensed phases, one refers to the dipole moment per unit volume, termed the polarisation, **P**. In an electric field

$$\mathbf{P} = \mathbf{P}^{(0)} + \varepsilon_0 \chi^{(1)} \mathbf{E} \tag{2.2}$$

where the dimensionless linear susceptibility, $\chi^{(1)}$, takes the place of the polarisability, and ε_0 is the permittivity of the vacuum.* Few materials exhibit a static polarisation so the $\mathbf{P}^{(0)}$ term shall be dropped from here on. Like α, $\chi^{(1)}$ is a second-order tensor, since the linear response to an electric field may be in a different direction from that field. The linear polarisation is isotropic only in cubic materials, where $\chi^{(1)}$ is diagonal with all three elements equal.

* This expression for **P** is in SI units, Cm^{-2}. $\chi^{(n)}$ has units $(mV^{-1})^{n-1}$ and **E** has units Vm^{-1}. In electrostatic units, the factor ε_0 is not included.

For a simple molecular material, the susceptibility depends on the number of molecules per unit volume, N, multiplied by the molecular polarisability averaged over all orientations of the molecules in the material.

$$\chi^{(1)} = N \langle \alpha \rangle / \varepsilon_0 \tag{2.3}$$

The linear optical properties of isotropic materials are described by the complex refractive index, n, which is related to the susceptibility, $\chi^{(1)}$, by

$$n = \sqrt{(1 + \chi^{(1)})} \tag{2.4}$$

The real component of n affects the speed of light in the medium, $v = c$ / Re(n) and the imaginary component of n determines the absorption coefficient, also described by α

$$\alpha = (4\pi / \lambda_0) \, \mathrm{Im}(n) \tag{2.5}$$

where λ_0 is the wavelength of light in a vacuum. Figure 2.1 compares the properties of linear and non-linear optics.

As **E** approaches the magnitude of the field that binds an electron to its atomic nucleus, non-linear effects become apparent, though these are often weak. NLO effects are significantly increased by resonant enhancement or phase matching. In sum-frequency generation (SFG), resonant enhancement occurs when an incident beam approaches resonance with a molecular energy level. Two incident photons excite a molecule to a virtual state and a single photon at the sum-frequency is emitted. If a molecular energy level coincides with either of the virtual levels, resonance enhancement occurs.

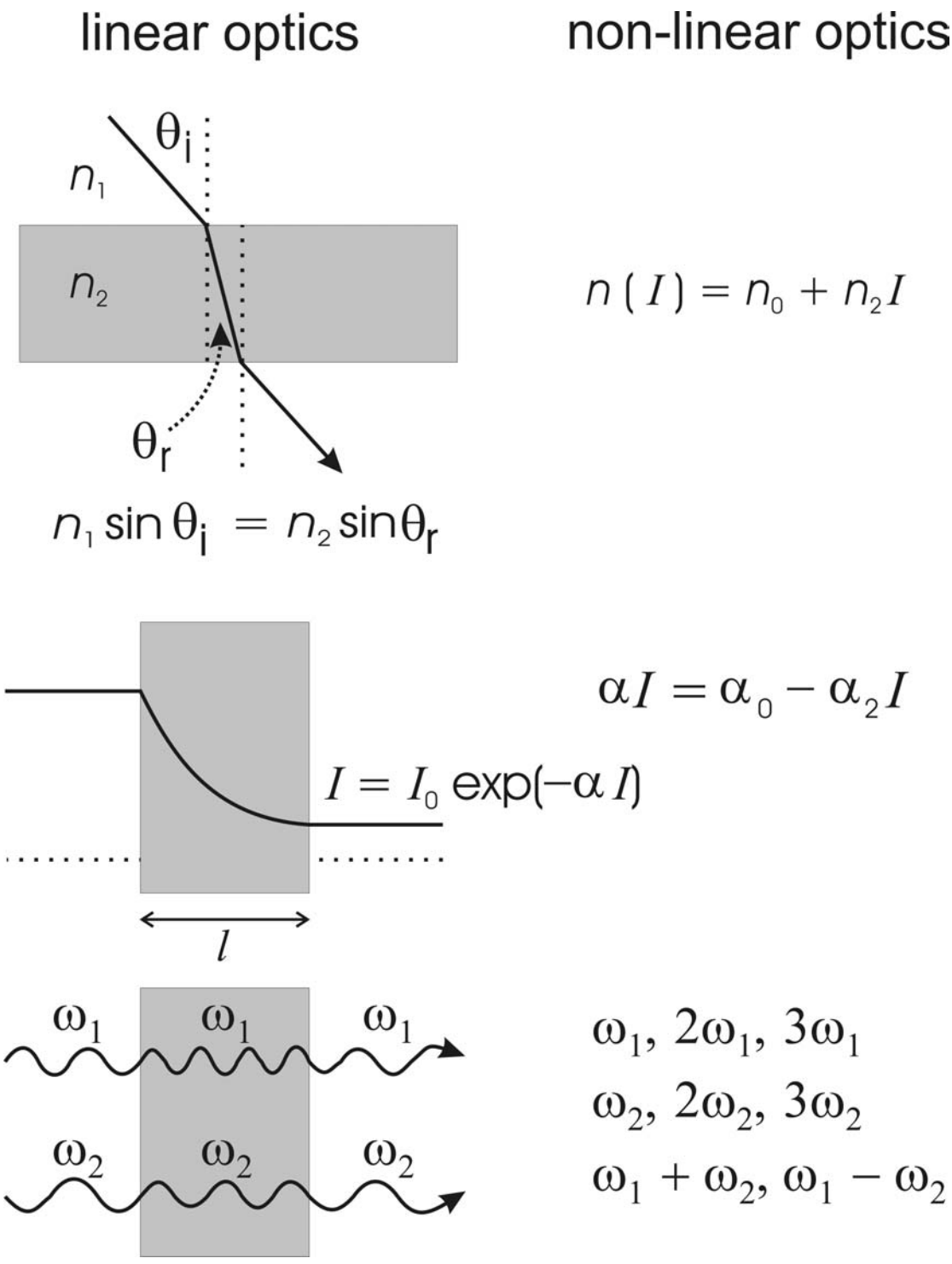

Figure 2.1 *Comparison of linear and non-linear optics. In linear optics, the frequency of the light stays constant as it passes through different optical media. In non-linear optical materials, new frequencies can be generated, and the refractive index (n), and absorption coefficient (α), depend on the intensity of the light.*

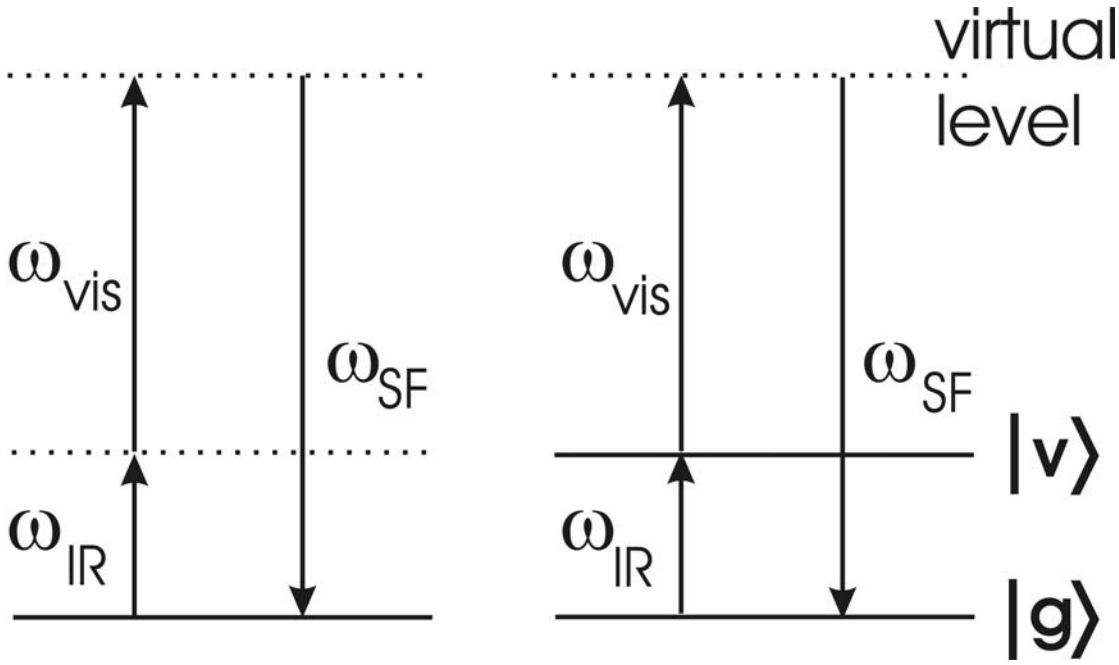

Figure 2.2 *Energy level diagram for SFG. On the left, the incident beam energies do not correspond to any molecular energy levels. On the right, the infrared radiation is at the same energy as a molecular vibrational state, v, and the process is resonantly enhanced.*

For sum-frequency generation, the phase-matching condition relates to the conservation of photon momentum, such that the wave-vector of the SF beam should equal the sum of the wave-vectors of the incident beams

$$\mathbf{k}(\omega_1 + \omega_2) = \mathbf{k}(\omega_1) + \mathbf{k}(\omega_2) \tag{2.6}$$

In the simpler case of second-harmonic generation, the phase-matching condition requires that $n(\omega_1) = n(2\omega_1)$, which can be difficult for materials exhibiting normal dispersion, i.e. their refractive index is an increasing function of frequency. For this reason, NLO crystals often have angular requirements for the incident beam in order to achieve phase-matching.

In the intense light from lasers, the response of electrons to the strong field is no longer harmonic, and higher order terms in **E** must be included in the expression for the dipole moment. Equations 2.1 and 2.2 can be re-expressed as power series to account for non-linear effects. In a molecule, the dipole becomes

$$\boldsymbol{\mu} = \boldsymbol{\mu}^{\mathbf{0}} + \alpha\mathbf{E} + \beta\mathbf{E_1E_2} + \gamma\mathbf{E_1E_2E_3} + \ldots \tag{2.7}$$

where β and γ are the first and second hyperpolarisabilities. In a material, the polarisation is re-expressed as

$$\mathbf{P} = \varepsilon_0 (\chi^{(1)}\mathbf{E} + \chi^{(2)}\mathbf{E_1E_2} + \chi^{(3)}\mathbf{E_1E_2E_3} + \ldots) = \mathbf{P^{(1)}} + \mathbf{P^{(2)}} + \mathbf{P^{(3)}} + \ldots \tag{2.8}$$

The first, second, and third-order susceptibilities: $\chi^{(1)}$, $\chi^{(2)}$, and $\chi^{(3)}$, are tensors of rank 2, 3, and 4, respectively. A tensor of rank *n* has 3^n components. $\chi^{(2)}$ has 27 components which relate the magnitudes of the electric fields to the induced second order non-linear polarisation, $\mathbf{P^{(2)}}$. The higher order terms in eqn. 2.8 result in the refractive index and absorption coefficient exhibiting dependency on the intensity of the light. In addition, with these higher order terms, it becomes possible for the frequency of the light to change.

Let us consider what happens when an incident optical wave of frequency ω, $\mathbf{E}(r, t) = \mathbf{E}(r)\cos\omega t$, interacts with a material in which $\chi^{(2)}$ is non-zero.

$$\begin{aligned} \mathbf{P^{(2)}} &= \varepsilon_0 \chi^{(2)} : \mathbf{EE} \qquad \text{where } \chi^{(2)} : \mathbf{EE} = \textstyle\sum_{j,k} \chi_{ijk}^{(2)} \mathbf{E_jE_k} \\ &= \varepsilon_0 \chi^{(2)} : \mathbf{E}(r)\mathbf{E}(r) \cos^2\omega t \\ &= \tfrac{1}{2} \varepsilon_0 \chi^{(2)} : \mathbf{E}(r)\mathbf{E}(r) (1 + \cos 2\omega t) \end{aligned} \tag{2.9}$$

The first term in the parenthesis represents the static electric field in the material (dc component),[†] while the second term describes a dipole oscillating at 2ω (ac component), a process known as second-harmonic generation. An alternative way to generate a second-order polarisation is to overlap two optical waves on the material simultaneously. If two laser beams with frequencies ω_1 and ω_2 are present simultaneously in a material, then additional terms appear in the expression for $\mathbf{P^{(2)}}$

[†] This term describes a process called optical rectification. Optical rectification is caused by the induced static polarisation which produces a non-oscillating electric field in the medium. If $\mathbf{E_1}$ is a dc field ($\omega_1 = 0$) then an oscillating polarisation is induced at a frequency of ω_2 with a magnitude proportional to the dc field. The dielectric constant becomes a linear function of the dc field strength, and this phenomenon is known as the Pockels effect.

$$\mathbf{P^{(2)}} = \varepsilon_0 \chi^{(2)} : \mathbf{E_1}(r)\mathbf{E_2}(r) \cos\omega_1 t \cos\omega_2 t \qquad (2.10)$$

Eqn. 2.10 leads to the production of a sum-frequency wave ($\omega_1 + \omega_2$) and a difference frequency wave ($\omega_1 - \omega_2$)

$$\mathbf{P^{(2)}} = \tfrac{1}{2} \varepsilon_0 \chi^{(2)} : \mathbf{E_1}(r)\mathbf{E_2}(r) ((\cos(\omega_1 + \omega_2)t + \cos(\omega_1 - \omega_2)t) \qquad (2.11)$$

These processes are known as sum-frequency generation and difference frequency generation (DFG). SHG, SFG, and DFG are used in laser designs to create tuneable light from fixed-frequency lasers. In this thesis, however, we focus on the use of SFG at liquid interfaces, and term this technique sum-frequency spectroscopy.

2.2 Sum-Frequency Spectroscopy

2.2.1 Foundations

Sum-frequency spectroscopy applies SFG to the study of interfaces. In the work described here, SFS utilises the features of second-order non-linear optics such that analysis of SF spectra yields structural information about the interface. In SFS, ω_1 is typically set at a fixed frequency in the visible, while ω_2 is tunable in the mid-infrared. Our spectrometer employs a counter-propagating geometry between the two incident beams and the SF light, ω_{SF}, is detected within the plane defined by the incident laser beams, as shown in Figure 2.3. Across an interface, the component of the electric field parallel to the surface must be continuous. For SFG, the direction of emission is governed by conservation of momentum (see eqn. 2.6) parallel to the interface

$$k_{SF} \sin\theta_{SF} = k_{vis} \sin\theta_{vis} - k_{IR} \sin\theta_{IR} \qquad (2.12)$$

where k_{SF}, k_{vis}, and k_{IR} are the three wavenumbers ($2\pi/\lambda$), θ_{vis} and θ_{IR} are the angles of incidence of the visible and IR lasers, and θ_{SF} is the angle of emission of the SF light.[‡] The angle of emission thus changes as ω_{IR} is scanned through a spectrum. The

[‡] In a co-propagating geometry, the minus sign would be replaced by a plus sign.

primary advantage of counter-propagating geometry is its spatial separation of the visible and SF beams.

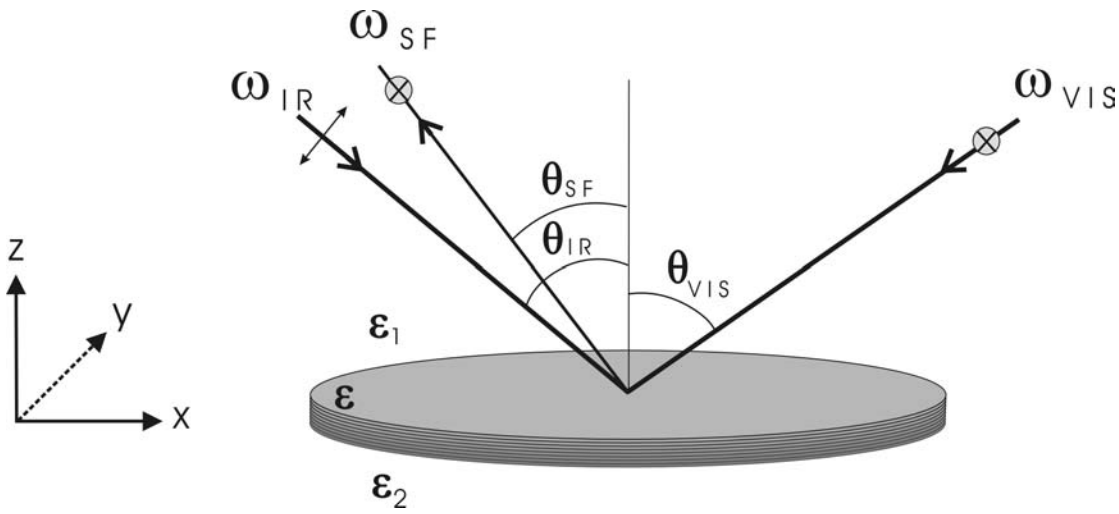

Figure 2.3 *SFG at an interface. The visible and IR beams are incident upon the interface in counter-propagating geometry, and the SF beam is emitted at a defined angle. The dielectric constants of the bulk media are ε_1 and ε_2, and the interfacial region is given a constant of ε. The ssp-polarisation shown is that used in most experiments described here: s- SF beam, s- green beam, p-polarised IR beam. P-polarised beams oscillate in the plane defined by the surface normal and the incident and reflected beams, and s-polarised beams oscillate perpendicular to the plane of incidence (for the reader, through this page).*

The second order susceptibility can be expressed as the sum of a resonant component, $\chi^{(2)}_{\mathrm{R},v}$, due to the vibrational modes of the interfacial molecules, and a non-resonant component, $\chi^{(2)}_{\mathrm{NR}}$, which arises from the substrate

$$\chi^{(2)} = \chi^{(2)}_{\mathrm{NR}} + \sum_{v} \chi^{(2)}_{\mathrm{R},v} \tag{2.13}$$

Over a limited frequency range, $\chi^{(2)}_{\mathrm{NR}}$ can be treated as frequency independent. The resonant and non-resonant susceptibilities are both complex quantities,

$$\chi^{(2)}_{\mathrm{NR}} = \left|\chi^{(2)}_{\mathrm{NR}}\right| e^{i\varepsilon} \tag{2.14}$$

$$\chi^{(2)}_{\mathrm{R}} = \left|\chi^{(2)}_{\mathrm{R}}(\omega_{\mathrm{IR}})\right| e^{i\delta(\omega_{\mathrm{IR}})} \tag{2.15}$$

where ε is the phase of $\chi^{(2)}_{NR}$ and $\delta(\omega_{IR})$ is the phase of $\chi^{(2)}_{R}$. Since SFG is a coherent process, there is interference between the resonant and non-resonant contributions to $\chi^{(2)}$. The intensity of the SF light is proportional to the square modulus of the second-order polarisation.

$$I \propto \left|\chi^{(2)}\right|^2 = \left|\chi^{(2)}_{NR}\right|^2 + \left|\chi^{(2)}_{R}\right|^2 + 2\left|\chi^{(2)}_{NR}\chi^{(2)}_{R}\right|\cos(\varepsilon - \delta(\omega_{IR})) \qquad (2.16)$$

The intensity of the emitted SF light depends on the square of $\chi^{(2)}_{NR}$, the square of $\chi^{(2)}_{R}$, and a cross term which depends on the phase difference, $(\varepsilon - \delta(\omega_{IR}))$.[§] This cross term is not very significant for the experiments described in this thesis since $\chi^{(2)}_{NR}$ is very small and $\left|\chi^{(2)}_{R}\right|^2$ dominates. In contrast, for SFS experiments on metallic substrates such as Au or Ag, this cross term makes a major contribution and the phase relationship between the resonant and non-resonant contributions dictates the line shapes of SF spectra. A large non-resonant background also substantially increases the total SF signal level.

$\chi^{(2)}_{R,v}$ is proportional to the number of molecules, *N*, per unit area and to the molecular hyperpolarisability, β, averaged over all orientations of molecules at the interface.

$$\chi^{(2)}_{R,v} = f\frac{N}{\varepsilon_0}\langle\beta_v\rangle \qquad (2.17)$$

For completeness, we have included in equation 2.17 a factor ***f***, which relates the local electric field experienced by the molecules to the macroscopic electric field in the medium. Local field effects will be discussed further in section 2.2.3. $\chi^{(2)}$ and β are third-rank tensors and change sign under inversion. Surfactant molecules in the bulk

phase are randomly orientated and therefore contributions to $\chi^{(2)}$ from molecules with one orientation are cancelled by contributions from molecules with an opposing orientation. The orientational average over β thus vanishes in the bulk. Although the monolayers examined here are isotropic within the monolayer plane, they are asymmetric with respect to the surface normal. This anisotropy creates non-zero values of $\chi^{(2)}$ which lead to SF emission. The SF signal strength is sensitive to the orientation of the molecules within the monolayer.

Away from a vibrational or electronic resonance, β is negligible. When the IR frequency nears the vibrational frequency, ω_v, of an SF-active mode in the molecule, β is enhanced. Within the electric dipole approximation, β can be expressed in terms of the Raman tensor, α_v, the IR transition dipole moment μ_v, and the relaxation time, Γ^{-1}.

$$\beta_v = \frac{\alpha_v \mu_v}{2\hbar(\omega_v - \omega_{IR} - i\Gamma_v)} \tag{2.18}$$

A more detailed expression for β is found by second-order perturbation theory, as an infinite sum over the quantum states of the system.[1] The complicated general solution simplifies if neither ω_{vis} nor ω_{SF} is in resonance with an electronic transition within the material and only electric dipole transitions are considered. Near a vibrational transition, ω_v, in a molecule, β is given by

$$\beta_{lmn}(\omega_{SF} = \omega_{vis} + \omega_{IR}) = -\frac{1}{2\hbar}\sum_s \left[\frac{\langle g|\mu_l|s\rangle\langle s|\mu_m|v\rangle}{\hbar(\omega_{SF} - \omega_{sg})} - \frac{\langle g|\mu_m|s\rangle\langle s|\mu_l|v\rangle}{\hbar(\omega_{vis} + \omega_{sg})} \right] \left[\frac{\langle v|\mu_n|g\rangle}{\omega_{IR} - \omega_\nu + i\Gamma} \right] \tag{2.19}$$

[§] When the laser frequencies are far from any molecular electronic transitions, the phase of $\chi_R^{(2)}$ increases by π as the frequency is scanned through a vibrational resonance and is ±π/2 at the resonant frequency.

where $|g\rangle$ is the ground state, $|v\rangle$ the excited vibrational state, $|s\rangle$ any other state, Γ^{-1} the relaxation time of the excited vibrational state, $\boldsymbol{\mu}$ the electric dipole operator, and $\hbar\omega_v$ is the energy gap between the ground and excited vibrational state. When ω_{IR} approaches ω_v, β increases and is at a maximum when $\omega_{IR} = \omega_v$ and the SF signal is resonantly enhanced. Scanning ω_{IR} creates a vibrational spectrum of the interfacial molecules.

Eqns. 2.18 and 2.19 show that for a vibrational mode to be SF-active, it must be both Raman- and IR-active. The Rule of Mutual Exclusion states that when a molecule has a centre of inversion, none of its vibrational modes can be both infrared- and Raman-active. Centrosymmetric molecules obey the Rule of Mutual Exclusion and are SF-inactive. Each C–C bond in an all-trans polymethylene chain has a local inversion centre, with the result that the methylene modes of an all-trans chain separate into two sets of modes that are either Raman-active or IR-active, but not both. Consequently, the CH_2 vibrational modes of an all-trans chain are SF-inactive. When a hydrocarbon chain contains gauche conformations, the C–C bond loses its local symmetry, and methylene modes are observed in the SF spectrum. As a result of this sensitivity to local symmetry within the hydrocarbon chain, SFS provides information on the conformation of the chain that is not readily available from other spectroscopic techniques. While there is not yet any satisfactory theory for the intensity of the methylene modes in SF spectra of hydrocarbon chains, the ratio of the line strengths of the symmetric CH_2 (d^+) and symmetric methyl (r^+) stretches is an established qualitative measure of conformational disorder.[2]

2.2.2 Effects of Symmetry within the Molecule and Aggregate

Second-order optical effects cannot occur when the second-order non-linear susceptibility equals zero. All centrosymmetric media possess inversion symmetry which means that for all components of $\chi^{(2)}$,

$$\chi^{(2)}_{ijk} = \chi^{(2)}_{-i-j-k} \tag{2.20}$$

and since $\chi^{(2)}$ is a third-rank tensor, it must change signs upon inversion,

$$\chi^{(2)}_{ijk} = -\chi^{(2)}_{-i-j-k} \tag{2.21}$$

For these two equations to be met within a centrosymmetric environment, $\chi^{(2)} = 0$, and within the electric dipole approximation,[**] second-order NLO effects do not occur. Interfaces are intrinsically non-centrosymmetric, while most bulk phases are centrosymmetric,[††] and thus non-linear effects such as SFG usually are restricted to the interface. To understand the more subtle implications of symmetry on SF spectra, the 27 elements of $\chi^{(2)}$ should be identified. One important property of $\chi^{(2)}$ is that as a tensor, it possesses the same symmetry as the system it describes. Thus understanding the symmetry of the system allows the number of independent elements of $\chi^{(2)}$ to be reduced substantially, with some elements vanishing and others becoming equal.

The interfaces described in this thesis are isotropic in the interfacial plane (uniaxially symmetric). If domains exist that are anisotropic in the interfacial plane, then they are orientated randomly and are smaller than the coherence length of the experiment and therefore behave as though they are uniaxial. A uniaxial monolayer has $C_{\infty v}$ symmetry with the symmetry axis being the surface normal (Fig. 2.3). An

[**] Electric quadrupole and magnetic dipole processes are ignored in all work described in this thesis. These effects are much weaker than electric-dipole allowed second-order effects, typically by orders of magnitude, but could lead to second-order non-linear effects in centrosymmetric materials when the fields are sufficiently intense.

$\chi^{(2)}_{ijk}$ element with a x or y component that appears an odd (once or thrice) number of times does not possess the symmetry of the monolayer and is therefore zero. This condition leaves us with seven non-zero components of $\chi^{(2)}_{ijk}$, of which only four are independent: $\chi^{(2)}_{zzz}; \chi^{(2)}_{xxz} = \chi^{(2)}_{yyz}; \chi^{(2)}_{xzx} = \chi^{(2)}_{yzy}$; and $\chi^{(2)}_{zxx} = \chi^{(2)}_{zyy}$.[‡‡] The ability to probe separate elements of $\chi^{(2)}_{ijk}$ in SFS through polarisation-selection is described in section 2.2.3.1. In this thesis, we will focus on spectra of ssp-polarisation, which probes the component $\chi^{(2)}_{yyz}$.

The macroscopic quantity, $\chi^{(2)}_{ijk}$, is related to the first molecular hyperpolarisability by

$$\chi^{(2)}_{ijk} = \frac{N}{\varepsilon_0} \sum_{\alpha\beta\gamma} \left\langle R_{i\alpha} R_{j\beta} R_{k\gamma} \beta_{\alpha\beta\gamma} \right\rangle \tag{2.22}$$

where $R_{i\alpha} R_{j\beta} R_{k\gamma}$ is a product of transformation matrices from the molecular axis system of (α, β, γ) = (a, b, c) to the laboratory frame of reference. The brackets describe the average over all orientations. This equation is comparable to eqn. 2.3 for the linear susceptibility.

To relate the three unique components of $\chi^{(2)}_{ijk}$: $\chi^{(2)}_{xxz}$, $\chi^{(2)}_{xzx}$, and $\chi^{(2)}_{zzz}$ to the 27 elements of $\beta_{\alpha\beta\gamma}$, one considers the symmetry of the molecule and its normal modes of vibration. For the cationic surfactant molecules examined in this thesis, several symmetry generalisations can be made. The spectra in this thesis are carried out in the C–H stretching region, where the intense peaks of interest are the d^+ symmetric

[††] $\chi^{(2)}$ vanishes by symmetry within isotropic media such as gases, liquids, amorphous solids, as well as many crystalline solids.

[‡‡] Far from electronic resonances, the Raman tensor is symmetric and hence $\chi^{(2)}_{ijk} = \chi^{(2)}_{jik}$. This permutation symmetry reduces the number of independent components of $\chi^{(2)}$ to three.

CH_2 stretch at 2852 cm^{-1} and the r^+ symmetric CH_3 stretch at 2876 cm^{-1}. Figure 2.4 shows the normal modes of vibration for the methylene and methyl groups.

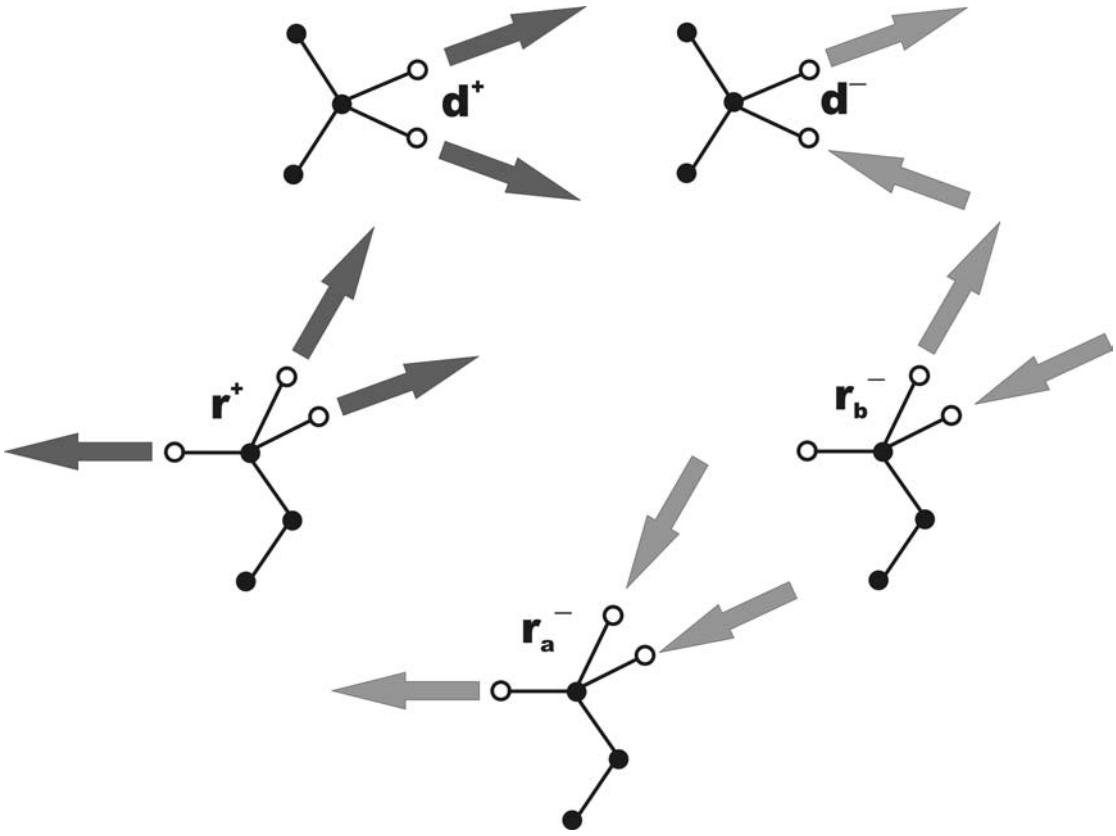

Figure 2.4 *Methyl and methylene stretching modes for an unbranched hydrocarbon chain.*

The d^+ mode is indicative of conformational disorder within the monolayer. For highly ordered monolayers with few gauche defects, the d^+ mode is very weak. As disorder increases, $<\beta_{yyz}>$ increases due to the presence of gauche defects. For a highly disordered monolayer, one might expect $<\beta_{yyz}>$ to decrease again due to cancellation between opposing conformations within the randomly orientated chains.[§§] A hydrocarbon chain with a sample gauche defect is compared to an all-trans hydrocarbon chain in Figure 2.5.

[§§] As will be shown later, such a decrease is not observed in practice.

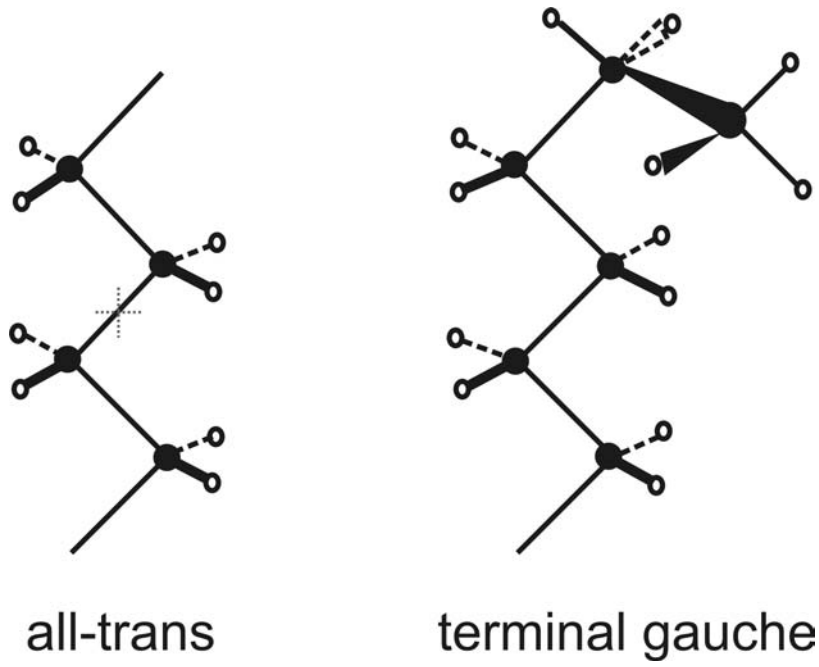

Figure 2.5 *An all-trans hydrocarbon chain compared with a hydrocarbon chain exhibiting a gauche defect. Note that the local centre of symmetry present in the all-trans chain is lost when the chain acquires a gauche defect.*

The key feature of interfacial molecules that differentiates them from the same molecules in solution is their polar orientation. $\chi^{(2)}$ depends on the polar angle, θ, of a functional group through the averages $\langle\cos\theta\rangle$ and $\langle\cos3\theta\rangle$. The line strength of the r^+ mode is dependent on the tilt of the terminal methyl group. The theory for calculating the orientation of the methyl group from the intensity of the r^+ mode in SFS is well established.[3,4,5,6] The methyl group is assumed to have C_{3v} symmetry and the r^+ mode is assumed to be totally symmetric with A_1 symmetry. This simplifies $\beta_{\alpha\beta\gamma}$ such that only three elements are non-zero: β_{ccc} and $\beta_{aac} = \beta_{bbc}$. The assumption of C_{3v} symmetry is weakened by the rotational restriction imposed upon the (terminal) methyl group by the attached hydrocarbon chain. At room temperature, the methyl group does not rotate without an energetic incentive. Furthermore, according to group theory, true C_{3v} symmetry is impossible for the terminal methyl group of a hydrocarbon chain. Group theory assigns a C_s point group to a methyl group attached

to an unbranched hydrocarbon chain. The C_s point group, however, unnecessarily complicates a meaningful quantitative analysis of SF spectra, so the assumption of approximate C_{3v} symmetry prevails.

It is possible to relate the molecular hyperpolarisability to the tilt of the terminal methyl group for β_{zzz}, β_{xxz}, and β_{xzx}. Because the spectra presented in this thesis are overwhelmingly of ssp-polarisation, only the expression for $\beta_{xxz} = \beta_{yyz}$ is shown. In an ssp-spectrum, the component of the hyperpolarisability responsible for the signal from this mode is expressed in molecular coordinates as[4]

$$\left\langle \beta_{yyz} \right\rangle = \frac{\beta_{ccc}}{8}\left\{ \left\langle \cos\theta \right\rangle (1+7r) + \left\langle \cos 3\theta \right\rangle (r-1) \right\} \tag{2.23}$$

where $r = \beta_{aac} / \beta_{ccc}$ and θ is the angle between the surface normal (z) and the C_3-axis of the terminally methyl group (the c-axis). The molecule-centred coordinates, (a,b,c) are related to the laboratory-centred coordinates as shown in Figure 2.6.

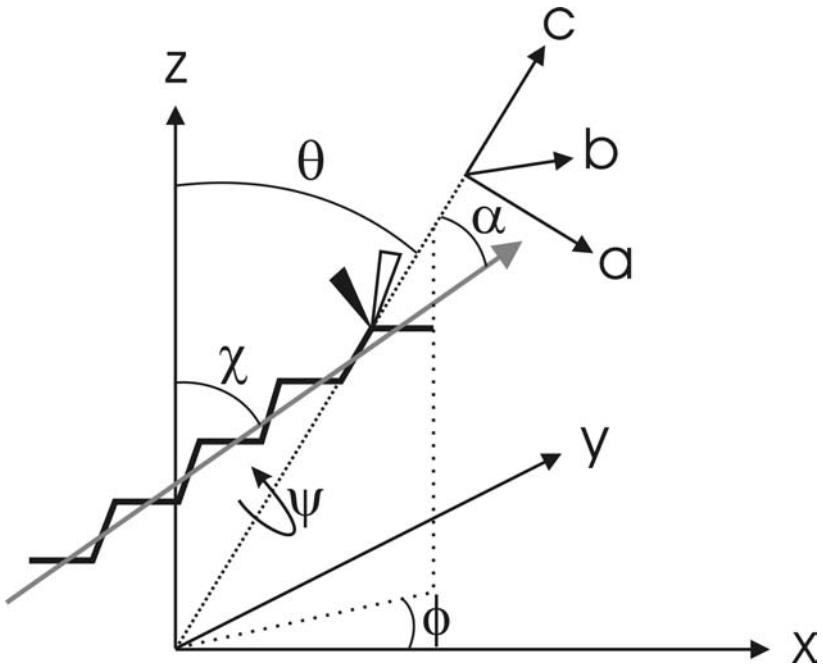

Figure 2.6 *Definition of the molecule-centred coordinates, (a,b,c), and the laboratory-centred coordinates, (x,y,z). For hydrocarbon chains, θ is defined as the angle between the surface normal and the C_3-axis of the methyl group. The angle between the methyl axis and the axis of the hydrocarbon chain is α, and the tilt of the chain from the surface normal is χ.*

The twist, ψ, of the chain is unimportant so long as C_{3v} symmetry is assumed. The azimuthal angle, ϕ, of each molecular chain axis is assumed to be random.

As the first bracketed term dominates in eqn. 2.23, $\langle\beta_{yyz}\rangle$ is proportional to $\langle\cos\theta\rangle$, to a good approximation. In a randomly orientated collection of molecules, $\chi^{(2)}$ vanishes, but if an interface imposes a net polar orientation on molecules at the interface, then $\chi^{(2)}$ is non-zero and SFG can occur.

To relate the tilt of the terminal methyl group to the tilt of the hydrocarbon chain from the surface normal, the relationship between the two must be defined. If the molecule can freely rotate about its molecular axis, then the molecular tilt of the chain from the surface normal is expressed by[7]

$$\langle\cos\theta\rangle = \cos\chi\,\cos\alpha \tag{2.24}$$

$$\langle\cos3\theta\rangle = \cos\chi\,\cos\alpha\,(\,3\cos2\chi\,\cos2\alpha - 2\cos^2\chi\,\cos^2\alpha\,) \tag{2.25}$$

where $\alpha = 34.5°$ is the angle between the molecular axis and the C_3-axis of the methyl group.

2.2.3 Electric Fields at an Interface

2.2.3.1 Effect of Polarisation on SF Emission. The elements of $\chi^{(2)}_{ijk}$ can be probed independently in SFS using polarised incident beams. Table 2.1 describes the available options.

Polarisation Combination	Elements of $\chi^{(2)}$
ppp	$\chi^{(2)}_{zzz}, \chi^{(2)}_{xxz}, \chi^{(2)}_{xzx}, \chi^{(2)}_{zxx}$
ssp	$\chi^{(2)}_{xxz}$
sps	$\chi^{(2)}_{xzx}$
pss	$\chi^{(2)}_{zxx}$

Table 2.1 *Polarisation combinations for SFS at an isotropic interface along with the components of the second-order susceptibility that contribute to spectra obtained with these polarisations (SF, visible, infrared).*

A p-polarised input beam has an electric field oscillating in the x-z plane, and an s-polarised beam has an electric field oscillating only in the y- direction. For the most commonly utilised polarisation, ssp, the visible beam is s-polarised, and the infrared beam is p-polarised. Only ppp-polarised spectra include contributions from more than one of the four independent $\chi^{(2)}$ components.

As introduced in section 2.2.2, for SF and visible frequencies far from any electronic resonances, the Raman tensor is symmetric and the Kleinman symmetry condition is valid.[***] In this case, *i* and *j* can be interchanged, and $\chi^{(2)}_{xzx} = \chi^{(2)}_{zxx}$, and the four independent components of $\chi^{(2)}$ are reduced to three. It is experimentally observed that sps and pss spectra are identical aside from a scaling factor which arises from the different magnitudes of the electric fields in the two cases.

2.2.3.2 Fresnel Coefficients. Light incident on an interface between two media is subject to boundary conditions described by electromagnetic theory. One requirement is that the component of **E** that is tangential to the interface must be continuous across it. A second requirement is that the normal component of **B** is continuous across the

[***] The Kleinman symmetry condition applies when there is full permutation symmetry with the result that $\chi^{(2)}_{ijk} = \chi^{(2)}_{jki} = \chi^{(2)}_{kij} = \chi^{(2)}_{ikj} = \chi^{(2)}_{jik} = \chi^{(2)}_{kji}$.

interface. From Maxwell's equations, the normal component of the product $\varepsilon\mathbf{E}$ and the tangential component of $\mu^{-1}\mathbf{B}$ are also continuous. Cartesian axes are defined in Figure 2.7 as before with *z* normal to the interface, the *x*-*y* plane describing the interface, and the *x*-*z* plane describing the plane of incidence.

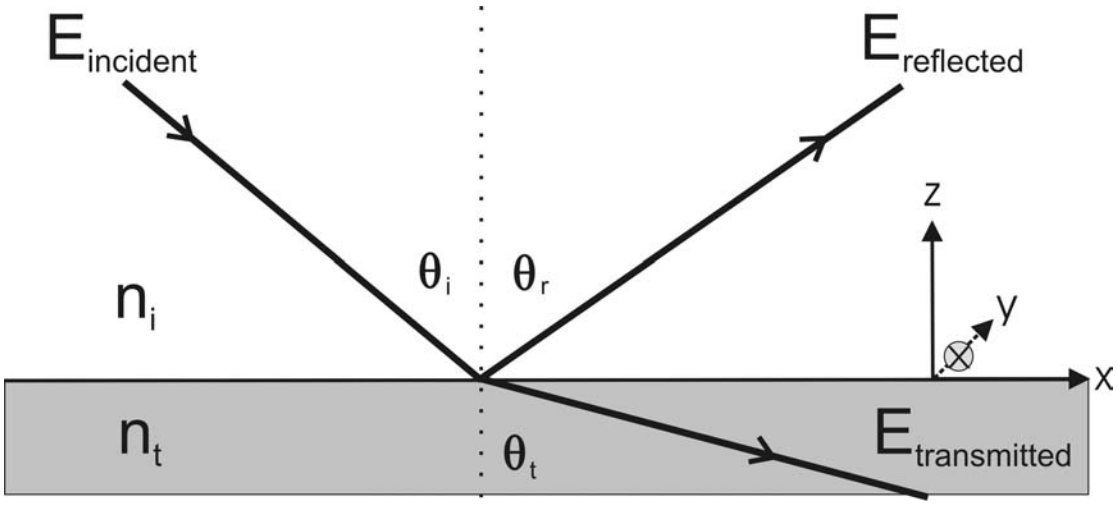

Figure 2.7 *The interface defined according to Cartesian axes with the y-axis extending into the page away from the reader. n_i and n_t are the refractive indices of the incident and transmitting media.*

From these boundary conditions, Fresnel derived equations for the reflected and refracted field strengths relative to the incident field. The two polarisations with respect to the plane of incidence give rise to two complementary sets of equations.

$$K_s^r = \left(\frac{E_{refl}}{E_{inc}}\right)_s = \frac{n_i\cos\theta_i - n_t\cos\theta_t}{n_i\cos\theta_i + n_t\cos\theta_t} \tag{2.26}$$

$$K_s^t = \left(\frac{E_{trans}}{E_{inc}}\right)_s = \frac{2n_i\cos\theta_i}{n_i\cos\theta_i + n_t\cos\theta_t} \tag{2.27}$$

$$K_p^r = \left(\frac{E_{refl}}{E_{inc}}\right)_p = \frac{n_i\cos\theta_i - n_t\cos\theta_t}{n_t\cos\theta_i + n_i\cos\theta_t} \tag{2.28}$$

$$K_p^t = \left(\frac{E_{trans}}{E_{inc}}\right)_p = \frac{2n_i\cos\theta_i}{n_t\cos\theta_i + n_i\cos\theta_t} \tag{2.29}$$

To interpret SFS of an interfacial monolayer, one must understand the electric field strengths in the monolayer. Transmitted field strengths are calculated and the electromagnetic continuity conditions are applied to convert the calculated values to the electric field strengths in the monolayer. The Fresnel transmission coefficients defined above can be correlated to their Cartesian components in the second medium.

$$K_{p,x}^{t} = \frac{2n_i \cos\theta_i}{n_t \cos\theta_i + n_i \cos\theta_t} \cos\theta_t \tag{2.30}$$

$$K_{s,y}^{t} = \frac{2n_i \cos\theta_i}{n_i \cos\theta_i + n_t \cos\theta_t} \tag{2.31}$$

$$K_{p,z}^{t} = \frac{2n_i \cos\theta_i}{n_t \cos\theta_i + n_i \cos\theta_t} \sin\theta_t \tag{2.32}$$

The superscript *t* indicates that we are referring to transmitted field strengths.

When the first medium is optically denser than the second medium, and the angle of incidence exceeds the critical angle defined by $\sin\theta_c = n_t / n_i$, total internal reflection (TIR) occurs. Since no light is transmitted through the boundary, θ_t is imaginary. The imaginary quantity $\cos\theta_t$ may be rewritten in terms of $\sin\theta_i$ using Snell's Law and the trigonometric identity $\cos^2\theta + \sin^2\theta = 1$.

$$\cos\theta_t = \sqrt{1 - \sin^2\theta_t} = \sqrt{1 - \left(\frac{n_i}{n_t}\right)^2 \sin^2\theta_i} \tag{2.33}$$

Eqn. 2.33 can be substituted for $\cos\theta_t$ in equations 2.30 – 2.32. The Fresnel transmission coefficients become complex quantities but are necessary for determining electric field strengths in the interfacial region.

Sum-frequency emission is described by a similar set of coefficients. For SF emission propagating from the interface into medium 1[4]

$$L^{r}_{p,x} = -i4\pi\frac{\omega_{SF}}{c}\frac{\cos\theta_t}{n_t\cos\theta_r + n_i\cos\theta_t} \tag{2.34}$$

$$L^{r}_{s,y} = i4\pi\frac{\omega_{SF}}{c}\frac{1}{n_i\cos\theta_r + n_t\cos\theta_t} \tag{2.35}$$

$$L^{r}_{p,z} = i4\pi\frac{\omega_{SF}}{c}\left(\frac{n_t}{n'}\right)^2\frac{\sin\theta_t}{n_i\cos\theta_t + n_t\cos\theta_r} \tag{2.36}$$

where n′ is the refractive index of the monolayer.

2.2.4 Lineshapes of SF Spectra

The SF signal generated in response to a vibrational resonance at the interface convolutes the resonant signal from the interfacial molecules with any existing non-resonant signal. The intensity of the signal is determined by $|\mathbf{P^{(2)}}|^2$

$$I(\omega_{SF}) \propto \left|F^{R}_{ijk}\chi^{(2)}_{R} + F^{NR}_{ijk}\chi^{(2)}_{NR}\right|^2 \tag{2.37}$$

where F^{R}_{ijk} and F^{NR}_{ijk} represent the combined Fresnel factors for the resonant and non-resonant signal, and $\chi^{(2)}_{R}$ and $\chi^{(2)}_{NR}$ are the second-order susceptibilities of the resonant and non-resonant media, respectively. All four quantities are complex and have an associated phase. From eqn. 2.18 for β_{lmn}, eqn. 2.37 can be rewritten as

$$I(\omega_{SF}) \propto \left|\frac{S_R}{\omega_v - \omega_{IR} - i\Gamma}e^{i\varphi} + S_{NR}e^{i\xi}\right|^2 \tag{2.38 a}$$

where the resonant and non-resonant line strengths, S_R and S_{NR}, are real. φ and ξ are phase factors associated with the resonant and non-resonant SF signal, respectively. Our SF experiments only detect the phase difference ε = ξ − φ.

$$I(\omega_{SF}) \propto \left|\frac{S_R}{\omega_v - \omega_{IR} - i\Gamma} + S_{NR}e^{i\varepsilon}\right|^2 \tag{2.38 b}$$

The phase δ, associated with the resonant term in eqn. 2.38 b, is given by

$$\delta = \tan^{-1}\left(\frac{\Gamma}{\omega_v - \omega_{IR}}\right) \tag{2.39}$$

Interference between δ and ε creates the lineshape of a resonance. The two terms can add constructively to form a peak, add destructively to form a dip, or can form a derivative lineshape if the interference is constructive on one side of ω_v and destructive on the other. For spectra from the air-water and oil-water interfaces, $\chi_R^{(2)} >> \chi_{NR}^{(2)}$, and the non-resonant contribution is small. Resonances in the spectra examined in this thesis therefore are comprised of peaks, with the contribution from S_{NR} only affecting the shape of the peak in its wings. $\chi_{NR}^{(2)}$ plays a significant role in the spectra of GaAs, which lacks of a centre of symmetry and serves as our reference in air-water spectra, and gold, which serves as our reference in oil-water spectra.

2.3 Ellipsometry

Ellipsometry is an optical technique that has been used over the past 150 years, since Jamin first studied water in 1851.[8] Ellipsometry is often employed to analyse organic monolayers on water,[9] but only recently has it become possible to interpret ellipsometric data from monolayers quantitatively. Four problems obstructed quantitative analysis: (i) the results of different experimenters were in poor agreement; (ii) it was difficult to eliminate all impurities and the surface was easily contaminated; (iii) only recently have theoretical developments taken into account the effect of roughness on ellipsometric measurements; (iv) ellipsometry only provides a single measurement for any solution and this measurement does not relate simply to the surface excess. Strachan[10] and Drude[11] were the main theoreticians who developed models for ellipsometry. Drude's theory is widely used today and we have employed it here.

Reflected light is a convenient, non-invasive probe for studying interfaces if one of the bulk phases is transparent. When light is incident on a planar interface between two media with different refractive indices, some of the light is reflected and some is transmitted. Using the notation defined through figure 2.7, with the condition that $\theta_i = \theta_r$, and the angles of the reflected and transmitted beams given by Snell's Law, $n_i \sin\theta_i = n_t \sin\theta_t$, Fresnel's equations describe the amplitude of the transmitted (*t)* and reflected (*r*) fields for ideal, sharp interfaces.[12] The fraction of the incident beam reflected and transmitted can be expressed in terms of θ_i and θ_t.

$$t_s = \frac{2\sin\theta_t \cos\theta_i}{\sin(\theta_i + \theta_t)} \tag{2.40}$$

$$t_p = \frac{2\sin\theta_t \cos\theta_i}{\sin(\theta_i + \theta_t)\cos(\theta_i - \theta_t)} \tag{2.41}$$

$$r_s = -\frac{\sin(\theta_i - \theta_t)}{\sin(\theta_i + \theta_t)} \tag{2.42}$$

$$r_p = -\frac{\tan(\theta_i - \theta_t)}{\tan(\theta_i + \theta_t)} \tag{2.43}$$

Equation 2.43 implies that for $\theta_i + \theta_t = \pi/2$, the in-plane reflection coefficient, r_p, vanishes. This situation occurs if the incident beam obeys $\tan\theta_i = \tan\theta_B = n_t / n_i$, where θ_B is known as the Brewster angle. The ratio r_p / r_s is given by

$$\frac{r_p}{r_s} = \frac{\cos(\theta_i + \theta_t)}{\cos(\theta_i - \theta_t)} \tag{2.44}$$

which vanishes at the Brewster angle. For real interfaces, the situation is more complex, as the refractive index changes smoothly at the interface rather than discontinuously. At a real interface, r_p goes through a minimum but does not vanish.[13] The Brewster angle for a real interface is alternatively defined by $\mathrm{Re}(r_p / r_s) = 0$. For interfaces of a thickness much less than the wavelength of light, θ_B is the same for real and ideal interfaces.

Plane-polarised light incident on an interface reflects with an altered amplitude and polarisation. The optical properties of the interface determine the nature of this change. The technique of ellipsometry is so named since the reflected light is elliptically polarised. In ellipsometry, the ratio r_p / r_s is measured. Because the phase of the light changes upon reflection, this ratio is complex, but the ratio is independent of the absolute intensity of the incident light.

Ellipsometric measurements are reported in one of two ways. Readings are conventionally reported as two angles, Ψ and Δ, where $r_p / r_s = \tan \Psi \, e^{i\Delta}$. When measurements are taken at the Brewster angle, θ_B, the angle at which $\mathrm{Re}(r_p / r_s) = 0$, the experimentally determined quantity is the coefficient of ellipticity, $\bar{\rho} = \mathrm{Im}(r_p / r_s)$ at θ_B. The latter type of measurement is typically taken with phase-modulated ellipsometers, where the effects of static phase shifts from optical components are reduced, and measurements are more sensitive to changes in interfacial structure. Phase-modulated ellipsometers have the additional advantage of taking measurements more quickly and more accurately than conventional ellipsometers, where phase angles are physically measured.[13]

Since $\bar{\rho}$ vanishes for an ideal interface, ellipsometry is particularly sensitive to deviations from ideality at an interface, and can measure these deviations precisely. Drude derived corrections to Fresnel's equations that addressed the transition region between two isotropic continuous phases.[14] When the thickness of the transition region (which is assumed to be optically isotropic) is much less than the wavelength of light, the deviations from Fresnel's equations could be described in terms of a single parameter, η, determined by the permittivity profile of the interface.

$$\eta = \int \frac{(\varepsilon - \varepsilon_1)(\varepsilon - \varepsilon_2)}{\varepsilon} dz \tag{2.45}$$

η describes the change in dielectric constant, ε, across the interface, and ε_1 and ε_2 are the dielectric constants of the first and second media, respectively. The coefficient of ellipticity is given in terms of η by

$$\bar{\rho} = \frac{\pi}{\lambda} \frac{\sqrt{\varepsilon_1 + \varepsilon_2}}{\varepsilon_1 - \varepsilon_2} \eta \tag{2.46}$$

Typical permittivity profiles are shown in Figure 2.8. $\bar{\rho} = 0$ for an ideal Fresnel interface. At the interface between pure water and air, the interface exhibits a transition region[†††] with a permittivity intermediate between that of water and air, and $\bar{\rho} > 0$. Since the permittivity of a hydrocarbon liquid exceeds that of water, the presence of adsorbed surfactant at the air-water interface leads to a negative contribution to $\bar{\rho}$. Typically, increasing the amount of adsorbed surfactant makes $\bar{\rho}$ become increasingly negative.

[†††] The thickness of the transition region, for pure water, is < 1 nm. For a surfactant monolayer, it is 2-3 nm.

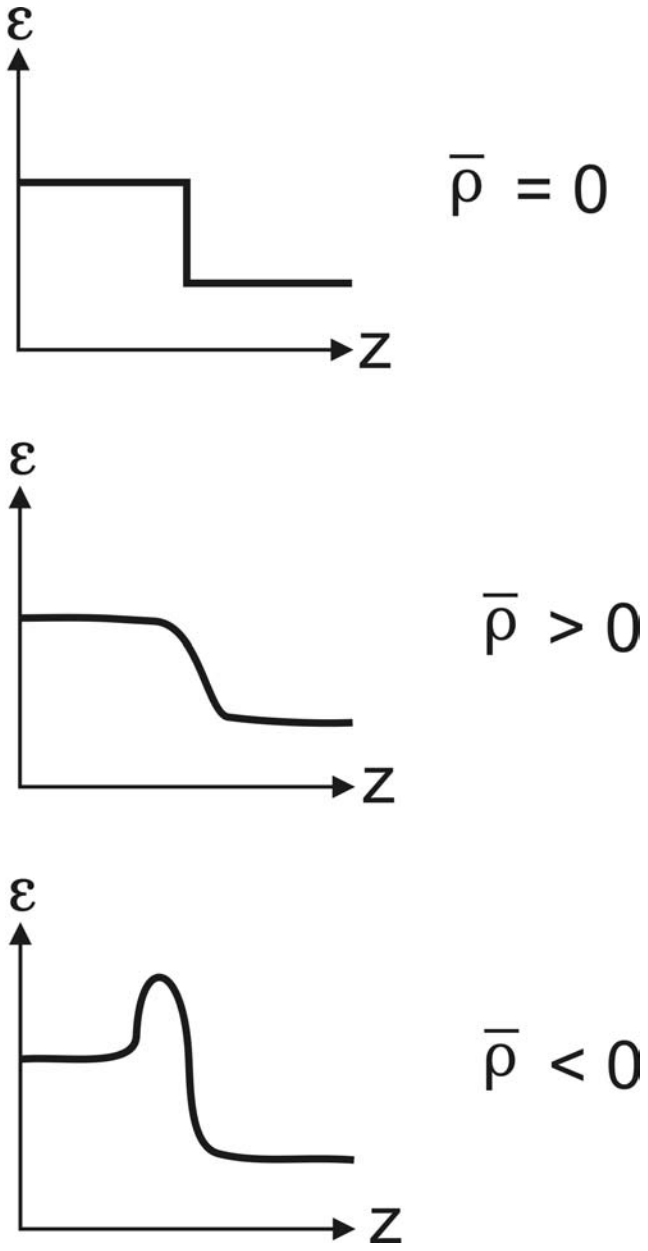

Figure 2.8 *Illustration of permittivity profile through the air-water interface.* $\bar{\rho} = 0$ *represents an ideal Fresnel interface;* $\bar{\rho} > 0$ *is a real interface;* $\bar{\rho} < 0$ *is a real interface in the presence of a surfactant monolayer.*

2.3.1 Surface Roughness and Interfacial Profile

The technique of ellipsometry developed from interest in whether r_p truly falls to zero at θ_B, as predicted by Fresnel's equations.[15] By 1851, measurements of the air-water interface were being made with sunlight,[15] and by 1892, Rayleigh showed that the surface of water has a small, positive ellipticity.[16]

Although the transition in ε does in some way account for roughness, Drude's theory for evaluating the coefficient of ellipticity does not directly consider the contributions of roughness arising from thermally excited capillary waves.[17] It also neglects the contribution of anisotropy, contributed to by the orientation of molecules at the surface.[18,19] In many cases, anisotropy is negligible. Roughness, however, can be significant at liquid interfaces. For pure water, roughness contributes approximately $+4 \times 10^{-4}$ to $\overline{\rho}$. For non-rigid monolayers, the contribution to $\overline{\rho}$ by roughness depends on ε_1, ε_2, and the surface tension, scaling as $\gamma^{-½}$. At solid surfaces, surface defects contribute to surface roughness.

Roughness can be interpreted as the deviation from the step profile ($\overline{\rho} = 0$) at the interface to a transition layer profile where $\overline{\rho} \neq 0$. In a step profile, ε_1 becomes ε_2 over an infinitely small thickness, whereas in a profile with a transitional layer, there is a region where $d\varepsilon/dz \neq 0$. In this region, $\varepsilon_1 < \varepsilon(z) < \varepsilon_2$ and for the air-water interface, $\varepsilon_1 = 1$ and $\varepsilon_2 = 1.77$. This model does not directly address the effect of capillary waves on the reflective properties of the interface.[13]

Meunier has detailed the the effect of capillary wave roughness on ellipsometry at the Brewster angle.[9] The ellipsometric parameter, η, can be split into two terms: η_d attributed to the thickness of the interface, and η_R due to the roughness of the interface. A clean fluid interface without any adsorbate has a thickness of zero and $\overline{\rho}$ arises solely from η_R.

Two parameters describe capillary wave roughness: **q**, the wavevector parallel to the surface, and ζ_q, the amplitude of the sinusoidal wave. According to Fresnel's equations, the reflectivity of p-polarised light at the Brewster angle is zero. Capillary wave roughness deforms the electric field of light at the interface such that light is reflected by a double scattering process. The incident field, at the Brewster angle, is

scattered first by a capillary wave, **q**, and then is scattered a second time by a capillary wave, **−q**. Higher orders (> 2) of scattering can be ignored so long as $|\zeta_q| << \lambda$.

The relative wavelength of the capillary wave to the incident light is important. For $\lambda << 2\pi/q$, the two scattering components are real and the reflected light has the same or opposite phase as the incident light. For $\lambda >> 2\pi/q$, the first-order scattering is evanescent, second-order scattering is imaginary, and thus a phase change of $\pi/2$ is introduced into the reflected beam. Ellipsometry measures phase changes, thus $\overline{\rho}$ is only sensitive to roughness on a scale smaller than the wavelength of light ($2\pi/q < \lambda$).

The amount of scattering, as well as the reflected field, depends on the difference in interfacial dielectric constants ($\varepsilon_1 - \varepsilon_2$), and the curvature of the capillary waves, $q\zeta_q$. The contribution made by capillary wave roughness to the ellipticity is given by[9,13]

$$\eta_R = -\frac{3}{2}\frac{(\varepsilon_1 - \varepsilon_2)^2}{(\varepsilon_1 + \varepsilon_2)}\sum_{\frac{2\pi}{\lambda}}^{q_{max}} q\left\langle \zeta_q^2 \right\rangle \tag{2.47}$$

where $\left\langle \zeta_q^2 \right\rangle$ is the average of the square of the amplitude of a mode **q**.

Capillary waves at the surface of a liquid experience three different restoring forces: gravity, *g*, surface tension, γ, and in the presence of a surface film, the bending modulus of the film, *K*. *K* represents the rigidity imposed by the film onto the interface. $\left\langle \zeta_q^2 \right\rangle$ is then given by,

$$\left\langle \zeta_q^2 \right\rangle = \frac{kT}{g\Delta\rho + \gamma q^2 + Kq^4} \tag{2.48}$$

where $\Delta\rho$ represents the difference in density between the two media. For longer wavelength capillary waves (> 1 mm), or for low q, *g* dominates. For short wavelength **q** ($q > 2\pi/\lambda$) that affect ellipticity measurements, γ and *K* dominate.

When $K >> kT$, as in the case of a condensed monolayer at the air-water interface, wavevectors of high q are suppressed, and eqn. 2.47 can be summed to infinity to obtain η_R. In the case $K << kT$, eqn. 2.47 diverges for high q. For the purpose of calculation, a limit can be introduced, and is usually set at the scale of molecular length. This limit, however, is arbitrary, and η_R varies according to the chosen cut-off point. Meunier has shown that if mode coupling between capillary waves is allowed, γ and K become functions of q, and the summation converges. η_R is then given by[17]

$$\eta_R = -\frac{3}{2}\frac{(\varepsilon_1 - \varepsilon_2)^2}{(\varepsilon_1 + \varepsilon_2)}\sqrt{\frac{\pi kT}{6\gamma}} \tag{2.49}$$

This equation can overestimate the measured value of $\bar{\rho}$ but follows experimentally observed trends.[17] For the oil–water interface, $\bar{\rho}_R$ is negative.

2.3.2 Optical Properties of Monolayers

For an isotropic film, the thickness term is given by

$$\eta_d = \frac{(\varepsilon - \varepsilon_1)(\varepsilon - \varepsilon_2)}{\varepsilon} d \tag{2.50}$$

A measured value of $\bar{\rho}$ depends on two unknowns, ε and d, which can add complexity to the process of analyzing ellipsometric data.

In condensed, ordered monolayers, the elements of the dielectric constant tensor must be considered separately since they are no longer equivalent. At least two values must be considered for the dielectric constant. In monolayers (or Langmuir-Blodgett films) of long-chain hydrocarbon molecules, polarisability along the chain axis is greater than polarisability perpendicular to the chain axis. This molecular differentiation is also present in the condensed film, and the dielectric constant of the film is anisotropic. The precise anisotropy of ε depends on the arrangement of the molecular film. For optically uniaxial films, ε_z is distinguishable from $\varepsilon_x = \varepsilon_y$. ε_z is

termed the extraordinary dielectric constant, ε_e, and $\varepsilon_x = \varepsilon_y$ are termed the ordinary dielectric constant, ε_o. Optically uniaxial anisotropic films include films with molecules normal to the interface, or films with a collective tilt in which the tilt domains are much smaller than the area being analysed, and the azimuthal tilt angle, ϕ, is randomly distributed across the interfacial plane (see fig. 2.6).

Ellipticity is affected by anisotropy. A uniaxially anisotropic film has η_d described by[9,20]

$$\eta_d = \frac{\varepsilon_\perp \varepsilon_\parallel + (\varepsilon_\perp \sin^2\chi + \varepsilon_\parallel \cos^2\chi)(\varepsilon_\perp - 2(\varepsilon_1 + \varepsilon_2)) + 2\varepsilon_1\varepsilon_2}{2(\varepsilon_\perp \sin^2\chi + \varepsilon_\parallel \cos^2\chi)} d_0 \cos\chi \qquad (2.51)$$

where χ is the molecular tilt from the surface normal and $\varepsilon_\perp$ and $\varepsilon_\parallel$ are the dielectric constants perpendicular and parallel to the molecular chain axis. $\varepsilon_\perp$ and $\varepsilon_\parallel$ can be evaluated from the molecular polarisability parallel and perpendicular to the chain axis, $\alpha_\perp$ and $\alpha_\parallel$, using the Lorentz-Lorenz equation

$$\chi^{(1)} = \varepsilon - 1 = \frac{N\alpha}{\varepsilon_0 - \frac{N\alpha}{3}} \qquad (2.52)$$

If the molecular tilt from the surface normal is zero, $\varepsilon_\perp = \varepsilon_o$ and $\varepsilon_\parallel = \varepsilon_e$, and eqn. 2.51 simplifies to[9,21]

$$\eta_d = \frac{(\varepsilon_e - \varepsilon_1)(\varepsilon_e - \varepsilon_2)}{\varepsilon_e} d + (\varepsilon_o - \varepsilon_e) d \qquad (2.53)$$

This equation is the sum of the thickness term for an isotropic monolayer (eqn. 2.50) and a correction for anisotropy. For monolayers at the air-water interface, the first term is usually positive and the second term negative, with possibly comparable magnitudes.

2.3.3 Establishing Molecular Contributions through Ellipsometry

The composite value for $\overline{\rho}$ contains more than a roughness contribution and a single contribution from the thickness of the monolayer. Further analysis can be performed on ellipsometric results to resolve a sum such as $\overline{\rho} = \overline{\rho}_{R} + \overline{\rho}_{chain} + \overline{\rho}_{headgroup} + \overline{\rho}_{counterion}$, where the monolayer thickness contribution is now composed of three different terms from the different parts of the surfactant molecule. $\overline{\rho}_{chain}$ is dependent on the optical density and anisotropy of the monolayer and its calculation through equations 2.53 and 2.50 is described in the preceding section 2.3.2. $\overline{\rho}_{headgroup}$ depends upon the surface excess of the monolayer (calculation described below.) The counterion contribution, $\overline{\rho}_{counterion}$, can be calculated similarly to the head group contribution. Alternatively, one can treat the counterions as being uniformly distributed over a depth of solvent equal to the Debye length and then use tabulated values of the refractive index, *n*, of KX solutions,[22] where X is the halide counterion, as a function of concentration to determine the value of ε to substitute into the Drude equation.[‡‡‡] By either method, $\overline{\rho}_{counterion}$ typically is a linear function of surface excess and the slope is independent of the precise value chosen for the Debye length.

To calculate $\overline{\rho}_{headgroup}$ we first estimate the intrinsic dielectric constant of head groups from the Clausius-Mossotti relationship

$$\frac{\varepsilon - 1}{\varepsilon + 2} = \frac{R_{m}}{V_{m}} \tag{2.54}$$

The molar refractivity, R_m, can be estimated from tabulated values of bond refractivities.[23] For the trimethylammonium head groups of the surfactants examined

[‡‡‡] The contribution of K^+ to *n* can be neglected due to the small size and polarisability of the K^+ ion.

in this thesis, the molar volume, V_m, of $N(CH_3)_3Br$ has been taken to be 140 Å^3,[24] from which the molar volume of Br^- (32 Å^3) is subtracted.

We next assume that the head groups are hydrated and form a mixed layer with water of some thickness estimated from neutron scattering profiles. The dielectric constant of this layer is obtained from the Lorentz-Lorenz effective medium approximation

$$\frac{\varepsilon - 1}{\varepsilon + 2} = \varphi_{\text{water}} \left(\frac{\varepsilon_{\text{water}} - 1}{\varepsilon_{\text{water}} + 2} \right) + \varphi_{\text{head group}} \left(\frac{\varepsilon_{\text{headgroup}} - 1}{\varepsilon_{\text{headgroup}} + 2} \right) \tag{2.55}$$

where the volume fractions φ_{water} and $\varphi_{\text{headgroup}}$ are determined from the surface excess of the surfactant and the molar volume of the head group. The contribution of the head groups to the ellipsometric thickness is given by the isotropic version of the Drude equation (eqn. 2.50) and $\bar{\rho}_{\text{headgroup}}$ is then given by eqn. 2.46. Through these calculations, the experimentally measured value for $\bar{\rho}$ can resolve into a detailed understanding of the optical and conformational properties of the monolayer. Particularly when used in tandem with another surface-sensitive technique such as SFS, ellipsometry supplements the molecular understanding of an interfacial monolayer.

References

(1) Shen, Y. R. *Principles of Non-Linear Optics*, Wiley: New York, 1984.

(2) Ward, R. N.; Duffy, D. C.; Davies, P. B.; Bain, C. D. *J. Phys. Chem.* **1994**, *98*, 8536.

(3) Guyot-Sionnest, P.; Hunt, J. H.; Shen, Y. R. *Phys. Rev. Lett.* **1987**, *59*, 1597.

(4) Hirose, C.; Akamatsu, N.; Domen, K. *Appl. Spectr.* **1992**, *46*, 1051.

(5) Hirose, C.; Akamatsu, N.; Domen, K. *J. Chem. Phys.* **1992**, *96*, 997.

(6) Hirose, C.; Yamamoto, H.; Akamatsu, N.; Domen, K. *J. Phys. Chem.* **1993**, *97*, 10064.

(7) Braun, R.; Casson, B. D.; Bain, C. D. *Chem. Phys. Lett.* **1995**, *245*, 326.

(8) Jamin, J. *Ann. De Phys. Et Chemie* **1851**, *31*, 165.

(9) Meunier, J. In *Light Scattering by Liquid Surfaces and Complementary Techniques*, Langevin, D., Ed. Marcel Dekker: New York, 1992; Chapter 17.

(10) Strachen, C. *Proc. Cambridge Philos. Soc.* **1933**, *29*, 166.

(11) Drude, P. *The Theory of Optics*, Dover: New York, 1959.

(12) Lyklema, J. *Fundamentals of Colloid and Interface Science, Vol. 1: Fundamentals*, 2nd ed., Chap. 7, Academic Press: New York, 1959.

(13) Beaglehole, D. *Physica* **1980**, *100B*, 163.

(14) Drude, P. *Ann. Phys. Chem. (Leipzig)* **1891**, *41*, 126.

(15) Beaglehole, D. *J. Phys. (Paris)* **1983**, supplement to volume *44*, C10-147.

(16) Lord Rayleigh *Phil. Mag.* **1892**, *33*, 1.

(17) Meunier, J. *J. Physique (Paris)* **1987**, *48*, 1819.

(18) Abeles, F. *Ann. Physique* **1950**, *5*, 596.

(19) Engelsen, D. D.; Koning, B. D. *J. Chem. Soc. Faraday Trans. I* **1974**, *70*, 1603.

(20) Lekner, J. *Mol. Phys.* **1983**, *49*, 1385.

(21) Beaglehole, D. *J. Phys. (Paris)* **1983**, supplement to volume *44*, C10-147.

(22) *Handbook of Chemistry and Physics*, 64th Ed.; CRC: Boca Raton, FL, 1984.

(23) Atkins, P. *Physical chemistry,* 3rd Ed., Oxford University Press: Oxford, 1986, chapter 24.

(24) Lu, J.; Simister, E.; Thomas, R. K. T.; Penfold, J. *J. Phys. Chem.* **1993**, *97*, 6024.

CHAPTER 3

Experimental

Chapter 3: Experimental

3.1 The Sum-Frequency Spectrometer

Sum-frequency vibrational spectroscopy requires two laser beams to overlap in space and time at the interface in order to generate light at the sum-frequency. One laser contributes a fixed-frequency visible beam and the second produces a tunable infrared laser beam.[1] Differences in SF systems arise primarily from the method by which tunable infrared light is generated. Optical parametric devices, able to generate picosecond pulses from 2.5-10 μm (4000-1000 cm^{-1}), are a popular choice. Lithium niobate (2.5-4 μm),[2] lithium iodate (2.6-5 μm),[3] and silver gallium sulphide (3-10 μm)[4] are usually employed as non-linear materials. Free-electron lasers, which generate picosecond tunable infrared pulses at wavelengths up to 100 μm, have been used for SFS, though they are dependent on a linear accelerator, and thus unsuitable for use in the typical laboratory.[5] There also are four groups, Oxford included, who have used stimulated Raman scattering to generate tunable infrared light. Either high pressure hydrogen[6] or caesium vapour[7] is used for scattering of nanosecond laser light, for a wavelength range of 3-10 μm.

3.1.1 Laser System. Figure 3.1 shows diagrams of the SF spectrometer we use at Oxford for the air-water (3.1 (a)) and oil-water (3.1 (b) and (c)) SF experiments. This laser system is based on a Q-switched Nd:YAG (Yttrium Aluminium Garnet) laser (Spectron Laser Systems, SL812) which produces a fundamental output at 1064 nm in a 4.4 ns pulse with a repetition rate of 20 Hz. The fundamental output is frequency doubled by a non-linear crystal of $Cs_2D_2AsO_4$ (DCDA) which converts the infrared 1064 nm light to 532 nm green light with a pulse length of 3.5 ns. The temperature of the crystal was maintained at 40 °C and the angle was adjusted to optimise

conversion. Roughly 250 mJ pulse^{-1} or less of green light is produced and is separated from the 1064 nm output by a dichroic mirror. Approximately 10% of the green output is diverted by a beam splitter for use as the visible beam in the SF experiment. The remainder is used to pump a tunable dye laser (Spectron Laser Systems, SL4600).

The dye laser contains a diffraction grating, the angle of which is controlled from a PC via a stepper motor. The grating allows frequency selection of the broadband laser emission of the dye. DCM dye (Exciton) dissolved in Spectrasol®-grade methanol at concentrations of 200 mg dm^{-3} for the oscillator and 80 mg dm^{-3} for the amplifier produces tunable red laser light in the range 630-660 nm. The conversion efficiency of the dye laser is approximately 20% but depends on the Nd:YAG output. The dye laser output also varies with wavelength.

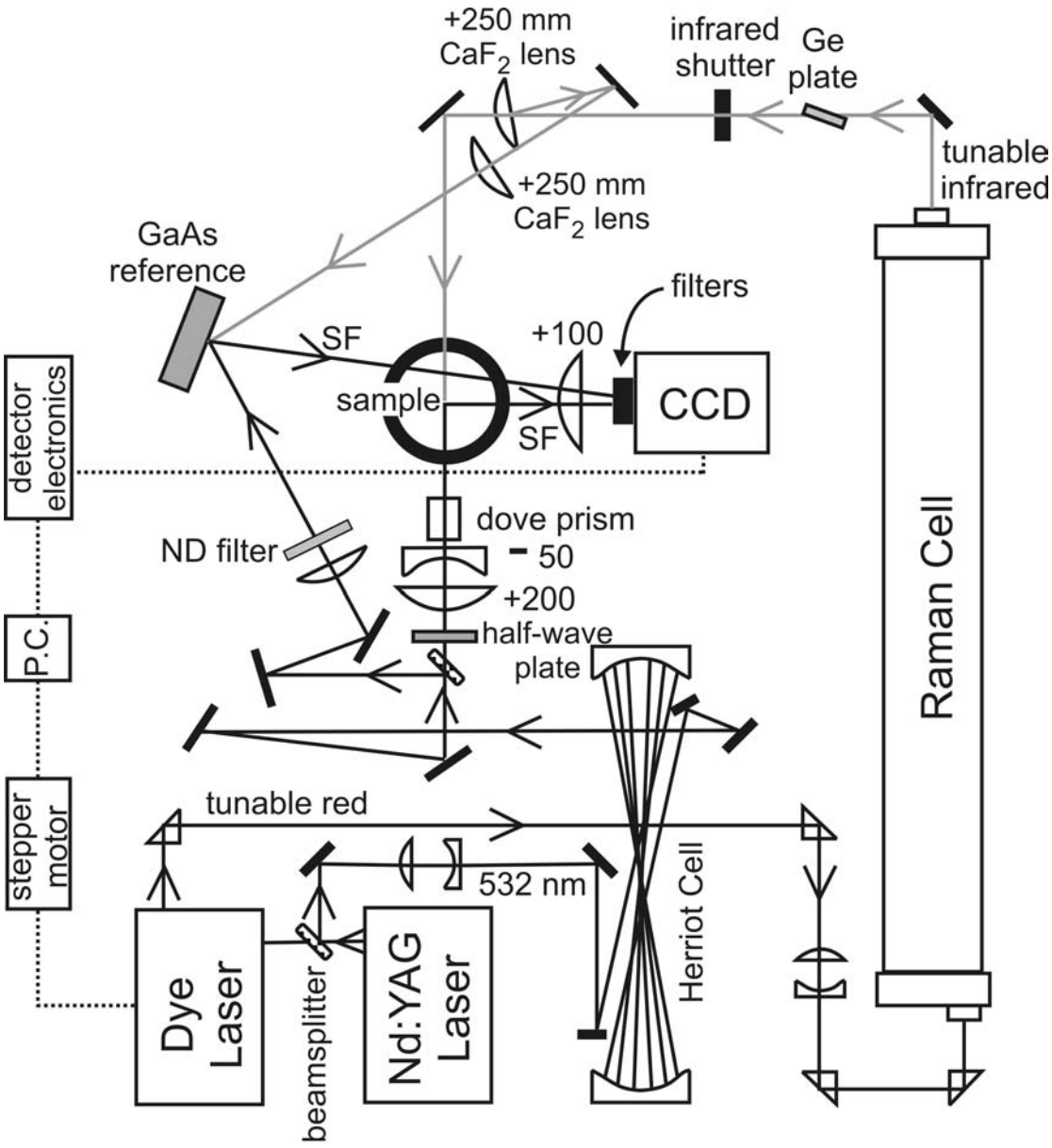

Figure 3.1 (a) *A schematic diagram of the sum-frequency spectrometer during experiments at the air-water interface. The 532 nm beam is steered with dielectric-coated mirrors, the tunable red light with anti-reflection coated prisms, and the infrared with gold-coated mirrors. Two dielectric-coated mirrors are used to steer the SF beam into the CCD.*

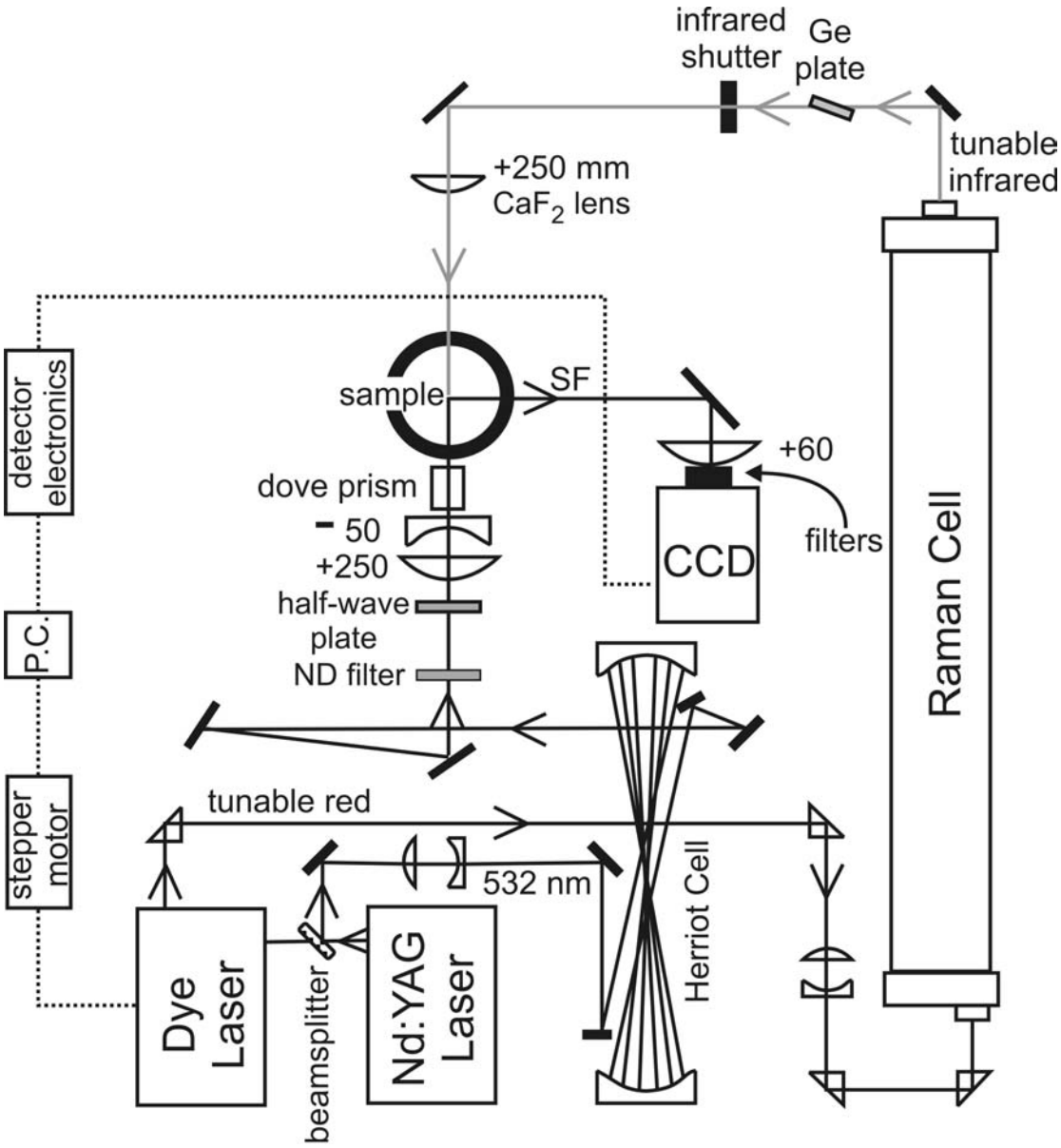

Figure 3.1 (b) *A schematic diagram of the sum-frequency spectrometer during experiments at the oil-water interface. The 532 nm beam is steered with dielectric-coated mirrors, the tunable red light with anti-reflection coated prisms, and the infrared with gold-coated mirrors. Three dielectric-coated mirrors (only the largest final one is illustrated) are used to steer the SF beam into the CCD.*

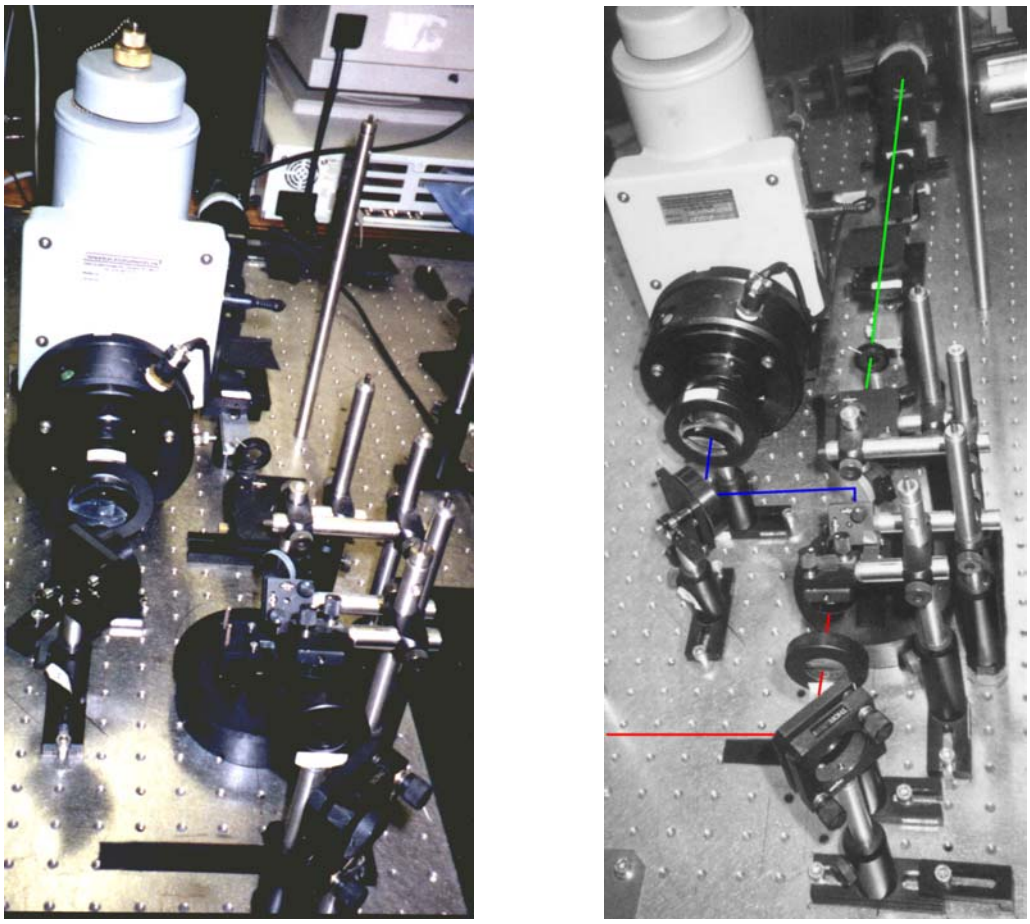

Figure 3.1 (c) *Two complementary photographs of the optics surrounding the oil-water setup. In the black and white photograph on the right, incident green light is depicted by green line; incident infrared light is depicted by red line, and emitted SF light is depicted by blue line. In comparison to Figure 3.1 (b), these photographs view from the opposite side of the optical table.*

3.1.2 Raman Cell. The tunable red light from the dye laser is shifted into the infrared region by stimulated Raman scattering (SRS) in a multi-pass cell filled with high pressure hydrogen (26 bar). SRS is coherent process in which a pump beam loses energy to vibrational excitation of the medium through which it passes. The direction of the beam is maintained. In hydrogen, the most intense transition is the Stokes Q(1) v = 0 to v =1 transition, which corresponds to a shift of 4155 cm^{-1}. A red photon is absorbed and a photon is emitted at 4155 cm^{-1} lower in frequency. To shift into the infrared, a red pump photon undergoes three successive Stokes shifts, each

corresponding to a shift of 4155 cm^{-1}, producing a total shift of 12465 cm^{-1}. Visible red light is thereby converted into tunable mid-infrared radiation.

The optical design of the Raman Cell is based upon a Herriot cell.[6] The Raman Cell consists of a stainless steel cylinder able to withstand pressures of up to 60 bar. Each end contains a concave circular mirror (1 m radius of curvature), and the two mirrors are separated by approximately 2 m. As in a Herriot cell, the mirrors enable the laser beam to travel a long distance in a confined space. The beam enters the cell at one end (4 cm from the centre) through a fused silica window and a hole in the input mirror. The beam is steered by a prism into the cell at an angle such that it strikes the output mirror in a diagonally opposed position from its entry. The beam reflects back and forth between the two concave mirrors a given number of passes such that it traces out a circular path on the mirrors. The beam would exit the cell through the original entry hole but before it can do so, it is reflected out of the Raman cell with a pick-off mirror (2 m radius of curvature), which also serves to recollimate the beam. The beam departs the cell through a hole in the centre of the exit mirror followed by a CaF_2 window. The energy of the third Stokes ouput is maximised at 22 passes,[8] so the eleventh spot on the input mirror is picked off.

The number of passes required for the beam to complete a circular trace on the mirrors is set by the distance between the two mirrors. With our 22 passes, the ten reflections, entry hole, and pick-off mirror form twelve spots on the input mirror that trace out a circular clock shape. The careful adjustments necessary to achieve such alignment are made on three micrometers that control each concave mirror. Two of the micrometers at one end, as well as the pick-off mirror, are motor-controlled and can be moved remotely. Other adjustments must be carried out when the Raman cell is depressurised.

The dye laser beam is focussed at the centre of the cell by a telescope preceding the Raman cell. This situation maximises SRS and ensures the beam is not focussed onto the mirrors, thereby damaging them. We also limit the energy of the red input beam to 30 mJ pulse^{-1} to keep below the damage threshold of the mirrors and input window. Although the ideal situation of mode-matching would have the beam focus at the centre of the cell with each pass, this condition is difficult to achieve without damaging the mirrors. In practice, the spot size was variable, increasing and then decreasing with the 22 passes. Under conditions of mode-matching, the beam would focus at the centre of the cell with each pass, and the radius of curvature of the wavefront of the beam striking the mirror at each reflection in the cell would equal the radius of curvature of the mirrors. The radius of curvature of the wavefront of the beam, however, is a function of the wavelength of the beam, the diameter of the beam at the focus, and the distance between the mirrors.* It is therefore impossible to fulfill mode-matching conditions for both the dye laser frequency and the various Stokes frequencies due to differences in their wavelengths. In addition, the dye laser beam does not have a well-behaved Gaussian profile.

In the required frequency range of 3000-2800 cm^{-1}, the Raman cell produces tunable infrared radiation of approximately 1.0-0.5 mJ pulse^{-1} at 3000 cm^{-1}and 0.6-0.2 mJ pulse^{-1} at 2800 cm^{-1}. This infrared beam has a bandwidth of < 0.2 cm^{-1} and a pulse length of ~1 ns. The polarisation of the infrared light is the same as that of the incident light from the dye laser, which is also the same as the light from the Nd:YAG

* Assuming a Gaussian beam profile, the radius of curvature of the beam wavefront, *r*, at the input mirror after n passes through the Raman cell is given by $r = \frac{L}{2}\left[1+\left(\frac{2L\lambda}{\pi d^2}\right)^2\right]$, where L is the separation between the two mirrors, *d* is the diameter of the beam that strikes the input mirror after n passes, and λ is the wavelength of the beam. [Ward, R. N. *Sum-Frequency Spectroscopy of Molecules at Interfaces*, Ph.D. Thesis, University of Cambridge, 1993.]

laser: parallel to the optical table (horizontal; i.e. s-polarised at a horizontal sample). The infrared polarisation is converted to vertically polarised light when required by successive reflections from two gold mirrors at right angles to each other.

3.1.3 Optical Path. In SFS, the visible and infrared beams must overlap in space and time at the sample. The green and infrared paths are described separately.

3.1.3.1 Herriot Cell and 532 nm Optical Path. In practice, temporal overlap is achieved by delaying the green pulses. The primary delay is accomplished by a Herriot cell, which mimics the path followed by the red beam through the Raman cell, described earlier. The theory for the design of a Herriot cell was given by Herriot and coworkers in 1964,[9] and is based on the optics of a series of equally spaced thin lenses, an analogous situation to a series of reflections between two identical concave mirrors, such as is used in these experiments. The Herriot cell consists of a pair of mirrors (dielectric coating), each with a 1 m radius of curvature and a separation of approximately 2 m. A pair of lenses (+100 mm, –75 mm) reduce the size and re-collimate the green beam. A 12.5 mm diameter mirror (2 m radius of curvature) focuses the beam at the midpoint of the mirrors. The mirror orientations are adjusted with micrometers to obtain a circle of evenly sized spots. The green beam passes through 44 m in the Herriot cell to match the extra distance travelled by the red beam in the Raman cell and dye laser. The green beam makes 25 passes through the Herriot cell before it is picked off. Finer adjustments were made to the length of the delay line by altering the distance travelled by the beam between the mirrors and the sample.

The 532 nm output from the Nd:YAG laser is polarised perpendicular to the optical bench (i.e. p-polarised at a horizontal sample). After the delay line, the green beam passed through a half-wave plate which was used to control the polarisation. A polarising cube was placed after the half-wave plate to check the polarisation of the light. Once the half-wave plate had been adjusted so that there was only s- or p-polarised light, the polarising cube was removed.

3.1.3.2 IR Optical Path. The output from the Raman cell was a mixture of pump, first, second, third Stokes and anti-Stokes radiation. The third Stokes radiation (3200 – 1700 cm^{-1}) was separated from the rest using a germanium plate at the Brewster angle (n = 4.04 at 2900 cm^{-1}; θ_B = 76°). Germanium transmits mid-infrared but reflects or absorbs the other frequencies. This method of separating the infrared is non-dispersive so the direction of light does not change as the frequency is scanned. Gold-coated mirrors were prepared by evaporating chromium (~5 nm thick) and then gold (~200 nm thick) onto a mirror blank.[†] These mirrors were used to steer the infrared beam.

3.1.4 Detection and Optimisation of the SF Signal. The weak signal levels in SFS require a sensitive means of detection. The SF signal was detected by a liquid-nitrogen cooled charge coupled device (CCD). The CCD (Princeton Instruments) contains a chip that is composed of an array of 512 × 512 pixels each 27 μm square. One count on a pixel corresponds to eight detected photons with a detection efficiency as high as 70% at 460 nm. In addition, the low readout noise of approximately one

[†] Previously coated, damaged gold mirrors were stripped of gold and most chromium in a solution of aqua regia prior to recoating.

count per pixel and the very low dark count charge of less than one electron per pixel per hour make the CCD ideal for detecting SF signals.

Pixels may be grouped together, or binned, into larger pixels, quickening the readout time and decreasing the total readout noise. The sample and reference (described in 3.1.5.1) signals were simultaneously detected on different areas of the chip. The SF beams were focussed onto the chip by a 10 cm focal length convex lens. A computer programme tracked the movement of the spot across the chip as the infrared wavelength was scanned during spectral acquisition.

Spectra were acquired in the dark, but scattered light from the visible laser as it struck optics and the sample surface, swamped any SF signal. Two optical filters before the detector were used to block scattered light, while transmitting the SF light at approximately 460 nm. An edge filter (Omega 452DF103) blocked light at wavelengths longer than 502 nm and a bandpass filter (Omega 461.4DF20) blocked light throughout the visible region except for a 20 nm wide window centred at 461.4 nm.

3.1.5 Setup for the Air-Water Interface. The air-water setup is shown in Figure 3.2.

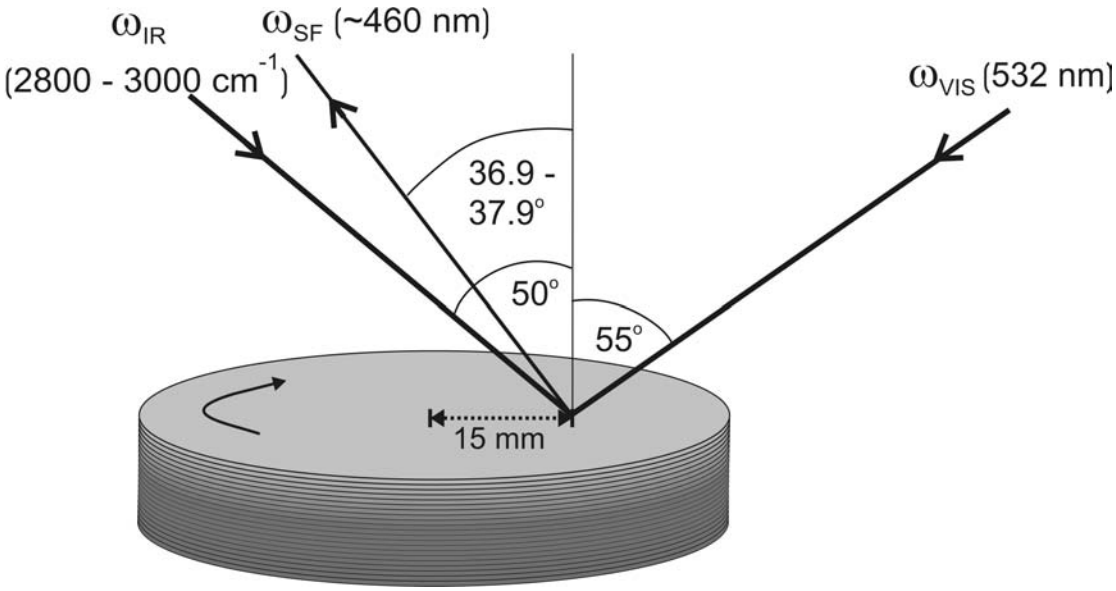

Figure 3.2 *Sum-frequency spectroscopy at the air-water interface. The surfactant solution is rotated to minimise heating by the infrared beam. A lid (not shown) reduces evaporation. The temperature is set by the surrounding cell (not shown), which is connected to a Grant heating and cooling pump unit (LTD6G for SFS, LVF6 for ellipsometry).*

3.1.5.1 Experimental Design of the Air-Water Setup. A telescope reduces the diameter of the green beam to a collimated 2 mm. The infrared is focused at the sample surface with a 250 mm focal length CaF_2 lens to give a diameter of < 1 mm, where the sample is approximately 1 cm from the focal point.

To account for the variation in infrared power with wavelength, a reference is used to normalise the sample SF signal. We use the SF signal from the (111) face of GaAs as a reference. GaAs is a non-centrosymmetric crystal, which allows bulk sum-frequency generation and thus gives a strong SF signal. About 10% of the green beam and 4% of the infrared beam are split off and directed onto the GaAs to generate the reference SF signal. The green beam is split off with a beam splitter and the infrared beam comes from the back reflection off the plano-convex lens used to focus

the infrared on the sample surface. The sample and reference SF signals are detected simultaneously.

A dove prism directs the visible beam down to the sample surface and a gold-coated mirror directs the infrared beam. The angles of incidence for the visible and infrared beams at the sample surface were $\theta_{vis} = 55°$ and $\theta_{IR} = 50°$ with the beams arriving in a counter-propagating geometry. Although co-propagating beams would give more signal, as would total internal reflection geometry, the choice of these incident angles and of counter- rather than co-propagating beams is determined by the practical requirements of the experiment. The incident angles are a compromise that ensures reasonable signal levels with different beam polarisations. The angles of incidence for the reference were practically determined and were $\theta_{vis} = 48°$ and $\theta_{IR} = 64°$. Table 3.1 summarises the properties of the green and infrared beams at the sample.

	Visible	**Infrared**
Wavelength	532 nm	3.6-3.3 μm (2800-3000 cm^{-1})
Energy	8-10 mJ $pulse^{-1}$	0.5-1.0 mJ $pulse^{-1}$
Pulse Length	4 ns	1 ns
Diameter	2 mm	< 1 mm
Angle of Incidence	55°	50°

Table 3.1 *A summary of the properties of the beams incident upon the sample surface at the air-water interface in the sum-frequency spectrometer.*

For both the SFS and ellipsometry experiments the surfactant solutions were contained in a 50 mm diameter glass dish, which was thermostatted by the sample chamber to ± 0.1 °C. A neutral density filter placed in the bottom of the dish absorbed the green beam to reduce scattered light. In the SF experiments, 9 mL of

solution was measured into the dish from a measuring cylinder. For the ellipsometry experiments, the neutral density filter was not necessary and a larger volume of solution was used. For experiments involving phase transitions, temperatures were measured by a Chromel-Alumel thermocouple dipped into the solution at a depth of approximately 1 mm. The precision of these measurements was ± 0.1 °C with an accuracy of ± 0.5 °C.

The sample was rotated to minimise heating due to absorption of the infrared beam by the surfactant solution. A rotation speed of 14 rpm was sufficient to ensure that successive laser pulses struck a different part of the sample surface, thus minimising steady-state heating of the sample. At this speed, the meniscus changed the angles of incidence by < 0.3°. It has been shown previously that with sample rotation, heating by the infrared beam is small enough to be neglected.[10]

Though steady-state heating can be minimised, transient heating by the infrared laser is still unavoidable. Transient laser heating is reduced in all SF experiments described here by using D_2O in place of H_2O. The absorption coefficient of H_2O is much greater than that of D_2O in the 2800-3000 cm^{-1} region.[11] D_2O has an additional advantage over H_2O since the non-resonant background SF signal from H_2O is stronger and thus significantly interferes with the vibrational features of the surfactant molecules in SF spectra. This effect could be useful in the determination of phases for molecular susceptibilities, but in practice, the interference of the background signal makes fitting spectra more difficult.

Any effect of transient heating on SF spectra can be assessed by evaluating the timescale of molecular rearrangments. During the 1 ns pulse, the density of the monolayer and the conformation and orientation of the molecules could change. The speed of sound in water is 1.5×10^3 m s^{-1}, and this speed would be similar for liquid

hydrocarbons. This value limits the rate at which a density fluctuation can be transmitted through the monolayer. Hundreds of nanoseconds are required to transport material out of a region the size of the irradiated area. Transient heating thus does not affect the area per molecule. Molecular dynamics simulations predict that a dense monolayer at constant density reaches thermal equilibrium in 100 ps,[12] suggesting that the conformation and orientation of a molecule could change during the 1 ns infrared pulse. Experimentally, it has been shown that SF spectra of a densely packed monolayer of undecanol in the solid phase are identical at temperatures up to 7 °C apart, with the exception of a scaling factor.[10] This observation suggests that molecular structure is determined principally by the packing density and is insensitive to small changes in temperature at constant density. Since the packing density does not change on a 1 ns timescale, we can assume transient heating has no appreciable effect on molecular structure.[‡] A constant density monolayer simulation of a sixteen-carbon chain in a densely packed structure confirmed this result, showing only small changes in molecular tilt (<1°) and gauche defect density (<1%) with a 10 °C temperature increase.[13] Spectra of CTAB monolayers taken at 313 K were comparable to spectra taken at 303 K.[14]

3.1.5.2 Acquisition of Spectra at the Air-Water Interface. SF signal levels are highly dependent on the overlap of green and infrared beams. The temporal overlap did not change from day-to-day, but the spatial overlap of the two beams was

[‡] Diffusion-controlled adsorption of surfactant molecules from solution to a linear surface is described by $\left(\frac{\Gamma}{C}\right)^2 = \frac{2D}{t}$ where C is the surfactant concentration (prior to adsorption), Γ is the surface excess, D is the diffusion coefficient, and t is the time to reach equilibrium.

optimised* nearly each time a fresh sample was placed in the sample cell. At the start of an experimental run, the green beam would be overlapped visually on the sample with red light travelling along the infrared path. Then, the germanium plate would be replaced and the infrared beam would be realigned along the infrared path. Once SF signals were detectable, they were optimised by steering the infrared beam in small steps across the larger green spot, whilst monitoring the strength of the SF signal.

Before the start of a spectrum, the height and width of the two spots and their extrapolated positions at 2800 and 3000 cm^{-1} (see appendix) were entered into a computer programme that tracked the spots as the infrared frequency was scanned (figure 3.3). Spectra were acquired in 2 cm^{-1} intervals with 36 s per point (720 pulses). Immediately after a spectrum was finished, a background was acquired with the infrared beam blocked. Backgrounds were acquired in 20 cm^{-1} intervals. Every few spectra, and at the beginning and end of each day, the green and infrared powers were measured at 2800 and 3000 cm^{-1}. Binning selected pixels together at each wavelength minimises the amount of background light and read-out noise, while still collecting all the SF photons. The sizes of the sample and reference spots were evaluated for each experiment. The larger the spot, the greater the number of pixels binned together during the acquisition of a spectrum. The protocol for CCD tracking at the air-water interface using the CSMA programs SCNREFD3 and SCNREFDC is provided in the appendix following this chapter.

* When the overlap was optimised on one sample and the sample was then replaced with another, the optimal overlap was retained if the volume of both solutions was carefully measured. The only occasions on which overlap was not re-optimised when the sample was replaced was when the new sample had such a weak signal that it was impossible to carry out the optimisation procedure.

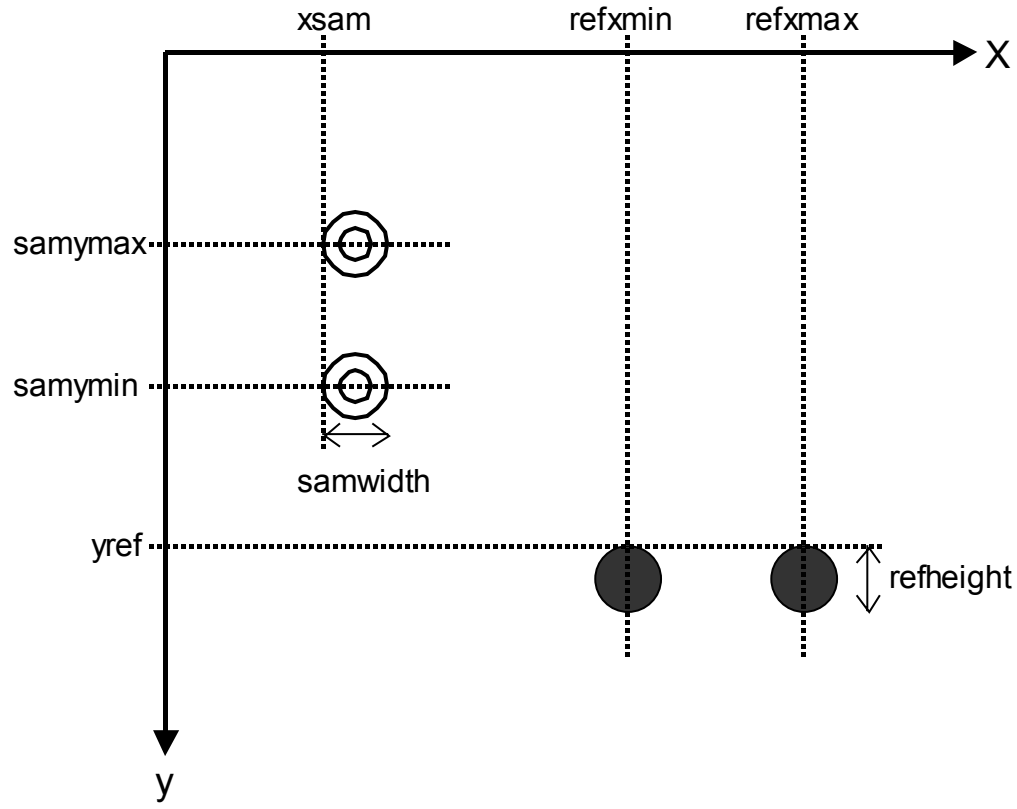

Figure 3.3 *The parameters for tracking the sample (open) and reference (filled) SF spots on the CCD chip during a spectrum. At 2800 cm^{-1} the spots are at samymin and refxmin; at 3000 cm^{-1} the spots are at samymax and refxmax (the y-axis direction is such that samymax < samymin). Since no SF signal is typically present at these frequencies, samymin and samymax are obtained by extrapolation from the positions of the SF spots at 2876 cm^{-1} and 2940 cm^{-1} resonances in an ssp spectrum.*

Linear fits to the sample and reference backgrounds were subtracted from the original sample and reference spectra, and the resultant sample spectrum was divided by the reference. This (spectral) result was then multiplied by the average reference intensity (to eliminate occasional large fluctuations in the absolute day-to-day reference signal) and divided by the green laser power and the average infrared power. After conversion from counts to photons and a division by the number of pulses at each point, the SF signals for spectra at the air-water interface are presented in units of photons $pulse^{-1}$ mJ^{-2}.

Within a continuous set of experiments, spectra were directly comparable. Between sets of experiments, however, variations in SF signal were observed, probably due to variations in beam shape. To allow comparison between different sets of data, I acquired a spectrum of CTAB above the cmc on each occasion. CTAB monolayers above the cmc provided a suitably intense and highly reproducible calibration spectrum. The precision and repeatability of SF spectra were tested by the repeated acquisition of CTAB spectra both above and below the cmc. Spectra taken of CTAB stock solutions at 2×10^{-3} M, which is just over twice the cmc of 9.2×10^{-4} M, were used as standards to ensure that spectra acquired on different days were comparable. Standard CTAB spectra taken above the cmc were found to have a peak line strength at 2853 cm^{-1}, the frequency of the symmetric methylene stretch, with a standard deviation of 7%. The line strength of the symmetric methyl stretch at 2878 cm^{-1} had a standard deviation of 5%.[14]

3.1.6 Setup for the Oil-Water Interface. The design of the oil-water setup is shown in Figure 3.4.

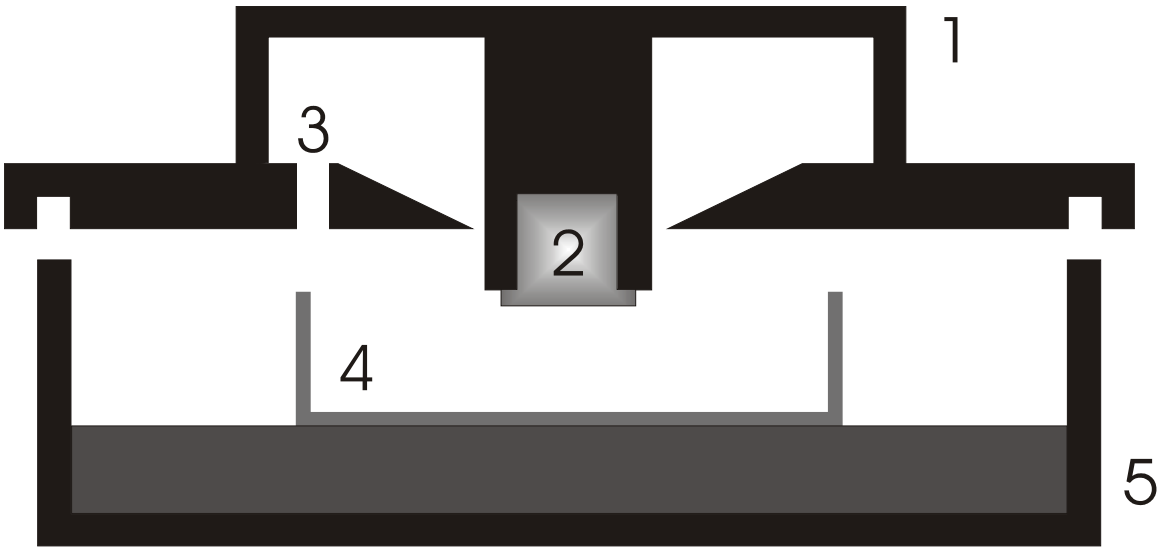

Figure 3.4 *Cross-section of oil-water sample cell used in SFS experiments.* (1) *adjustable height prism brace;* (2) *hydrophobed sapphire prism;* (3) *inlet for adjusting depth of CTAB solution;* (4) *sample dish;* (5) *adjustable height sample cell.*

3.1.6.1 Experimental Design of the Oil-Water Setup. The visible beam (s-polarised, 532 nm, 4 ns, 5 mJ pulse^{-1}, 20 Hz) was overlapped with the tunable infrared beam (p-polarised, 2800-3000 cm^{-1}, ~1 ns, 0.2-0.5 mJ pulse^{-1}) in a counter-propagating geometry at the oil-water interface. The resulting SF signal was emitted in a narrow beam and directed through the edge and band-pass filters into the CCD camera. The angles of the incident laser beams and resulting SF signal at the chosen total internal reflection geometry are discussed in chapter 7. No polarisation-selecting element was placed in the SF beam since for an interface that is isotropic in the interfacial plane, the polarisation of the SF radiation is defined by the choice of input polarisations.

The oil-water sample cell consists of a cylindrical metal lid and chamber. A glass sample dish is placed within the metal chamber and below its lid. This glass

sample dish sits at a predetermined height and contains surfactant solution below a thin oil film. The lid to the sample chamber has one primary opening through which the removable prism holder descends into the sample chamber to a chosen depth. An additional small hole in the lid allows the solution level in the sample dish to be adjusted easily using a Pasteur pipette. Figure 3.4 illustrates a cross-section of the sample cell.

3.1.6.2 Alignment with Gold. SFS requires temporal and spatial overlap between the visible and infrared beams. This alignment is not trivial since the laser beams pass through a number of surfaces before intersecting at the oil–water interface. Optimisation of the alignment on the o-w interface itself is difficult since only a small misalignment leads to vanishing of the SF signal. Initial alignment was therefore carried out with a sapphire prism identical to those used in the oil-water experiments but with the lower face coated with a thin layer of gold, which generates a strong non-resonant SF signal at all IR wavelengths. For the alignment measurements, the ppp-polarisation combination was employed and energy of the visible laser reduced to 0.5 mJ $pulse^{-1}$ to avoid ablation of the gold surface. The beam paths that gave the maximum signal from gold also gave the maximum signal from a surfactant monolayer at the oil-water interface.

3.1.6.3 Acquisition of Spectrum from Gold. After alignment with the gold-coated prism, a ppp-polarised SF spectrum (where the letters refer to the polarisation of the SF, visible, IR fields in order) of gold was acquired in 2 cm^{-1} increments with 200 laser pulses per data point. The variation in SF signal from gold over the 3000-2800 cm^{-1} wavelength range arises principally from the variations in the IR power

generated by the Raman shifter and was used subsequently to normalise the SF spectra from the o-w interface.

3.1.6.4 Acquisition of Spectra at the Oil-Water Interface. CTAB solutions were prepared in D_2O at room temperature and placed in a clean 50-mm diameter glass dish inside the sample chamber. A drop of d_{34}-hexadecane was drawn over one surface of the sapphire prism with a tissue* and a second drop was placed on the surface of the CTAB solution. The second drop normally broke up into a series of small lenses in equilibrium with a microscopically thin mixed monolayer of oil and CTAB. The lid containing the sapphire prism was placed on top of the sample chamber and the level of the CTAB solution was carefully raised by addition of CTAB solution until the surface of the CTAB solution made contact with the prism. Contact can be observed visually from the weakening of reflections of ambient light from the lower prism face. (Incomplete wetting of the prism or penetration of the CTAB solution through the thin oil film is easily observed through perturbations in reflected ambient light.) To confirm that the o-w interface is planar, the lasers were directed (at reduced power) into the sample chamber and a check made that the green and IR beams reflected from the o-w interface follow the same path as the beams incident on the prism-oil interface.

For SF spectra of CTAB solutions under hexadecane, the emitted SF signal is strongest at 2876 and 2938 cm^{-1}. These two peaks were located on the CCD image and used to determine the pixels of maximum signal at all other wavelengths. Before the start of a spectrum, the height and width of the sample spot and its extrapolated positions at 2800 and 3000 cm^{-1} were entered into a computer programme that

* Coating the sapphire prism with a hydrophobic layer is described in section 3.4.4.

tracked the spot as the infrared frequency was scanned (figure 3.3, ignoring reference spot). The protocol for CCD tracking at the oil-water interface using the CSMA programs SCNREFD3 and SCNREFDC is provided in the appendix following this chapter. Spectra were acquired at 2 cm^{-1} intervals between 2800 and 3000 cm^{-1} with 720 laser pulses for each data point (1 h in total per spectrum). The IR beam was then blocked and a background spectrum acquired at 10 cm^{-1} intervals. A linear fit to the background was subtracted from the original sample spectrum. The average IR pulse energies at 3000 and 2800 cm^{-1} were measured after each sample spectrum and subsequently used in the normalisation procedure, which is described in chapter 8. All surfactant spectra were obtained with ssp-polarisation. For this polarisation only one component of χ, $\langle\chi_{yyz}\rangle$, contributes to the SF signal.

3.1.6.5 Acquisition of IR Transmission Spectrum of Oil Film. After the acquisition of a SF spectrum of CTAB at the oil-water interface, the visible laser beam was blocked and the transmitted IR beam was monitored with a laser energy meter (Gentec Sun Em-1) in 2 cm^{-1} increments from 3000 to 2800 cm^{-1}. This process was repeated on different samples and the transmission spectra were averaged.

3.1.7 Fitting SF Spectra. To fit SF spectra,* each peak was characterised by a line strength S_v, a resonant frequency, ω_v, and a homogeneous line width, Γ_v, where

$$S_v(\omega_{IR}) = \frac{S_v}{\omega_v - \omega_{IR} - i\Gamma_v} \tag{3.1}$$

This complex function was convoluted with a Gaussian distribution of resonance frequencies of line width σ to account for inhomogeneous broadening.[15] The resulting function, f_v, was computed numerically for each resonance with preexisting software written in the group. Since the signal-to-noise ratio in these experiments was too low to separate the contributions of Γ and σ to the observed line width, Γ was fixed at a value of 2 cm^{-1} and only σ was allowed to vary. The non-resonant background from the oil-water interface was negligible. Each spectrum $S_{SF}(\omega_{IR})$ was then fitted with the function

$$S_{SF} = \left| \sum_v f_v(\omega_{IR}) \right|^2 \tag{3.2}$$

For spectra acquired at the air-water interface, a weak non-resonant background, S_{NR}, was included in all the fits with a phase of 0° and the spectrum was fitted with the function

$$S_{SF} = \left| S_{NR} + \sum_v f_v(\omega_{IR}) \right|^2 \tag{3.3}$$

* In the case of SF spectra of monolayers at the oil-water interface, spectra were normalised as described in chapter 8 prior to fitting.

3.2 The Ellipsometer

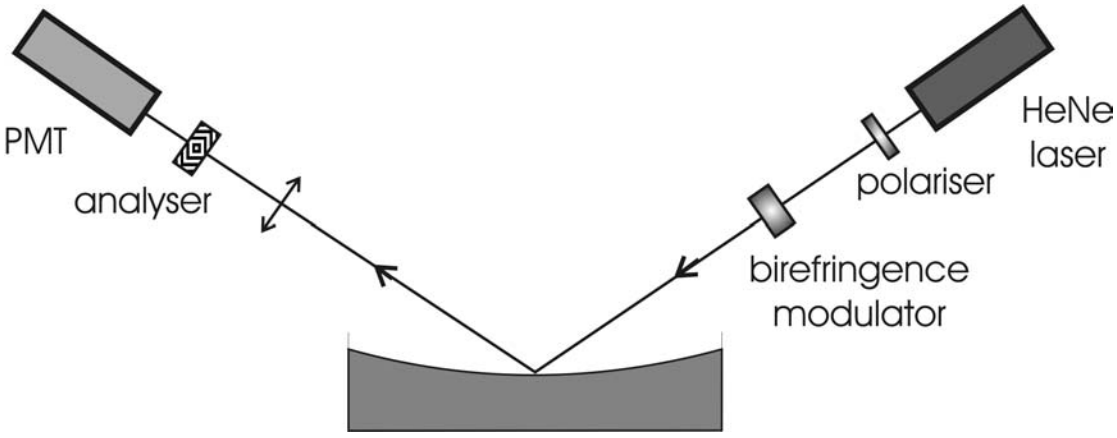

Figure 3.5 *A schematic diagram of the ellipsometer. The analyser flips between its two positions at a frequency of 1.5 Hz.*

Traditional ellipsometry is performed by measuring orientational angles of a polariser, analyser, and compensator at null settings.[16] Our ellipsometer (Beaglehole Instruments, Wellington, New Zealand) is based on a design of Jasperson and Schnatterly.[17] This design incorporates phase modulation of the incident light, providing a faster and more accurate method for ellipsometric measurements on dielectric substrates.

Figure 3.5 depicts our ellipsometer. A 1 mW helium-neon laser provides a plane-polarised red light source at 632.8 nm with a beam diameter of ~ 0.5 mm. The polariser sets the polarisation of the incident beam to roughly equal proportions of s- and p-polarised light, linearly polarised at 45° to the plane of incidence. The birefringence modulator is a quartz slab set into oscillation about its length at its resonant frequency, 50 kHz. The longitudinal oscillation produces a varying birefringence at 50 kHz. Polarised light passing through the birefringence modulator is transmitted with a phase shift between its s- and p-polarised components, which oscillates at a frequency of 50 kHz.

Light reflected from the sample surface is detected by a photomultiplier tube (PMT) and lock-in amplifiers extract signals at 50 kHz and 100 kHz. Instead of measuring the absolute intensity of the reflected light, the high voltage to the PMT is controlled to maintain the photomultiplier current at a constant dc level of 9.8 μA. The amplitude of the ac signals at 50 kHz and 100 kHz is proportional to the constant dc intensity. The feedback into the PMT thus removes the effect of any dc intensity fluctuations that arise from laser variations or changes of sample on the high-frequency signals.

With the dc signal held constant, the signal at 50 kHz is proportional to $\mathrm{Im}(r_p/r_s)$ and the signal at 100 kHz is proportional to $\mathrm{Re}(r_p/r_s)$, where r_p and r_s are the amplitude reflectivities of p- and s-polarised light, respectively.[18] At the Brewster angle, $\mathrm{Re}(r_p/r_s)$ and the signal at 100 kHz is at a minimum. The signal at 50 kHz is then measured and converted into the coefficient of ellipticity with a calibration signal. Each run of experiments is preceded by measurement of the calibration signal. With each measurement, we choose to have the angle of incidence automatically set to the Brewster angle, which is found from the null point in the signal at 100 kHz.

Two Polaroid pieces which transmit s- and p-polarised light (± 45° to the plane of incidence), are placed before the detector in the analyser. The analyser switches between these two positions at a frequency of 1.5 Hz and this signal is detected with a third lock-in amplifier. This low-frequency modulation removes the effects of imperfections in the birefringence modulator on the ellipticity.

The sample cell used for ellipsometry was the same as for SFS. Ellipsometry was typically performed without rotation of the sample, which consisted of solutions prepared in H_2O rather than in D_2O. The coefficient of ellipticity was recorded every second and an average of 50 readings was calculated. The occasional stray reading

caused by noise spikes in the electronics, photon noise, or external vibrations was excluded by establishing acceptance limits on the ellipsometer readings. Less than 5% of readings were rejected in this manner. At least 200 readings contributed to each data point in the experiments described here. An acceptable coefficient of ellipticity was repeatable to within 0.02×10^{-3} and maintained its averaged value for three minutes. A gradual decline of the ellipticity from its pure value indicates adsorption of surface-active molecules at the air-water interface.

3.3 Surface Tensiometry

3.3.1 du Noüy Ring Method. The du Noüy ring method is a simple way to determine the static surface tension.[19] The static maximum pulling force on a wire ring is measured by a balance prior to detachment of the ring from the surface of a liquid. Soon after the development of the ring method, empirically and theoretically verified correction factors were developed to correct for the density of the liquid, the maximum pull on the ring, and the dimensions of the ring.[20] In all surface tensiometry described here, a plot of the correction factor data of Zuidema and Waters was used to correct our du Noüy ring surface tension measurements.[21]

Equilibrium surface tension measurements at the air-water interface were made with a Pt-Ir ring of 20 mm diameter on a Krüss K10 tensiometer. The platinum ring was thoroughly rinsed with UHQ water and flamed before each measurement. An acceptable surface tension was repeatable to within 0.1 mN m^{-1} and drifted less than 0.02 mN m^{-1} during the first minute of measurement. A gradual depression of the surface tension from its pure value indicates adsorption of surface-active molecules at the air-water interface.

3.3.2 Drop Shape Analysis. Surface tensiometry was also performed by axisymmetric drop shape analysis (IT Concept, Longessaigne, France) on digital images of a rising captive drop of hexadecane in water or in aqueous solutions of CTAB at 298 K. The shape of the drop is determined by a balance between buoyancy, which tries to distend the drop, and surface tension, γ, which favors a spherical drop with a minimum surface area. The profile of the drop is computed by balancing the Laplace pressure, $p = \gamma (r_1^{-1} + r_2^{-1})$, where r_1 and r_2 are the local radii of curvature of the drop, against the hydrostatic pressure, and relates the change in pressure and surface tension to the radii of a curved surface. Laplacian drops were analysed to derive the interfacial tension at 298 K. The precision of the readings obtained using this method can be related to a factor termed the bond number,

$$B = \frac{\Delta\rho g r^2}{\gamma} \qquad (3.3)$$

where $\Delta\rho$ is the density difference between the two phases, g is the force of gravity, r is the mean radius of the drop, and γ is the interfacial tension. The volume of the drop was varied so that B was in the range 0.01 – 0.2.

An important experimental detail related to the use of this surface drop analysis method relates to the definition of the "frontier," which defines the area of the drop's picture (and thus the drop's shape) that is analysed. The manual for this tensiometer states that the frontier for a 'sessile' drop should be set at or above the level of the tip of the syringe needle.[22] Unfortunately, following this lax advice can lead to inaccurate results. My work with this machine indicated that it was essential to determine a well-defined method for frontier setup that led to repeatable surface tension results. If one varies the method for selecting a frontier from measurement to measurement, a range of surface tension values becomes available, perhaps as wide as

several mN m^{-1}, depending on the sample. Such variation is unacceptable. If one relies on surface tension data for the analysis of a system, it is important to achieve repeatable results. The figures below indicate the range of surface tension values obtained for different frontier settings for the same sample drop. This captive drop of oil is approximately 3 μL volume and is in contact with a very dilute solution of CTAB in water.

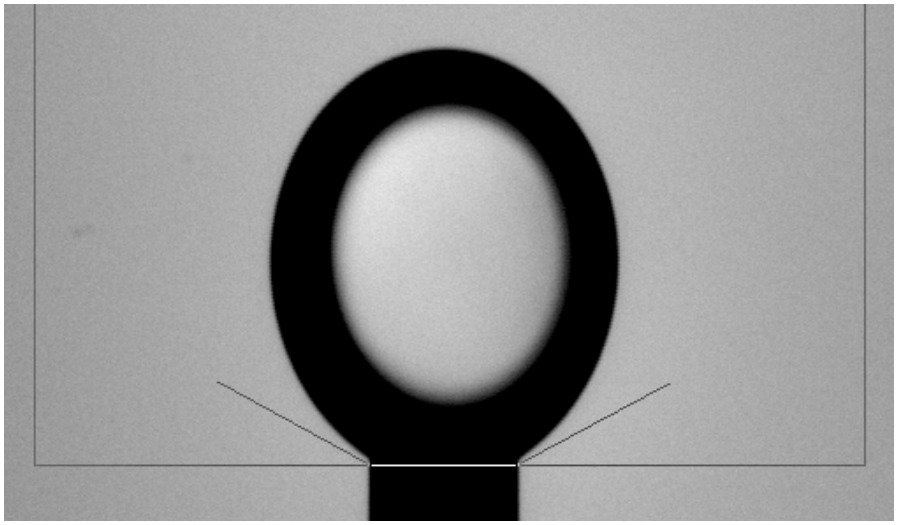

Figure 3.6 (a) *Frontier definition below the edge of the syringe (height = 372) results in erroneous drop shape analysis. γ = 38.378 mN/m*

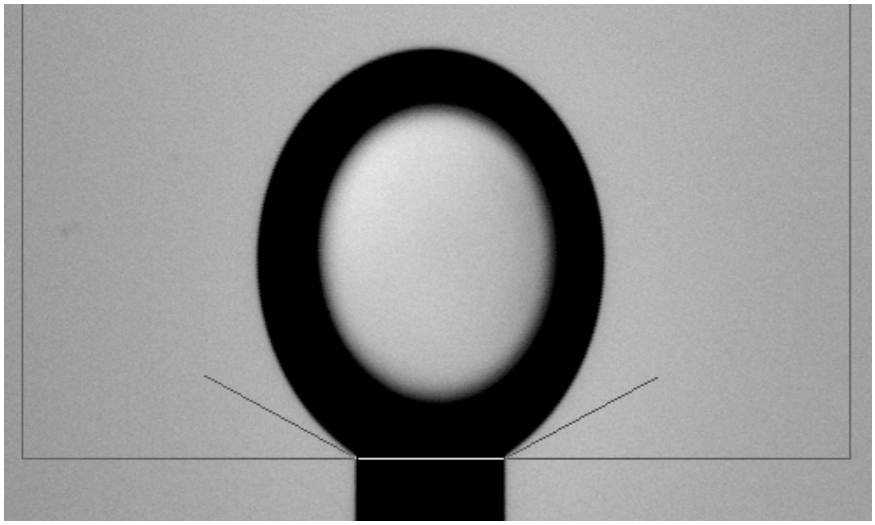

Figure 3.6 (b) *Frontier definition just below the edge of the syringe (height = 370) results in erroneous drop shape analysis. γ = 42.920 mN/m*

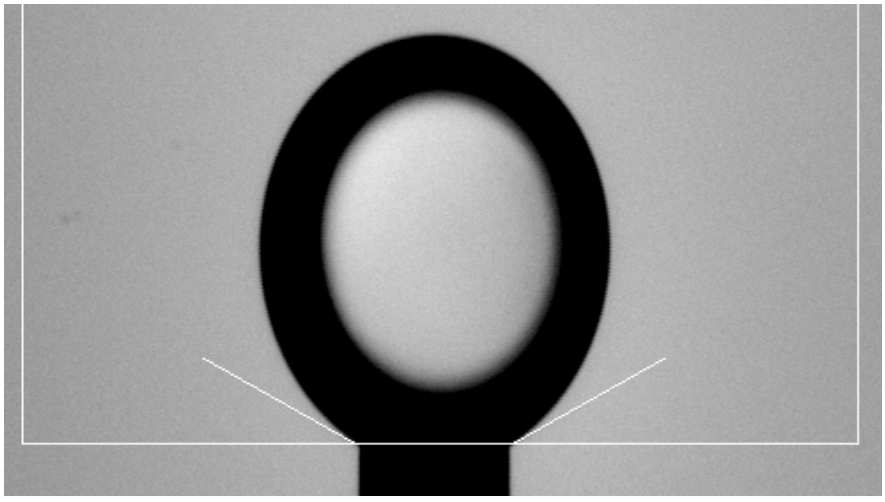

Figure 3.6 (c) *Frontier definition just at the edge of the syringe (height = 367) results in acceptable drop shape analysis. γ = 46.173 mN/m*

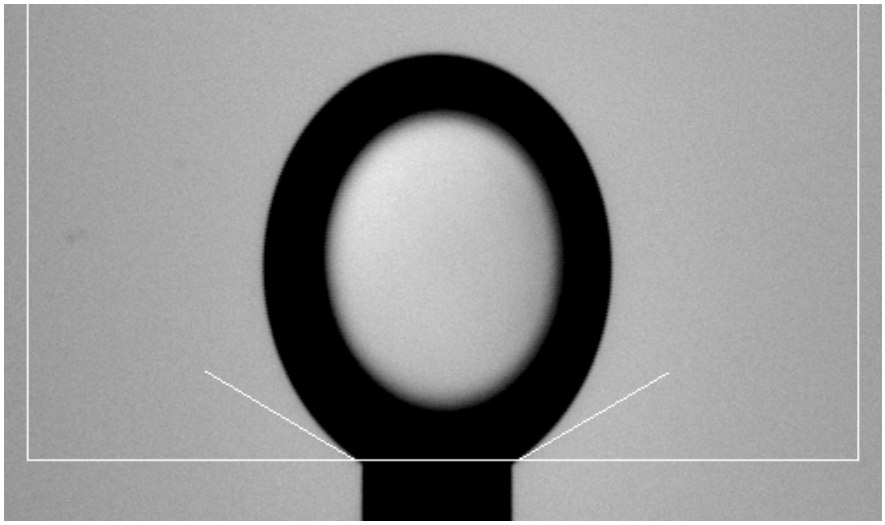

Figure 3.6 (d) *Frontier definition one increment above the edge of the syringe (height = 366) results in acceptable drop shape analysis. γ = 46.354 mN/m*

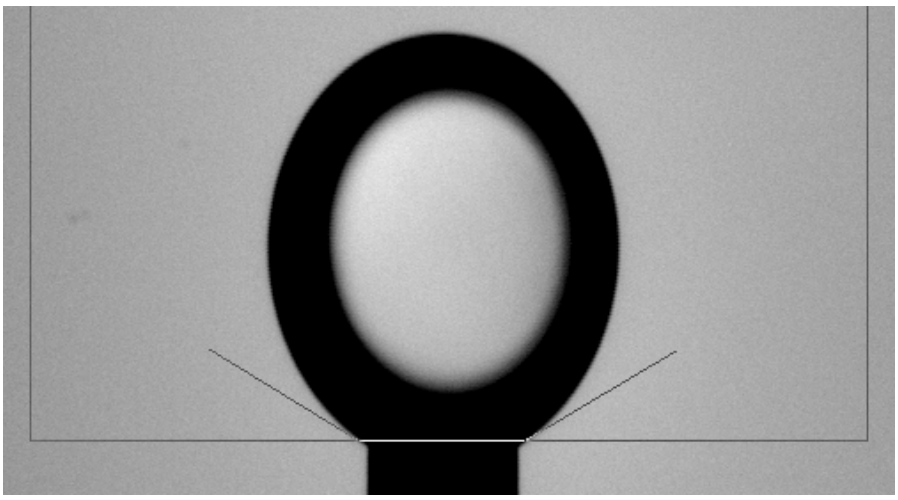

Figure 3.6 (e) *Frontier definition two increments above the edge of the syringe (height = 365) results in acceptable drop shape analysis. γ = 46.912 mN/m*

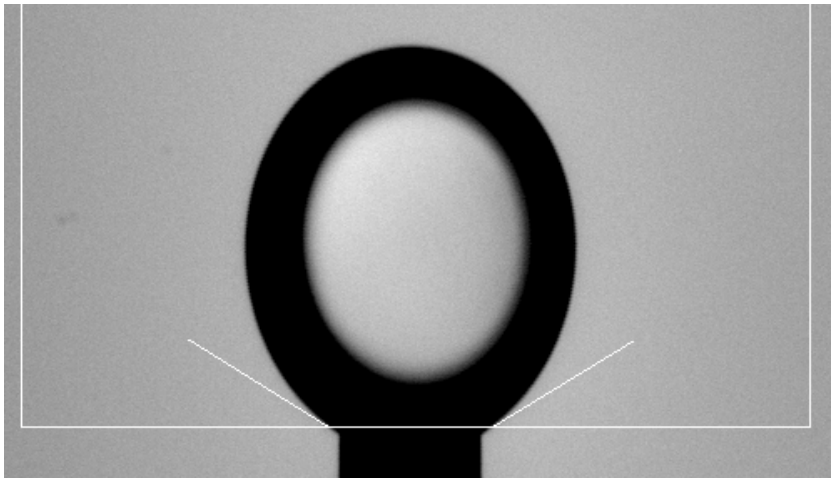

Figure 3.6 (f) *Frontier definition three increments above the edge of the syringe (height = 364) overestimates the interfacial tension from drop shape analysis.* $\gamma = 47.036$ *mN/m*

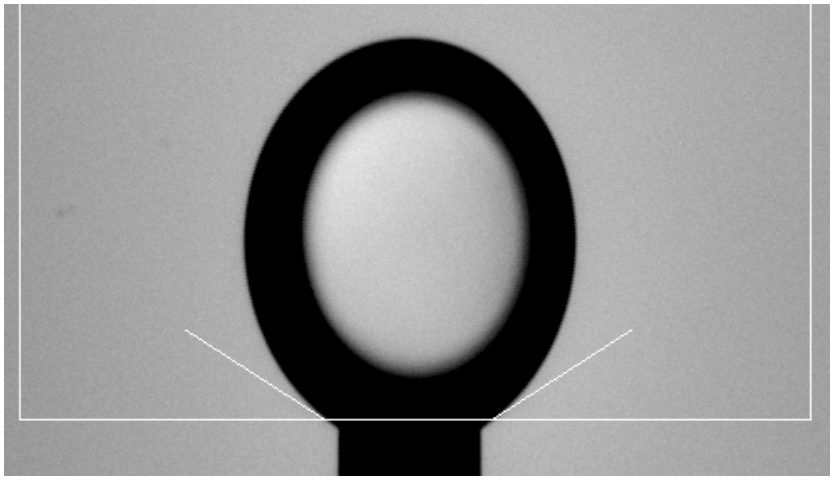

Figure 3.6 (g) *Frontier definition four increments above the edge of the syringe (height = 363) overestimates the interfacial tension from drop shape analysis.* $\gamma = 47.509$ *mN/m*

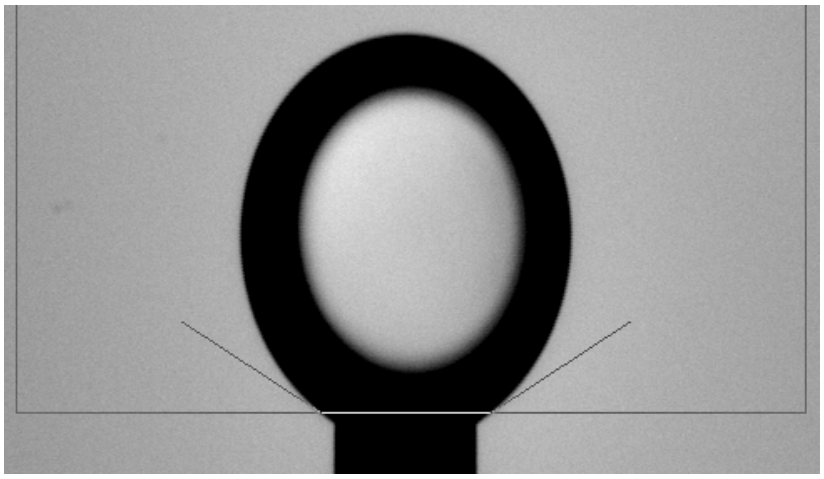

Figure 3.6 (h) *Frontier definition five increments above the edge of the syringe (height = 362) overestimates the interfacial tension from drop shape analysis.* $\gamma = 48.082$ *mN/m*

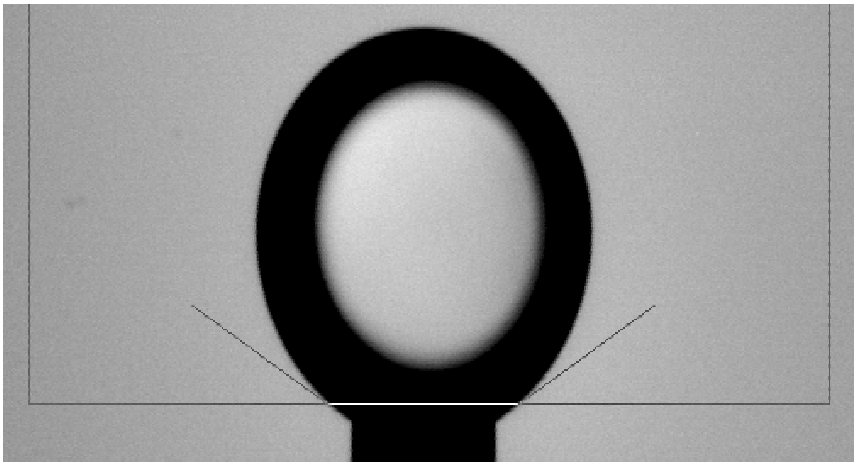

Figure 3.6 (i) *Frontier definition nine increments above the edge of the syringe (height = 358) overestimates the interfacial tension from drop shape analysis.* $\gamma = 48.494$

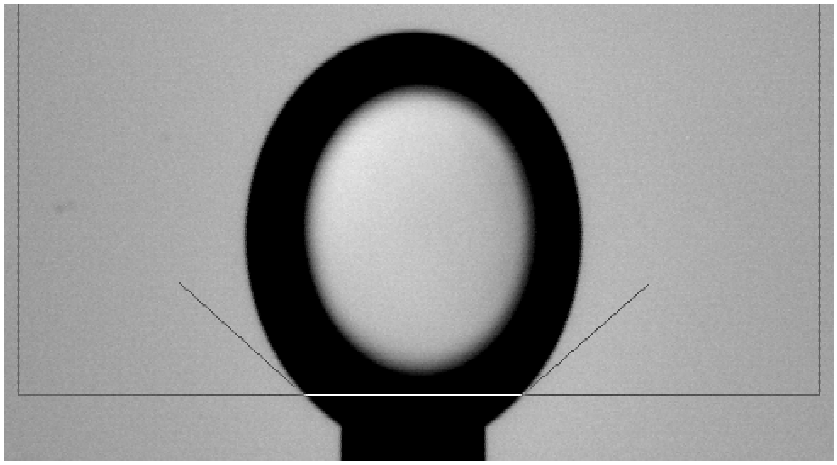

Figure 3.6 (j) *Frontier definition seventeen increments above the edge of the syringe (height = 350) overestimates the interfacial tension from drop shape analysis.* $\gamma = 49.583$ *mN/m*

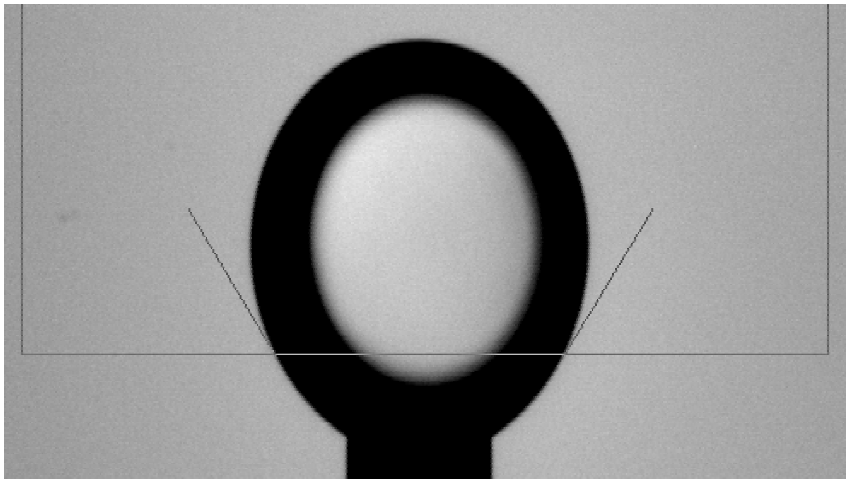

Figure 3.6 (k) *Frontier definition forty seven increments above the edge of the syringe (height = 320) overestimates the interfacial tension from drop shape analysis.* $\gamma = 50.997$ *mN/m*

The digital images shown in figure 3.6 that were collected and simultaneously analysed by the drop shape analysis machine indicate the range of accepted (by the machine and analysis software) frontiers that lead to a wide range of seemingly accurate interfacial tension values. The correlation between the chosen frontier increment from the edge of the syringe needle and the resulting interfacial tension value calculated by the drop shape analysis machine and software is shown in Figure 3.7.

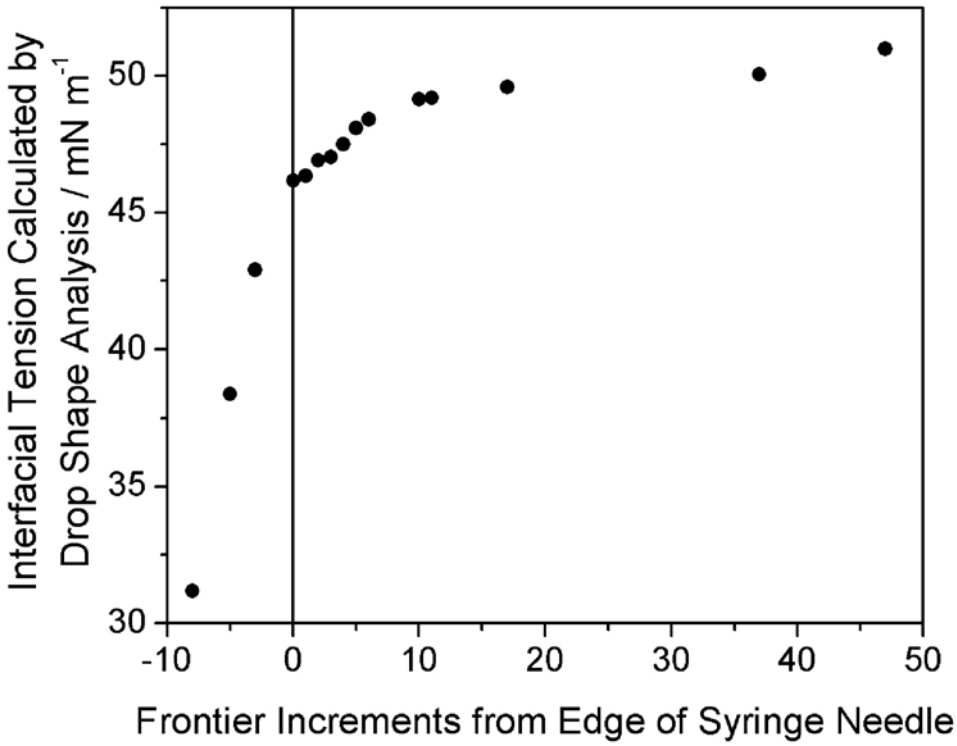

Figure 3.7 *Relationship between the chosen frontier definition and the interfacial tension value which results from drop shape analysis. x = 0 represents a frontier definition that is set at the edge of the syringe needle [see Figure 3.6 (c)] Negative values represent frontiers whose definition overlaps with the syringe needle [see Figures 3.6 (a) and (b)], and positive values represent frontiers that overlap with the drop instead of with the syringe needle [see Figures 3.6 (d) – (k)].*

As is seen in figure 3.7, setting the frontier to overlap with the syringe needle yields highly variable and incorrect values for the interfacial tension. This is understood

from Figures 3.6 (a) and (b), which show the measuring tangents bearing no relationship to the shape of the drop. This manual for the tensiometer indicates that one should not set the frontier to overlap with the syringe. It is interesting to note, however, that surface tension values can still be acquired. As for frontier definitions that overlap with the drop, it is unfortunate that different frontier definitions along the height of the drop result in different surface tension results from drop shape analysis. The manual for the tensiometer states that all the frontier settings illustrated in figures 3.7 (c)-(k) are allowed. The same drop, however, cannot simultaneously have a surface tension ranging from 46 to 51 mN m^{-1}. In my surface tensiometry results from drop shape analysis, I accept frontier definitions at one to two increments above the edge of the syringe needle. Increments below (negative) or more above (positive) these three are not used in any results presented here. Acceptable frontier definitions are illustrated in Figures 3.6 (c), (d), and (e). It is important to check more than one frontier illustration in case one has incorrectly identified the edge of the syringe needle. I recommend that images be saved from all important surface tension experiments. Without the images, there is no way one can verify whether the frontiers were chosen correctly after the experiment has been completed. It is therefore very easy to misidentify a calculated value as correct, even if it had been made with a frontier that was out of range from the edge of the syringe. The only disadvantage to saving images is the typically large file size of images. The software that runs this drop shape analysis machine allows the operator to save representative images, i.e. one image out of every *n* images in a particular experimental file. Choosing a higher value for *n* can save disk space, if disk space is limited. Other drop shape analysis tensiometers which employ different drop shape analysis algorithms may be less affected by the choice of frontier than the particular tensiometer described here.

3.4 Sample Preparation

3.4.1 Materials, Cleanliness, and Purity. Glassware was cleaned in an alkaline detergent (Decon 90) and rinsed thoroughly with ultra-high-purity water (Elga, UHQ). To test for cleanliness, glassware was equilibrated with water and then the water was examined by ellipsometry and surface tensiometry. The glassware was judged to be clean if the ellipticity was greater than 0.38×10^{-3} and the surface tension was found to be 72.0 mN m^{-1} by the du Noüy ring method at 298 K. Once the integrity of routine cleaning procedures was established by surface tensiometry and ellipsometry, glassware cleanliness was carefully monitored and periodically verified. Cleaned glassware such as sample dishes were kept submerged under UHQ water until shortly before use, when they were rinsed in further fresh UHQ.

The presence of any residual oils or alcohols on sample cells or syringes was eliminated through successive cleaning with acetone, methanol, dichloromethane, and acetone. When possible, this was achieved through successive sonication of the cell or syringe pieces in the solvents (approximately 10 minutes per solvent). When cell pieces were too large to fit in our ultrasonic bath, they were cleaned three times per solvent using Kimwipes. Chloroform (Aldrich, HPLC grade) was used to make dilute solutions of alkanes for some mixed monolayer experiments.

D_2O (99.9 atom %D, Aldrich) was used as received. Hexadecane (99%, Aldrich) was passed through activated alumina three times and tested negative for the presence of polar impurities.[23] Dodecane (Aldrich, 99+%) and tetradecane (Aldrich, 99+%) were percolated twice through a column of activated alumina to remove polar impurities. D_{34}-hexadecane (99 atom %D) was obtained from CDN Isotopes, Quebec, Canada, and was used as received. Deuterated dodecane and tetradecane (98 %D)

were used as received from Cambridge Isotope Laboratories. Recrystallised deuterated CTAB was a kind gift from Dr. R. K. Thomas.

The sapphire prisms used in the SF oil-water experiments were obtained from Crystran Crystals (BDH Advanced Materials Division, England). Decyltrichlorosilane (97%, Aldrich), dodecyltrichlorosilane (>99%, Fluka), decane (99+%, Aldrich), dodecane (99+%, Aldrich), and 1,1,1-trichloroethane (99%, Aldrich) were used as received to hydrophobe the sapphire prism.

3.4.2 Hexadecyltrimethylammonium Halide Surfactants and Halide Salts. CTAB (99%) and CTAC (99%) were obtained from Aldrich and were recrystallised three times from 1:1 acetone/methanol. CTAF and CTAI were prepared by titration of an aqueous hexadecyltrimethylammonium hydroxide solution (Fluka, halides ≤ 0.1%, assay ≥ 98%) by HF (Aldrich, 99.99%) and HI (Aldrich, 99.99%), respectively. Both of the resulting powders were then recrystallised three times from acetone with a trace amount of methanol. KBr, KCl, and KF were of 99.99% purity and were obtained from Aldrich. CTAI was found to have a Krafft point that was well above room temperature: ~ 330 K.

3.4.3 Mixed Monolayers of Surfactant and Alkane at the Air-Water Interface. Published work on mixed monolayers was carried out by Caroline E. McKenna and myself during Caroline's Part II project in our laboratory. Work on mixed monolayers was later continued by Dr. Qunfang Lei, a visiting scientist from the Department of Chemistry at Zhejiang University (Hangzhou 310027; P. R. China) though her work has not yet been published.

For mixed monolayers of CTAB and alkanes, the alkane may be introduced as a lens on the surface of the surfactant solution as well as by condensation of vapour from an oil reservoir within the sample cell. One microliter drops of a 10% solution (v/v) of dodecane or tetradecane in chloroform were placed on the surface of CTAB solutions. Initial spreading of the droplet was followed by retraction of the film, as the solvent evaporated, leaving many small alkane lenses in equilibrium with a mixed surfactant/oil monolayer. The oil lenses act as an oil reservoir that maintains equilibrium in the mixed monolayer. Large lenses spread and retract again to form smaller lenses. The greater the amount of oil used, the greater the number of lenses formed. Unfortunately, these lenses can interfere with the laser beams involved in SF and ellipsometric measurements, so the minimum amount of oil was employed to keep most of the surface free from oil lenses. As with nearly all experiments performed at the air-water interface, the sample cell was sealed except for small holes allowing entry and exit of the laser beams. Mixed monolayer experiments were left for approximately 20 minutes after preparation to ensure that the surface was saturated with oil. In some experiments, a pipe cleaner saturated with oil was placed at the base of the sample cell.

3.4.4 Hydrophobing the Sapphire Prism. A thin oil film between a clean sapphire prism and a solution of CTAB is only metastable and the surfactant solution was observed to break through the oil layer and preferentially wet the prism surface within five to ten minutes. To prevent the surfactant solution from displacing the hexadecane film, the sapphire surface was modified with a hydrophobic, oleophilic alkylsilane coating. These coatings were not particularly durable and needed to be repeated on a regular basis, typically after one or two experiments.

Before sapphire prisms were (re-)coated, the surfaces were washed with chloroform and UHQ water, to remove any oil or adsorbed surfactant, and then cleaned in 'piranha solution' (30% of 30% H_2O_2, 70% conc. H_2SO_4; *caution – piranha solution can react violently with organic materials*) for at least thirty minutes. After the piranha solution had cooled, the prisms were thoroughly rinsed with UHQ. Prisms were left submerged under UHQ until the time of their coating (typically a few hours).

No literature exists for silanisation of a sapphire surface, so various modifications of silanisation procedures used for other substrates were explored. The silanisation solution that worked best consisted of 1:1 mixture of 8 mL decane or dodecane with 8 mL 1,1,1-trichloroethane, to which approximately 5 mL of decyltrichlorosilane or dodecyltrichlorosilane, respectively, were added and well mixed. Solutions were used immediately.

Prisms were removed from the UHQ water and briefly allowed to dry in air until surface water was no longer visible to the eye. (The microscopic water layer that remains encourages polymerisation of the trichlorosilane at the prism surface. The absence of free –OH groups on the sapphire surface prevents covalent attachment of the polymerised silane monolayer to the surface, which probably accounts for the limited durability of these coatings compared to analogous films on silica.) The prisms were immersed in the silanisation solution and rotated after 10 minutes of immersion so that all three polished surfaces had equal initial exposure to the reaction solution. The prisms were left to coat for 24 hours or longer and were typically rotated once or twice more during that time. After two days, no discernible changes in the quality of the coating quality were observed.

The coating process was judged successful if the contact angle of water was > 90° across the full area of a prism face. Particular care was paid to quality of the coating at the edges of the face, since it is here that breakthrough of the surfactant solution was most likely to occur. The quality of the coating was usually significantly better on one prism face than on the other two, suggesting that the cut of the sapphire prism influenced the silanisation process. This preference was not investigated further.

Appendix: Protocol for CCD Tracking at the Air-Water Interface using the CSMA Programmes SCNREFD3 and SCNREFDC:

(1) Choose two strong resonances of your sample and take 120 second acquisitions at each one using no special program. At each resonance, record the top, bottom, left, and right edges of the sample and reference spots. Note that the numbers displayed are in 2 by 2 binning, so one should multiply the numbers on the screen by two when one is writing them down. Call the numerically smaller resonance in cm^{-1} res1 and the numerically bigger resonance in cm^{-1} res2.

(2) Calculate samwidth and samheight, refwidth and refheight from the recorded dimensions. For the sample dimensions, add a cushion of two to each value. When these dimensions differ between the two resonances, use the larger dimensions of the two.

(3) Calculate the tracking slopes:

For the sample, which moves vertically downwards on the display when moving from 3000 cm^{-1} to 2800 cm^{-1}, calculate this rise. The rise = abs [vertical centre at res2 - vertical centre at res1]. Calculate the run between the two resonances one has chosen, for res2 > res1, run = res2 - res1. Rise / run = SlopeSam

For the reference, which moves horizontally to the left on the display when moving from 3000 cm^{-1} to 2800 cm^{-1}, calculate this rise. The rise = abs [horizontal centre at res2 - horizontal centre at res1]. The run is the same as that calculated for the sample. Rise / run = SlopeRef

(4) Calculate (run) x-shifts:
For res2 > res1, x-shift2 = 3000 - res2 = a positive number
Whereas x-shift1 = 2800 - res1 = a negative number

(5) Calculate (rise) y-shifts for sample and reference spots:

To get rise-shift for sample:

samymin = SamVertCentre@res2 + SlopeSam × x-shift2

= sample position at 3000 cm^{-1}

samymax = SamVertCentre@res1 + SlopeSam × x-shift1

= sample position at 2800 cm^{-1}

samymin is numerically bigger than samymax

To get rise-shift for reference:

refxmin = RefHorCentre@res1 + SlopeRef × x-shift1

= reference position at 2800 cm^{-1}

refxmax = RefHorCentre@res2 + SlopeRef × x-shift2

= reference position at 3000 cm^{-1}

refxmax is numerically bigger than refxmin

(6) Calculate xsam as lowest dimension in x for sample. Calculate yref as lowest dimension (numerically) in y for reference.

(7) Record the data as follows for easy entry into the programmes SCNREFD3 (for spectrum) and SCNREFDC (for background). Both should use the same file name and have the same acquisition time of 36 seconds for a 1 hour spectrum, which tends to work well. {[refheight, refwidth, samheight, samwidth]; [refxmin, refxmax, yref]; [samymin, samymax, xsam]}

(8) Once one has both the spectrum and background, copy the files created from c:\csma\data to a floppy diskette.

(9) Use the programme nicenorm.bas to process the spectrum, and then import it as an ASCII file into the graphing programme Origin to see the final plotted spectrum.

Appendix: Protocol for CCD Tracking at the Oil-Water Interface using the CSMA Programmes SCNREFD3 and SCNREFDC:

The tracking procedure at the oil-water interface is the same as that described for the air-water interface, except that the inputs for the reference spot are set to null values: refheight = refwidth = 2; refxmin = 252; refxmax = 254. In step (8), the sample spectrum and background are then normalised by a different computer programme, nbacksub.bas, that ignores the null reference spectra generated by SCNREFD3 and SCNREFDC. Further details on the normalisation of SF spectra acquired at the oil-water interface are provided in chapter 8.

References

(1) SF spectra have also been obtained using a fixed-frequency infrared beam (1064 nm) and a tunable infrared beam [Potterton, E. A.; Bain, C. D. *J. Electroanalytical Chem.* **1996**, *409*, 109].

(2) (a) Akamatsu, N.; Domen, K.; Hirose, C. *J. Phys. Chem.* **1993**, *97*, 10070. (b) Guyot-Sionnest, P.; Hunt, J. H.; Shen, Y. R. *Phys. Rev. Lett.* **1987**, *59*, 1597.

(3) Zhang, D.; Gutow, J.; Eisenthal, K. B. *J. Phys. Chem.* **1994**, *98*, 13729.

(4) Guyot-Sionnest, P. *J. Electron Spectrosc. Relat. Phenom.* **1993**, *64*, 1.

(5) (a) Peremans, A.; Tadjeddine, A.; Zheng, W. Q.; le Rille, A. *Ann. Phys. Fr.* **1995**, *20*, 527. (b) van der Ham, E. W. M.; Vrehen, Q. H. F.; Eliel, E. R. *Surf. Sci.* **1996**, *368*, 96. (c) Braun, R.; Casson, B. D.; Bain, C. D.; van der Ham, E. W. M.; Vrehen, Q. H. F.; Eliel, E. R.; Briggs, A. M.; Davies, P. B. *J. Chem. Phys.* **1999**, *110 (9)*, 4634.

(6) Rabinowitz, P.; Perry, B. N.; Levinos, N. J. *IEEE J. Quantum Electron.* **1986**, *22*, 797.

(7) Harris, A. L.; Levinos, N. J. *Appl. Opt.* **1987**, *26*, 3996.

(8) Ward, R. N. *Ph.D. thesis*: University of Cambridge, 1993.

(9) Herriot, D.; Kogelnik, H.; Kompfner, R. *Applied Optics* **1964**, *3*, 523.

(10) Casson, B. D. *D.Phil. thesis*: University of Oxford, 1998.

(11) Bertie, J. H.; Ahmed, M. K.; Eysel, H. H. *J. Phys. Chem.* **1989**, *6*, 2210.

(12) Karaborni, S.; Toxvaerd, S.; Olsen, O. H. *J. Phys. Chem.* **1992**, *96*, 4965.

(13) Hautmann, J.; Klein, M. L. *J. Chem. Phys.* **1990**, *93*, 7483.

(14) Knock, M. M.; Bain, C. D. *Langmuir* **2000**, *16*, 2857.

(15) Bain, C. D.; Davies, P. B.; Ong, T. H.; Ward, R. N.; Brown, M A. *Langmuir* **1991**, *7*, 1563.

(16) Rothen, A. *Rev. Sci. Instrum.* **1945**, *16*, 26.

(17) Jasperson, S. N.; Schnatterly, S. E. *Rev. Sci. Instrum.* **1969**, *40*, 761.

(18) Beaglehole, D. *Physica* **1980**, *100B*, 163.

(19) du Noüy, Lecomte *J. Gen. Physiol.* **1919**, *1*, 521.

(20) (a) Harkins, W. D.; Jordan, H. F. *J. Am. Chem. Soc.* **1930**, *52*, 1772. (b) Freud, B. B.; Freud, H. F. *J. Am. Chem. Soc.* **1930**, *52*, 1772.

(21) Zuidema, H. H.; Waters, G. W. *Ind. Eng. Chem. Anal. Ed.* **1941**, *13(5)*, 312.

(22) Win-Tracker User's Manual, July 1998: Part A, III-6 p. 4 and Part B VI-5, p. 1-8.

(23) Bigelow, W. C.; Pickett, D. L.; Zisman, W. A. *J. Colloid Sci.* **1946**, *1*, 513.

CHAPTER 4

CTAB Monolayers at the Air-Water Interface

Chapter 4: CTAB Monolayers at the Air-Water Interface

4.1 Rationale for Experiment

A large body of data already exists for monolayers of CTAB at the air-water interface. Monolayers of CTAB at the air-water interface therefore form a convenient standard against which monolayers of other alkyltrimethylammonium halide surfactants may be compared. In this thesis, CTAB monolayers at the air-water interface serve as the primary standard of comparison for CTAB monolayers at the oil-water interface, which are discussed in chapter 8. For surfactant monolayers at the air-water interface, two of the most general techniques are neutron reflection (NR)[1] and sum-frequency spectroscopy (SFS).[2] NR and SFS have been used to address how the structure of a monolayer is determined by factors such as the area per molecule,[3] the length of the hydrophobic chain,[4] and the nature of the hydrophilic head group.[5] Here, I have used sum-frequency spectroscopy, ellipsometry, and surface tensiometry in conjunction to assess the purity of the surfactant monolayer, to establish the area per molecule, A, and to determine the structure and conformation of CTAB molecules at the air-water interface. The effect of area per molecule, A, on SF spectra of CTAB is studied in the absence of added electrolyte.

4.2 Sum-Frequency Spectroscopy

The effect of changing the surface area per molecule, A, on SF spectra of CTAB is seen in Figure 4.1, which shows SF spectra as a function of CTAB concentration from 0.01 to 2 times the critical micelle concentration (cmc). The similarity of the spectra at the cmc (Figure 4.1(b)) and twice the cmc (Figure 4.1(a)) is a good indication that CTAB is pure since trace surface-active impurities present in the monolayer at the

cmc would be largely solubilised into micelles at twice the cmc. A decrease in CTAB concentration below the cmc of 9.2×10^{-4} M is accompanied by an increase in *A*.

The assignment of peaks in the SF spectra of surfactant monolayers has been discussed in detail previously.[6] Two prominent peaks appear in CTAB spectra with ssp-polarisation: the d^+ symmetric CH_2 stretch at 2853 cm^{-1} and the r^+ symmetric CH_3 stretch at 2878 cm^{-1}. The d^+ mode is indicative of the conformational disorder within the monolayer. For highly ordered monolayers with few gauche defects, the d^+ mode is very weak. As disorder increases, $\langle\beta_{yyz}\rangle$ increases due to the presence of gauche defects. For a highly disordered monolayer one might ultimately expect $\langle\beta_{yyz}\rangle$ to decrease again due to the near-random orientation of the chains. As *A* increases, the initial increase in $\langle\beta\rangle$ is counteracted by a decrease in *N* (equation 2.17) with the result that the line-strength of the d^+ mode remains approximately constant until the area per molecule has nearly doubled, before gradually falling away to zero.

The line strength of the r^+ mode is dependent on the tilt of the terminal methyl group. In an ssp spectrum, the component of the hyperpolarisability responsible for the signal from this mode is expressed in molecular coordinates by (equation 2.23)

$\left\langle\beta_{yyz}\right\rangle = \frac{\beta_{ccc}}{8}\left\{\left\langle\cos\theta\right\rangle\left\langle 1+7r\right\rangle + \left\langle\cos 3\theta\right\rangle(r-1)\right\}$ where $r = \beta_{aac} / \beta_{ccc}$ and θ is the angle between the surface normal (z) and the C_3-axis of the terminal methyl group (the c-axis.) As the first bracketed term dominates in this equation, $\langle\beta_{yyz}\rangle$ is proportional to $\langle\cos\theta\rangle$, to a good approximation.

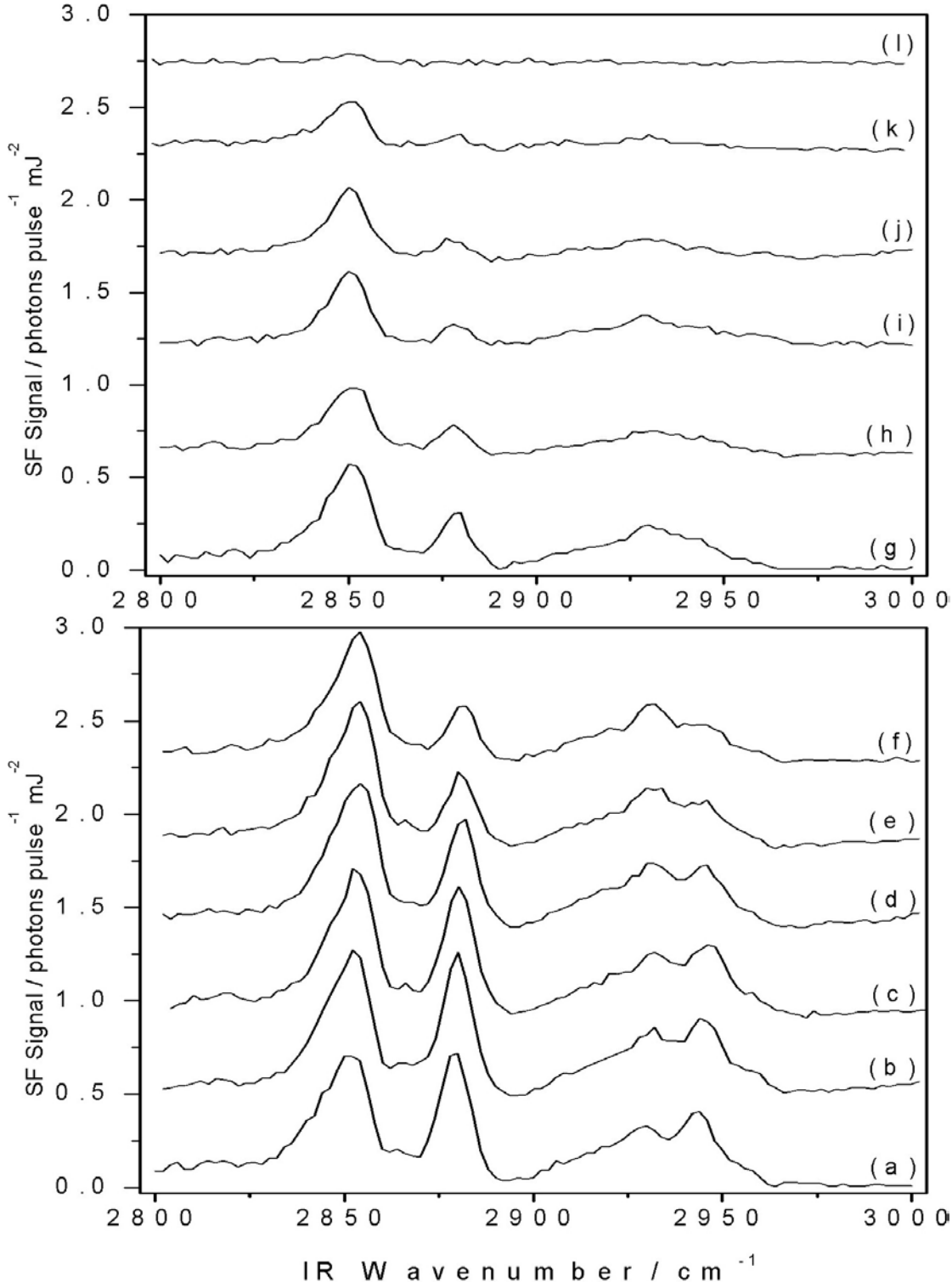

Figure 4.1 *SF spectra of CTAB monolayers as a function of concentration. ssp-polarised. All spectra except (a) and (g) were offset vertically for clarity.*

[CTAB] / mM	(a) 2	(b) 0.92	(c) 0.88	(d) 0.5	(e) 0.25	(f) 0.2	(g) 0.125	(h) 0.06	(i) 0.044	(j) 0.03	(k) 0.022	(l) 0.01
Γ *	3.7	3.7	3.5	3.3	2.8	2.6	2.2	1.6	1.3	1.1	~0.5	~0.1
A *	44	44	47	50	59	64	76	104	128	151	~330	--

* *For Γ / 10^{-6} mol m^{-2}; A / Å^2 mol^{-1}. Values of Γ were determined from the calibration curve of Manning-Benson, et al[7] (see text).*

4.3 Surface Tensiometry and the Determination of Area per Molecule via Ellipsometric Calibration

It is difficult to determine the area per molecule accurately from sum-frequency spectroscopy alone. I have used several approaches to establish the areas per molecule in the monolayers shown in figure 4.1. The two most direct approaches are the application of the Gibbs equation to the surface tension data of Manning-Benson, *et al*,[7] and the neutron reflection measurements of Lu and coworkers.[3,8,9] Reliable measurements on static solutions of CTABs are difficult, possibly because of the effect of trace ionic impurities. As a result, the neutron reflection measurements are not in good agreement with the integrated form of the Gibbs equation:

$$\int_0^{cmc} \Gamma d \ln C = \frac{\pi_{cmc}}{2RT} \tag{4.1}$$

where π_{cmc} is the surface pressure at the cmc (a well-defined quantity.) Furthermore, the area per molecule obtained from tensiometric measurements is sensitive to the form of curve used to fit the γ vs. ln C plots, especially at low concentrations.

As a consequence of the limitations encountered in surface tensiometry, I have also adopted a less direct, but possibly more accurate, approach. The coefficient of ellipticity and the surface excess (by NR) were measured on the expanding surface of CTAB solutions in an overflowing cylinder by Manning-Benson *et al.*[7,10] These measurements are more precise than measurements on static solutions and do not suffer from errors introduced by trace impurities. From these dynamic measurements a calibration curve of $\Gamma_{dyn}(\overline{\rho}_{dyn})$ was established. Since both NR and ellipsometry are sensitive only to the immediate interfacial region (~ nm thick), this calibration curve is also valid under static conditions. Ellipsometry measurements on equilibrium

solutions can therefore be converted readily to surface excesses.* While these measurements may still be affected by trace ionic impurities (which would invalidate tensiometric measurements), the derived values of *A* will still be approximately correct. A comparison of adsorption isotherms determined by these three methods is shown in Figure 4.2. The surface excesses derived from NR on static solutions are in good agreement with the indirect approach, whereas the tensiometric route yields significantly lower coverages at all concentrations.

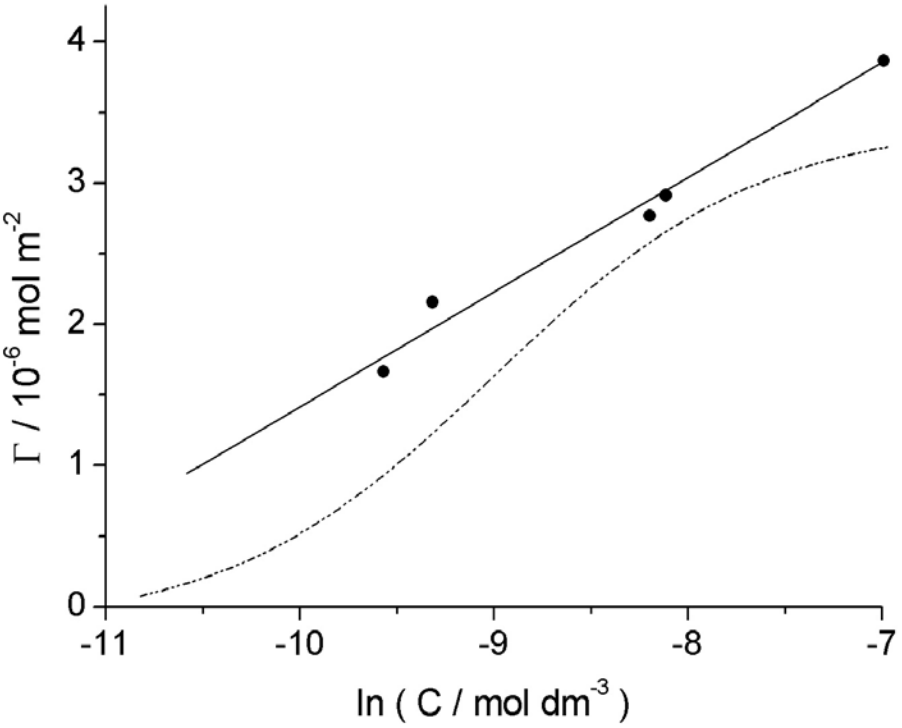

Figure 4.2 *Adsorption isotherms for CTAB monolayers determined by the calibration method of Manning-Benson et al*[7] *(solid line), the Gibbs equation (dashed line), and the neutron reflection results of Lu et al.*[3,8,9] *(solid circles).*

* All ellipsometry measurements at the air-water interface on CTAB solutions without added electrolyte were carried out by Samantha Manning-Benson.

4.4 SFS Line Strength and Surface Excess

The line strengths of the symmetric methylene and methyl stretches at 2853 and 2878 cm^{-1}, S_{d+} and S_{r+}, were obtained from computer fits to the spectra, as explained in chapter 3. To interpret the resulting line strengths in terms of changes in the conformation or orientation of the molecules in the monolayer, I first must correct for the area per molecule. Since $S \alpha N$, this normalisation is achieved by multiplication of the line strength S by $A = N^{-1}$. The values for A used for this normalisation were determined via ellipsometry, as described in 4.3, and are given in the table below Figure 4.1. Figure 4.3 shows the normalised line strengths of the d^+ and r^+ modes for A = 44 - 186 $Å^2$ per molecule.

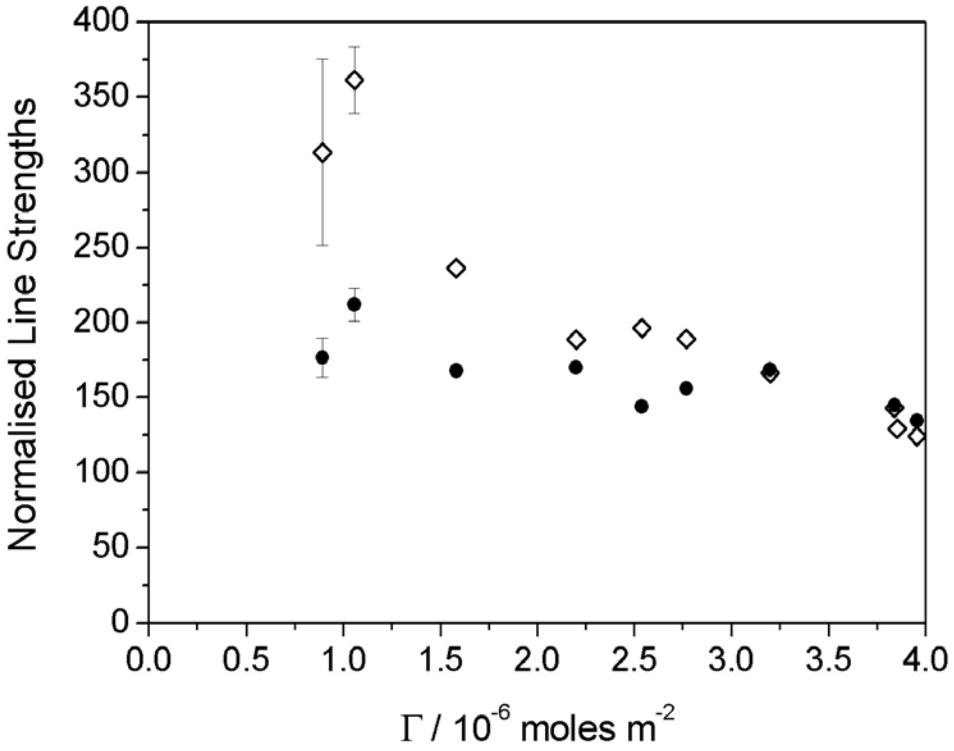

Figure 4.3 *Dependence of the line strengths, S, of the* d^+ *and* r^+ *modes on the surface excess,* Γ. *Normalised line strengths of the* d^+ *and* r^+ *modes are corrected for area per molecule:* (◇) d^+ *mode at 2853* cm^{-1}, (●) r^+ *mode at 2878* cm^{-1}.

The normalised strength of the d^+ mode increases with increasing A, indicating a growing number of SF-active gauche defects in the hydrocarbon chains. For a completely disordered monolayer, one would expect the normalised line strength to fall to zero, but no significant decrease was observed over the range of surface coverages accessible in this experiment. The normalised line strength of the r^+ mode is independent of A to within experimental error, which indicates that the average angle of the terminal methyl group (and by implication the tilt of the hydrocarbon chains within the monolayer) remains approximately constant as A increases. These observations argue against the intuitive picture of chains lying flat on the water surface as the area per molecule increases. The behaviour of the d^+ and r^+ modes is consistent in this respect.

The interpretation of the normalised line strengths is susceptible to systematic errors in the determination of A. The ratio S_{d+} / S_{r+} is independent of A and has been correlated empirically with the amount of conformational disorder in surfactant monolayers.[5,6] Figure 4.4 shows that S_{d+} / S_{r+} increases with increasing A (decreasing Γ), consistent with increasing chain disorder.

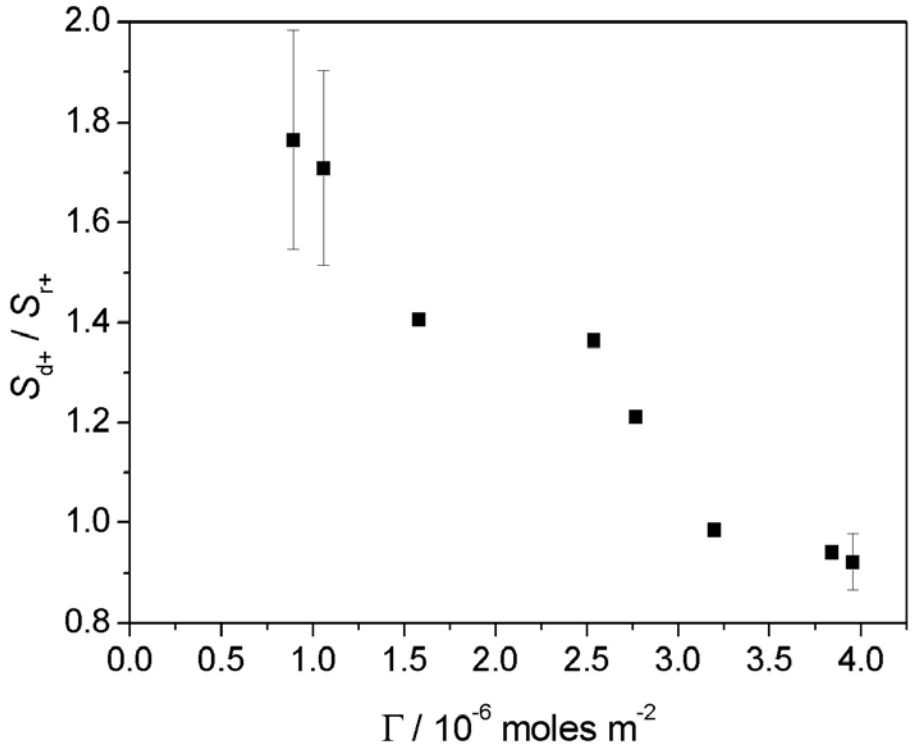

Figure 4.4 *Dependence of the line strengths, S, of the* d^+ *and* r^+ *modes on the surface excess,* Γ. *The ratio of the line strengths,* S_{d+} / S_{r+} *is correlated to the degree of conformational disorder in the monolayer.*

4.5 Comparison with Other Experiments

Monolayers of CTAB and its alkyltrimethylammonium bromide analogues (C_nTABs, where *n* represents the length of the hydrocarbon chain) at the air-water interface have been studied extensively by neutron reflection and surface tensiometry. Attempts to correlate *n* with the structure of the monolayer at the air-water interface have been made by both SFS[11] and NR.[12] The initial finding of Thomas *et al* by NR was that the thickness of the monolayer was independent of chain length, suggesting that the density of the monolayer and the tilt of the chains from the surface normal increased with increasing chain length. The later SFS study by Bain *et al*, which was in quantitative agreement with structural data found for C_{12}TAB and C_{16}TAB by NR,

found no structural differences between alkyltrimethylammonium bromide monolayers of different chain lengths for n = 12, 14, 16, 18 at fixed A of 44 Å^2 mol^{-1}. A mean chain tilt of 58° near the methyl terminus was determined, and the density of the chain region in the monolayers was close to that of a liquid hydrocarbon.

Thomas and coworkers have studied the structure of C_{14}TAB[13,14,15] and C_{16}TAB[3,8,9,16] monolayers in great detail. They found that the first half of the carbon chain that is nearest to the head group is oriented closer to the surface normal than the outer parts of the chain, which are orientated increasingly far from the surface normal. Different angular tilt distributions for the two ends of the hydrocarbon chain also indicate that gauche defects exist within the chain. Tilting away from the surface normal begins within the first block of two carbon atoms which is adjacent to the hydrophilic head group. Tilting is understood in light of the favourability of full hydration of the tetrahedral trimethylammonium group, which has maximum contact with water when the C–N bond is as vertical as possible. A near vertical orientation for the C–N bond prevents an all-trans hydrocarbon chain from coming out an angle strongly tilted (i.e. near 70-80°) from the surface normal. Gauche defects within the chain, however, free the chain to tilt without disturbing the hydration of the head group. The greater tilt of the second block of four atoms from the head group towards the chain terminus suggests that gauche defects are likely to occur even within the first few segments of the hydrocarbon chain.

A correlation between surface excess and monolayer structure was found for C_{16}TAB which generally agrees with the results described in this chapter.[9] At the cmc, the NR results for a CTAB monolayer gave A = 43-44 Å^2; for [CTAB] = 2.76 × 10^{-4} M, A = 60 Å^2; and for [CTAB] = 0.70 × 10^{-4} M, A = 100 Å^2. Near these bulk concentrations for CTAB, I found areas per molecule of nearly 44 Å^2 at the cmc, 59

$Å^2$ for [CTAB] = 2.5 $\times 10^{-4}$ M; and 104 $Å^2$ for [CTAB] = 0.6 $\times 10^{-4}$ M, which is in excellent agreement with the results determined by NR for static solutions of CTAB.

An earlier study by Thomas and coworkers on C_{14}TAB tried to identify the source of disagreement between measurements from surface tension and neutron reflection.[14] A common assumption has been that errors in surface excess values calculated from surface tensiometry data are due to trace ionic impurities in the bulk surfactant. These impurities concentrate at the interface and cause a discrepancy between the real and the acknowledged activity coefficient for the surfactant that is applied in the Gibbs equation. Additional possible sources of error include incomplete wetting of the ring (or plate) or a slight curvature in the surface tension vs. ln C plot, which could be missed if too few measurements are made over an insufficiently large range of concentrations. Because all measurements (i.e. surface tensiometry and neutron reflection) in Thomas's study were performed on the same sample, the authors conclude that discrepancies between surface tensiometry and NR isotherms were entirely due to systematic problems associated with the measurement and interpretation of the surface tension of surfactant solutions obtained by the ring or plate method. The calibration method described in this chapter bypasses the traditional and commonly accepted problems of surface tensiometry since it is based upon dynamic measurements by Manning-Benson, *et al* at the expanding surface of an overflowing cylinder.[7] At a static air-water interface, the tensiometric approach yields significantly lower surface coverages at all bulk concentrations.

4.6 Conclusion

The relationship between area per molecule and the structure of a CTAB monolayer at the air-water interface has been investigated by sum-frequency spectroscopy. Areas per molecule were derived from results by Manning-Benson, *et al*,[7] which correlate surface excesses determined by neutron reflection with coefficients of ellipticity at the expanding surface of an overflowing cylinder. As A increased (Γ decreased), the number of SF-active gauche defects within the hydrocarbon chain increased. In addition, the average tilt of the hydrocarbon chains did not change in response to an increase in A. Although an increase in conformational chain disorder was observed as A was increased, the textbook picture of adsorbed surfactant layers at low coverage in which the polar groups are immersed in the water and the hydrocarbon chains lie flat on the water surface is not supported by SF spectra of CTAB monolayers as a function of concentration, at least for surface coverages greater than 1×10^{-6} mol m^{-2}.

References

(1) Penfold, J. *et. al. J. Chem. Soc. Faraday Trans.* **1997**, *93*, 3899.

(2) Bain, C. D. In *Modern Characterization Methods of Surfactant Systems*; Binks, B. P., Ed.; Marcel Dekker: New York, 1999; chapter 9.

(3) Lu, J. R.; Hromadova, M.; Simister, E. A.; Thomas, R. K.; Penfold, J. *J. Phys. Chem.* **1994**, *98*, 11519.

(4) (a) Bell, G. R.; Manning-Benson, S.; Bain, C. D. *J. Phys. Chem B.* **1998**, *102*, 218. (b) Lyttle, D. J.; Lu, J. R.; Su, T. J.; Thomas, R. K.; Penfold, J. *Langmuir*. **1995**, *11*, 1001.

(5) (a) Bell, G. R.; Bain, C. D.; Ward, R. N. *J. Chem. Soc. Faraday Trans.* **1996**, *92*(4), 515. (b) Goates, S. R.; Schofield, D. A.; Bain, C. D. *Langmuir* **1999**, *15*(4), 1400. (c) Conboy, J. C.; Messmer, M. C.; Richmond, G. L. *J. Phys. Chem. B* **1997**, *101*(34), 6724. (d) Lu, J. R.; Thomas, R. K.; Penfold, J. *Adv. Coll. Interface Sci.* **2000**, *84*, 143.

(6) Ward, R. N.; Duffy, D. C.; Davies, P. B.; Bain, C. D. *J. Phys. Chem.*, **1994**, *98*, 8536.

(7) Manning-Benson, S.; Parker, S. R. W.; Bain, C. D.; Penfold, J. *Langmuir* **1998**, *14*, 990.

(8) Lu, J. R.; Hromadova, M.; Simister, E.; Thomas, R. K.; Penfold, J. *Physica B* **1994**, *198*, 120.

(9) Lu, J. R.; Li, Z. X.; Smallwood, J.; Thomas, R. K.; Penfold, J. *J. Phys. Chem.* **1995**, *99* (20), 8233.

(10) Manning-Benson, S.; Bain, C. D.; Darton, R. C. *J. Colloid Interface Sci.* **1997**, *189*, 109.

(11) Bell, G. R.; Manning-Benson, S.; Bain, C. D. *J. Phys. Chem. B* **1998**, *102*, 218.

(12) Lyttle, D. J.; Lu, J. R.; Su, T. J.; Thomas, R. K. *Langmuir* **1995**, *11*, 1001.

(13) Simister, E. A.; Lee, E. M.; Thomas, R. K.; Penfold, J. *J. Phys. Chem.* **1992**, *96*, 1373.

(14) Simister, E. A.; Thomas, R. K.; Penfold, J.; Aveyard, R.; Binks, B. P.; Cooper, P.; Fletcher, P. D. I.; Lu, J. R.; Sokolowski, A. *J. Phys. Chem.* **1992**, *96*, 1383.

(15) Lu, J. R.; Simister, E. A.; Thomas, R. K.; Penfold, J. *J. Phys. Chem.* **1993**, *97*, 13907.

(16) CTAB adsorbed at the quartz/aqueous interface: McDermott, D. C.; McCarney, J.; Thomas, R. K.; Rennie, A. R. *J. Coll. Interface Sci.* **1994**, *162*, 304.

CHAPTER 5

Effect of Halide Counterion on CTAX Monolayers

Chapter 5: Effect of Halide Counterion on CTAX Monolayers

5.1 Rationale for Experiment

For surfactant monolayers at the air-water interface, two of the most general techniques are neutron reflection (NR)[1] and sum-frequency spectroscopy (SFS).[2] NR and SFS have been used to address how the structure of a monolayer is determined by factors such as the area per molecule,[3] the length of the hydrophobic chain,[4] or the nature of the hydrophilic head group.[5] Very limited attention has been dedicated to the effect of counterion on the structure of monolayers,[6] despite its obvious importance for ionic surfactants. In this chapter, I present a comparative study of monolayers of hexadecyltrimethylammonium halides (CTAX, for iodide (CTAI), bromide (CTAB), chloride (CTAC), and fluoride (CTAF) counterions) at the air-water interface. Classical tensiometric measurements are complemented by two optical techniques, sum-frequency spectroscopy and ellipsometry, that are sensitive to the structure of the monolayer on a molecular length scale.

5.2 Known Effects of Salt in the Bulk and at the Interface

The effect of both the concentration and the nature of the counterion on aggregation of ionic surfactants in the bulk phase has been studied extensively.[7] Increasing the counterion concentration increases the electrostatic screening of the repulsions between the head groups of the surfactant molecules and increases the tendency towards aggregation, thus lowering the critical micelle concentration (cmc) for the 'salted' surfactant.[8] The addition of electrolyte to solutions of sodium dodecyl sulfate (SDS), an anionic surfactant, or CTAB, a cationic surfactant, changes the

shape of their micelles from spheres to cylindrical rods.[9] This change in the shape of the aggregate is due to the closer packing of head groups in the presence of excess counterion, and is in accordance with Israelachvili's geometric model for the aggregation of lipids.[10] For CTAB, this transition happens at surfactant concentrations significantly above the critical micelle concentration (cmc) or when the concentration of added counterion exceeds 0.1 M.[11] The electrostatic repulsion between head groups within the Stern layer of an ionic micelle is mitigated by the presence of bound counterions. General studies have shown that the order of ion binding to positive micelles such as those formed by cetyltrimethylammonium halide (CTAX) surfactants is $I^- > Br^- > Cl^- > F^-$. Larger, more polarisable ions are less strongly hydrated and bind more effectively.[12] The comparable effects of the counterion on monolayers at the air-water interface have not been studied systematically. In this chapter, I look at the effect of the halide ion on the area per molecule in CTAX monolayers and address the question of whether the nature of the counterion has any specific influence on the structure of the monolayer beyond its effect on the area per molecule.

Previous SFS studies on counterion effects have focused on large organic counterions bound to charged surfactant monolayers at the air-water[13] and solid-water interfaces.[14] These systems are especially interesting, since the transition from spherical to rod-shaped aggregates in the bulk is often associated with viscoelasticity, flow birefringence, and irridescence,[7,15] but they are hardly representative of the action of small, halide counterions. To obtain a sufficiently large scattering length, NR studies have also been limited to large, organic counterions such as the tetramethylammonium ion.[16] One SFS study on monolayers of $C_{14}TA^+ SCN^-$ showed that the bound counterions were oriented with the sulfur atom nearest to the

monolayer,[14(a)] but to date, there have been no studies by either SFS or NR of the effect of simple inorganic ions on the structure of monolayers. CTAB and CTAC have been studied by surface tensiometry, but I am not aware of tensiometric data for CTAI or CTAF.[17]

A large body of data already exists for monolayers of CTAB at the air-water interface, obtained by surface tensiometry, NR, and ellipsometry. Monolayers of CTAB therefore form a convenient standard against which monolayers of CTAI, CTAC, and CTAF may be compared. I have used sum-frequency spectroscopy, ellipsometry, and surface tensiometry in conjunction to assess the purity of the surfactant monolayer, to establish the area per molecule, *A*, and to determine the structure and conformation of CTAX molecules at the air-water interface. To establish the role of the counterion in CTAX monolayers, I have examined the following factors.

(i) *The effect of the nature of the halide counterion on saturated monolayers of CTAF, CTAC, CTAB, and CTAI.* On a simple model of surfactant behaviour, the surface coverage reaches its maximum value at the cmc and then remains constant at higher concentrations. In practice, the coverage continues to increase with concentration above the cmc, due to intermicellar interactions in the bulk solution, but changes at a rate that is very much less than at concentrations below the cmc. Below the cmc, trace ionic impurities, in particular divalent ions,[18] concentrate at the interface and compete for binding with X^-. For cationic surfactants, carbonate and silicate are the most probable multiply charged counterions. At concentrations above the cmc, however, such impurities partition

between the monolayer and the micelles, reducing ionic contamination of the saturated monolayer.

(ii) *The effect of added counterion, in the form of 0.1 M KX, on the structure of CTAX monolayers at limiting coverage.* To observe the effect of added electrolyte, I studied CTAX monolayers in the presence of 0.1 M KX salt. The presence of excess halide further reduces the influence of ionic contamination by mass action.

(iii) *Specific effects of halide counterions.* A comparison of monolayers of CTAX at saturation coverage with monolayers of CTAB at various areas per molecule reveals whether the nature of the halide counterion has any specific effect on the structure of the monolayer other than simply changing the surface excess.

5.3 Effect of the Nature of the Counterion on Saturated Monolayers of CTAX

Figure 5.1 illustrates the effect of the counterion on the surface tension of salted CTAX monolayers for X = Br^-, Cl^-, and F^-. Electrolyte was added to minimise the effects of ionic contamination, especially that of more strongly adsorbed ions such as Br^-, on CTAC and CTAF. The limiting slopes in the γ vs. ln C plot (figure 5.1) were used to determine the limiting areas per molecule at the cmc (Table 1).

Table 1. Limiting Adsorption in CTAX Monolayers in the Presence of 0.1 M KX, Determined by Tensiometry.

T = 303 K

	Br^-	**Cl^-**	**F^-**
cmc / M	$(4.9 \pm 0.4) \times 10^{-5}$	$(9.1 \pm 0.2) \times 10^{-5}$	$(2.3 \pm 0.05) \times 10^{-4}$
Γ / 10^{-6} mol m^{-2}	3.7	2.5	1.8
A / $Å^2$	44	65	94

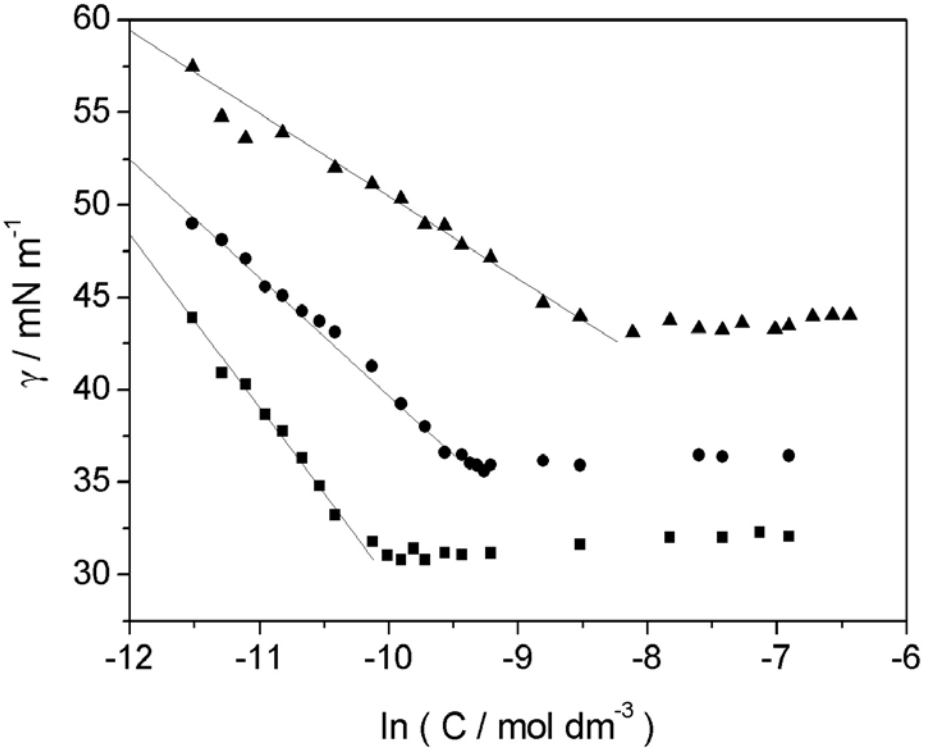

Figure 5.1 *Surface tension of CTAX monolayers in the presence of 0.1 KX. Linear regressions were used to determine A for salted CTAF, CTAC, and CTAB at saturation coverage from the Gibbs equation (see Table 1):*
(▲) *CTAF;* (●) *CTAC;* (■) *CTAB. T = 303 K.*

Replacing Br^- with Cl^- and then with F^- decreases both the efficiency and the effectiveness of the surfactant: the cmc increases and the surface tension at the cmc increases. The reduced ability of the smaller halide ions to screen the electrostatic repulsions between the trimethylammonium groups increases the limiting area per molecule in the monolayer from 44 $Å^2$ in CTAB to 94 $Å^2$ in CTAF.

CTAI is excluded from the comparison in Figure 5.1 because at 303 K, it was found to be well below the Krafft temperature* and the solubility was too low to obtain an accurate γ vs. ln C plot. The surface tension of the saturated CTAI solution

* The Krafft temperature of CTAB is 297 K. [Adam, H. K.; Pankhurst, K. G. A. *Trans. Faraday Soc.* **1946**, *42*, 523.] The Krafft temperatures of CTAC and CTAF were not measured but are expected to be at temperatures below the 297 K observed for CTAB.

at 303 K was 57.0 mN m^{-1} suggesting that the surface excess of the monolayer was very low.

Figure 5.2 shows the SF spectra of monolayers of salted CTAX above the cmc.

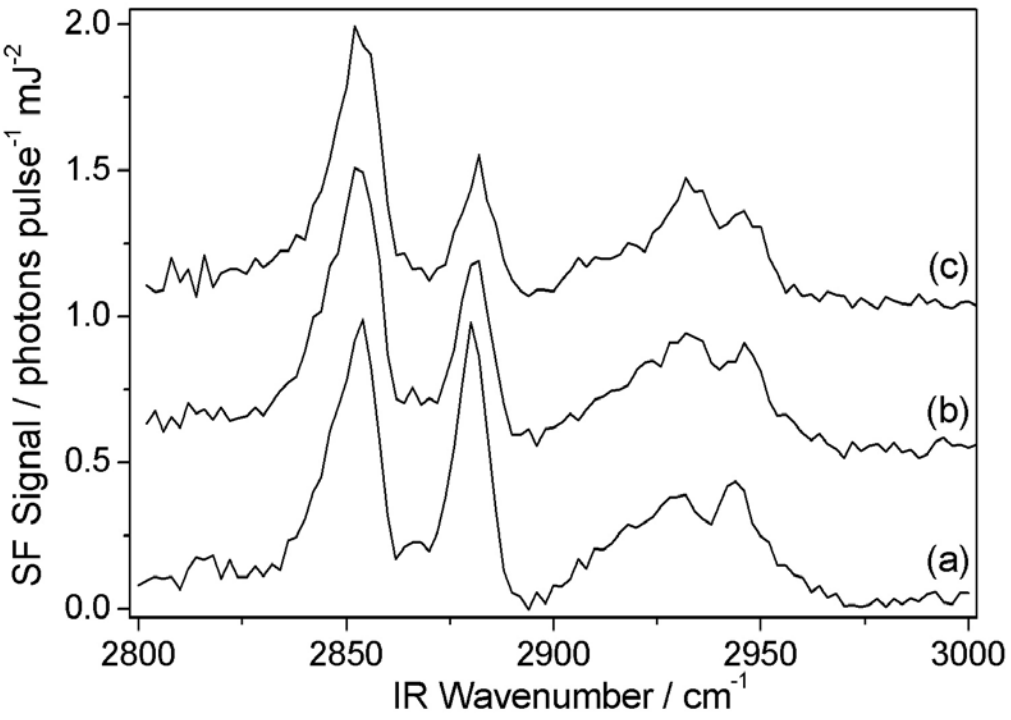

Figure 5.2 *Comparison of the SF spectra of saturated monolayers of CTAB, CTAC, and CTAF in the presence of 0.1 M KX:* (a) 2×10^{-4} M CTAB; (b) 2×10^{-4} M CTAC; *and* (c) 4×10^{-4} M CTAF. *Spectra of CTAC and CTAF have been offset vertically for clarity. ssp-polarised. T = 303 K.*

The assignment of peaks in the SF spectra of surfactant monolayers has been discussed in detail previously.[19] Two prominent peaks appear in CTAX spectra with ssp-polarisation: the d^+ symmetric CH_2 stretch at 2853 cm^{-1} and the r^+ symmetric CH_3 stretch at 2878 cm^{-1}. The d^+ mode is indicative of the conformational disorder within the monolayer. For highly ordered monolayers with few gauche defects, the d^+ mode is very weak. As disorder increases, $\langle\beta_{yyz}\rangle$ increases due to the presence of gauche

defects. For a highly disordered monolayer one might ultimately expect $\langle\beta_{yyz}\rangle$ to decrease again due to the near-random orientation of the chains. My results for CTAB monolayers at the air-water interface (chapter 4) indicate that as *A* increases, the initial increase in $\langle\beta\rangle$ is counteracted by a decrease in *N* (equation 2.17) with the result that the line-strength of the d^+ mode remains approximately constant until the area per molecule has nearly doubled, before gradually falling away to zero.

The line strength of the r^+ mode is dependent on the tilt of the terminal methyl group. In an ssp spectrum, the component of the hyperpolarisability responsible for the signal from this mode is expressed in molecular coordinates by (equation 2.23)

$\left\langle\beta_{yyz}\right\rangle = \frac{\beta_{ccc}}{8}\left\{\left\langle\cos\theta\right\rangle\left\langle 1+7r\right\rangle + \left\langle\cos 3\theta\right\rangle(r-1)\right\}$ where $r = \beta_{aac} / \beta_{ccc} > 1$ and θ is the angle between the surface normal (z) and the C_3-axis of the terminal methyl group (the c-axis.) As the first bracketed term dominates in this equation, $\langle\beta_{yyz}\rangle$ is proportional to $\langle\cos\theta\rangle$, to a good approximation.

As shown in figure 5.2, the d^+ mode is unaffected by the differences in *A* observed for CTAB, CTAC, and CTAF. The strength of the r^+ mode, however, decreases significantly from CTAB to CTAC to CTAF. The S_{d+} / S_{r+} ratio, which is a measure of conformational disorder in a surfactant monolayer, increases from 0.7 for salted CTAB, to 1.0 for salted CTAC, to 1.2 for salted CTAF.

Due to its high Krafft point, CTAI demonstrated very limited solubility at 303 K. Figure 5.3 presents a SF spectrum of CTAI from a saturated solution of CTAI at 303 K. The low overall intensity of the SF spectrum compared to the spectra of CTAX in figure 5.2 is consistent with a lower surface excess in the monolayers of CTAI.[†]

[†] The spectra from saturated CTAI solutions were variable and I do not analyse them further.

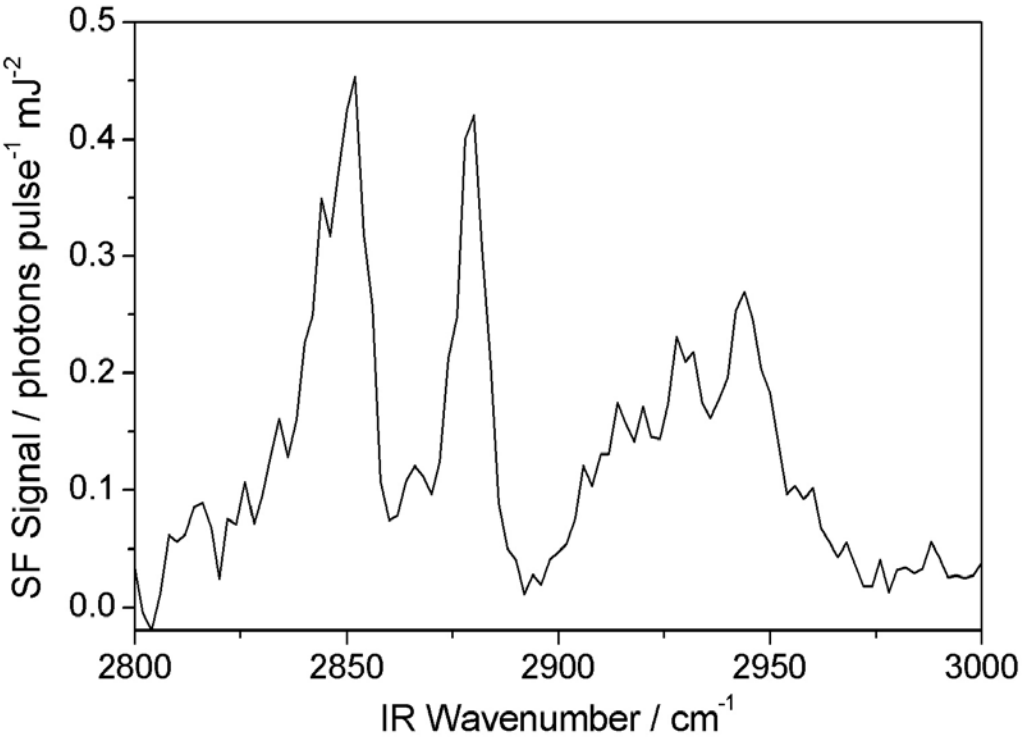

Figure 5.3 *SF spectrum of monolayer at the surface of a saturated solution of CTAI at 303 K. ssp-polarised.*

5.4 Effect of Added Electrolyte on the Structure of CTAX Monolayers at Limiting Coverage

Salinity is an important physical parameter controlling the structure of micelles and microemulsions. The general effect of added salt on micellar structure can be ascribed to a decrease in the area per ionic head group at the micelle-water interface, due to screening of electrostatic repulsions between the head groups by the added salt. It is therefore of interest to see whether the SF spectra support an analogous reduction in the area per molecule for monolayers at the air-water interface. In Figure 5.4, I compare the SF spectra of monolayers of CTAB, CTAC, and CTAF above the cmc in the presence and absence of 0.1 M KBr, KCl, and KF, respectively.‡ Surprisingly, the

‡ Since these measurements are performed above the cmc, the effect of trace impurities on the monolayer is small, even for the experiments conducted in the absence of added electrolyte.

addition of electrolyte had no effect on the SF spectra of CTAX monolayers at limiting coverage, to within the reproducibility of individual spectra. A small increase in the signal intensity was observed for the CTAB and CTAC monolayers upon addition of salt, but a large number of repetitions of the experiment would be required to establish whether this increase is statistically significant. In any event, the decrease in area per molecule caused by the addition of salt is small (< 10%).

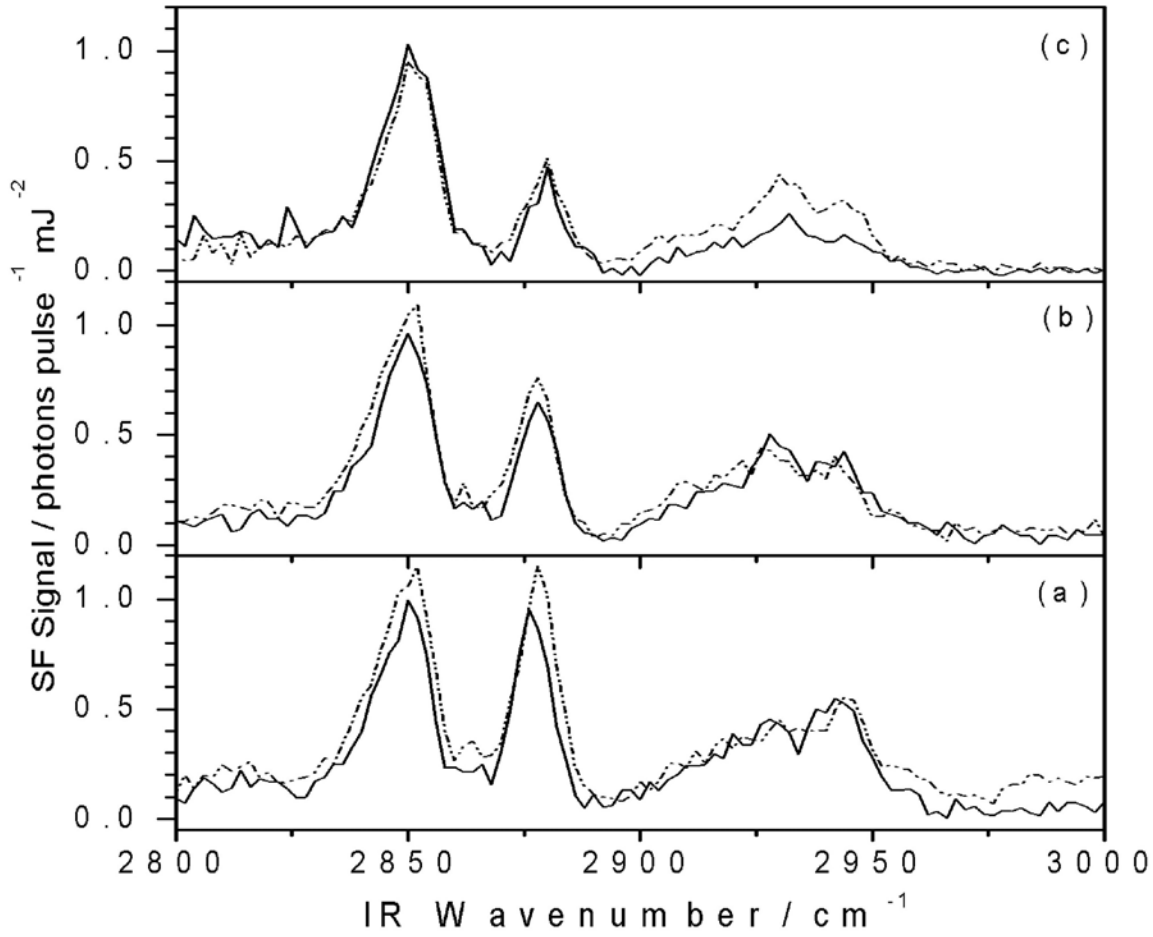

Figure 5.4 *Comparison of SF spectra of salted and unsalted CTAX monolayers: (a) CTAB [unsalted CTAB* 2×10^{-3} M*, salted CTAB* 2×10^{-4} M*]; (b) CTAC [unsalted CTAC* 2×10^{-3} M*, salted CTAC* 2×10^{-4} M*]; and (c) CTAF [unsalted CTAF* 2×10^{-3} M*, salted CTAF* 4×10^{-4} M*]. Solid line is unsalted CTAX and dotted line is CTAX in the presence of 0.1 M KX. ssp-polarised. T = 303 K.*

Measurements of the coefficient of ellipticity support the inferences drawn from the SF spectra. The values of $\overline{\rho}$ for salted and unsalted CTAX monolayers at limiting coverage are given in Table 2. In order to interpret these numbers, however, I first need to establish the effect of the counterion alone on $\overline{\rho}$.

Table 2. Coefficient of Ellipticity for CTAX Monolayers at Limiting Coverage

	CTAB	CTAB + 0.1 M KBr	CTAC	CTAC + 0.1 M KCl	CTAF	CTAF + 0.1 M KF
$\overline{\rho} \times 10^3$	−2.09	−2.28	−1.40	−1.53	−0.87	−0.90
$\overline{\rho} \times 10^3$ for CTAB [a]				−1.63		−1.2
A / Å^2 [b]	44	40	56	53	79	78

[a] *$\overline{\rho}$ for monolayers of CTAB with the same SF spectrum. T = 303 K.*
[b] *Area per molecule calculated from the calibration curve of Manning-Benson, et al.*[20]

A simple calculation serves to show that the contribution of the halide counterion to $\overline{\rho}$ is approximately independent of the thickness of the electric double layer and linear in the surface coverage. For each adsorbed surfactant molecule, charge neutrality requires that an excess counterion is present in the electrical double layer. I take a simple four-layer model for the interface comprising air, surfactant monolayer, an electrical double layer of uniform composition and of thickness equal to the Debye length, and bulk solution. The Debye length, r_D, is approximately 10 nm in the absence of added electrolyte and 1 nm in the presence of 0.1 M KX. Thus for a CTAB monolayer with a surface excess of 3.7×10^{-6} moles m^{-2} (the limiting coverage obtained by neutron reflection[21]), the average concentration of bromide ions in the double layer is approximately 0.37 M in the absence of electrolyte and 3.7 M in the presence of 0.1 M KBr. From equations 2.45 and 2.46, the contribution of the double layer to the coefficient of ellipticity, $\overline{\rho}_{dl}$, is given by

$$\bar{\rho}_{dl} = \frac{\pi\sqrt{\varepsilon_1 + \varepsilon_2}}{\lambda(\varepsilon_1 - \varepsilon_2)} \frac{(\varepsilon - \varepsilon_1)(\varepsilon - \varepsilon_2)}{\varepsilon} r_D \tag{5.1}$$

In the absence of added salt, ε and ε_2 are set to the optical dielectric constants of 0.37 M KBr and of water, respectively, and substitute r_D = 10 nm. ε_1 is the optical dielectric constant of air. $\varepsilon = n^2$ is obtained from tabulated values of the refractive index of salt solutions at 589 nm,[22] neglecting the small difference from the HeNe wavelength of 633 nm. For salted solutions, ε and ε_2 are the optical dielectric constants of 3.7 M KBr and of 0.1 M KBr, respectively, and r_D = 1 nm. The use of the refractive indices of KBr solutions, even though the concentration of K^+ ions in the double layer is very low, is justified by the small volume and polarisability of the K^+ ions. The Lorentz-Lorenz effective medium approximation (equation 2.55) allows me to separate the contributions of the two ions to the dielectric constant, and hence to $\bar{\rho}_{dl}$:

$$\frac{\varepsilon - 1}{\varepsilon - 2} = \phi_{water}\left(\frac{\varepsilon_{water} - 1}{\varepsilon_{water} + 2}\right) + \phi_{K+}\left(\frac{\varepsilon_{K+} - 1}{\varepsilon_{K+} + 2}\right) + \phi_{Br-}\left(\frac{\varepsilon_{Br-} - 1}{\varepsilon_{Br-} + 2}\right) \tag{5.2}$$

The values of $(\varepsilon - 1) / (\varepsilon + 2)$ for the ions are calculated from tabulated values of R_m and V_m[22] according to the Clausius-Mossotti relationship (equation 2.54). The volume fractions, ϕ, are estimated from V_m and the molarity. From equation 5.2, it can be shown that the contribution of the K^+ ions to $\bar{\rho}_{dl}$ in the four-layer model is less than 10% of the contribution of Br^- ions and can reasonably be neglected.

For CTAB monolayers with $\Gamma = 3.7 \times 10^{-6}$ moles m^{-2}, we find $\bar{\rho}_{dl} = -0.65 \times 10^{-3}$ in the absence of salt and $\bar{\rho}_{dl} = -0.66 \times 10^{-3}$ in the presence of 0.1 M KBr.[§] Thus $\bar{\rho}_{dl}$ is insensitive to the detailed structure of the double layer. The evaluation of

$\bar{\rho}_{dl}$ for lower surface coverages shows that $\bar{\rho}_{dl}$ is linear in Γ to a good approximation.[**] This calculation can be repeated for CTAC monolayers at an area per molecule of 64 Å^2 to yield $\bar{\rho}_{dl} = -0.32 \times 10^{-3}$. For CTAF monolayers, I was unable to find literature data for the refractive index of aqueous solutions of KF, but using literature values of R_m and V_m for F^- ions, I estimate $\bar{\rho}_{dl} = -0.06 \times 10^{-3}$ at an area per molecule of 93 Å^2.

Changes in $\bar{\rho}$ ($\Delta\bar{\rho}$) brought about by the addition of salt are thus not due to changes in the structure of the double layer but must arise either from a change in surface coverage or a change in the structure of the monolayer (since $\bar{\rho}$ is a sensitive function of the density of the monolayer). Previous work on CTAB monolayers has shown that $\bar{\rho}$ is approximately a linear function of Γ.[23] The small negative values of $\Delta\bar{\rho}$ for the Br^- and Cl^- ions are thus most simply interpreted in terms of a small (<10%) increase in the surface excess in the monolayer, which is consistent with the SF spectra. For CTAF, $\bar{\rho}$ was unaffected by the addition of 0.1 M KF. As is the case with the SF spectra, numerous repetitions of these experiments would be required to establish a statistically significant change in surface excess.

The key conclusion from both the SF spectra and ellipsometry data is that adding electrolyte has very little effect on the limiting structure of the monolayer; it merely changes the bulk concentration at which that structure is reached. Let us briefly consider the aggregation behaviour in the bulk in the light of our results for CTAX monolayers. In Israelachvili's geometric model for the aggregation of lipids,[24] a surfactant molecule is characterised by three parameters: volume of the hydrophobic

---

[§] One can also estimate $\bar{\rho}_{dl}$ from literature values of R_m and V_m for Br^- ions. In the absence of added electrolyte one finds $\bar{\rho}_{dl} = -0.73 \times 10^{-3}$.

part of the molecule, V; the optimum head group area per molecule, a; and the length of the hydrophobic chain, l. A spherical micelle is formed when the critical packing parameter $V / la < 1/3$, and cylindrical micelles are formed when $1/3 < V / la < 1/2$. Assigning the C_{16} chain of CTAX molecules a molecular volume of 482 Å^3 [25] and a length of 22 Å, the minimum value of a is 66 Å^2 for spherical micelles, and 44 Å^2 for cylindrical micelles. If a at the micelle-water interface is identified with A at the air-water interface, one would expect, based on tensiometric values of A, that CTAC and CTAF would form spherical micelles in the presence or absence of salt. Experimentally, micelles in CTAC solutions remain spherical when KCl is added.[7] For CTAB, the values of A would suggest that cylindrical micelles should form both with and without added KBr. The unresolved question is therefore not why a sphere-rod transition occurs when KBr is added, but why CTAB does not form cylindrical micelles in solution even in the absence of salt.

5.5 Specific Effects of Halide Counterions

The data presented earlier show that the choice of halide counterion has a large effect on the limiting coverage of CTAX that is attainable at the air-water interface. I am also interested in the question of whether different halide ions result in significantly different monolayer structures. The first point of comparison is of monolayers of CTAC and CTAF at their saturation coverage with monolayers of CTAB as a function of concentration. In Figure 5.5, I have overlaid CTAC and CTAF spectra with the CTAB spectra to which they have the closest match.

[**] This would be expected from an expansion of the Lorentz-Lorenz effective medium approximation at the limit of low φ.

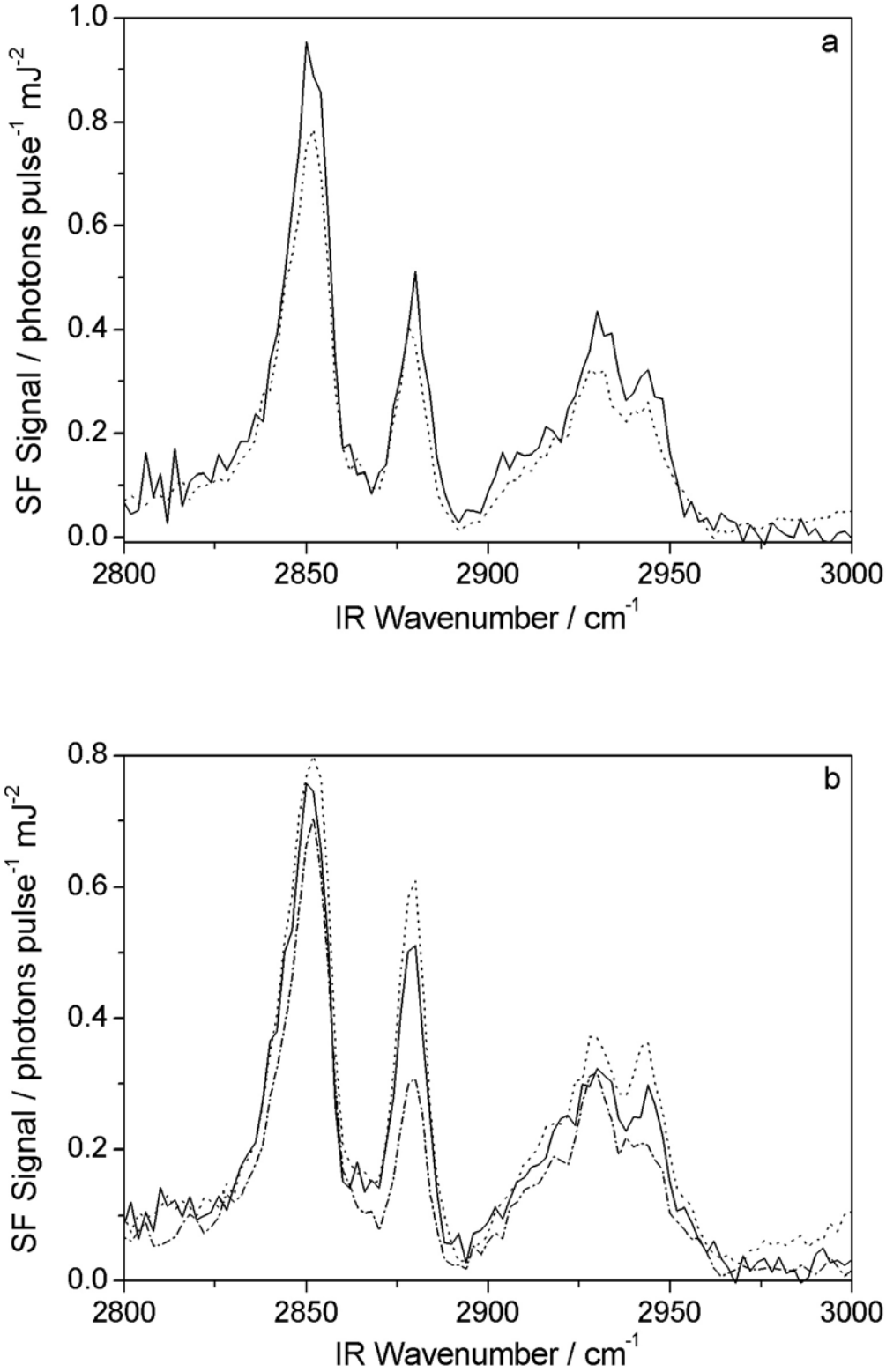

Figure 5.5 *Comparison of spectra from salted CTAC and CTAF at their limiting coverages with similar CTAB spectra. (a) Saturated monolayer of salted CTAF (solid line) and 0.25 mM CTAB (dotted line). (b) Saturated monolayer of salted CTAC (solid line), 0.5 mM CTAB (upper dotted line), and 0.25 mM CTAB (lower dashed line). ssp-polarisation. T = 303 K.*

Figure 5.5 (a) shows that the SF spectrum of CTAF above its cmc is very similar to that of CTAB at a concentration of 0.25 mM (the small difference in overall intensity is within the variability observed between spectra taken on different occasions). The CTAC spectrum (Figure 5.5 (b)) does not match perfectly any of the CTAB spectra in chapter 4 (Figure 4.1), but is intermediate between CTAB spectra at 0.25 and 0.5 mM. For neither CTAC nor CTAF are there features anywhere in the C-H stretching region that differ qualitatively from those in CTAB.

Different counterions might result in monolayers that differed in ways that are not evident in SF spectra. Ellipsometry is very sensitive to the density of the monolayer and a comparison of the ellipsometric data will therefore reveal if different counterions result in any significant differences in the packing of the hydrocarbon chains in the monolayer. The CTAF and CTAC spectra correspond to the CTAB spectra at 0.25 mM and 0.4 mM (by interpolation), respectively. The coefficients of ellipticity of CTAB monolayers at these concentrations may be read off the calibration data of Manning-Benson *et al*[20] in Figure 5.6 and are shown in Table 2. The measured values of $\overline{\rho}$ contain contributions from the double layer as well as the surfactant monolayer. To compare the latter I must first correct for the contributions made by different counterions in the double layer.[††] After making this correction, the

[††] I have estimated areas per molecule of 65 Å^2 and 94 Å^2 at the cmc for CTAC and CTAF in the presence of added electrolyte from surface tension measurements. The calculated contribution of the Cl^- and F^- ions to the measured value of $\overline{\rho}$ at the cmc was $\overline{\rho}_{dl} = -0.32 \times 10^{-3}$ for Cl^- and -0.06×10^{-3} for F^-. For CTAB monolayers, I calculate $\overline{\rho}_{dl} = -0.45 \times 10^{-3}$ and -0.31×10^{-3} at areas per molecule of 65 Å^2 and 94 Å^2, respectively. In other words, to compare the contribution of the surfactant to $\overline{\rho}$, one must first add approximately 0.13×10^{-3} to $\overline{\rho}$(CTAB), in the case of CTAC, or 0.25×10^{-3} in the case of CTAF. After making these corrections, the values of $\overline{\rho}$ for the CTAB monolayers are equal to those of CTAC and CTAF monolayers (Table 2) with the same SF spectra to within experimental error.

values of $\overline{\rho}$ for the CTAF and CTAC spectra are in good agreement with the values of $\overline{\rho}$ for CTAB monolayers at 0.25 and 0.4 mM, respectively.

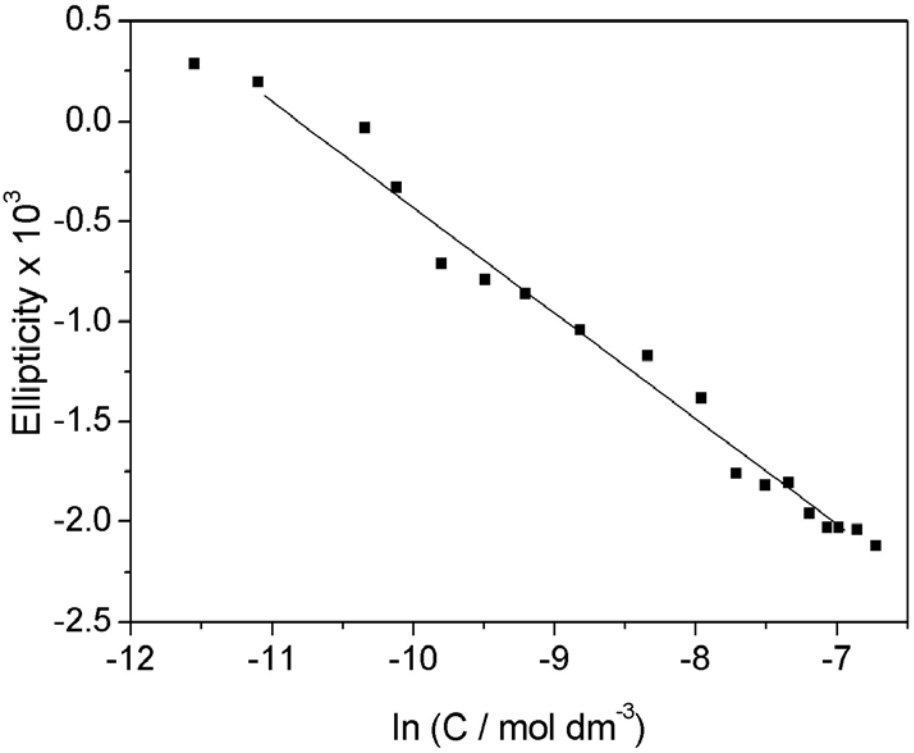

Figure 5.6 *Coefficient of ellipticity vs ln [CTAB] data of Manning-Benson, et al.*[23]

The surface excess in CTAB monolayers at concentrations of 0.25 and 0.4 mM, determined from the Gibbs equation in chapter 4, is 2.5×10^{-6} and 2.9×10^{-6} mol m^{-2}, respectively. These surface coverages are significantly greater than those determined tensiometrically for CTAF (1.8×10^{-6} mol m^{-2}) and CTAC (2.6×10^{-6} mol m^{-2}) monolayers at saturation coverage. In other words, monolayers with the same ellipsometric constant and SF spectrum appear to have different surface coverages. This discrepancy might be taken as evidence that the halide ions are having specific effects on the structure of the monolayer. Given that the SF spectra and ellipsometric data provide no evidence of such effects, however, it is more likely

that the discrepancy is a consequence of systematic errors in the determination of surface coverages from surface tension plots.

5.6 Conclusion

Sum-frequency spectroscopy, ellipsometry, and surface tensiometry have been used to study the effect of the halide counterion on monolayers of CTAX (X = F^-, Cl^-, Br^-, and I^-). For the iodide counterion, aqueous solutions are well below the Krafft point at room temperature and CTAI therefore functions ineffectively as a surfactant under ambient conditions. CTAB, CTAC, and CTAF are all above the Krafft point at 30°C. Adding salt in the form of 0.1 M KX reduces the cmc but appears to have little effect on the limiting area per molecule attained at the cmc, which increases from 44 $Å^2$ for CTAB to 65 $Å^2$ for CTAC and ca. 94 $Å^2$ for CTAF. The principal effect of the counterion is to change the efficiency and effectiveness of the surfactant (both decreasing in order $Br^- > Cl^- > F^-$): neither sum-frequency spectroscopy nor ellipsometry provide any firm evidence for specific effects of the halide ions on the structure of the surfactant monolayers. Finally, in the course of the analysis of the ellipsometric data, the contribution of the double layer to the coefficient of ellipticity has been evaluated and shown to be linear in the surface coverage and insensitive to the thickness of the double layer.

References

(1) Penfold, J. *et. al. J. Chem. Soc. Faraday Trans.* **1997**, *93*, 3899.

(2) Bain, C. D. In *Modern Characterization Methods of Surfactant Systems*; Binks, B. P., Ed.; Marcel Dekker: New York, 1999; chapter 9.

(3) Lu, J. R.; Hromadova, M.; Simister, E. A.; Thomas, R. K.; Penfold, J. *J. Phys. Chem.* **1994**, *98*, 11519.

(4) (a) Bell, G. R.; Manning-Benson, S.; Bain, C. D. *J. Phys. Chem B.* **1998**, *102*, 218. (b) Lyttle, D. J.; Lu, J. R.; Su, T. J.; Thomas, R. K.; Penfold, J. *Langmuir*. **1995**, *11*, 1001.

(5) (a) Bell, G. R.; Bain, C. D.; Ward, R. N. *J. Chem. Soc. Faraday Trans.* **1996**, *92*(4), 515. (b) Goates, S. R.; Schofield, D. A.; Bain, C. D. *Langmuir* **1999**, *15*(4), 1400. (c) Conboy, J. C.; Messmer, M. C.; Richmond, G. L. *J. Phys. Chem. B* **1997**, *101*(34), 6724. (d) Lu, J. R.; Thomas, R. K.; Penfold, J. *Adv. Coll. Interface. Sci*. **2000**, *84*, 143.

(6) Knock, M. M.; Bain, C. D. *Langmuir* **2000**, *16*, 2857.

(7) (a) Lindman, B; Wennerström, H. *Top. Curr. Chem.* **1980**, *87*, 1. (b) Gravsholt, S. J. *J. Colloid Interface Sci.* **1976**, *57*, 575. (c) Rehage, H.; Hoffmann, H. *Faraday Discuss. Chem. Soc.* **1983**, *76*, 363. (d) Hoffmann, H.; Rehage, H.; Reizlein, K.; Thurn, H. *ACS Symp. Ser.* **1985**, *272*, 41. (e) Shikata, T.; Dahman, S. J.; Pearson, D. S. *Langmuir* **1994**, *10*, 3470. (f) Hoffmann, H. *Adv. Mater.* **1994**, *6*, 116. (g) Hoffmann, H.; Ebert, G. *Angew. Chem., Int. Ed. Engl.* **1988**, *27*, 902. (h) Hoffmann, H. *ACS Symp. Ser.* **1994**, *578*, 2. (i) Soltero, J. F. A.; Puig, J. E.; Manero, O.; Schulz, P. C. *Langmuir* **1995**, *11*, 3337. (j) Soltero, J. F. A.; Puig, J. E.; Manero, O. *Langmuir* **1996**, *12*, 2654. (k) *Structure and Flow in Surfactant Solutions*; ACS Symposium Series 578; Herb, C. A., Prud'homme, R. K., Eds.; American Chemical

Society: Washington, DC, 1994. (l) Gaillon, L.; Lelièvre, J.; René, G. *J. Coll. Interface Sci.* **1999**, *213*, 287.

(8) Underwood, A. L.; Anacker, E. W. *J. Coll. Interface Sci.* **1987**, *117*, 242.

(9) (a) Lindblom, G.; Lindman, B. *J. Coll. Interface Sci.* **1973**, *42*, 400. (b) Anacker, E. W. In *Solution Chemistry of Surfactants*; Mittal, K. L., Ed.; Plenum: New York, 1979, p. 247. (c) Porte, G. In *Micelles, Membranes, Microemulsions and Monolayers*; Gelbart, W. G., Ben-Shaul, A., Roux, D., Eds.; Springer: New York, 1994; Chapter 2.

(10) (a) Israelachvili, J. N. *Intermolecular and Surface Forces: With Applications to Colloidal and Biological Systems*, 2nd ed.; Academic Press: London, 1995; p. 256. (b) Israelachvili, J. N.; Mitchell, D. J; Ninham, B. W. *J. Chem. Soc., Faraday Trans. 1*. **1976**, *72*, 1525.

(11) Israelachvili, J. N. *Intermolecular and Surface Forces: With Applications to Colloidal and Biological Systems*, 2nd ed.; Academic Press: London, 1995; p. 252.

(12) (a) Hiemenz, P. C.; Rajagopalan, R. In *Principles of Colloid and Surface Chemistry*, 3rd ed. Marcel Dekker: New York, 1997; p. 361. (b) Parades, S.; Tribout, M.; Sepulveda, L. *J. Phys. Chem.* **1984**, *88*, 1871. (c) Morgan, J. D.; Napper, D. H.; Warr, G. G.; Nicol, S. K. *Langmuir* **1994**, *10*, 797.

(13) (a) Ward, R. N.; Duffy, D. C.; Bell, G. R.; Bain, C. D. *Mol. Phys*. **1996**, *88*(1), 269. (b) Bell, G. R.; Bain, C. D.; Li, Z. X.; Thomas, R. K.; Duffy, D. C.; Penfold, J. *J. Am. Chem. Soc.* **1997**, *119* (42), 10227. (c) Bell, G. R.; Li, Z. X.; Bain, C. D.; Fischer, P; Duffy, D. C. *J. Phys. Chem. B* **1998**, *102* (47), 9461.

(14) (a) Duffy, D. C.; Ward, R. N.; Davies, P. B.; Bain, C. D. *J. Am. Chem. Soc.* **1994**, *116* (3), 1125. (b) Duffy, D. C.; Davies, P. B.; Bain, C. D. *J. Phys. Chem.* **1995**, *99*, 15241

(15) (a) Hoffmann, H.; Rehage, H.; Reizlein, K.; Thurn, H. *ACS Symp. Ser.* **1985**, *272*, 41. (b) Shikata, T.; Dahman, S .J.; Person, D. S. *Langmuir* **1994**, *10*, 3470.

(16) Su, T. J.; Lu, J. R.; Thomas, R. K.; Penfold, J. *J. Phys. Chem. B.* **1997**, *101* (6), 937.

(17) *Critical Micelle Concentrations of Aqueous Surfactant Systems.* Mukerjee, P.; Mysels, K. J. Eds.; National Standard Reference Data System, National Bureau of Standards 36, 1971.

(18) Lu, J. R.; Purcell, I. P.; Lee, E. M.; Simister, E. A.; Thomas, R. K.; Rennie, A. R.; Penfold, J. *J. Coll. Int. Sci.* **1995**, *174*, 441.

(19) Ward, R. N.; Duffy, D. C.; Davies, P. B.; Bain, C. D. *J. Phys. Chem.*, **1994**, *98*, 8536.

(20) Manning-Benson, S.; Parker, S. R. W.; Bain, C. D.; Penfold, J. *Langmuir* **1998**, *14*, 990.

(21) (a) Lu, J. R.; Hromadova, M.; Simister, E. A.; Thomas, R. K.; Penfold, J. *J. Phys. Chem.* **1994**, *98*, 11519. (b) Lu, J. R.; Hromadova, M.; Simister, E.; Thomas, R. K.; Penfold, J. *Physica B* **1994**, *198*, 120. (c) Lu, J. R.; Li, Z. X.; Smallwood, J.; Thomas, R. K.; Penfold, J. *J. Phys. Chem.* **1995**, *99*, 8233.

(22) *Handbook of Chemistry and Physics*, 64th Ed., CRC: Boca Raton, Florida, 1984.

(23) Manning-Benson, S.; Bain, C. D.; Darton, R. C. *J. Coll. Interface Sci.* **1997**, *189*, 109.

(24) (a) Israelachvili, J. N. *Intermolecular and Surface Forces: With Applications to Colloidal and Biological Systems*; Academic Press: London, 1995; p. 256. (b) Israelachvili, J. N.; Mitchell, D. J; Ninham, B. W. *J. Chem. Soc., Faraday Trans. 1.* **1976**, *72*, 1525.

(25) Small, D. M. *Handbook of Lipid Research 4: The Physical Chemistry of Lipids From Alkanes to Phospholipids.* Plenum Press: New York, 1986; pp. 196-208.

CHAPTER 6

Mixed Monolayers of CTAB and Alkanes

Chapter 6: Mixed Monolayers of CTAB and Alkanes

6.1 Rationale for Experiment

The CTAB-alkane* mixed monolayer experiment was motivated by three compelling questions:

(i) What is the effect of alkane penetration into the hydrocarbon chains of a surfactant monolayer at the air-water interface?

(ii) Do mixed monolayers of surfactants and alkanes at the air-water interface undergo phase transitions?

(iii) Could the structure of a mixed monolayer of surfactant and alkane at the air-water interface provide insight into the structure of a surfactant monolayer at the bulk alkane-water interface?

(i) and (ii) above are closely related, as one of the most interesting effects of adding alkanes to a surfactant monolayer at the air-water interface is the resulting phase behaviour of the mixed monolayer. (iii) results from the intuitive supposition that the mixed surfactant-alkane monolayer in equilibrium with a small lens of alkane could serve as an conceptual intermediate between a monolayer of the surfactant at the air-water interface and a monolayer of the same surfactant at the alkane-water interface. Our results suggest that the liquid-condensed phase observed in a mixed surfactant-alkane monolayer hints at the well-ordered surfactant monolayer I observe at the alkane-water interface.

6.1.1 Phase Transitions in Monolayers. Insoluble (Langmuir) monolayers undergo phase transitions in response to compression and expansion of the monolayer within a

* In this thesis, CTAB always refers to hexadecyltrimethylammonium bromide, C_{16}TAB.

Langmuir trough. Were soluble monolayers subjected to such treatment, they would undergo adsorption/deadsorption of surfactant molecules from/to the bulk solution instead of exhibiting interesting polymorphism. To observe a phase change in a mixed (soluble) monolayer, the temperature is gradually adjusted until a change in the monolayer is detected by a surface sensitive technique such as surface tension, ellipsometry, sum-frequency spectroscopy, X-ray reflectivity, fluorescence or Brewster angle microscopy. The phase diagram of a soluble monolayer is less complex than that of an insoluble monolayer,[1] but both gas-liquid[2,3] and liquid-solid[4,5,6,7] phase transitions have been observed in Gibbs monolayers. In particular, a first-order phase transition was observed in mixed monolayers of dodecanol and cationic surfactants.[8]

Mixed alkane-surfactant monolayers are formed by placing droplets of long-chain alkanes onto a surfactant solution. These droplets initially spread out and then retract to form lenses in equilibrium with a molecularly thin oil film.[9,10,11,†] Mixed monolayers formed in this way have been studied by surface tensiometry,[9,10] neutron reflection,[11] light scattering,[10] and sum-frequency spectroscopy.[12]

It is beneficial to briefly consider what phase transitions occur within an insoluble monolayer. When the monomer is insoluble, phase transitions can take several forms, which may resemble those between the mesophases of liquid crystals.[13] At high temperature and low pressure or low density, the monolayer is in a liquid expanded state (L_1); at low temperatures and high pressure or high density, the monolayer is in a crystalline solid phase (CS). Several structurally distinct phases may lie between these two extremes, and these are typically mesophases. Crystalline

[†] For alkanes with chains much shorter than ones we have studied, films are observed that are macroscopically thin but molecularly thick. [Kelly, H.; Meunier, J.; Binks, B. P. *Phys. Rev. Lett.* **1992**, *69*, 1220.]

phases are characterised by long range translational and orientational order. Mesophases are characterised by short range translational order. Different liquid mesophases (L_n) are distinguished by different collective molecular tilts, while the solid phases (CS, S) exhibit varied degrees of packing and order. Transitions of tilt are second-order,[13,14] while other transitions are first-order. First-order phase transitions involve an abrupt change in enthalpy or volume and reflect a discontinuity in the first derivative of the chemical potential, consistent with typical phase transitions such as bulk melting. At a second-order phase transition, the first derivative of the chemical potential is continuous but there is a discontinuity in the second derivative. Second-order phase transitions are generally considered to be order-disorder transitions and, unlike first-order transitions, do not show a horizontal plateau region in a plot of their surface pressure as a function of area per molecule, $A = 1 / (N_A\Gamma)$, where N_A is Avogadro's number and Γ is the surface excess of the surfactant. A second-order phase transition is typically recognised by a kink in its surface pressure versus area per molecule isotherm. Figure 6.1 shows a generic, typical surface pressure versus area per molecule isotherm.

The phase diagram for an insoluble monolayer can be constructed from measurements of isotherms and monolayer structures by surface pressure or X-ray diffraction at different temperatures.[13,15] Figure 6.2 shows a generic phase diagram for insoluble monolayers of fatty acids and alcohols. The dotted vertical line marks the cross-section defined by the isotherm in figure 6.1. Shifts or distortions in the pressure and temperature axes generally allow such a phase diagram to describe the phase behaviour of different surfactant monolayers.

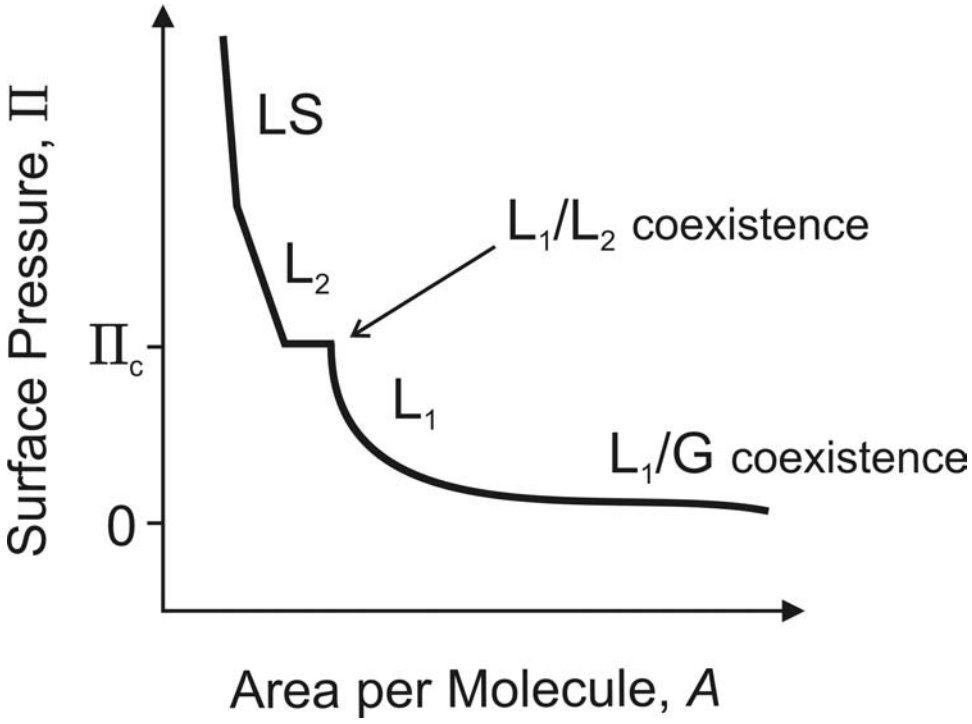

Figure 6.1 *A generic, typical isotherm for surface pressure versus area per molecule of an insoluble monolayer. The conditions and nature of the monolayer greatly affect the shape of its isotherm.*

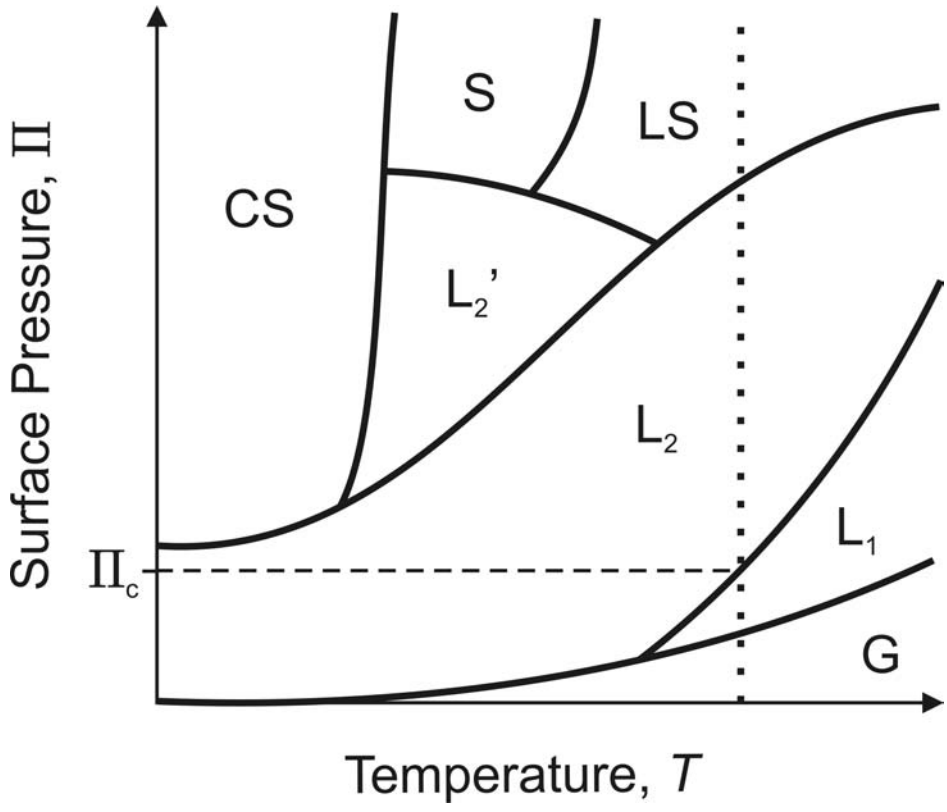

Figure 6.2 *Generic phase diagram for insoluble monolayers of fatty acids and alcohols. Each condensed phase (all phases except G and L_1) may be subdivided into more phases. The dotted line represents the isotherm shown in Figure 6.1.*

Research into mixed monolayers was originally inspired by the work of Powney and Addison, who in 1937 discovered that the curves for surface tension as a function of concentration for sodium alkyl sulphates, n = 12-18, showed breaks at certain concentrations.[16] These abrupt changes were identified later as the result of trace levels of surface active impurities such as dodecanol.[17] This effect was observed in a different manner by Ross and co-workers, who studied the film drainage transition temperatures of sodium dodecyl sulphate (sodium lauryl sulphate, SDS) and dodecanol (lauryl alcohol) and discovered that upon heating, a slow draining film would suddenly drain faster at a well-defined temperature.[18] They postulated that the slow draining was due to an ordered, rigid surface structure, and that the change in the drainage rate was due to a phase transition in this surface. These transitions for foam and film drainage were later correlated to transitions in surface viscosity[19] and surface tension.[20] A correspondence was noted between the sharp, reversible transitions in foam and film drainage and the transitions observed upon the compression and expansion of Langmuir films.

More recently, the same system of SDS and dodecanol was studied at the microscopic level by sum-frequency spectroscopy (SFS). Casson and Bain used SFS and ellipsometry to observe the first-order phase transition at 16 °C.[7] Below that temperature, the monolayer is conformationally ordered with equimolar quantities of SDS and dodecanol. Above it, a less dense and more conformationally disordered phase was observed with a 3:2 molar ratio between SDS and dodecanol.

This work was extended to study mixed monolayers of alkyltrimethylammonium bromide cationic surfactants (C_nTABs) with dodecanol for n = 12, 14, and 16.[8] C_nTABs, of which this thesis focuses on n = 16, have been studied in detail by neutron reflection,[21] ellipsometry, and sum-frequency

spectroscopy,[22] and form monolayers which are conformationally disordered and have a density close to that of a liquid hydrocarbon. A first-order phase transition was observed for this system at a fixed temperature which increases with *n*. The composition of this mixed monolayer in its liquid and solid phases is different from that found in the SDS-dodecanol mixed monolayer. For C_nTAB-dodecanol, the solid phase has a ratio of approximately 2:3, and the liquid phase is equimolar. The C_nTAB in the mixed monolayer is more disordered than dodecanol but much less disordered than in a pure C_nTAB monolayer in the absence of dodecanol.

Mixed monolayers of surfactants and alcohols are interesting and commercially important, but here I focus on mixed monolayers consisting of surfactants and alkanes. Neutron reflection measurements have been made for several selectively deuterated mixed surfactant-alkane systems: C_{14}TAB + dodecane;[11(a)] C_{12}TAB and C_{16}TAB + dodecane.[11(c)] For the C_{14}TAB + dodecane system, a semi-empirical calculation that uses previous data for pure CTAB monolayers seems to show that the experimental value for the area per molecule is consistent with the layer being a close-packed, smooth liquid layer. This simplistic view does not include the important detail that the surfactant tails were more extended in the mixed monolayer than in the pure monolayer. A later study on the C_{12}TAB and C_{16}TAB + dodecane systems showed that the initial conclusion that the oil was unevenly distributed in the monolayer was incorrect, and that the oil was evenly distributed throughout the monolayer. These two mixed monolayer systems also showed the surfactant layer thicker in the presence of dodecane than in its absence, and the oil seemed to cause the surfactant chains to adopt a more upright conformation.

6.1.2 Surface Freezing. Most materials exhibit surface melting, which arises from greater ordering across the three-dimensional bulk material as compared to the two-dimensional surface. Most metal,[23] semiconductor,[24] and ice[25] surfaces melt at a temperature lower than that of the bulk. In direct contrast to surface melting is the unusual phenomenon of surface freezing. Surface freezing could be considered the pure liquid counterpart to the intriguing phase behaviour observed in some surfactant monolayers and liquid crystals. Alkanes,[26,27,28,29] alcohols,[30,31] and liquid crystals[32] form ordered phases at the surface of their bulk liquids above the bulk freezing temperature. The surfaces of liquid alkanes freeze at a temperature up to 3 °C higher than their respective bulk freezing temperatures. Ocko, Wu and coworkers studied the vapour-liquid interface of normal alkanes using X-ray reflectivity and grazing incidence diffraction, while the thermodynamics were examined by surface tensiometry.[28] The phase transition point and structure of the ordered surface alkane monolayer differed according to the chain length, *n*, of the normal alkane, which varied from 15 to 50.[26,27,28,33] The combination of alkane ordering at liquid interfaces and surfactant ordering within mixed monolayers promises a rich and relatively unexplored field of fascinating phase behaviour for mixed monolayers of surfactants and alkanes.

6.2 Mixed Monolayers of CTAB and Alkanes at the Air-Water Interface

Most of the experimental results described in this chapter were carried out in partnership with Caroline McKenna, a Part II student in our laboratory. After Caroline McKenna's departure, the mixed monolayer project was continued with Dr. Qunfang Lei, who was a visiting scientist in our laboratory for one year. I would like

to graciously acknowledge their meticulous experimental work and thoughtful analyses. When we began our study of mixed monolayers of surfactants and alkanes, we chose to use dodecane since the CTAB + dodecane system had been studied previously by neutron reflection.[11(c)] Dodecane's relatively high vapour pressure enables two techniques for mixed monolayer formation. In one method, a microsyringe is employed to introduce a lens of alkane onto the surface of the surfactant solution, and in the other method, alkane vapour from a reservoir within the sample cell is allowed to condense onto the surface of the solution. The condensation method is limited to volatile oils (12 or fewer carbons) and requires an equilibration time of approximately 20 minutes within the sealed sample cell. The microsyringe method enables the precise deposition of longer-chain alkanes and is applicable to a variety of sample cells. When using the microsyringe method, it is essential that only a minimal amount of oil (~ 1 μL of 10% v/v solution of alkane in chloroform) is deposited on the surface of the surfactant solution. Excessive deposition of oil leads to a multitude of floating oil lens reservoirs. These lenses can interfere with the incident laser beam(s) in SFS and ellipsometry. I prefer the microsyringe deposition method since it enables direct comparison between experiments with longer-chain alkanes, and the equilibration time is more easily controlled. Even without the equilibration delays associated with alkane vapour condensation, experiments on temperature-controlled phase transitions are inevitably slowed by the equilibration times on the order of at least 10 minutes per 1 °C increment. Figure 6.3 shows two sum-frequency spectra comparing the vapour deposition and microsyringe application methods for dodecane on the surface of a 0.6 mM CTAB solution.

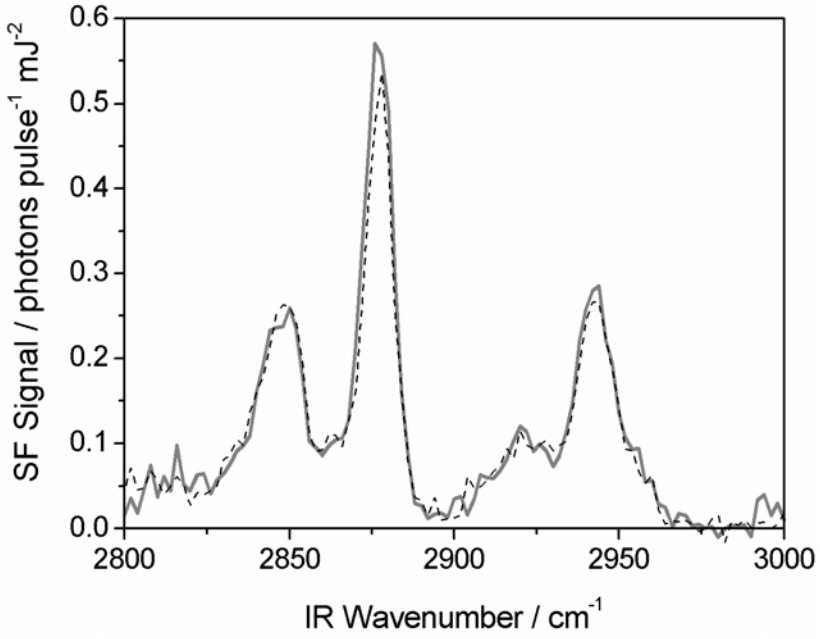

Figure 6.3 *Comparison of vapour deposition (dashed black line) and microsyringe application (solid gray line) of dodecane to a 0.6 mM CTAB solution. Sum-frequency spectra taken at room temperature, T = 298 K.*

From figure 6.3, the two methods of alkane application are seen to be effectively equivalent for dodecane.

6.2.1 Ellipsometry. Ellipsometry was performed on mixed monolayers of CTAB + tetradecane or dodecane. Dr. Qunfang Lei extended our ellipsometric measurements to include tridecane and longer-chain alkanes up to octadecane. Her ellipsometric results are presented in 6.2.1.3 to support the conclusions presented in this chapter.

6.2.1.1 CTAB + Tetradecane. Figure 6.4 shows $\overline{\rho}$ as a function of temperature for 0.6 mM CTAB (2/3 × cmc) to which 1 μL of tetradecane (10 % v/v in $CHCl_3$) has been added. A clear first-order phase transition occurs during both the heating and cooling cycles. The slight hysteresis is due to residual trace impurities. The phase

transition temperature, $T_m(2D)$ = 17 °C, is 11 °C above the bulk melting point of tetradecane (6 °C). Similar results were obtained for 0.3 mM CTAB + tetradecane.

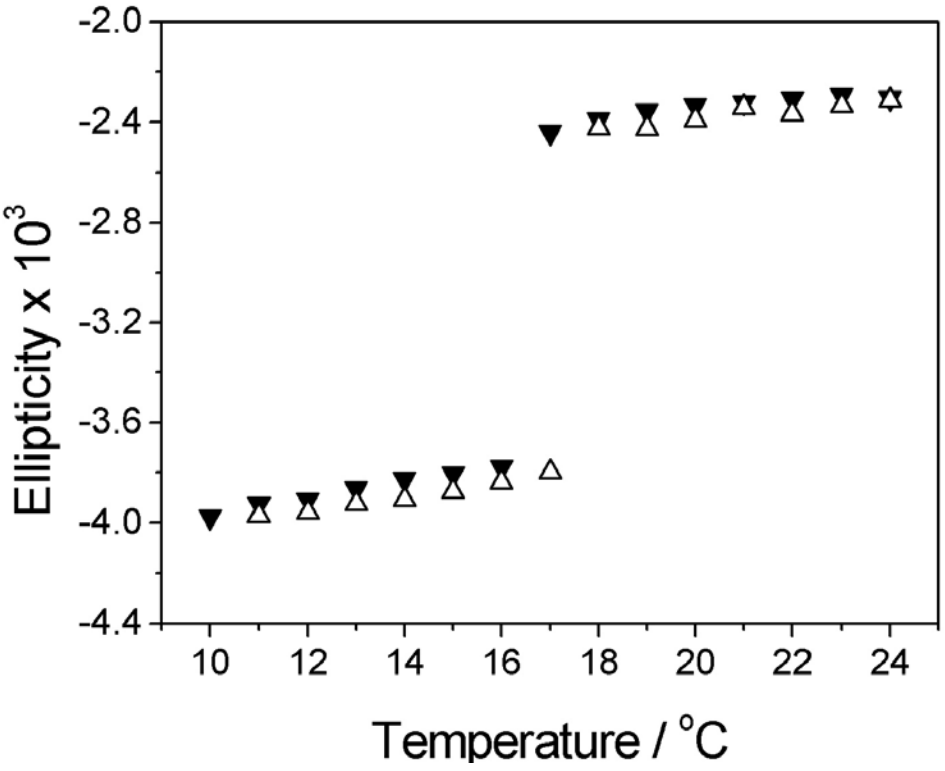

Figure 6.4 *Coefficient of ellipticity $\bar{\rho}$, as a function of temperature for tetradecane on a 0.6 mM CTAB solution. Filled triangles indicate cooling, and open triangles indicate heating.*

6.2.1.1.1 The Liquid Phase. For thin films, ellipsometric measurements yield one independent parameter, η, the ellipsometric thickness. Ellipsometry does not provide information on monolayer composition independently; supplementary information can be incorporated into analysis of ellipsometric measurements in order to determine the composition of a monolayer. Here, we construct a model for the liquid phase of the mixed monolayer. The chain region is assumed to be isotropic with a density equal to that of a liquid hydrocarbon, and the dielectric constant of the solution is assumed to be the same as that of pure water. For uniaxial isotropic monolayers,[34]

equation 2.46 applies, where ε_1 and ε_2 are the relative permittivities of air ($\varepsilon_1 = 1.0$) and water ($\varepsilon_2 = 1.777$). The coefficient of ellipticity is given by this equation in relation to the ellipsometric thickness, η. To calculate the ellipsometric thickness, we require values for the dielectric constant and the thickness of the monolayer, *d*. The dielectric constant for the isotropic monolayer can be calculated from the Clausius-Mossotti equation (equation 2.54). From the polarisability (R_m) and the molar volume (V_m) of the CH_2 unit, ε is found to equal 2.05.[35]

Neutron reflection experiments[11(c)] determined areas per molecule for the oil (dodecane) and surfactant (CTAB at the cmc) of $A_{oil} = 67 \pm 7$ Å^2 and $A_{surf} = 52 \pm 3$ Å^2 at 301 K. A_{oil} for tetradecane is assumed here to have the same value (70 Å^2) as that for dodecane in a CTAB + C_{12} mixed monolayer. The volume of the C_2H_4 unit is 60 Å^3, and that of the C_2H_5 unit is 65 Å^3 in the liquid phase near the freezing point.[36] The volume of the CTAB hydrocarbon chain is therefore $V_{surf} = 480$ Å^3 and the volume of the tetradecane is $V_{oil} = 426$ Å^3. The contributions to the monolayer thickness from the oil and surfactant are $d_{oil} = V_{oil} / A_{oil} = 6.1$ Å and $d_{surf} = V_{surf} / A_{surf} = 9.2$ Å, respectively. The monolayer's total thickess is thus 15.3 Å. Substituting ε and *d* into equation 2.50 yields the ellipsometric thickness, which can be substituted into equation 2.46 to give $\overline{\rho}_{chain} = -2.28 \times 10^{-3}$ for the chain region.

We next consider the contribution from the trimethylammonium head group and bromide counterion (TMAB). The contribution from TMAB at 44 Å^2 per molecule was estimated previously during investigations into the effect of hydrocarbon chain length on the ellipticity in a homologous series of C_nTABs.[22] A plot of ellipticity as a function of chain length, *n*, extrapolates to a value of approximately -0.5×10^{-3} at $n = 0$. As this value includes surface roughness of $+0.5 \times 10^{-3}$, the TMAB contribution is actually -1×10^{-3}. This value is appropriate for the

ellipticity of TMAB in CTAB at 44 Å^2 per molecule. In the mixed monolayer, A_{surf} = 52 Å^2. Accounting for this difference gives a contribution to the ellipticity from TMAB in the mixed monolayer of $\bar{\rho}_{TMAB} = -0.85 \times 10^{-3}$.

A roughness contribution of $\bar{\rho}_R = + 0.5 \times 10^{-3}$ was estimated from capillary wave theory, based on a value of $\bar{\rho}_R = 0.38 \times 10^{-3}$ for pure water and a scaling of $\bar{\rho}_R \propto \gamma^{-½}$, where γ is the surface tension. This leads to an overall sum for the ellipticity, $\bar{\rho}$, of $\bar{\rho} = \bar{\rho}_{chain} + \bar{\rho}_{TMAB} + \bar{\rho}_R = -2.6 \times 10^{-3}$. This compares favorably with ellipsometric data for 0.6 mM CTAB (2/3 × cmc), where the experimentally determined value was $\bar{\rho} = -2.4 \times 10^{-3}$.

6.2.1.1.2 The Solid Phase. SF spectra, described in 6.2.2.1, suggest that the hydrocarbon chains are fully extended in the solid phase. Based on the structure of pure dodecanol monolayers, it is likely that the chains are vertical rather than tilted. At an area per chain of ca. 21 Å^2, typical of an upright rotator phase, the tetradecane molecules fit neatly into the space between the CTAB chains. Figure 6.5 illustrates this packing. The van der Waals radii of adjacent methyl groups from each CTAB head group limit how close the tetradecane molecules can approach to the monolayer-water interface. Since the tetradecane molecule is two carbon atoms shorter than that of CTAB, the top methyl groups of both chains are at approximately the same height. This leads to maximum van der Waals interactions between the chains, which are lessened for the shorter dodecane molecule. This results in the liquid state of the CTAB + C_{12} mixed monolayer, which does not show a phase transition to a frozen state as the temperature is lowered since its projected 'melting point' is too low, falling below the solubility limit for CTAB in solution.

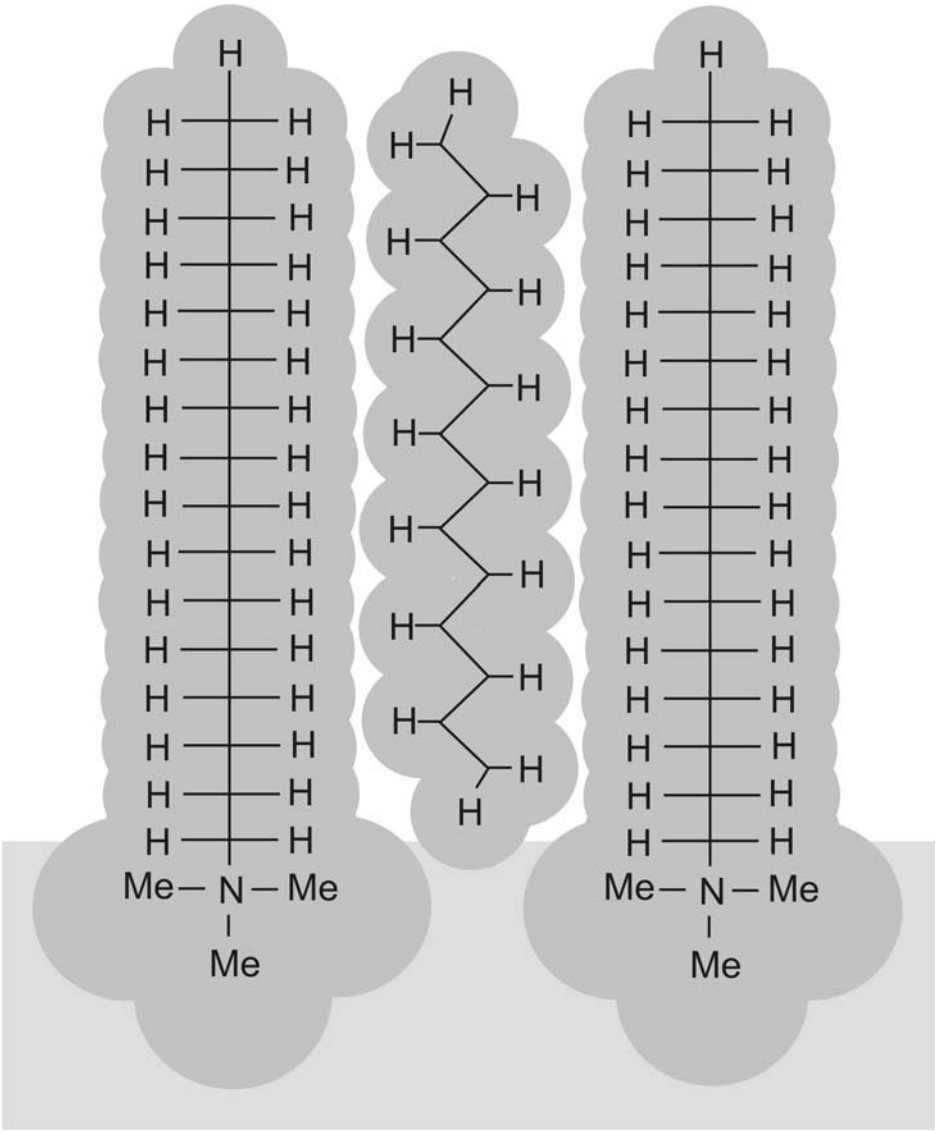

Figure 6.5 *Schematic illustration of a mixed monolayer of CTAB and tetradecane in the solid phase. The van der Waals radii of the atoms describe the size of the molecules.*

The solid phase mixed monolayer is anisotropic, with a polarisability along the chain axis greater than the polarisability perpendicular to it. Uniaxially anisotropic monolayers are described by ordinary (ε_o, parallel to the interface) and extraordinary (ε_e, perpendicular to the interface) dielectric constants. To determine the ellipsometric thickness, we must evaluate ε_o, ε_e, and monolayer's thickness, d.

ε_o and ε_e were evaluated for anisotropic hydrocarbon monolayers during the study of dodecanol:[37] $\varepsilon_o = 2.12$ and $\varepsilon_e = 2.29$. d is $16 \times d_o$, where $d_o = 1.27$ Å is the

length of a fully extended CH_2 unit, so $d = 20.32$ Å. Substitution of ε_o, ε_e, and d, into equation 2.53 gives η, which is then substituted into the Drude equation (equation 2.46), resulting in the coefficient of ellipticity for the chain region, $\overline{\rho}_{chain} = -2.57 \times 10^{-3}$.

In the solid phase, the head group contribution may differ from that in the liquid phase. The extrapolation from experimental results we used for the liquid phase may contain additional roughness that is not present in the solid phase. For the solid phase, we calculate the dielectric constants for the bromide (Br) and trimethylammonium (TMA) groups using the Clausius-Mossotti equation (equation 2.54), thus finding the ellipticity arising solely from these groups. Capillary wave roughness of $\overline{\rho}_R = + 0.5 \times 10^{-3}$ must still be included.

The molar refractivity, R_m, of the TMA group is the sum of the C–H and C–N bond refractivities, $R_m = 4$ (C–N at 1.3 cm^3/mol) + 9 (C–H at 1.65 cm^3/mol) = 20.05 cm^3/mol.[38] The molar volume of the head group is $V_m = 62.3$ cm^3/mol. Substituting these values into the Clausius-Mossotti equation gives $\varepsilon = 2.424$. The thickness of the layer, d, can be found by dividing V_m by A. Similar to dodecanol, where $A = 22$ $Å^2$, the solid phase of the mixed monolayer is a hexagonally packed rotator phase. Assuming that this phase has CTAB and tetradecane present in a 1:1 ratio, the area per CTAB molecule is 44 $Å^2$, which means $d = 2.35$ Å. Substituting these values for ε and d into the isotropic equation (equation 2.50) and the Drude equation (equation 2.46) predicts a coefficient of ellipticity for the TMA group of $\overline{\rho}_{TMA} = -0.8 \times 10^{-3}$. The contribution from the bromide ion was calculated to be $\overline{\rho}_{Br} = -0.6 \times 10^{-3}$ (chapter 5, section 5.4).[39]

The total calculated coefficient of ellipticity is the sum of the contributions from the chain, the head group, and the roughness of the interface. This sum is $\overline{\rho} =$

-3.5×10^{-3}, which is near the experimental value of -3.8×10^{-3} for 0.6 mM CTAB. While many assumptions have been incorporated into this model, the general agreement with the experimental results suggests that our physical picture for the monolayer is basically correct.

6.2.1.2 CTAB + Dodecane. We sought to find a similar phase transition during our initial studies of CTAB + dodecane by monitoring the coefficient of ellipticity for the mixed monolayer as a function of temperature. No jumps in $\overline{\rho}$ were observed when a 1/3 × cmc solution of CTAB plus dodecane was cooled from 20 °C to 0 °C. As the solution was cooled, the solubility of CTAB dropped until it fell below the solubility limit for CTAB, leading to crystallisation of the surfactant. For this system, the solubility limit was reached before the phase transition could occur.

6.2.1.3 CTAB + C_{13}, C_{15}, C_{16}, C_{17}, or C_{18}. Dr. Lei Qunfang repeated ellipsometry measurements for tetradecane (C_{14}) and dodecane (C_{12}) and extended our search for interesting phase behaviour in mixed monolayers with alkanes of chain lengths from C_{12} up to octadecane (C_{18}). The compiled ellipsometry results for C_{12} – C_{17} alkanes atop 0.6 mM solutions of CTAB are shown in Figure 6.6.

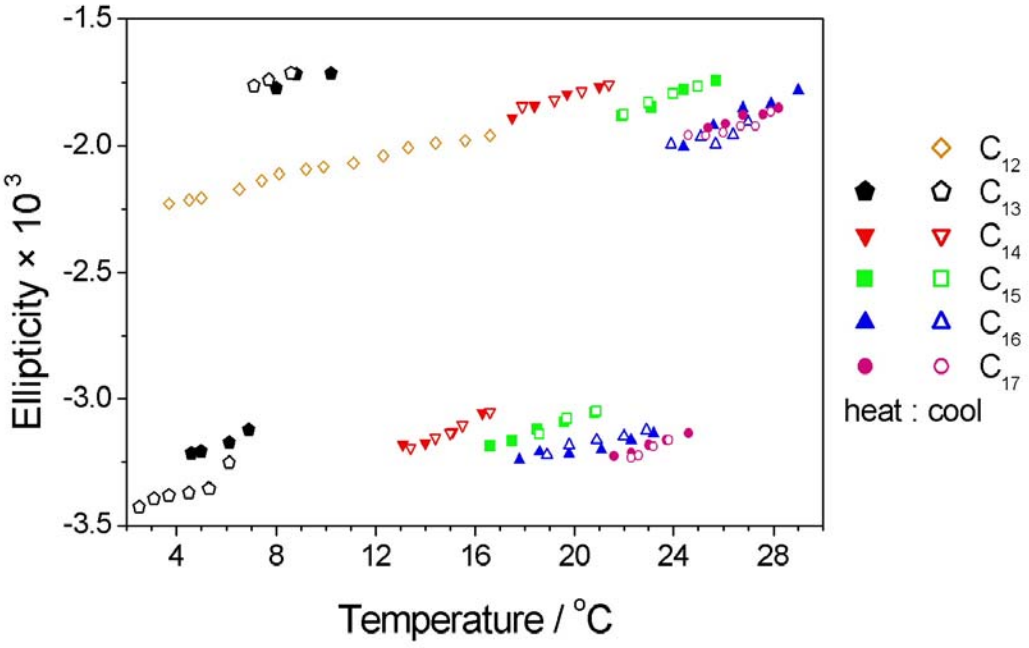

Figure 6.6 *Coefficient of ellipticity as a function of temperature and alkane chain length for mixed monolayers of 0.6 mM CTAB and alkane at the air-water interface. Heating cycle measurements are indicated by filled symbols while open symbols indicate measurements obtained during the cooling cycle.*

Figure 6.6 shows that T_m(2D) for the mixed monolayer increases with increased alkane chain length. Mixed monolayers of CTAB with C_{13}-C_{18} show phase transitions.

The T_m(2D) phase transition temperatures of the mixed monolayer are contrasted with the bulk melting temperature, T_m(3D), of each respective alkane in Figure 6.7.

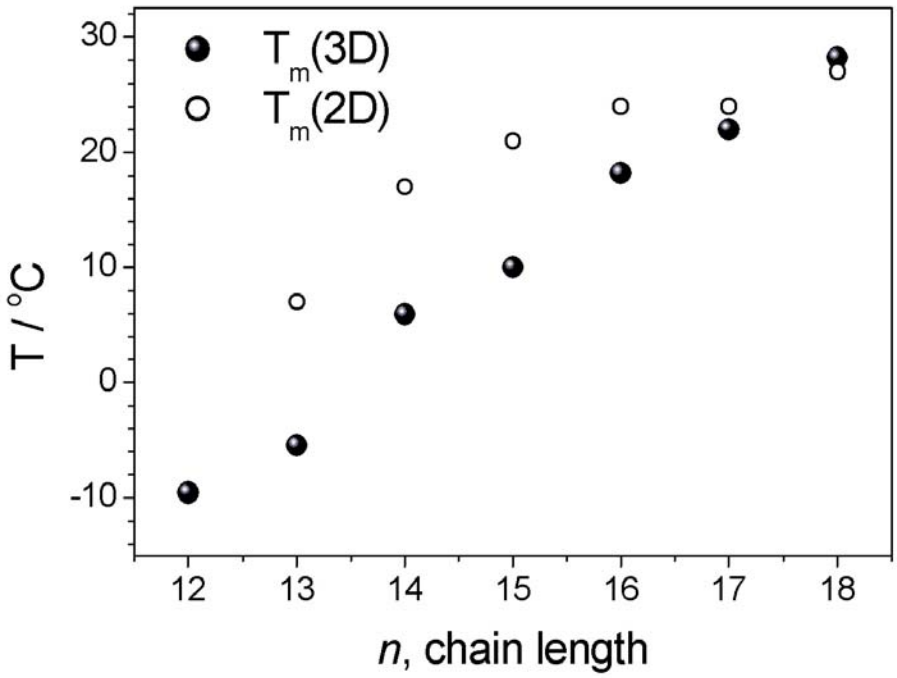

Figure 6.7 *Two-dimensional phase transition temperatures* (○) *for the mixed CTAB-alkane monolayer compared with three-dimensional bulk phase transition temperatures* (●) *for each pure alkane.*

For n = 13-17, T_m(2D) for the mixed monolayer is higher than T_m(3D) for the bulk alkane. To understand why this trend changes at n = 17 and 18, we must consider the thermodynamics of the system. The melting point, T_m, is defined by $T_m = \Delta H / \Delta S$. T_m is thus proportional to ΔH and inversely proportional to ΔS. If $T_m(2D) > T_m(3D)$, then either $\Delta H(2D) > \Delta H(3D)$ or $\Delta S(2D) < \Delta S(3D)$.

The differences in T_m are the result of a delicate balance between the changes in enthalpy and entropy. Melting involves a costly increase in enthalpy and a favourable increase in entropy. Freezing involves a favourable decrease in enthalpy and a costly decrease in entropy. In the mixed monolayer, freezing involves close-packing between the alkane and surfactant chains. This is unfavourable entropically,

but involves a favourable change in enthalpy provided that the chains of the surfactant and alkane pack efficiently. Enthalpically favourable packing occurs when the chains of the alkane fit neatly between the chains of the surfactant molecules within the monolayer. For alkane chain lengths shorter than the chain lengths of the surfactant, this enthalpic gain can counterbalance the unfavourable decrease in entropy that accompanies the freezing of the monolayer.

A further consideration is the additional roughness of the solid phase monolayer as compared to the bulk solid: molecules undergoing upwards displacement within the monolayer do not interfere with molecules above them. Clearly, in the bulk, vertically displaced molecules must be accommodated by the other molecules already above them. The greater roughness of the solid monolayer than the bulk solid means that the solid monolayer has more entropy per mole than the bulk solid. This entropy consideration suggest that ΔS(2D) is less than ΔS(3D), and contributes to the differences between the 2D and 3D melting points. Longer alkane chain lengths increase van der Waals interactions and raise the 2D melting point of the monolayer. As the alkane chain length approaches and exceeds the chain length of the surfactant, achieving a closely-packed frozen monolayer becomes more difficult, and T_m(3D) exceeds T_m(2D).

6.2.2 Sum-Frequency Spectroscopy. SFS was performed on mixed monolayers of CTAB and tetradecane or dodecane. Both dodecane and tetradecane had clear effects on the SF spectra of the mixed monolayer as compared to monolayers of pure CTAB, but only tetradecane produced a phase transition in response to a change in temperature.

6.2.2.1 CTAB + Tetradecane. Figure 6.8 shows SF spectra of 0.3 mM CTAB + tetradecane above and below T_m(2D).

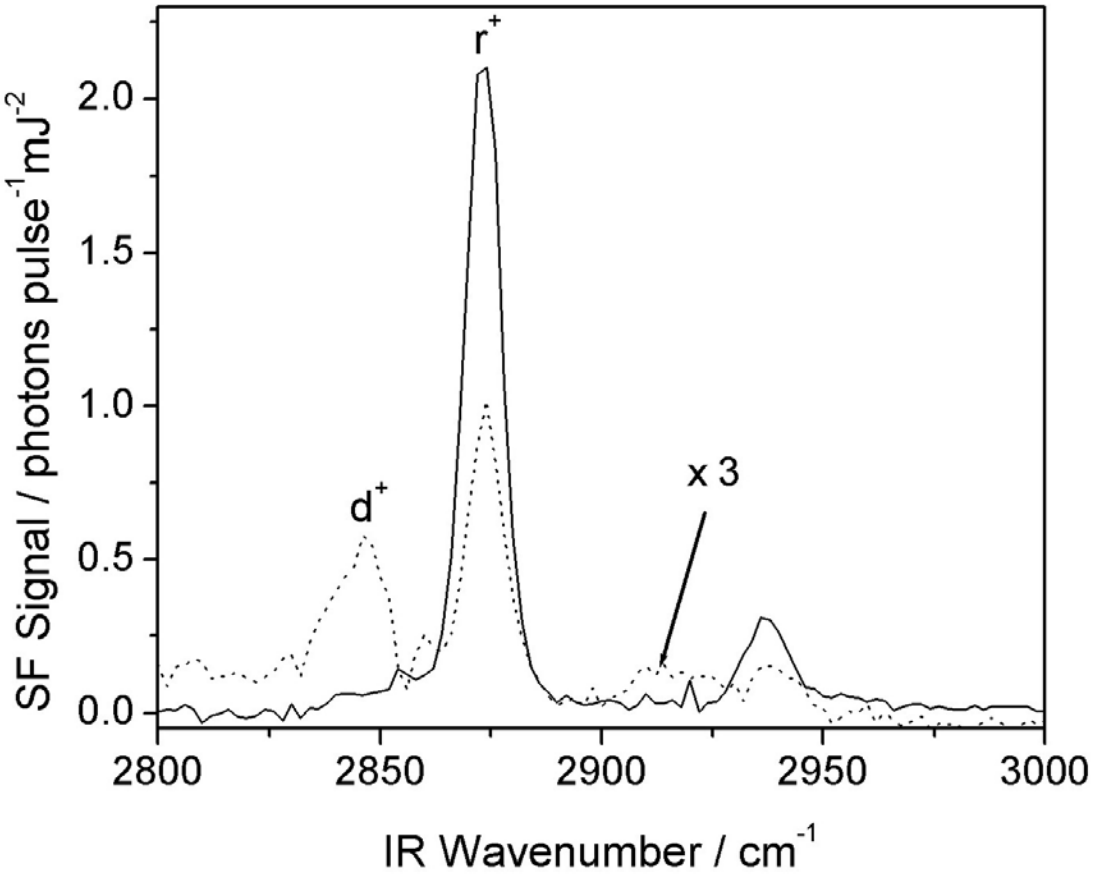

Figure 6.8 *Sum-frequency spectra for tetradecane on a 0.3 mM CTAB solution at 20 °C (dotted line; × 3)and 15 °C (solid line). d^+ and r^+ indicate the symmetric methylene and symmetric methyl stretches, respectively. The peak at 2935 cm^{-1} is a Fermi resonance of the r^+ mode.*

The peaks at 2850 and 2876 cm^{-1} are assigned to the symmetric methylene stretch (d^+) and the symmetric methyl stretch (r^+), respectively. The ratio of the line strengths of these two peaks has been found to be a good qualitative indicator of conformational order.[40] Above T_m(2D), the line strengths are comparable, indicating a conformationally disordered monolayer. Below T_m(2D), the d^+ peak is nearly absent, describing a state in which the chains are predominantly in an all-trans conformation. In addition, the spectra show a 6-fold increase in SF signal strength

from the r^+ mode in the conformationally ordered phase. Quantitative analysis of the monolayer requires spectra of selectively deuterated mixtures in order to separate out the contributions of the surfactant and the alkane to the SF spectra. This large increase in signal nevertheless suggests an increase in the number density, *N*, of surfactant and oil molecules at the surface as well as a decrease in the mean tilt of the chains. The SF signal from the r^+ mode is approximately proportional to $N^2 \langle\cos\theta\rangle^2$, where θ is the angle between the surface normal and the C_3 axis of the methyl group. In the spectra above, it is important to recognise that both ends of the tetradecane molecule contribute to the spectra, and that these two contributions can partially cancel.[41]

Figure 6.9 presents SF spectra that isolate CTAB from tetradecane in the mixed monolayer through selective deuteration. This figure presents monolayers of CTAB from a 0.6 mM solution rather than the 0.3 mM presented in figure 6.8. The minor discrepancy in signal strength is explained by adjustments to the laser system and experimental conditions that took place during the two years between the acquisition of the spectra in figures 6.8 and 6.9. We note, once again, the strong r^+ peak in the solid phase of the mixed monolayer, which weakens substantially in the liquid phase. As before, the d^+ peak is nearly absent in the solid phase of the mixed monolayer.

Additional information is provided by the deuteration of the alkane, (b), or the surfactant, (c), within the mixed monolayer. The most obvious difference between (a) and (b) & (c) is that the fully protonated mixed monolayer has a higher overall SF signal strength than either (b) or (c), which are both presented on a scale three times larger than (a). As all of these spectra are in the C–H stretching region, this increased signal strength is attributed to the increased number density of emitting C–H bonds in

the mixed monolayer when both the surfactant and alkane are fully protonated. The SF intensity, I, is given by $I = |\chi_{oil} + \chi_{CTAB}|^2$. This leads to a cross-term, $2\chi_{oil}\chi_{CTAB}$, in the expression for the intensity of the doubly protonated mixed monolayer shown in (a): $I = \chi_{CTAB}^2 + \chi_{oil}^2 + 2\chi_{CTAB}\chi_{oil}$. The singly protonated mixed monolayers have contributions of solely χ_{CTAB}^2 for the h-CTAB, d-oil combination shown in (b), and solely χ_{oil}^2 for the h-oil, d-CTAB combination shown in (c). The presence of the cross-term helps explain the enhancement seen in the spectrum (a).

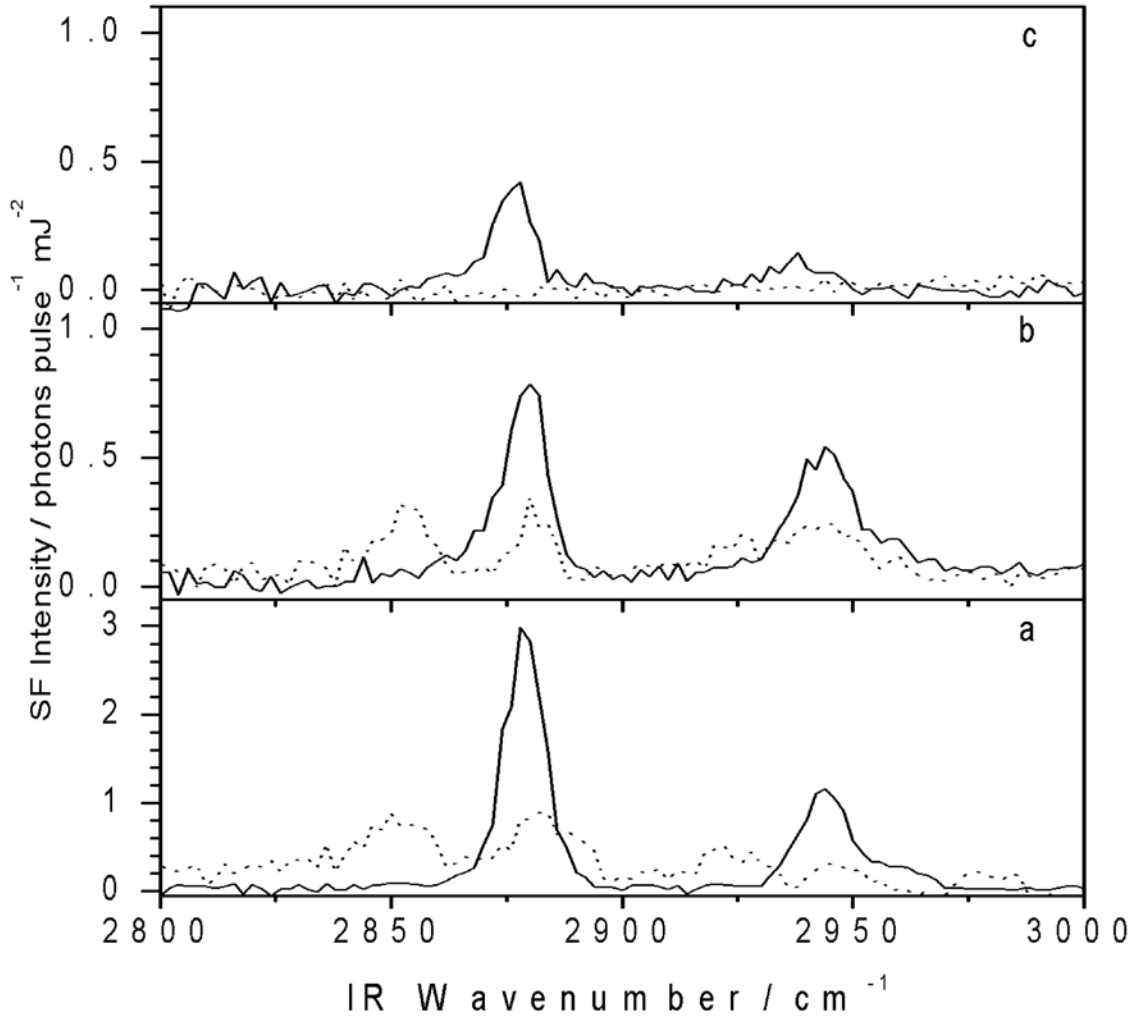

Figure 6.9 *SF spectra of mixed monolayers of 0.6 mM CTAB + tetradecane above and below T_m(2D). (a) h-CTAB + h-tetradecane; (b) h-CTAB + d-tetradecane; (c) d-C_{16} h-TAB + h-tetradecane. Solid phase monolayer indicated by solid line, liquid phase monolayer indicated by dotted line. Please note that spectra in (b) and (c) are on a y-axis scale that is three times greater than that of (a). ssp-polarised.*

In (b) and (c), the strong r^+ peak persists in the solid phase of the mixed monolayer, indicating that the hydrocarbon chains of the surfactant and the alkane both contribute to the signal strength of the r^+ mode. This suggests a model in which the alkane molecules pack interstitially between the chains of the surfactant when the mixed monolayer is in its solid phase. The r^+ signal strength from the alkane is less than that from the CTAB. This could be due to a difference in number density at the interface, or due to partial cancellation in the signal from the two methyl end groups of the tetradecane molecule in the solid monolayer. The total SF signal is significantly lower than for a dodecanol monolayer, suggesting that the latter effect is occurring. One might ask why tetradecane in an all-trans conformation would give an SF signal at all, given that it is centrosymmetric. There are two possible explanations. First, the orientations of the two terminal methyl groups are not identical and therefore only partial cancellation of the hyperpolarisabilities occurs. Second, the two ends of the tetradecane molecule experience different local fields due to their different environments: although the β's cancel, the χ's do not.

The signal strength of the d^+ mode provides additional information about the conformation of the monolayers. Both (a) and (b) show d^+ peaks in the liquid phase of the mixed monolayer. Indeed, the liquid phase spectra of (a) and (b) are qualitatively identical, which suggests that in (a), the liquid phase spectra is predominantly that of a CTAB monolayer in contact with disordered tetradecane. In contrast to (b), the liquid phase of (c) shows only trace resonances. This suggests that the liquid phase spectra are dominated by contributions from the hydrocarbon chains of CTAB rather than of tetradecane. As the mixed monolayer freezes below T_m(2D), however, the r^+ peak present in (c) indicates that the tetradecane becomes ordered

within the mixed monolayer. The upright chain conformation places each tetradecane molecule inbetween the chains of surrounding CTAB molecules.

Figure 6.10 shows the intensity of the r^+ mode as a function of temperature for the three isotopic combinations shown in figure 6.9. The strength of the r^+ mode from the selectively deuterated combinations presented in 6.9 are tracked in 6.10 as a function of temperature.

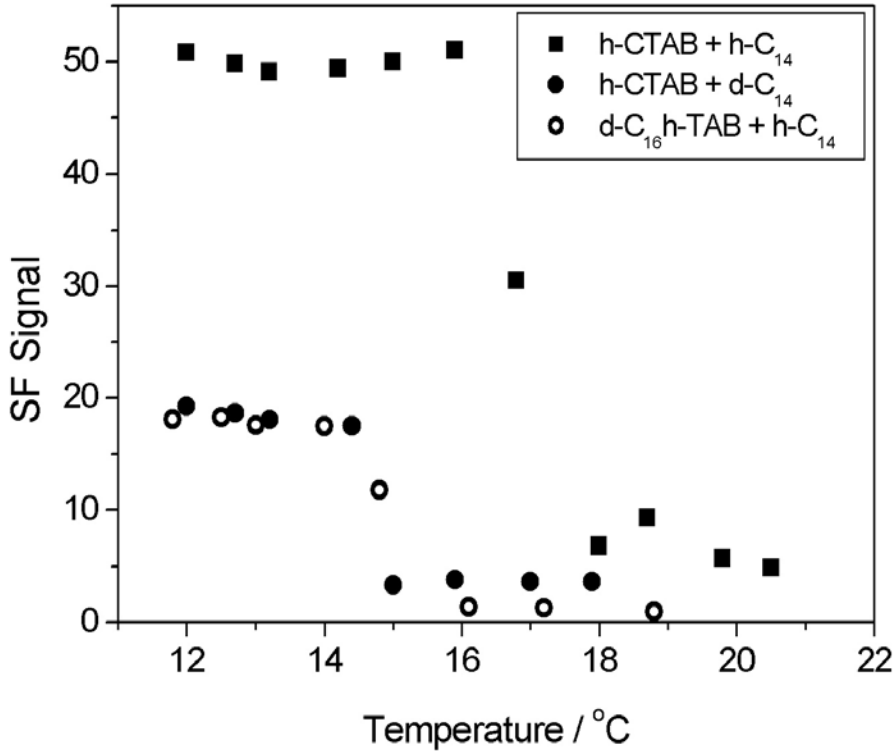

Figure 6.10 *SF signal (in arbitrary units) from the r^+ mode of a mixed monolayer of 0.6 mM CTAB and tetradecane as a function of temperature and selective deuteration. ■ indicates protonated CTAB and tetradecane, ● indicates protonated CTAB and deuterated tetradecane, ⭘ indicates deuterated C_{16} h-TAB and protonated tetradecane. ssp-polarised.*

This data restates the comparable contribution of CTAB and tetradecane to the r^+ mode in the solid state of the mixed monolayer, and the greater contribution of CTAB to the r^+ mode in the liquid state of the mixed monolayer. In addition, it highlights phenomenon of melting point depression in isotopic mixtures. Deuteration of one

component lowers the melting point of the mixed monolayer by approximately 2 °C.[‡,42] This lowering of T_m(2D) is accompanied by mild smearing of the phase transition caused by trace impurities present in the samples of deuterated CTAB and the commercial deuterated oils. Both deuterated components are too expensive to purify extensively before use. Melting point depression resulting from the use of a deuterated component and associated trace impurities makes analysis of the SF spectra acquired from liquid-state deuterated mixed monolayers much more difficult. Weak SF intensities from the disordered mixed monolayer are further obscured by melting point depression and smearing from the deuterated component and any associated impurities.

6.2.2.2 CTAB + Dodecane. Although we did not observe a phase transition for mixed monolayers of CTAB and dodecane, it is worth considering the effect of the alkane on the monolayer independently from the phenomenon of interfacial phase transitions. Figure 6.11 compares SF spectra of CTAB and CTAB + dodecane with spectra in which either the alkane or the surfactant is deuterated. These spectra are not completely consistent with the results for CTAB + tetradecane but are included in this thesis for the sake of completeness. SFS spectra of the CTAB + tetradecane mixed monolayer system obtained more recently by Katherine Wilkinson in our group confirm the results presented earlier in this chapter for the CTAB + tetradecane mixed monolayer system. SFS results for CTAB + dodecane have not been repeated since due to the absence of a phase transition in this system.

---

‡ The melting point difference, $\Delta T_m = T^H_m - T^D_m$, between a hydrogenated (H) *n*-alkane and its deuterated (D) counterpart is linearly dependent on the length of the alkane and is always > 0. The longer the alkane chain, the greater ΔT_m. For tetradecane, ΔT_m is between 2.5 (for decane) and 4 °C (for hexadecane). [Dorset, D. L.; Strauss, H. L.; Snyder, R. G. *J. Phys. Chem.* **1991**, *95*, 938.]

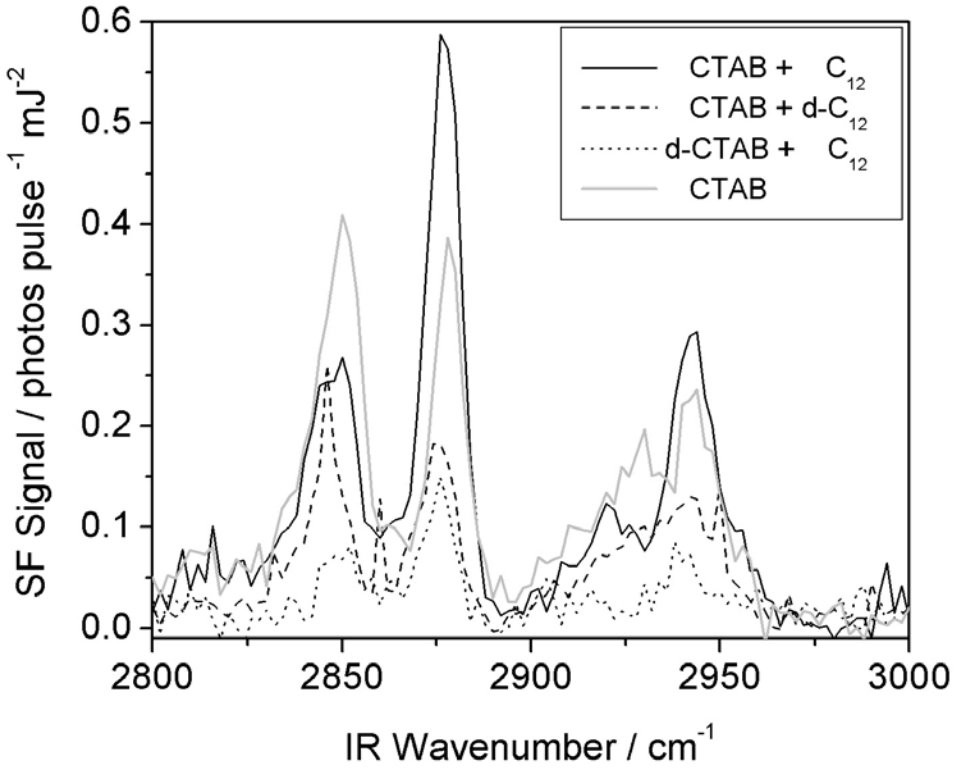

Figure 6.11 *SF spectra for mixed monolayers of 0.6 mM CTAB + dodecane at 298K. Monolayer of 2 mM CTAB (gray solid line) contrasted with mixed monolayer of CTAB + dodecane (black solid line), mixed monolayer of protonated CTAB + deuterated dodecane (dashed line), and mixed monolayer of deuterated CTAB + protonated dodecane (dotted line). ssp-polarised.*

Apart from the gray line which represents an oil-free monolayer of CTAB, the three spectra in black are of mixed monolayers of CTAB + dodecane. These mixed monolayers all represent a mixed monolayer in a liquid state. In this system, crystallisation of the CTAB from solution occurs before the mixed monolayer can undergo a freezing transition. The spectrum of the fully protonated CTAB + dodecane combination most clearly indicates a higher degree of order than that of the pure CTAB monolayer. In this spectrum, the strength of the r^+ peak clearly exceeds that of the d^+ peak. To the same effect, the weaker spectrum from deuterated CTAB + protonated dodecane indicates conformational order in the dodecane chains with its faint d^+ peak and much more prominent r^+ peak. This spectrum does not agree with

results obtained for the CTAB + tetradecane mixed monolayer system discussed earlier. Since this spectrum has a low signal to noise ratio, however, it is difficult to interpret. Its weakness is likely due to partial cancellation between the two terminal methyl groups in dodecane, which lowers the overall SF signal level. In contrast, the weak spectrum of protonated CTAB + deuterated dodecane depicts a conformationally disordered monolayer – apparently slightly more disordered than a pure, oil-free CTAB monolayer. When compared with the deuterated CTAB + protonated dodecane spectrum, this spectrum implies that the conformational order within the mixed CTAB + dodecane monolayer is enforced by the dodecane rather than by the CTAB. This spectrum also does not agree with the results obtained for the CTAB + tetradecane mixed monolayer system. Interpretation of SF spectra for isotopic combinations of the CTAB + dodecane mixed monolayer system are limited by the poor signal strength present in both spectra with deuterated components. SF spectra from isotopic combinations of the CTAB + tetradecane mixed monolayer system can be interpreted with greater confidence.

6.3 Conclusion

Mixed monolayers of CTAB and tetradecane at the air-water interface show a first-order phase transition from a conformationally disordered phase to a denser, conformationally ordered phase as the temperature is lowered. Comparison with pure alcohol and mixed surfactant + alcohol monolayers suggests the existence of a liquid-solid phase transition, although grazing incidence X-ray diffraction experiments would be required to prove that the low-temperature phase is solid. The 2D phase transition occurs 11 °C above the bulk melting point, T_m(3D), of tetradecane. By comparison, pure alcohol monolayers on water melt approximately 15 °C above

T_m(3D), while the surface phase transition in long-chain alkanes occurs approximately 3 °C above T_m(3D). Our data suggest that the interface between bulk tetradecane and aqueous CTAB solutions will also crystallise over a range of temperatures at which both bulk phases are liquid.

Upon the addition of alkane to the surfactant monolayer, the CTAB molecules are separated from each other as the alkane occupies the spaces between them. This greater distance between the CTAB molecules is reflected by an increased area per CTAB molecule. The hydrocarbon chain of an alkane can approach a CTAB molecule more closely than can another CTAB molecule since there is no electrostatic repulsion between head groups. Closer packing necessitates adjustments in tilt and chain disorder to minimise the van der Waals interactions between the hydrocarbon chains. As alkanes insert themselves into the surfactant monolayer, gauche defects are reduced and the chains adopt a more upright conformation.

To classify the CTAB + tetradecane mixed monolayer phases, I will refer back to figure 6.2 which illustrates a monolayer phase diagram for insoluble fatty acids and alcohols. The high-temperature phase is L_1, a liquid expanded state that exists at high temperatures and low surface pressure. From the phase diagram, the phase transition we observe in our mixed monolayer could either be $L_1 - L_2$ or $L_1 - LS$. The L_2 phase has a collective tilt, while the LS phase is distinguished by upright molecules in a hexagonal lattice. Ellipsometry data and comparison with other monolayer phases suggest that the solid phase in our mixed monolayer is most likely to be LS, although X-ray scattering experiments would be needed to confirm this assignment.

Mixed monolayers of CTAB and alkanes of chain length n = 13 and 15-18 also undergo phase transitions at the air-water interface. Ellipsometric measurements indicate a correlation between chain length and T_m(2D), just as a correlation exists

between chain length and T_m(3D). We expect future studies of these combinations of surfactants + alkanes at the air-water interface by sum-frequency spectroscopy and surface tensiometry to concur with the results from ellipsometry, and further develop our understanding of the effect of alkane integration into surfactant monolayers at the air-water interface.

At the start of this chapter, I posed three questions as motivations for the mixed surfactant + alkane experiment. The effect of alkane penetration into the hydrocarbon chains of a surfactant monolayer is one of conformational ordering, resulting in the elimination of gauche defects and the reduction in chain tilt to a more upright chain orientation. This ordering can result in a first-order phase transition to a densely-packed LS phase. The interesting behaviour and structure of mixed surfactant + alkane monolayers suggests that fascinating phenomena may also exist at the interface between bulk oil and water. The predictive power of the mixed monolayer experiment for the bulk oil-water interface is incomplete, however, since experiments investigating the phase behaviour of the bulk oil-water interface show that some systems in which a mixed monolayer undergoes a phase change do not also undergo a phase change at the bulk oil-water interface. The example we have found thus far is the CTAB + hexadecane system, in which the mixed monolayer undergoes a phase change at the air-water interface, but the monolayer between the bulk aqueous CTAB and hexadecane media does not.[43] These results demonstrate that the bulk oil-water interface is distinct from the mixed oil + surfactant monolayer at the air-water interface.

References

(1) Kaganer, V. M.; Möhwald, H.; Dutta, P. *Rev. Mod. Phys.* **1999**, *71*, 779.

(2) Aratono, M.; Uryu, S.; Hayami, Y.; Motomura, K.; Matuura, R. *J. Colloid Interface Sci.* **1984**, *98*, 33.

(3) Casson, B. D.; Bain, C. D. *J. Am. Chem. Soc.* **1999**, *121*, 2615.

(4) Berge, B.; Konovalov, O.; Lajzerowicz, J.; Renault, A.; Rieu, J. P.; Vallade, M. *Phys. Rev. Lett.* **1994**, *73*, 1652.

(5) Casson, B. D.; Braun, R.; Bain, C. D. *Faraday Discuss.* **1996**, *104*, 209.

(6) Ross, J.; Epstein, B. *J. Phys. Chem.* **1958**, *62*, 533.

(7) Casson, B. D.; Bain, C. D. *J. Phys. Chem. B* **1998**, *102*, 7434.

(8) Casson, B. D.; Bain, C. D. *J. Phys. Chem. B* **1999**, *103*, 4678.

(9) Aveyard, R.; Cooper, P.; Fletcher, P. D. I. *J. Chem. Soc. Faraday Trans.* **1990**, *86*, 3623. Aveyard, R.; Binks, B. P.; Fletcher, P. D. I.; McNab, J. R. *Langmuir* **1995**, *11*, 2515. Aveyard, R.; Binks, B. P.; Fletcher, P. D. I.; McNab, J. R. *Ber. Bunsen-Ges. Phys. Chem.* **1996**, *100*, 224. Binks, B. P.; Crichton, D.; Fletcher, P. D. I.; McNab, J. R.; Li, Z. X.; Thomas, R. K.; Penfold, J. *Colloids Surf.* **1999**, *146*, 299.

(10) Jayalakshmi, Y.; Langevin, D. *J. Colloid Interface Sci.* **1997**, *194*, 22.

(11) (a) Lu, J. R.; Thomas, R. K.; Aveyard, R.; Binks, B. P.; Cooper, P.; Fletcher, P. D. I.; Sokolowski, A.; Penfold, J. *J. Phys. Chem.* **1992**, *96*, 10971. (b) Lu, J. R.; Li, Z. X.; Thomas, R. K.; Binks, B. P.; Crichton, D.; Fletcher, P. D. I.; McNab, J. R.; Penfold, J. *J. Phys. Chem. B* **1998**, *102*, 5785. (c) Lu, J. R.; Thomas, R. K.; Binks, B. P.; Fletcher, P. D. I.; Penfold, J. *J. Phys. Chem.* **1995**, *99*, 4113.

(12) McKenna, C. E.; Knock, M. M.; Bain, C. D. *Langmuir* **2000**, *16*, 5853.

(13) Bibo, A. M.; Knobler, C. M.; Peterson, I. R. *J. Phys. Chem.* **1991**, *95*, 5591.

(14) Kaganer, V. M.; Loginov, E. B. *Phys. Rev. Lett.* **1993**, *71*, 2599.

(15) (a) Kaganer, V. M.; Indenbom, V. L. *J. Phys. II France* **1993**, *3*, 813. (b) Peterson, I. R.; Kenn, R. M. *Langmuir* **1994**, *10*, 4645. (c) Kenn, R. M.; Böhm, C.; Bibo, A. M.; Peterson, I. R.; Möhwald, H.; Kjaer, K.; Als-Nielson, J. *J. Phys. Chem.* **1991**, *95*, 2092. (d) Barnes, G. T.; Lawrie, G. A. *J. Coll. Int. Sci.* **1994**, *162*, 36. (e) Kaganer, V. M.; Peterson, I. R.; Kenn, R. M.; Shih, M. C.; Durbin, M .C.; Dutta, P. *J. Chem. Phys.* **1995**, *102*, 9412.

(16) Powney, J.; Addison, C. C. *Trans. Faraday Soc.* **1937**, *33*, 1243.

(17) Miles, G. D.; Shedlovsky, L. *J. Phys. Chem.* **1944**, *48*, 57.

(18) Epstein, M. B.; Wilson, A.; Jakob, C. W.; Conroy, L. E.; Ross, J. *J. Phys. Chem.* **1954**, *58*, 860.

(19) Ross, J. *J. Phys. Chem.* **1958**, *62*, 531.

(20) Ross, J.; Epstein, B. *J. Phys. Chem.* **1958**, *62*, 533.

(21) Simister, E. A.; Thomas, R. K.; Penfold, J.; Aveyard, R.; Binks, B. P.; Cooper, P.; Fletcher, P. D. I.; Lu, J. R.; Sokolowski, A. *J. Phys. Chem.* **1992**, *96*, 1383.

(22) Bell, G. R.; Manning-Benson, S.; Bain, C. D. *J. Phys. Chem. B* **1998**, *102*, 218.

(23) Frenken, J. W. M.; van der Veen, J. F. *Phys. Rev. Lett.* **1985**, *54*, 134.

(24) Takeuchi, N.; Selloni, A.; Tosatti, E. *Phys. Rev. Lett.* **1994**, *72*, 2227.

(25) Elbaum, M.; Wettlaufer, J. S. *Phys. Rev. E* **1993**, *48*, 3180.

(26) Earnshaw, J. C.; Hughes, C. J. *Phys. Rev. A* **1992**, *46*, R4494.

(27) Wu, X. Z.; Ocko, B. M.; Sirota, E. B.; Sinha, S. K.; Deutsch, M.; Cao, B. H.; Kim, M. W. *Science* **1993**, *261*, 1018.

(28) Ocko, B. M.; Wu, X. Z.; Sirota, E. B.; Sinha, S. K.; Gang, O.; Deutsch, M. *Phys. Rev. E* **1997**, *55*, 3164.

(29) Pfohl, T.; Beaglehole, D.; Riegler, H. *Chem. Phys. Lett.* **1996**, *260*, 82.

(30) Deutsch, M.; Wu, X. Z.; Sirota, E. B.; Sinha, S. K.; Ocko, B. M.; Magnussen, O. M. *Europhys. Lett.* **1995**, *30*, 283.

(31) Gang, O.; Ocko, B. M.; Wu, X. Z.; Sirota, E. B.; Deutsch, M. *Phys. Rev. Lett.* **1998**, *80*, 1264.

(32) Ocko, B. *Phys. Rev. Lett.* **1990**, *64*, 2160.

(33) Smith, P.; Lynden-Bell, R. M. *Molec. Phys.* **1999**, *96*, 249.

(34) Meunier, J. In *Light Scattering by Liquid Surfaces and Complementary Techniques*; Langevin, D., Ed.; Marcel Dekker: New York, 1992; Chapter 17.

(35) *Handbook of Chemistry and Physics*, 64th Ed.; CRC: Boca Raton, FL, 1984.

(36) Small, D. M. *Handbook of Lipid Research 4: The Physical Chemistry of Lipids from Alkanes to Phospholipids*; Plenum Press: New York, 1986; pp 196-208.

(37) Casson, B. D.; Bain. C. D.; *Langmuir* **1997**, *13*, 5465.

(38) Atkins, P.W., *Physical Chemistry*, 3rd Ed.; Oxford University Press: Oxford, 1986, Table 24.3, p. 829.

(39) Knock, M. M.; Bain, C. D. *Langmuir* **2000**, *16*, 2857.

(40) (a) Ward, R. N.; Duffy, D. C.; Davies, P. B.; Bain, C. D. *J. Phys. Chem.* **1994**, *98*, 8536. (b) Duffy, D. C.; Davies, P. B.; Creeth, A. M. *Langmuir* **1995**, *11*, 2931.

(41) Sefler, G. A.; Du, Q.; Miranda, P. B.; Shen, Y. R. *Chem. Phys. Lett.* **1995**, *235*, 347.

(42) (a) Dorset, D. L.; Strauss, H. L.; Snyder, R. G. *J. Phys. Chem.* **1991**, *95*, 938.

(b) Bates, F. S.; Wignall, G. D. *Phys. Rev. Lett.* **1986**, *57(12)*, 1429.

(43) Lei, Q.; Knock, M. M.; Bain, C. D. unpublished results.

CHAPTER 7

Design of the Oil-Water SFS Experiment

Chapter 7: Design of the Oil-Water SFS Experiment

7.1 Rationale for Experiment

Oil-water (o-w) interfaces in both natural and synthetic contexts are frequently modified by surfactants. Examples include the use of detergents to dissolve soil, oil-water emulsions for the cosmetic, food, petrochemical, and pharmaceutical industries,[1] and environmental ground water remediation.[2] Though the consequences of surfactant adsorption at these interfaces are well-studied, there is little information available on the structure of surfactant monolayers at the oil-water interface – a critical step towards understanding the structure-function relationship between the surfactant monomer and its aggregates at the o-w interface.

In this chapter, I describe the development of a method for obtaining vibrational spectra of surfactant monolayers at the bulk o-w interface by sum-frequency spectroscopy (SFS). SFS is a form of nonlinear vibrational spectroscopy that is sensitive only to molecules in noncentrosymmetric environments. In my experiments the bulk oil and water phases are isotropic and therefore sum-frequency (SF) inactive. Surfactant molecules adsorbed at the interface, however, are in a noncentrosymmetric environment and give rise to SF spectra. The intensity and phase of peaks in SF spectra can be analysed to obtain the polar orientation and tilt of molecules absorbed at interfaces. A unique feature of SFS, which is particularly useful for the study of surfactant molecules with their long hydrocarbon chains, is the sensitivity of the C–H stretching modes to the extent of conformational order in polymethylene chains. I have chosen as my model system the cationic surfactant hexadecyltrimethylammonium bromide ($CH_3(CH_2)_{15}N^+(CH_3)_3Br^-$, known as CTAB) at the interface between hexadecane and solutions of the surfactant in D_2O. CTAB has been widely studied at a variety of interfaces by our group[3,4,5] and others[6,7,8] and

the adsorption behaviour and sum-frequency spectroscopy of the surfactant is reasonably well-understood.

To set my work in context, chapter 1, section 1.4, provides a brief review of other techniques that have been used to study the o-w interface and of previous efforts to study liquid-liquid interfaces by nonlinear optical techniques. In this chapter, I describe the design of a cell for the acquisition of SF spectra from the oil-water interface and discuss the various considerations that influenced the design. In chapter 8, I present and analyse SF spectra of the hexadecane-water interface for aqueous solutions of CTAB at different bulk concentrations.

7.2 Design of Oil-Water Setup

7.2.1 Transparency of Bulk Phases. The main challenge in obtaining SFS from the oil-water interface is delivering the IR radiation to the interface. One might think that absorption by the bulk phase could easily be circumvented by studying protonated surfactants with deuterated alkanes or deuterated surfactants with normal alkanes. However, normal alkanes have an overtone in the C–D stretching region and commercial deuterated alkanes are only ca. 99% deuterated. Water and D_2O both have a significant adsorption cross-section throughout the mid-IR. Consequently, the liquid phase through which the IR radiation passes can be at most a hundred microns or so in thickness. Given that the alkane-water interface is bounded by a thin liquid film, there will be a second interface capable of generating SF light that will interfere with the SF signal of interest. Any design must therefore discriminate against this unwanted signal, either by physically blocking the signal or by ensuring that it is weak enough to be neglected.

Since water does not wet a pure alkane, nor a pure alkane water (except for pentane and shorter homologues, which are inconveniently volatile) the thin liquid phase needs to be confined by a solid surface. I chose to confine a thin film of hexadecane between a sapphire prism and a bulk aqueous surfactant solution. The problem of ensuring that the oil wets the prism is discussed in section 7.4.

7.2.2 Total Internal Reflection. The SF signal from the oil-water interface is maximised when the visible and IR lasers are incident at the critical angle, θ_c, for total internal reflection (TIR). For green light, hexadecane (n = 1.435) has a higher refractive index than water (n = 1.333) so the conditions for TIR can be fulfilled if the visible laser is incident through the alkane at an angle above the critical angle, θ_c = 68.3°. In the infrared, there are two ways of achieving TIR: protonated surfactants with deuterated oil and D_2O or deuterated surfactants with normal oil and H_2O. I designed a cell suitable for either combination, but in chapter 8, only report measurements on protonated surfactants in the C–H stretching region (2800-3000 cm^{-1}). Our laser system performs better between 2800 and 3000 cm^{-1} than between 2000 and 2200 cm^{-1}, C–H stretches are inherently more intense than C–D stretches, and there is a greater body of literature available on protonated surfactants than on deuterated surfactants to aid the interpretation of our results.

The two laser beams are introduced through an equilateral prism, rather than simply a window, in order to achieve the correct angle of incidence at the oil-water interface for TIR. Sapphire was chosen as window material since it is insoluble in water, robust, and transparent in the wavelength range of 3-5 microns where C–H and C–D stretches are found. The high refractive index of sapphire relative to water also

makes alignment easier than would be the case with, for example, calcium fluoride. Figure 7.1 shows the angles used during oil-water experiments in the C–H stretching region. For sapphire, an angle of incidence of the visible laser $\theta_i = 20°$ at the air–prism interface is required for TIR at the critical angle for the hexadecane-water interface. For an angle of incidence of the IR laser, $\theta_i = 21°$, at the air-prism interface, θ_i at the hexadecane-water interface varies from 63.3° at 2800 cm^{-1} to 64.2° at 3000 cm^{-1}. The critical angle meanwhile varies from 58.9° to 63.5° over the same wavelength range, so the IR is always incident above the critical angle. In my calculations I have used values of 1.779, 1.771, and 1.689-1.702 for the refractive index of sapphire[9] at ω_{SF}, ω_{vis} and ω_{IR} (2800-3000 cm^{-1}), respectively, and neglected the small birefringence of sapphire. The refractive index of the D_2O, n_t, varies from $1.199 + 0.0040i$ at 2800 cm^{-1} to $1.253 + 0.0014i$ at 3000 cm^{-1}.[10] For hexadecane I have assumed a value of n = 1.40 at frequencies in the IR that are well away from vibrational resonances.

7.2.2.1 C–H Stretching Region.

Figure 7.1 shows the angles used in all oil-water SF experiments described in this thesis, namely, those in the C–H stretching region.

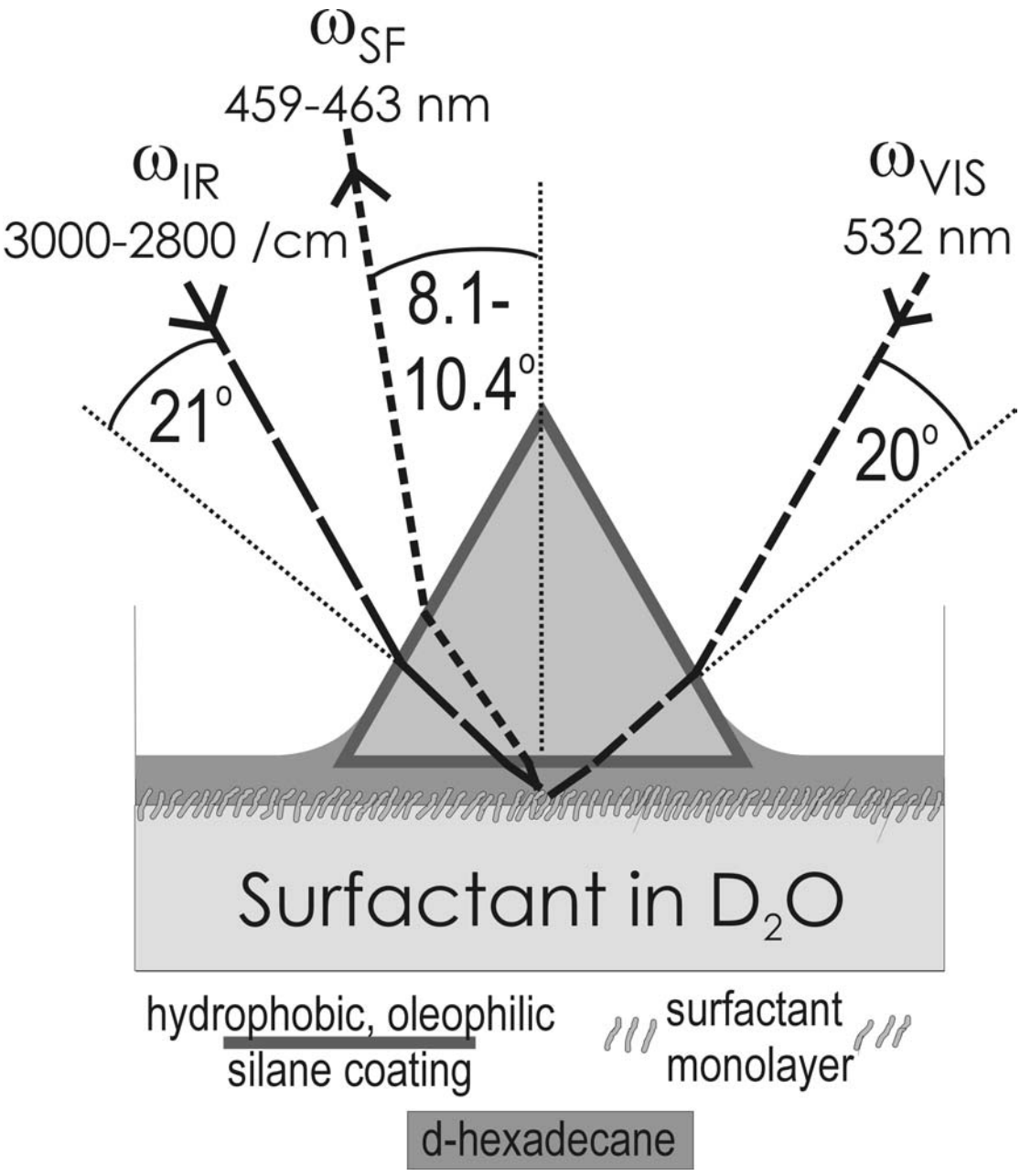

Figure 7.1 *Optical geometry for total internal reflection at the oil-water interface for the C–H stretching region. Angles for incident green and infrared light are shown with respect to the prism surface normals. Angles of SF emission are shown with respect to the surface normal of the optical table and interfacial plane.*

7.2.2.2 C–D Stretching Region.

Figure 7.2 shows angles for TIR relevant for use in the C–D stretching region. This experiment is accomplished by using deuterated surfactant in H_2O, in contact with normal (protonated) hexadecane.

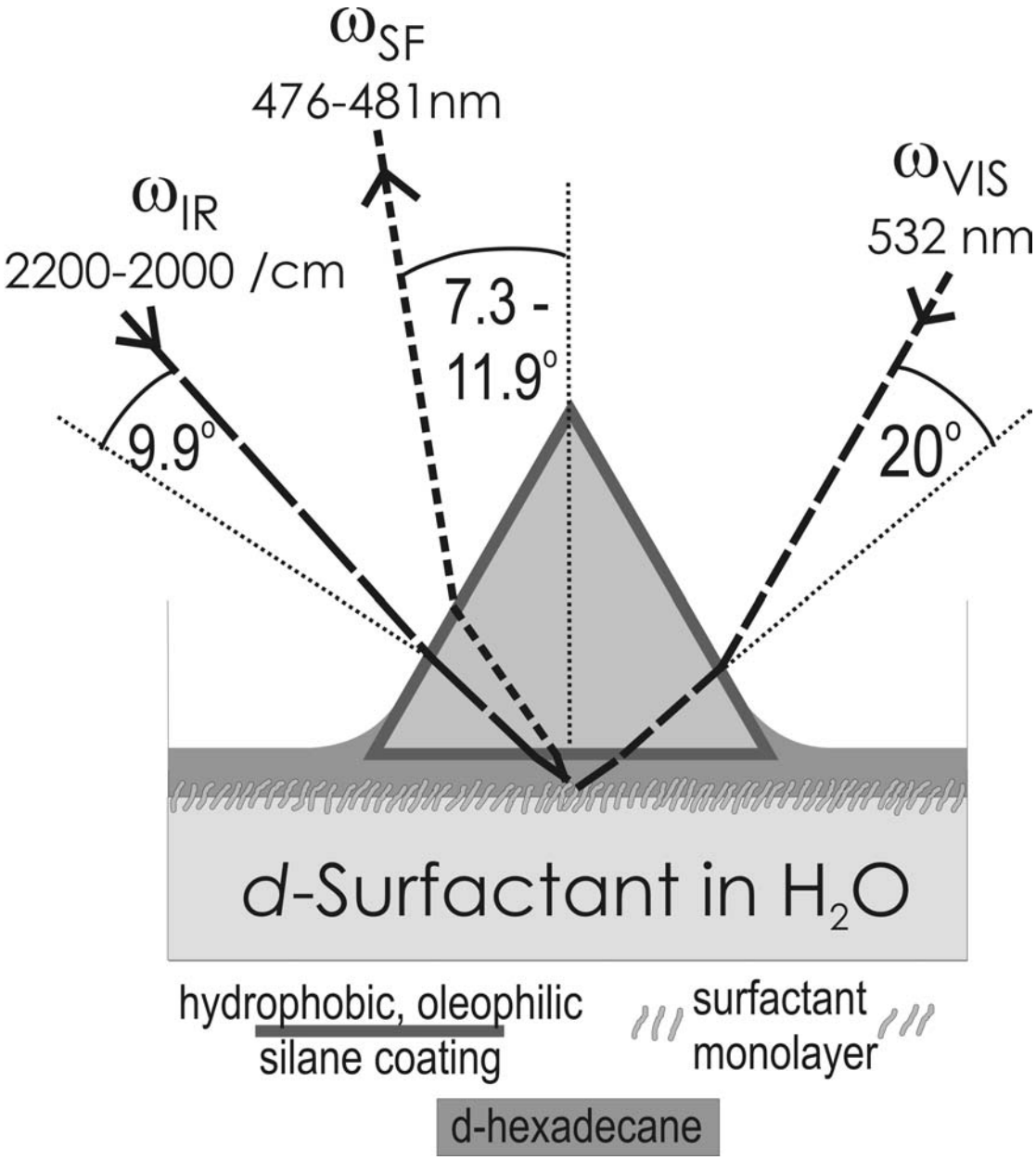

Figure 7.2 *Optical geometry for total internal reflection at the oil-water interface for the C–D stretching region. Angles for incident green and infrared light are shown with respect to the prism surface normals. Angles of SF emission are shown with respect to the surface normal of the optical table and interfacial plane.*

7.2.3 The Oil-Water Setup. For a visual perspective on the SFS oil-water experiment, a photograph of the sample chamber and surrounding optics follows.

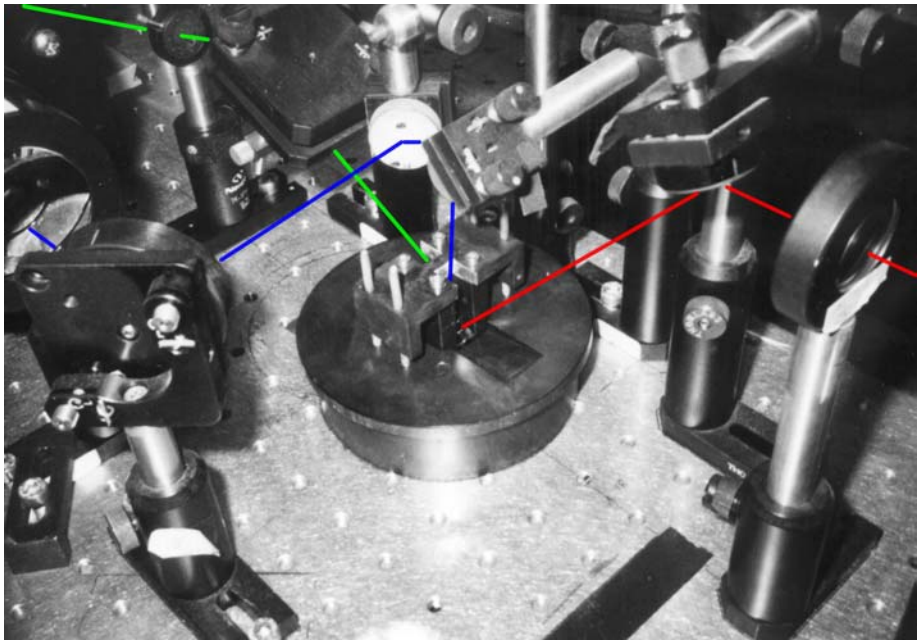

Figure 7.3 *Photograph of the oil-water sample cell used in SFS experiments. Incident green laser light depicted by green line, incident IR laser light depicted by red line, and emitted SF light depicted by blue line.*

7.3 Fresnel Coefficients

Given that the laser beams pass through two interfaces, prism-oil and oil-water, it is important to establish that the SF spectra arise from the oil-water interface, rather than from the prism-oil interface. For the ssp-polarised spectra reported here, the SF signal, $S_{SF,s}$, (in photons per pulse) from a monolayer at the oil-water interface can be expressed as[11]

$$S_{SF,s} = \frac{2\varepsilon_0 A\tau \cos\theta_{SF} I_{vis,s} I_{IR,p}}{\hbar\omega_{SF} c}\left|L^{r}_{SF,s,y}\chi^{(2)}_{yyz}K_{vis,s,y}K_{IR,p,z}\right|^2 \qquad (7.1)$$

where K_{vis} and K_{IR} are Fresnel coefficients that relate the electric fields at the interface to the fields in the incident medium (oil) and L_{SF} relates the nonlinear

polarisation of the interface at the sum-frequency to the electric field of the SF beam emitted into the oil. In labeling the Fresnel factors, the subscript *s* denotes that the electric field **E** is perpendicular to the plane of incidence, the subscript *p* that **E** is parallel to the plane of incidence, and the superscript *r* that the field is evaluated in reflection rather than transmission. A Cartesian coordinate system is employed in which the *x*-*z* plane contains the incident and reflected beams, *z* is normal to the interface, pointing upwards from the water to the oil, and the oil-water interface lies in the *x*-*y* plane. *A* and τ are the spatial and temporal overlap of the laser beams at the surface. θ_{SF} is the angle between the wavevector of the emitted SF light and the surface normal. An analogous expression can be written for the prism-oil interface.

I first consider the wavelength and angle dependence of each Fresnel factor for the oil-water interface. For non-absorbing media, $|K_{vis,s,y}|$ always has the value 2 at the critical angle. Since E_y is continuous across the interface, the Fresnel coefficient has the same value whether evaluated in the D_2O, monolayer or the oil.

To compute $|K_{IR,p,z}|$, I first calculate the reflection coefficient, r_p, from[12]

$$r_p = \frac{n_t \cos\theta_i - n_i \cos\theta_t}{n_t \cos\theta_i + n_i \cos\theta_t} \tag{7.2}$$

where n_t is the complex refractive index of the D_2O and $\cos\theta_t$ is a complex number defined by $(1 - \sin^2\theta_t)^{1/2}$ and $\sin\theta_t$ is found from Snell's Law. θ_i is the (real) angle of incidence at the oil-water interface. $|K_{IR,p,z}|$ is then given by $|(1 + r_p)\sin\theta_i|$, where the electric field is evaluated in the oil. I assume that the chain region of the surfactant monolayer has the same dielectric properties as the oil, so continuity of εE_z yields the same expression for $|K_{IR,p,z}|$ in the monolayer. The variation in $|K_{IR,p,z}|$ with IR wavelength is shown in Figure 7.4.

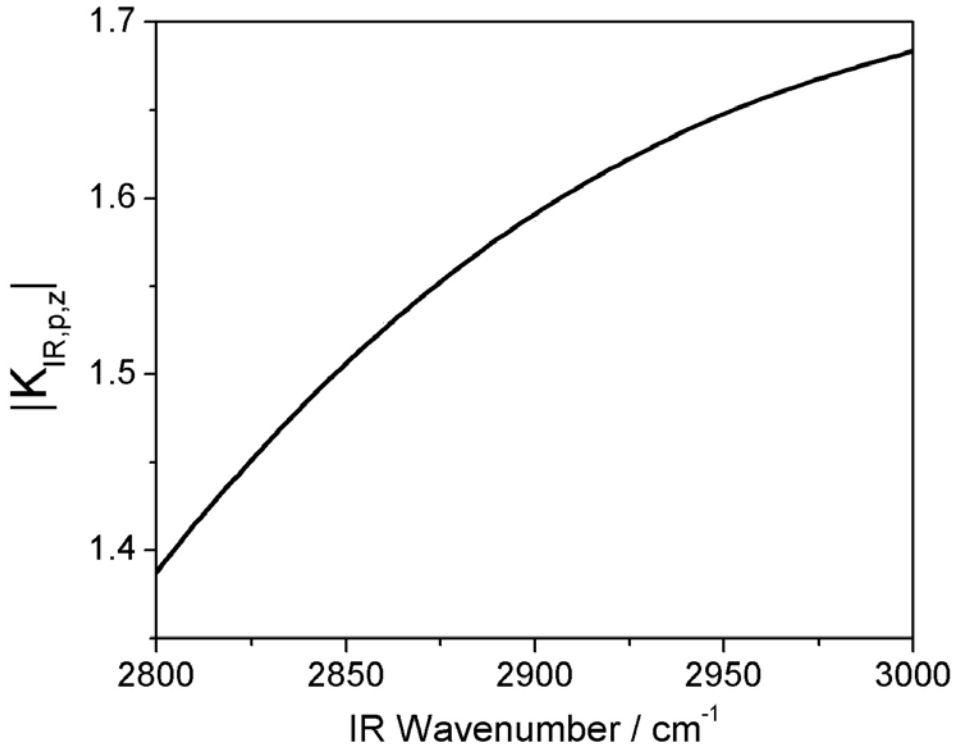

Figure 7.4 *The variation in the Fresnel coefficient* $|K_{IR,p,z}|$ *with IR wavelength.* $|K_{IR,p,z}|$ *is the ratio of the z-component of the electric field at the oil-water interface to the incident field in a p-polarised beam in the oil.*

The variation in $|L^r_{SF,s,y}|$ with wavelength arises from the fact that the angle of emission of the SF beam varies with wavelength as a result of conservation of photon momentum, $\hbar\mathbf{k}$, parallel to the surface: $\mathbf{k}_{SF}\sin\theta_{SF} = \mathbf{k}_{vis}\sin\theta_{vis} - \mathbf{k}_{IR}\sin\theta_{IR}$. The effect of the dispersion in the refractive indices over the small range of wavelengths (459 – 463 nm) is insignificant. Figure 7.5 shows the variation in $|L^r_{SF,s,y}|$ with angle of emission: arrows on the graph indicate the range of angles of emission in this experiment. The inset to figure 7.5 shows $|L^r_{SF,s,y}|$ as a function of incident IR wavenumber for our chosen geometry.

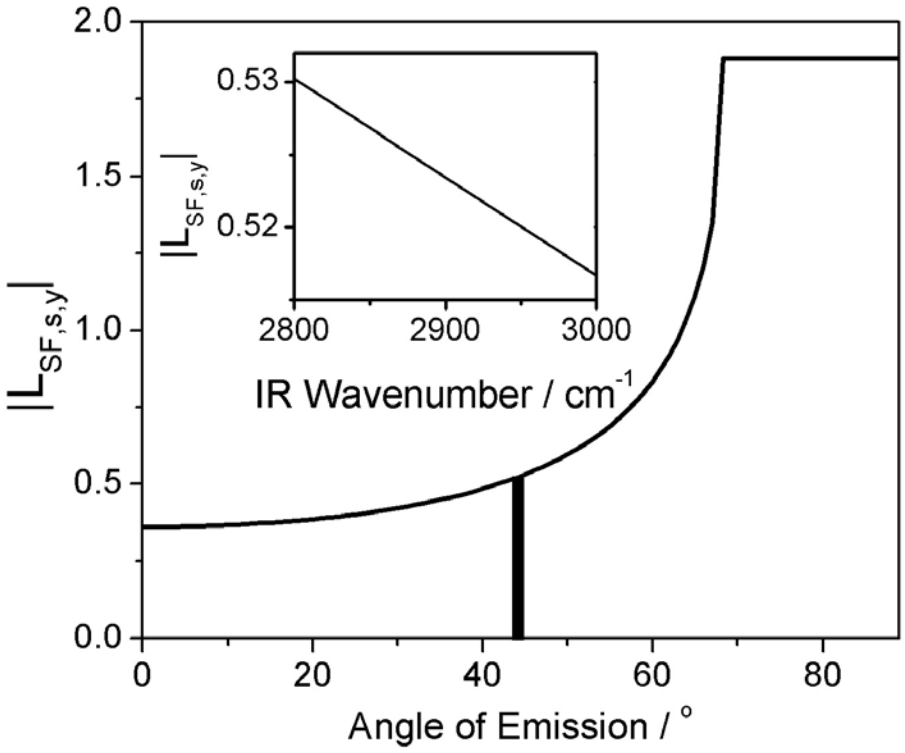

Figure 7.5 *Variation in* $|L_{SF,s,y}|$ *with angle of emission at the oil-water interface.* $|L_{SF,s,y}|$ *relates the y-component of nonlinear polarisation of the oil-water interface at the sum-frequency to the electric field of the s-polarised SF beam emitted into the oil. The shaded block indicates the range of angles arising in these experiments. The inset graph shows the small variation in* $|L_{SF,s,y}|$ *as the IR wavelength is scanned.*

The angles of incidence at the o-w interface are chosen to maximise the electric fields of the incident lasers at that interface. Plots of the three Fresnel coefficients as a function of angle of incidence at the prism-oil interface are shown in Figure 7.6, with the experimental angles indicated by arrows.

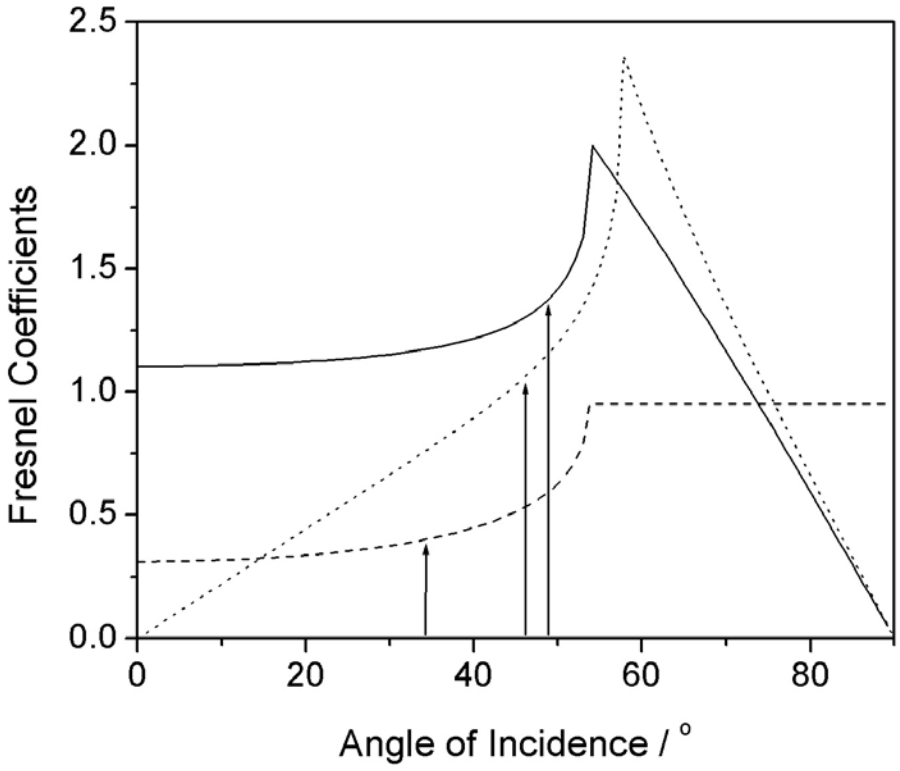

Figure 7.6 *Fresnel coefficients calculated for the prism-oil interface, correlating the electric fields at the prism-oil interface to the electric fields in the prism: solid line -* $|K_{vis,s,y}|$*, dotted line -* $|K_{IR,p,z}|$ *at 2900 cm*$^{-1}$*, dashed line -* $|L_{SF,s,y}|$*. The x-axis shows the angle of incidence at the prism-oil interface. The arrows indicate the angles actually employed in these experiments. Angles were chosen for total internal reflection (TIR) at the oil-water interface rather than the prism-oil interface, hence the distance of the arrows from the peak values for TIR at the prism-oil interface shown in this figure. The ordinate scale does not directly give the values of the Fresnel coefficients in equation 7.3 since the interfacial fields in this figure are referenced, by convention, to incident fields in the prism.*

At this interface, the electric fields are well below their maximum values. To demonstrate that the cell design is indeed specific to the oil-water interface, one can compare the geometric factors affecting the sum-frequency signal. From equation (7.1),

$$I_{SF} \propto \cos\theta_{SF} \left| L^{r}_{SF} K_{vis} K_{IR} \right|^{2} \tag{7.3}$$

The ratio of these geometric factors for the oil/water to the prism/oil interface at 2900 cm^{-1} is

$$\frac{I_{oil-water}}{I_{prism-oil}} = \frac{\cos 44°}{\cos 34°} \times \left(\frac{0.522}{0.353}\right)^2 \times \left(\frac{2}{1}\right)^2 \times \left(\frac{1.588}{\sin 64°}\right)^2 = 24$$

Thus TIR at the oil-water interface is expected to amplify the SF signal such that it overwhelms any SF signals arising from the prism-oil interface. This prediction was confirmed experimentally, as is shown later in chapter 8.

We have employed a counter-propagating geometry with respect to the visible and IR beams. Theoretically, one could obtain even greater SF signal from the oil-water interface by choosing a co-propagating geometry in which the angle of emission of the SF beam was closer to the critical angle (figure 7.5). A co-propagating geometry would be more difficult experimentally given the design of our optical bench and, as the spectra themselves demonstrate (chapter 8), the counter-propagating geometry produces ample signal from the surfactants at the o-w interface.

7.4 Establishing the Submerged Oil-Water Interface

7.4.1 Stability of the Oil Film: the Importance of Contact Angle. Maintaining the stability of a thin film of oil between the prism and the surfactant solution is not trivial; after all, surfactants are designed to remove oil from solid surfaces. For a thermodynamically stable film, we require that, for all concentrations of surfactant, the interfacial tensions satisfy

$$\gamma_{sw} > \gamma_{so} + \gamma_{ow} \tag{7.4}$$

where s, w and o refer to the sapphire, aqueous solution and oil, respectively. If eqn. 7.4 is not satisfied, there is a tendency for the water to break through the thin oil film and cause the oil to retract from the prism. Equation 7.4 can be rewritten in terms of the contact angles (in air) of the oil (θ_o) and the surfactant solution (θ_w) on the prism:

given
$$\gamma_{sa} = \gamma_o \cos\theta_o + \gamma_{so}$$
$$\gamma_{sa} = \gamma_w \cos\theta_w + \gamma_{sw} \qquad \text{then}$$
$$\gamma_{sw} - \gamma_{so} = \gamma_o \cos\theta_o - \gamma_w \cos\theta_w$$

$$\gamma_o \cos\theta_o - \gamma_w \cos\theta_w > \gamma_{ow} \tag{7.5}$$

where γ_o and γ_w are the surface tensions of oil and the aqueous solution, respectively. To satisfy this inequality, we seek to minimise θ_o and maximise θ_w. Functionalising the prism with a methyl-terminated self-assembled monolayer (SAM) is one possibility, but substitution of literature values for $\gamma_o = 27$ mN m^{-1}, $\theta_o = 45°$, $\gamma^0_w = 72$ mN m^{-1}, $\theta^0_w = 115°$, $\gamma^0_{ow} = 53$ mN m^{-1} shows that this inequality is not satisfied for pure water (indicated by the superscript ^{0}). It is known that introducing chain disorder into a SAM has a much greater effect on the oleophobicity than the hydrophobicity.[13] If a disordered monolayer reduces θ_o to zero while retaining a value of $\theta^0_w > 111°$, then the inequality in equation 7.5 is satisfied, at least for pure water.† In practice, the requirements on the contact angles should not be as severe as this, since contact angle hysteresis will work in favor of the prism remaining wet by oil. I therefore sought a protocol for silanising the sapphire prism in order to make it oleophilic yet hydrophobic. The procedure I adopted is described in section 3.4.4, but the success of the coating process was mixed and the durability of the coating was limited: improved coating procedures would be desirable.

7.4.2 Overview of Experimental Attempts to Achieve Stability. Prior to the successful procedure described in chapter 3.4.4, numerous attempts to create a stable layer of oil between a sapphire prism and CTAB solution failed. Thus began the long process of achieving a stable oil-water interface compatible with TIR geometry.

Various surface modifications were attempted on sapphire prisms. For some of them, contact angles for an oil droplet on a sapphire prism surface submerged in water or aqueous solution were measured using a contact angle goniometer with a custom-designed perspex plastic sample dish, illustrated by Figure 7.7. Measurements on small sapphire disks (small sapphire window plates) were found incomparable with measurements on the actual prisms used in SF experiments. I presume this is due to differences in the cut of the sapphire. Once this disparity was noted, all surface modifications were performed on sapphire prisms rather than other sapphire samples. This method for contact angle measurement worked well. Because plastic is sensitive to organic solvents, however, I recommend that future cells be constructed from glass or quartz.

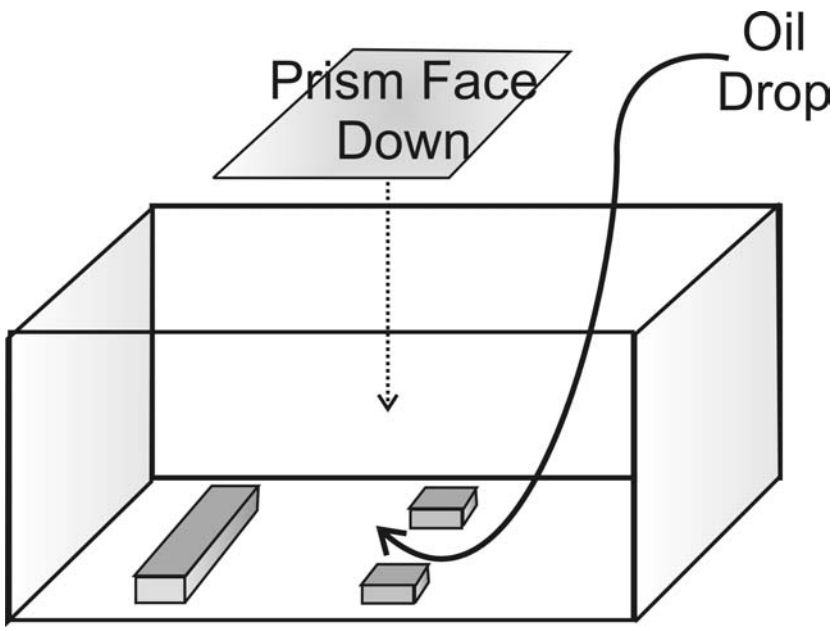

Figure 7.7 *Sketch of perspex plastic liquid cell used for contact angle measurements of alkanes on the (surface-modified) faces of sapphire prisms submerged in water or aqueous surfactant solution. Contact angle measurements were performed using a standard goniometer. Contact angles were viewed from front to back as shown in perspective in this diagram. Prism was placed face down on support posts shown on base of liquid cell, which contained either water or surfactant solution. Oil drops were deposited from beneath the prism face using a curved syringe needle.*

[†] Experimentally, I found that it was most difficult to maintain a wetting film of hexadecane on the prism with pure water.

A thorough literature search did not reveal a previously established successful method for hydrophobing sapphire. Various experimental coating procedures were tried in light of silanisation procedures that had been shown to be successful on surfaces other than sapphire.[14,15,16,17,18] After cleaning sapphire prisms in piranha solution prior to each and every coating, the following coating applications were attempted and the resulting surfaces were found to be insufficiently oleophilic, hydrophobic, and/or stable for use in SFS experiments:

- fluorinated alkyltrichlorosilane such as "FTS" $CF_3(CF_2)_5CH_2CH_2SiCl_3$ applied in a 4:1 mixture of anhydrous hexadecane and anhydrous carbon tetrachloride
- "OTS" octadecyltrichlorosilane in a similar anhydrous or hydrated solvent mixture[19,20,21,22]
- gas-phase coating of prism with "DTS" dodecyltrichlorosilane in a small lidded glass chamber. A hydrophobic polymerised coating did form, but would not adhere to the prism surface when in contact with an organic solvent.
- DTS in a 1:1 solvent mixture of toluene and hexane
- 0.05 – 0.2 M or more concentrated solution of "OPA" *n*-octadecylphosphonic acid $CH_3(CH_2)_{17}PO_3H_2$ in 99.9% THF [23,24]
- dimethyldichlorosilane in a solution of (anhydrous or hydrated) organic solvents, or via gas-phase deposition[25]
- diethyldichlorosilane in 2:1 solvent mixture of alkane (decane) and carbon tetrachloride or various other solvent combinations[26]
- Fluka's Silanisation Solution I (Fluka 85126): 5% dimethyldichlorosilane solution in heptane; this solution also didn't work when the concentration of the silane was increased

- Fluka's Silanisation Solution II (Fluka 85127): 2% dimethyldichlorosilane in 1,1,1-trichloroethane; this solution weakly hydrophobed sapphire prism
- "freezing" a thin layer of hexadecane on an insufficiently hydrophobed or uncoated prism by placing the oiled prism in the refrigerator (or freezer) prior to SF experiments did not result in the formation of a stable oil-water interface
- The deposition of a thin layer of SiO_2 on sapphire was considered but not applied due to the involved nature of the application process and the uncertainties in its durability in cleaning and its stability over time. Given more time to complete SF experiments at the oil-water interface, this approach could prove useful in the future.[27,28]

As in the method detailed in experimental section 3.4.4, the conclusions drawn from the involved trials of various silanes and solvent combinations were that: (1) 1,1,1-trichloroethane in a 1:1 combination with an alkane of equivalent or shorter chain length than the alkyltrichlorosilane made the best solvent mixture, and (2) the alkyltrichlorosilanes should be of chain length 12 or 10. Alkanes that were not anhydrous had equivalent or better coating success rates than anhydrous alkanes. Any coated prism with a contact angle (by eye) of greater than 90° for a drop of water in air was a candidate for success in SF experiments at the oil-water interface.

References

(1) (a) Walstra, P.; Deroos, A. L. *Food Rev. Int.* **1993**, *9*, 503. (b) Krog, N. *A.C.S. Symposium Series* **1991**, *448*, 138. (c) Taylor, J. A. G.; Mingis, J.; Pethica, B. A.; Yan, B. Y. J.; Jackson, C. M. *Biochim. Biophys. Acta* **1973**, *323*, 157.

(2) Harwell, J. H.; Sabatini, D. A.; Knox, R. C. *Colloids and Surfaces A: Physicochem. and Eng. Aspects* **1999**, *151*, 255.

(3) (a) Manning-Benson, S.; Bain, C. D.; Darton, R. C. *J. Coll. Interface Sci.* **1997**, *189*, 109. (b) Manning-Benson, S.; Bain, C. D.; Darton, R. C.; Sharpe, D.; Eastoe, J.; Reynolds, P. *Langmuir* **1997**, *13 (22)*, 5808. (c) Manning-Benson, S.; Parker, S. R. W.; Bain, C. D. *Langmuir* **1998**, *14 (5)*, 990.

(4) Knock, M. M.; Bain, C. D. *Langmuir* **2000**, *16*, 2857.

(5) (a) Bell, G. R.; Manning-Benson, S.; Bain, C. D. *J. Phys. Chem. B* **1998**, *102*, 218. (b) Casson, B. D.; Bain, C. D. *J. Phys. Chem. B* **1999**, *103 (22)*, 4678.

(6) Lu, J. R.; Thomas, R. K.; Binks, B. P.; Fletcher, P. D. I.; Penfold, J. *J. Phys. Chem.* **1995**, *99*, 4113.

(7) (a) Adamczyk, Z.; Para, G.; Warszynski, P. *Langmuir* **1999**, *15*, 8383. (b) Velegol, S. B.; Fleming, B. D.; Biggs, S.; Wanless, E. J.; Tilton, R. D. *Langmuir* **2000**, *16*, 2548.

(8) Rosen, Milton J. *Surfactants and Interfacial Phenomena*, 2nd Ed.; John Wiley and Sons: New York, 1989.

(9) Crystran Crystals, BDH Advanced Materials Division, England.

(10) Bertie, J. E.; Khalique-Ahmed, M.; Baluja, S. *J. Phys. Chem.* **1989**, *93*, 2214.

(11) Bell, G. R.; Li, Z. X.; Bain, C. D.; Fischer, P.; Duffy, D. C. *J. Phys. Chem. B* **1998**, *102*, 9463.

(12) Born. Max; Wolf, Emil. *Principles of Optics*, 6th ed.; Cambridge University Press: Cambridge, 1980, p. 40.

(13) Bain, C. D. *J. Am. Chem. Soc.* **1989**, *111*, 7164.

(14) Cave, N. G.; Kinloch, A. J. *Polymer* **1992**, *33 (6)*, 1162.

(15) Banga, R.; Yarwood, J. *Langmuir* **1995**, *11*, 4393.

(16) Vallant, T.; Kattner, J.; Brunner, H.; Mayer, U.; Hoffmann, H. *Langmuir* **1999**, *15*, 5339.

(17) Brunner, H.; Vallant, T.; Mayer, U.; Hoffman, H. *Langmuir* **1999**, *15*, 1899.

(18) Kacker, N.; Kumar, S. K.; Allara, D. L. *Langmuir* **1997**, *13*, 6366.

(19) Hair, M. L.; Tripp, C. P. *Colloids and Surfaces* **1995**, *105*, 95.

(20) Kojio, K.; Takahara, A.; Omote, K.; Kajiyama, T. *Langmuir* **2000**, *16*, 3932.

(21) Parikh, A. N.; Schivley, M. A.; Koo, E.; Seshadri, K.; Aurentz, D.; Mueller, K.; Allara, D. L. *J. Am. Chem. Soc.* **1997**, *119*, 3135.

(22) Lambert, A. G.; Neivandt, D. J.; McAloney, R. A.; Davies, P. B. *Langmuir* **2000**, *16*, 8377.

(23) (a) Messerschmidt, C.; Schwartz, D. K. *Langmuir* **2001**, *17*, 462.

(b) Woodward, J. T.; Ulman, A.; Schwartz, D. K. *Langmuir* **1996**, *12*, 3626.

(c) Woodward, J. T.; Gwin, H.; Schwartz, D. K. *Langmuir* **2000**, *16*, 2957.

(e) Doudevski, I.; Schwartz, D. K. *Langmuir* **2000**, *16*, 9381.

(f) Risse, T.; Hill, T.; Beckendorf, M.; Katter, U. J.; Schlienz, H.; Hamann, H.; Freund, H.-J. *Langmuir* **1996**, *12*, 5512.

(g) Woodward, J. T.; Schwartz, D. K. *Langmuir* **1997**, *13*, 6873.

(24) OPA is difficult to procure but was obtained from Oryza Laboratories at the recommendation of D. K. Schwartz.

(25) Yaminsky, V. V.; Claesson, P. M.; Eriksson, J. C. *J. Coll. Interface Sci.* **1993**, *161*, 91.

(26) Schmidt, J.; Stuhlmann, Ch.; Ibach, H. *Surf. Sci.* **1994**, *302*, 10.

(27) Brunner, H.; Vallant, T.; Mayer, U.; Hoffmann, H. *Langmuir* **1996**, *12*, 4614.

(28) Clark, T. Jr.; Ruiz, J. D.; Fan, H.; Brinker, J.; Swanson, B.; Parikh, A. N. *Chem. Mater.* **2000**, *12*, 3879.

CHAPTER 8

CTAB Monolayers at the Hexadecane – D_2O Interface

Chapter 8: CTAB Monolayers at the Hexadecane – D_2O Interface

In chapter 7, I described the design of the oil-water sum-frequency spectroscopy experiment. Here, I present results for CTAB monolayers at the oil-water interface.

8.1 Normalisation of SF spectra

Figure 8.1 shows a raw SF spectrum of a solution of 0.6 mM CTAB at the oil-water interface, together with the spectrum after correction for all the wavelength-dependent factors that affect the intensity of the SF spectrum but are unrelated to the nonlinear susceptibility of the interface. Careful normalisation is required before quantitative analysis and therefore I set out the various steps in detail.

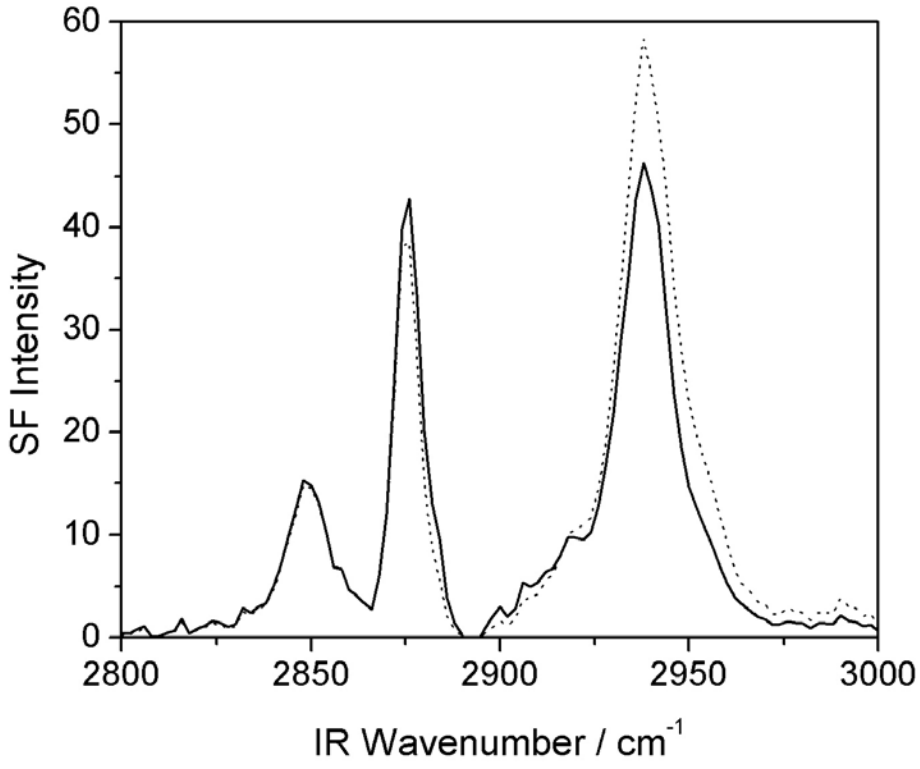

Figure 8.1 *SF spectrum of CTAB monolayer at the oil-water interface, before (dotted line) and after (solid line) normalisation. Units for the raw spectrum are in photons per pulse; units after normalisation are arbitrary. The dc offset of the detector and any background light from the green laser have been subtracted.*

8.1.1 Fresnel Coefficients. For ssp-polarised spectra, the SF signal is given by equation 7.1. The Fresnel coefficients, $K_{vis,s,y}$, $K_{IR,p,z}$, and $L^r_{SF,s,y}$ and their wavelength dependence are discussed in section 7.3. In computing $K_{IR,p,z}$ I have assumed a constant value of $\varepsilon_{monolayer} = \varepsilon_{oil} = 1.96$. I note that $\varepsilon_{monolayer}$ may vary significantly over the wavelength of interest due to the adsorption by the C–H stretching modes in the surfactant, but it is difficult to correct quantitatively for the dispersion in $\varepsilon_{monolayer}$. The combined effect of the Fresnel coefficients at the oil–water interface on the SF spectrum is represented by a term $F_{ssp} = (L^r_{SF,s,y})^2 (K_{vis,s,y})^2 (K_{IR,p,z})^2$, which is plotted in Figure 8.2.

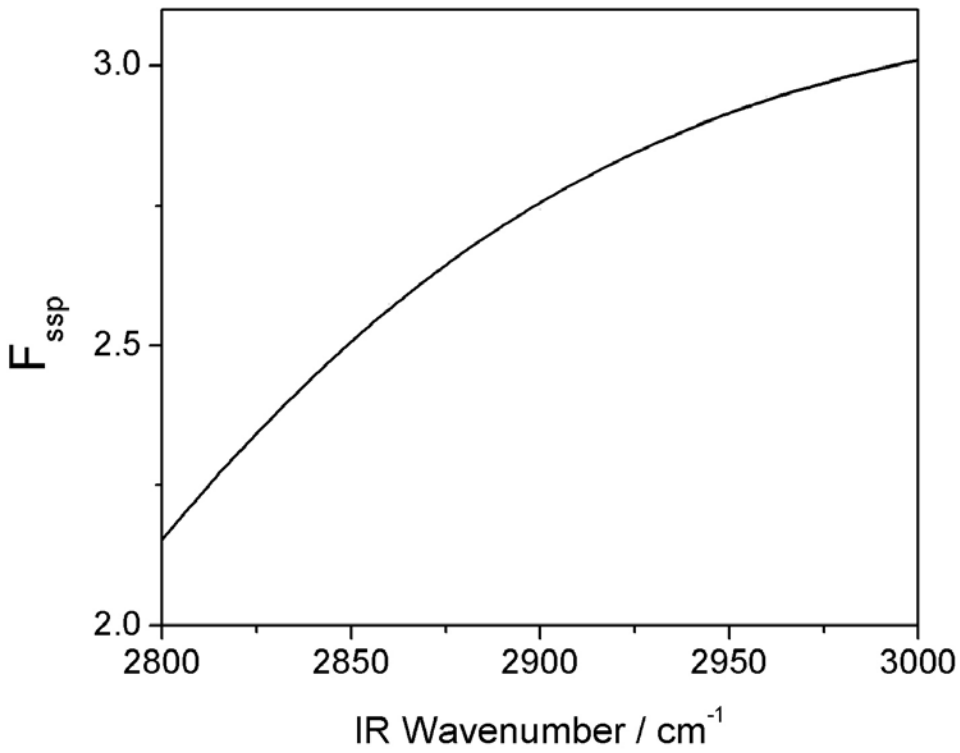

Figure 8.2 *F_{ssp} as a function of IR wavenumber. The combined effect of the Fresnel coefficients at the oil-water interface on the SF spectrum is represented by a term $F_{ssp} = (L^r_{SF,s,y})^2 (K_{vis,s,y})^2 (K_{IR,p,z})^2$.*

8.1.2 Laser Output. The performance of the laser system makes a major contribution to the variation in SF intensity with IR wavelength. The output power of the Raman cell decreases with increasing wavelength and also contains small dips due to traces of water vapour in the Raman cell. I quantified this variation by acquiring an SF spectrum from a sapphire prism in which the face normally in contact with the oil had been coated with a thin film of gold. Spectra of gold were taken at intervals during the course of the experiments and the average spectrum is shown in Figure 8.3(a). The small loss of blue SF light due to reflection within the prism is present in the SF spectrum of gold and is thus accounted for as well. Variations in transmitted SF power with wavelength for the IR beam at the entry face of the prism and at the prism-oil interface are negligible.

I accounted for day-to-day fluctuations in the average IR pulse energy by measuring the IR energy at 3000 and 2800 cm^{-1} before each spectrum and dividing the SF spectrum by the mean pulse energy. The pulse energy in the visible did not vary significantly.

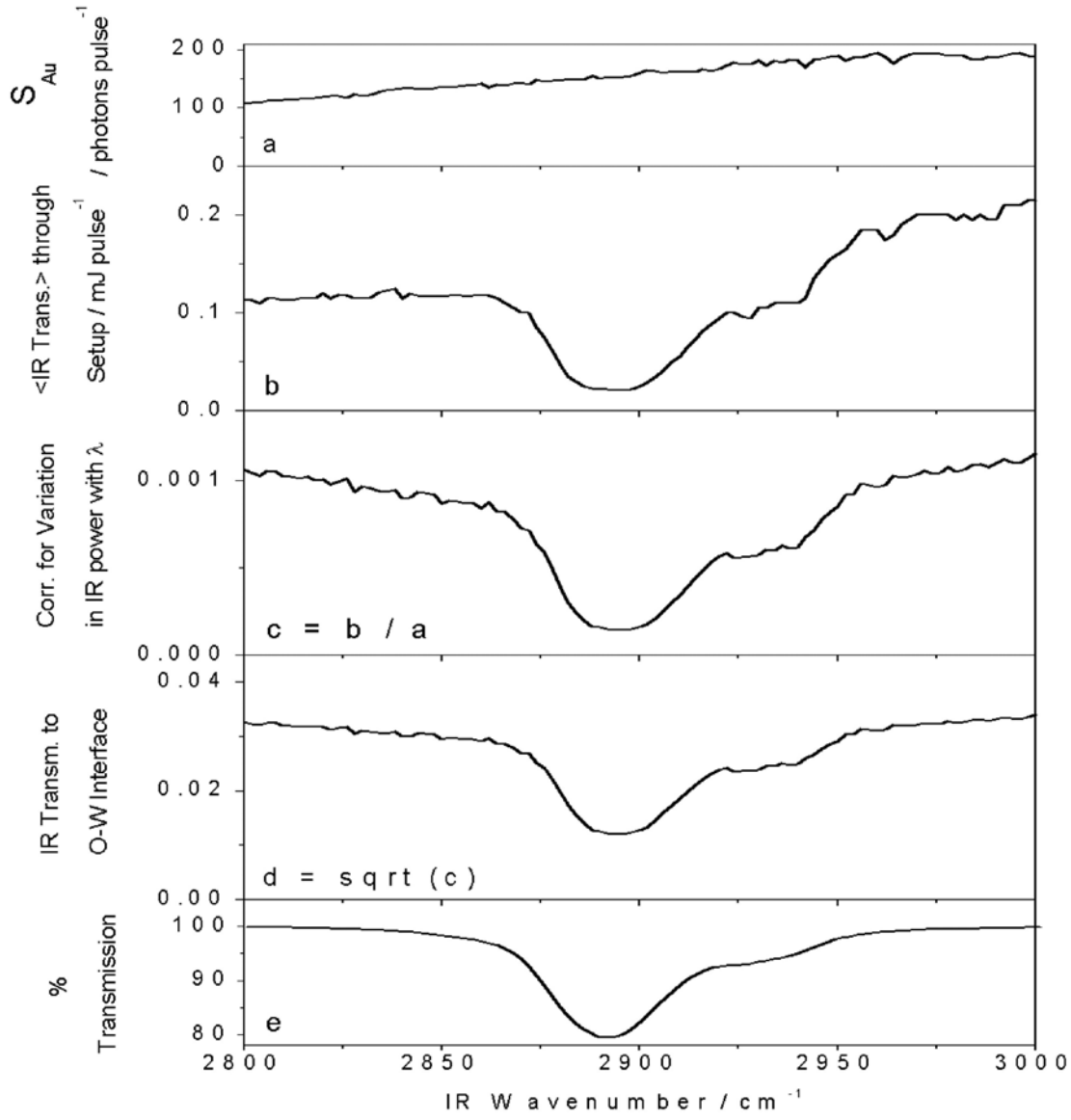

Figure 8.3
(a) Average SF spectrum (S_{Au}) of gold (ppp-polarisation) in photons per pulse;
(b) IR transmission through oil-water setup in mJ per pulse;
(c) IR transmission corrected for variation in IR power with wavelength: c = b/a;
(d) IR transmission to oil-water interface: d = √c;
(e) FTIR % Transmission of 8.7 × 10^{-3} M d*-hexadecane in CCl_4*
(path length = 0.95 cm).

8.1.3 Absorption of IR by Oil. The most significant correction arises from the small percentage (ca. 2%) of C–H bonds in the sample of deuterated hexadecane. Isolated CHD groups absorb IR light at 2892 cm^{-1} while CHD_2 groups have two absorptions at 2940 and 2926 cm^{-1}, depending on whether the C–H bond is in or out of the plane of the carbon skeleton, respectively.[1] The significance of these absorptions is seen in Figure 8.3(b), which shows the intensity of the IR beam after reflection from the oil-water interface. The variation observed in figure 8.3(b) with wavelength has three contributions: (i) the wavelength dependence of the output power of the Raman cell; (ii) absorption of IR in the evanescent wave in the D_2O; (iii) absorption by C–H bonds during two passages of the IR beam through the oil. The variation in the incident IR power can be removed through division of the spectrum in figure 8.3(b) by the spectrum in figure 8.3(a), the result of which is shown in figure 8.3(c). The absorption by D_2O in the evanescent field is found by computing the reflectivity, $\mathcal{R}_{ow} = |r_p|^2$ (eqn. 7.2), of the oil-water interface, which is equal to 0.91 at 2900 cm^{-1} and approximately independent of wavelength. The lack of wavelength dependence is at first sight surprising, but it arises from the cancellation of two effects. As the wavelength increases, the imaginary part of the refractive index increases but at the same time the penetration depth of the evanescent wave decreases since the difference between the angle of incidence and the critical angle increases with increasing wavelength. The constancy of $\mathcal{R}_{ow}$ means that absorption of IR by D_2O can be ignored for the purpose of determining the intrinsic absorption of the oil film from the reflection spectra of the o-w interface. The SF signal is determined by the IR intensity after only one pass through the oil film and therefore to correct for absorption by C–H bonds in the oil, I need to take the square root of the transmission

spectrum 8.3(c), which is shown in figure 8.3(d). For comparison, the IR absorption spectrum of a dilute solution of d_{34}-hexadecane in CCl_4 is shown in figure 8.3(e).

The composite correction factor, taking into account Fresnel coefficients, reflection losses in the prism, variations in laser power and absorption by the oil, is shown in Figure 8.4. The result of applying this correction to a sample SF spectrum of a CTAB monolayer is shown in figure 8.1.

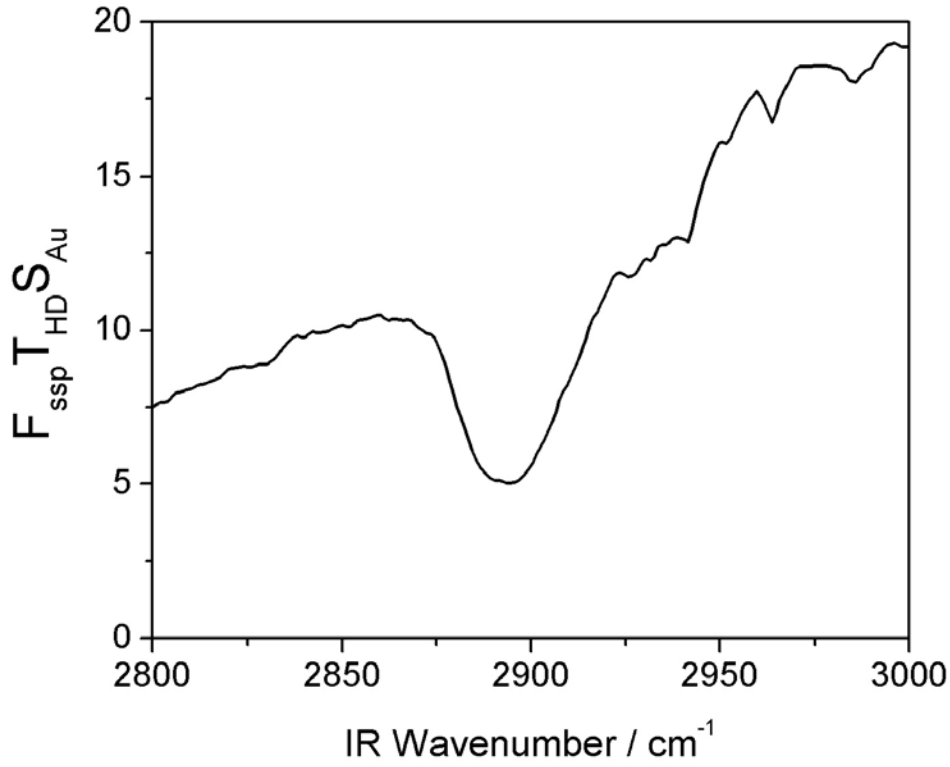

Figure 8.4 *The composite correction factor for normalisation of SF spectra at the oil-water interface. This factor accounts for Fresnel coefficients, reflection losses in the prism, variations in laser power and absorption by the oil. To normalise an SF spectrum, this factor is multiplied by the average IR power associated with that spectrum, and then the product is divided into the spectrum.*

8.2 Thickness of the Oil Layer

We determined the thickness of the oil film by comparing the IR transmission spectrum of the oil film, described in section 3.1.6.5 and shown in Figure 8.3(d), with reference spectra of the oil. FTIR spectra of solutions of deuterated and normal hexadecane in CCl_4 (4.0, 4.2, 8.4, and 8.7×10^{-3} M for d_{34}-hexadecane; 2.0×10^{-3} M for *h*-hexadecane) were obtained. A transmission spectrum of 8.7×10^{-3} M d_{34}-hexadecane in CCl_4 is shown in Figure 8.3(e). The molar absorption coefficient, $\varepsilon = 10.8 \pm 0.1$ dm^3 mol^{-1} cm^{-1}, at the peak maximum of the CHD stretch (2891 cm^{-1}) arising from residual hydrogen in the deuterated hexadecane was determined from the Beer-Lambert Law. By comparing the integrated molar absorption coefficient over the C–H stretching region in deuterated and normal hexadecane, I estimate that the residual level of hydrogen in the d_{34}-hexadecane is 3%, compared with the nominal value of <1%.

The transmission spectrum of the IR laser through the thin film of deuterated hexadecane between the prism and water (Figure 8.3(d)) yields an absorbance of 0.43 at 2891 cm^{-1}, relative to a region of the spectrum where the oil does not absorb. Using the value of ε determined above and the neat concentration of 3.40 mol dm^{-3} of hexadecane, I calculate a path length, *l*, for the IR laser in the oil of $l = d/\cos\theta = 117$ μm, where *d* is the mean thickness of the oil layer and θ is the angle that the IR beam makes with the surface normal in the oil. Since $\theta \sim 64°$, $d \sim 50$ μm. This value agrees well with the average film thickness estimated from the volume of deuterated hexadecane applied to the surfaces of the prism and surfactant solution.

For deuterated oils of commercial purity (ca. 98%), the practical upper limit for the thickness of the oil film is thus ca. 100 μm. For normal protonated surfactants and oils, the limiting film thickness would be only about 2 μm.

8.3 SF Spectrum of a CTAB Monolayer at the Oil-Water Interface

Figure 8.5(e) shows an overlay of SF spectra acquired from the interface between deuterated hexadecane and both 0.6 mM CTAB and pure D_2O. The solid line through the CTAB spectrum is a best fit to equation 3.2. The solid line through the spectrum of pure water connects data points only. The faint peaks discernible in the spectrum of the pure oil-water interface probably arise from the alkylsilane coating on the prism. The weakness of these peaks confirms the prediction that SF signals from the oil-water interface in the TIR geometry are much stronger than those from the prism-oil interface (Section 7.3). Spectra were acquired at room temperature (T ~ 298 K).

The assignment of peaks in the SF spectra of surfactant monolayers has been discussed in detail previously.[2] Ssp-polarised CTAB spectra have three prominent peaks: the d^+ symmetric CH_2 stretch at 2852 cm^{-1}, the r^+ symmetric CH_3 stretch at 2876 cm^{-1} and the r_{FR}^+ mode at 2938 cm^{-1}, which arises from a Fermi resonance of the symmetric CH_3 stretch with the overtone of the CH_3 bend. Of these peaks, the first two provide structural information about the monolayer.

The d^+ mode is indicative of conformational disorder within the monolayer. For highly ordered monolayers with few gauche defects, the d^+ mode is very weak. As disorder increases, $<\beta_{yyz}>$ increases due to the presence of gauche defects. For a highly disordered monolayer, one might expect $<\beta_{yyz}>$ to decrease again due to cancellation between opposing conformations within the randomly orientated chains.

The line strength of the r^+ mode is dependent on the tilt of the terminal methyl group. In an ssp-spectrum, the component of the hyperpolarisability responsible for the signal from this mode is expressed in molecular coordinates as

$\left\langle \beta_{yyz} \right\rangle = \frac{\beta_{ccc}}{8}\left\{ \left\langle \cos\theta \right\rangle (1+7r) + \left\langle \cos 3\theta \right\rangle (r-1) \right\}$ where $r = \beta_{aac} / \beta_{ccc}$ and θ is the angle

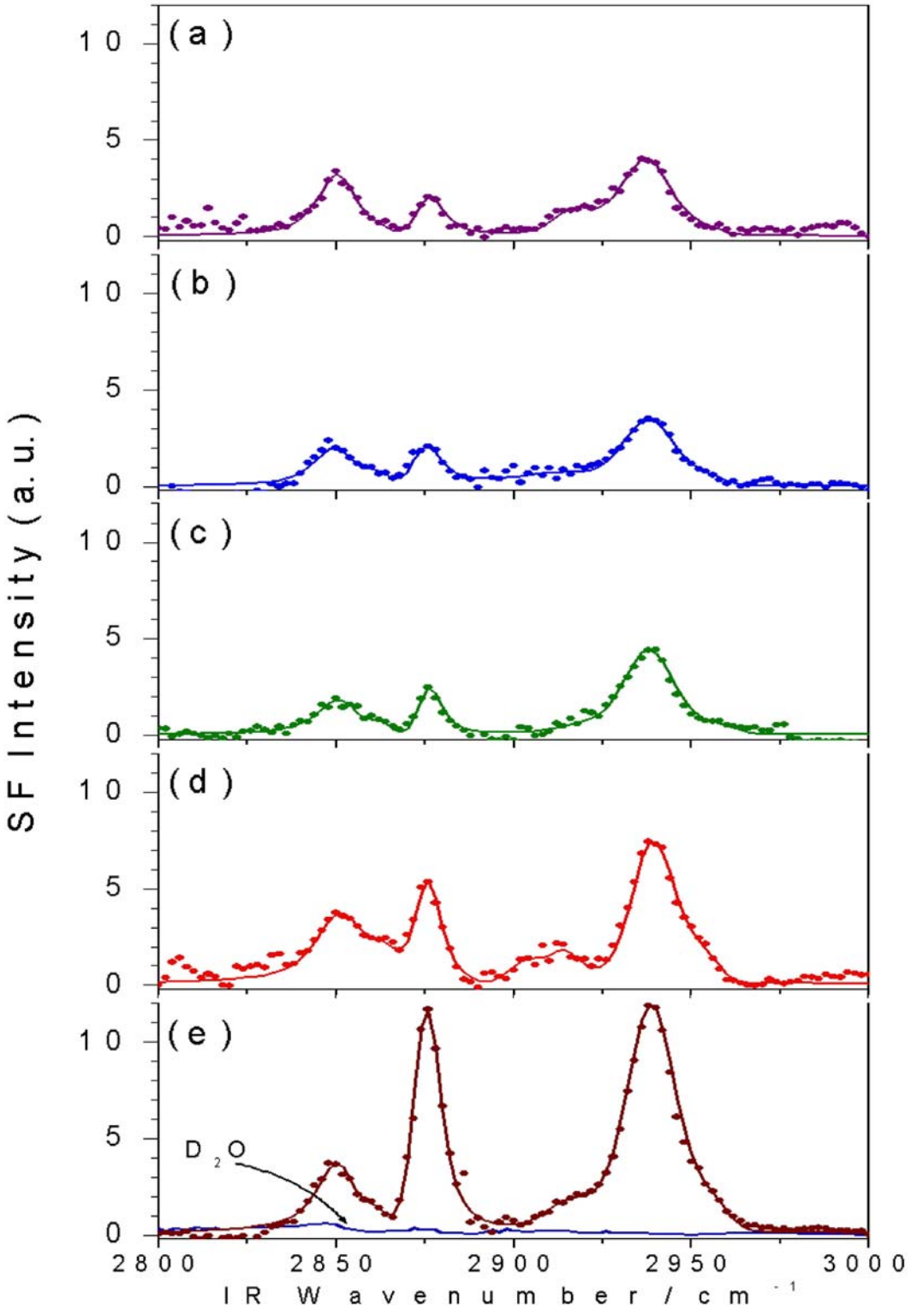

Figure 8.5 *SF spectra of CTAB at the oil-water interface (ssp-polarisation). From top to bottom: (a) 0.05 mM CTAB, (b) 0.1 mM CTAB, (c) 0.3 mM CTAB, (d) 0.5 mM CTAB, (e) 0.6 mM CTAB compared with pure D_2O.*

between the surface normal (z) and the C_3-axis of the terminally methyl group (the c-axis).[3] As the first bracketed term dominates in this equation, $<\beta_{yyz}>$ is proportional to $<\cos\theta>$, to a good approximation.

8.4 Effect of Concentration on SF Spectra

The effect of concentration on the SF spectra of CTAB monolayers at the oil-water interface is shown in Figure 8.5 for five concentrations of CTAB ranging from 0.05 mM to 0.6 mM. The concentration of CTAB was kept below the critical micelle concentration (cmc = 0.92 mM) to prevent solubilisation of the oil within micelles. In previous experiments on CTAB monolayers at the air-water interface, I found little difference between the spectrum of a monolayer formed from a 0.6-mM solution and from a solution at the cmc (see chapter 4).[4]

In constructing a microscopic picture of the adsorbed surfactant film it is more useful to correlate the spectra with the surface concentration of the surfactant, Γ, than the bulk concentration. It is difficult to determine Γ from SFS spectra alone, with any accuracy, so I determined Γ independently by drop-shape analysis. Figure 8.6 shows surface tension measurements on drops of hexadecane in CTAB solutions in the concentrations range 0.0048 – 1.2 mM. The data were fit to the Szyszkowski equation[5]

$$\gamma = \gamma_0 - 2RT\Gamma_{max} \ln(1 + K_L C) \qquad (8.1)$$

At 298 K, the maximum surface excess, Γ_{max}, was found to be $2.8 \pm 0.1 \times 10^{-6}$ mol m^{-2} with $K_L = 18 \pm 1$ m^3 mol^{-1}. The Szyszkowski equation is consistent with the Langmuir adsorption isotherm, $\Gamma = \Gamma_{max} [K_L C / (1 + K_L C)]$, from which Γ can be obtained at all other concentrations. The fit is poor at low concentrations of CTAB, reflecting the fact that the Szyszkowski equation does not take account of electrostatic

interactions, but is quite good at the concentrations employed in the SFS experiments, for which Γ varies from $1.3 - 2.6 \times 10^{-6}$ mol m^{-2}.

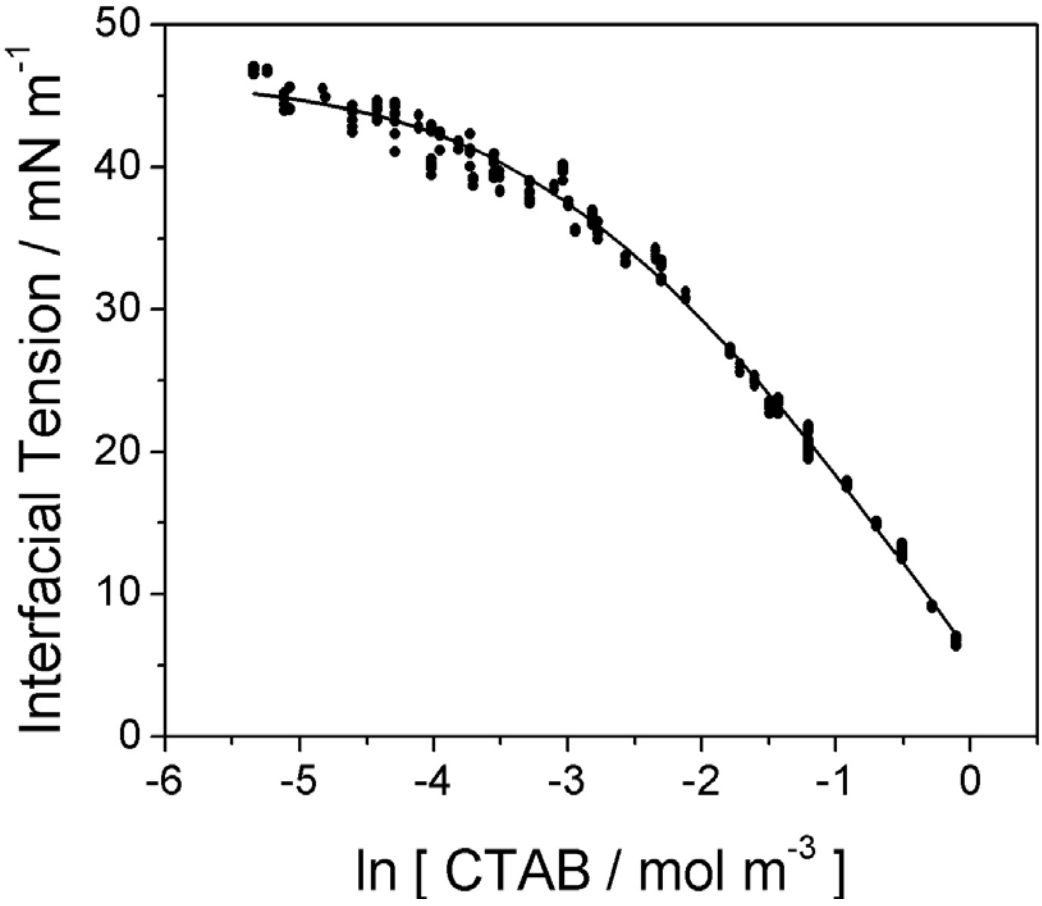

Figure 8.6 *Interfacial tension of CTAB at the oil-water interface as a function of bulk CTAB concentration. Experimental data points (dots) fit to Szyszkowski equation (line). T = 298 K.*

8.5 Effect of Area per Molecule on the SF Spectra of CTAB Monolayers

To interpret SF line strengths, *S*, in terms of changes in the conformation or orientation of molecules within the monolayer, I first must correct for the area per molecule, *A*. Since $S \propto \Gamma$, multiplication of *S* by $A = \Gamma^{-1}$ normalises the line strength on a per molecule basis. Figure 8.7 depicts the variation in the normalised line

strengths of the d^+ and r^+ modes with Γ. The normalised intensity of the d^+ mode decreases as Γ increases, indicating an increase in trans segments in the hydrocarbon chain as the density of CTAB molecules at the interface increases. The r^+ mode tells us about the orientation of the terminal methyl group, which is a reflection of the average tilt of the hydrocarbon chains within the monolayer. The most notable feature is the sharp increase in the r^+ line strength as the bulk concentration approaches the cmc, suggesting a transition to a much more upright configuration in the chains.

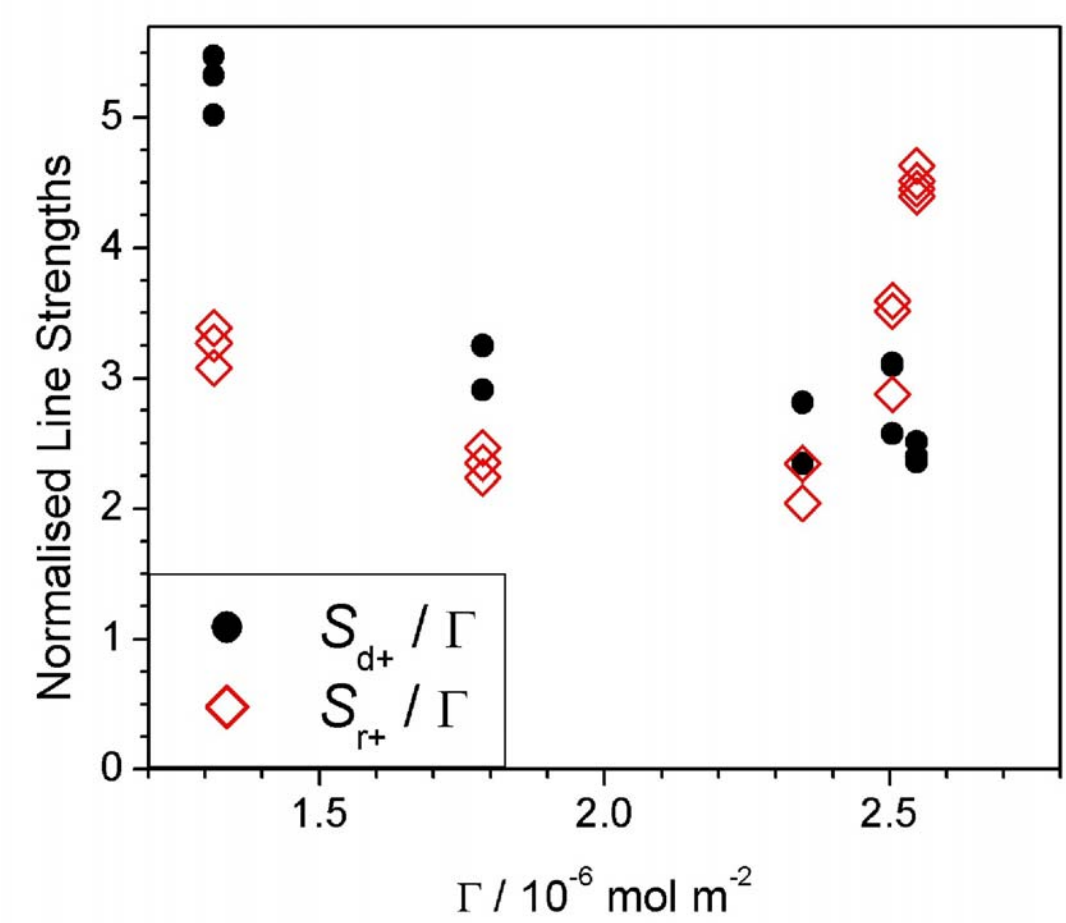

Figure 8.7 *d^+ (●) and r^+ (◇) line strengths from SF spectra of CTAB at the oil-water interface. Line strengths were normalised for area per molecule.*

Interpretation of the normalised line strengths is susceptible to systematic errors in the determination of A. The ratio S_{d+} / S_{r+} is independent of A. This ratio has

been correlated empirically to the degree of conformational disorder in surfactant monolayers.[6,7] Figure 8.8 shows that S_{d+} / S_{r+} decreases with increasing surface excess, with a particularly sharp decrease as Γ approaches its limiting value at high surface coverage. This analysis supports the picture of a more upright, ordered conformation at higher surface coverages.

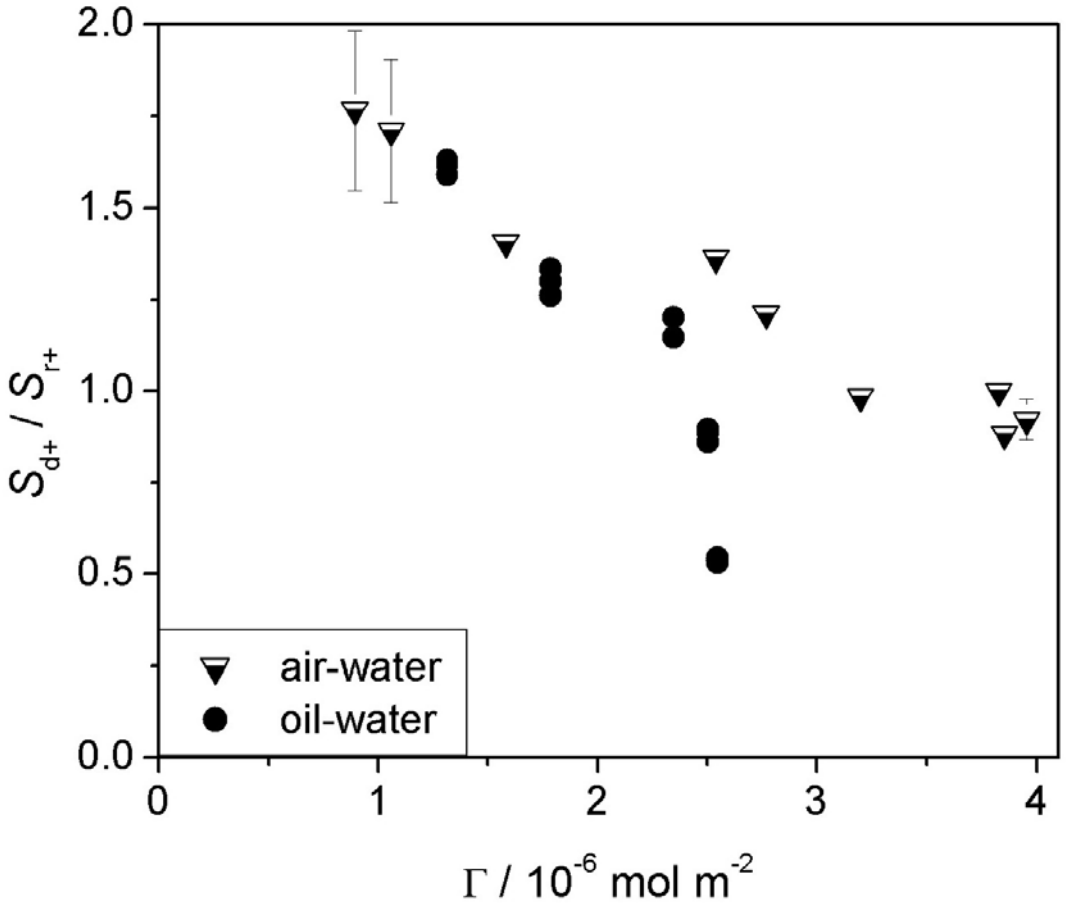

Figure 8.8 *S_{d+} / S_{r+} as a function of surface excess. Results from SF spectra of CTAB at the oil-water interface (●) are compared with results from SF spectra of CTAB at the air-water interface (triangles).*

8.5.1 Supplementary Results from Ellipsometry. The sharp increase in the normalised value of S_{r+} and the decrease in the ratio of S_{d+} / S_{r+} over a very small change in the surface excess is unexpected, and I have looked for supporting evidence for a structural change in other measurements. Such evidence is to be found by ellipsometry. The results of recent measurements by Hannah J. Turner, a Part II

student in our laboratory, on CTAB at the hexadecane–water interface are shown in Figure 8.9.[8]

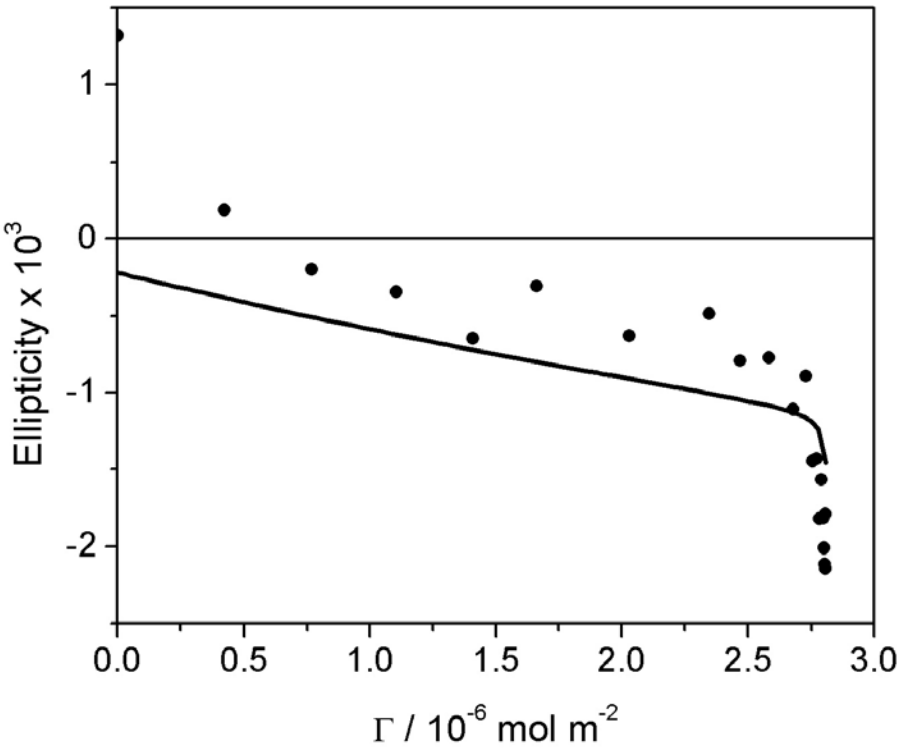

Figure 8.9 *$\overline{\rho}$, the coefficient of ellipticity, for a CTAB monolayer at the oil-water interface, shown as a function of surface excess. Experimental values are indicated by dots; the predicted model is shown by a solid line.*

The ordinate is the coefficient of ellipticity, $\overline{\rho}$, which is defined as the imaginary part of the ratio r_p / r_s at the Brewster angle, where r_p and r_s are the reflection coefficients for s and p-polarised light, respectively. The abscissa is the surface excess, derived from independent measurements of the interfacial tension. The predicted values of $\overline{\rho}$, calculated on the assumption that the hydrocarbon part of the surfactant chain has identical optical properties to hexadecane (see section 8.5.2), is shown by a solid line. We see that the agreement between the experimental and predicted trends in $\overline{\rho}$ is quite good, except for the pure hexadecane-water interface (which we will not discuss

here) and for values of Γ near the limiting surface excess, where there is a steep fall in the $\bar{\rho}$ against Γ plot. To explain this discrepancy, we need to look at the contribution of the hydrophobic chains of the surfactant to $\bar{\rho}$. For a monolayer with uniaxial symmetry, the optical properties of the chain region of the monolayer are characterised by two dielectric constants, ε_e, perpendicular to the surface, and ε_o, in the plane of the surface. $\bar{\rho}$ is given by equation 2.46 where ε_1 and ε_2 are the dielectric constants of the alkane and water, respectively, λ is the wavelength of light and the ellipsometric thickness η is given by equation 2.53, where *d* is the thickness of the chain region. We see that for $\varepsilon_e = \varepsilon_o = \varepsilon_1$, the contribution to η from the hydrocarbon chains vanishes. One might expect that at high surface coverages of CTAB, the chain region would become denser than neat hexadecane, but this would lead to $\varepsilon_e > \varepsilon_1$ and a positive contribution to η and $\bar{\rho}$. If, however, the chains adopt a preferred orientation along the surface normal – which is the implication of the SFS data – then $\varepsilon_e > \varepsilon_o$ and there is a negative contribution to $\bar{\rho}$, in agreement with the observed ellipsometric data. An anisotropy $\Delta\varepsilon = \varepsilon_e - \varepsilon_o \approx 0.03$ would be sufficient to explain the experimental observations. For comparison, $\Delta\varepsilon \approx 0.17$ in a monolayer of vertically oriented hydrocarbon chains in a hexagonal phase.[9]

8.5.2 Calculation of Coefficient of Ellipticity for CTAB Monolayers at the Oil-Water Interface.* We divide the contribution of the interface to $\overline{\rho}$ into four terms arising from the hydrocarbon chains, the TMA head groups, the Br^- counterions and the roughness of the interface. We then have

$$\overline{\rho} = \overline{\rho}_{chain} + \overline{\rho}_{TMA} + \overline{\rho}_{Br} + \overline{\rho}_{R} \tag{8.2}$$

The evaluation of the contribution $\overline{\rho}_{chain}$ from the hydrocarbon chains is described in section 8.5.1. To calculate $\overline{\rho}_{TMA}$, we first estimate the intrinsic dielectric constant of TMA groups from the Clausius-Mossotti relationship (eqn. 2.54) where the molar refractivity, $R_m \sim 20.05$ cm^3 mol^{-1} can be estimated from tabulated values of bond refractivities[10] and the molar volume of $N(CH_3)_3Br$ has been taken to be 140 Å^3,[11] from which the molar volume of Br^- (32 Å^3) is subtracted.

We next assume that the TMA head groups are hydrated and form a mixed layer of TMA groups and water with a thickness of 8 Å – a value estimated from neutron scattering profiles.[11] The dielectric constant of this layer is obtained from the Lorentz-Lorenz effective medium approximation (the choice of EMA has a minimal effect on the results), equation 2.55:

$$\frac{\varepsilon - 1}{\varepsilon + 2} = \phi_{water}\left(\frac{\varepsilon_{water} - 1}{\varepsilon_{water} + 2}\right) + \phi_{TMA}\left(\frac{\varepsilon_{TMA} - 1}{\varepsilon_{TMA} + 2}\right) \tag{8.3}$$

where the volume fractions ϕ_{water} and ϕ_{TMA} are determined from the surface excess of CTAB and the molar volume of TMA. The contribution of the TMA groups to the ellipsometric thickness is given by the isotropic version of the Drude equation (eqn. 2.50) and $\overline{\rho}_{TMA}$ is then given by eqn. 2.46.

The counterion contribution $\overline{\rho}_{Br}$ could be calculated in an analogous manner to the head group contribution or alternatively one can treat the counterions as being

* This calculation is derived from the Part II Thesis of Hannah Turner.[8]

uniformly distributed over a depth of solvent equal to the Debye length and then use tabulated values of the refractive index, *n*, of KBr solutions[12] as a function of concentration to determine the value of ε to substitute in eqn. 2.50. (The contribution of K^+ to *n* can be neglected due to the small size and polarisability of the K^+ ion.) By either method, $\overline{\rho}_{Br}$ is a linear function of Γ and the slope is independent of the precise value chosen for the Debye length.

The roughness contribution $\overline{\rho}_R$ arises from scattering by capillary waves and can be evaluated from capillary wave theory:[13]

$$\overline{\rho}_R = -\frac{3\pi(\varepsilon_1 - \varepsilon_2)}{2\lambda(\varepsilon_1 + \varepsilon_2)^{3/2}}\sqrt{\frac{\pi kT}{6\gamma}} \tag{8.4}$$

where γ is the interfacial tension. For the oil–water interface, $\overline{\rho}_R$ is negative and a highly nonlinear function of Γ. These three contributions to $\overline{\rho}$ are shown in Figure 8.10 and their sum is shown in figure 8.9.

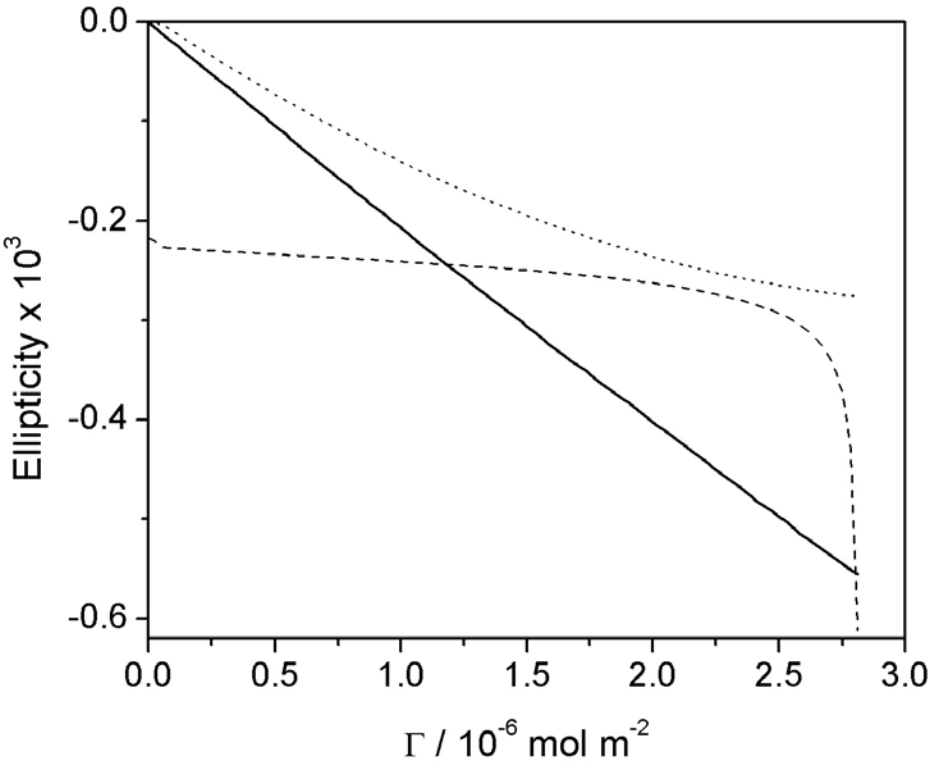

Figure 8.10 *Three contributions to* $\overline{\rho}$ *for a CTAB monolayer at the oil-water interface:* $\overline{\rho}_{TMA}$ *from the trimethylammonium head groups (dotted line),* $\overline{\rho}_{Br}$ *from the bromide counterions (solid line), and* $\overline{\rho}_{R}$ *from the roughness of the interface (dashed line), all shown as a function of surface excess.* $\overline{\rho}_{chain}$ *is assumed to be zero in an isotropic chain model. The sum* $\overline{\rho} = \overline{\rho}_{chain} + \overline{\rho}_{TMA} + \overline{\rho}_{Br} + \overline{\rho}_{R}$ *is shown in Figure 8.9.*

8.6 Comparison with Monolayers at Other Interfaces

8.6.1 CTAB at the Oil-Water and Air-Water Interfaces. In comparison with the o-w interface, there is wealth of information about the structure of surfactant monolayers at the a-w interface, principally from neutron reflection, X-ray reflection, FTIR and SFS.[14] CTAB monolayers at the a-w interface have been studied in detail by NR[15] and by SFS.[4]

The first point of comparison is that the maximum surface excess of CTAB is significantly higher at the a-w interface ($\Gamma = 3.9 \times 10^{-6}$ mol m^{-2}) than at the o-w

interface ($\Gamma = 2.9 \times 10^{-6}$ mol m^{-2}). This difference can be ascribed to the mixing of oil and surfactant chains in the monolayer. In figure 8.8, I compare the ratio S_{d+} / S_{r+} for CTAB monolayers at the o-w and a-w interfaces. At low surface coverages, the degree of conformational order is similar, but at higher surface coverages the ratio S_{d+} / S_{r+} is much lower at the o-w interface than for a comparable a-w interface. A priori, this difference could be ascribed either to a smaller number of gauche defects at the o-w interface or to a more upright configuration (and hence a larger value of <cosθ>); in practice, a combination of both effects is likely. I note that for monolayers of CTAB at the air-water interface, $\overline{\rho}$ is a linear function of the surface excess: there is no anomaly at high surface coverages due to anisotropic chain distributions.[16]

8.6.2 Mixed Monolayers of Surfactants and Alkanes at the Air-Water Interface. Mixed monolayers of surfactants and alkanes at the a-w interface have been studied in some detail.[17,18,19] Investigations of the surfaces of pure alkanes have shown that alkanes tend to form ordered interfacial phases in contact with air, with the hydrocarbon chains oriented normal to the interface.[20,21,22] NR results for mixed monolayers of CTAB and dodecane by Lu *et al*,[19] showed that the area per molecule of CTAB (at the cmc) increased to 52 Å^2 in the presence of the alkane from 43 Å^2 in the absence of the alkane and that the thickness of the hydrocarbon region of the surfactant also increased, which was interpreted in terms of a more upright conformation of the hydrocarbon chains. The *combined* surface concentration of the alkane and surfactant ($\Gamma = 5.67 \times 10^{-6}$ mol m^{-2}) was 47% higher combined than for the pure surfactant alone ($\Gamma = 3.86 \times 10^{-6}$ mol m^{-2}). If one assumes that the interfacial density is similar to that of bulk oil (or, in the terminology used in NR, the volume fraction is unity) then an increase in the combined surface excess is a

prerequisite for an upright conformation, since oil is required to 'fill in the gaps' between the CTAB molecules. Ellipsometry and SFS of mixed monolayers of tetradecane and CTAB at the a-w interface show a first-order phase transition (as the temperature is lowered) to a conformationally ordered state in which the d^+ mode loses all its intensity (i.e. an all-trans conformation) and the chains are oriented along the surface normal.[17] This phase has similar characteristics to the ordered monolayer formed at the interface between many alkanes and air at temperatures just above the bulk melting point of the alkane.[21,22,23] While we have no evidence for the existence of a similar phase transition at the aqueous CTAB-hexadecane interface, the fluid phase appears to adopt some of the features of the condensed phase at the a-w interface, with a preferred orientation normal to the interfacial plane.

8.6.3 Surfactant Monolayers at the CCl_4-Water Interface. Richmond and coworkers have employed SFS to study an extensive range of surfactants at the CCl_4-water interface,[24,25] including both simple single-chained ionic surfactants and phospholipids. The general trend of an increasing ratio S_{d+}/S_{r+} with increasing bulk concentration was observed for simple ionic surfactants at the CCl_4-water interface, in agreement with the data presented here for the alkane-water interface. The closest comparison with CTAB in Richmond's work in terms of molecular structure is dodecyltrimethylammonium chloride (DTAC).[25(d)] The SF spectrum of DTAC at its limiting coverage is similar to my spectrum 8.5(d), with a ratio S_{d+}/S_{r+} significantly higher than the limiting value for CTAB at the alkane-water interface. The limiting coverage measured by Richmond for DTAC is, however, only $\Gamma_{max} = 1.8 \times 10^{-6}$ mol m^{-2} which is significantly lower than $\Gamma_{max} = 2.5 \times 10^{-6}$ mol m^{-2} that I measure for CTAB. Sodium dodecyl sulphate and sodium dodecyl sulfonate had limiting surface

coverages at the CCl_4-water interface similar to that of CTAB at the hexadecane-water interface,[25(b)(c)(d)] but, surprisingly, showed a lower degree of conformational order than DTAC. The smallest value of S_{d+}/S_{r+} for simple ionic surfactants was found for dodecylammonium chloride at a limiting coverage of $\Gamma_{max} = 4.5 \times 10^{-6}$ mol m^{-2}, but even this spectrum showed more conformational disorder than I observed for CTAB at 0.6 mM. None of the surfactants studied at the CCl_4-water interface show the sharp increase in conformational order near Γ_{max} that I have observed for CTAB at the alkane-water interface. For phospholipids adsorbed at the CCl_4-water interface, a decrease in conformational order with increasing chain length was observed.[25(e)] Shen *et al* reported that this unexpected behaviour may be caused by solvation of the alkyl chains by the CCl_4, which screens chain-chain interaction and promotes chain disorder.[26] Under these circumstances, increasing the chain length leads to an increase in the number of defects,[25(c)] an effect not observed for monolayers of alkyl chains at interfaces without carbon tetrachloride.[26] This behaviour marks an important difference between CCl_4-water and the oil-water interfaces. For example, when an alkane replaces carbon tetrachloride as the liquid in contact with a dioctadecyldimethylammonium chloride (DOAC) monolayer on quartz, the longer length alkanes (C_{14} and C_{16}) promote order in the DOAC hydrocarbon chains.[26]

8.6.4 Surfactant Monolayers at the Hydrophobic Solid-Liquid Interface. Davies, Bain, and coworkers have used SFS to study the interface between a hydrophobic solid and aqueous solutions of surfactants.[27] The hydrophobic solid was a self-assembled monolayer of d_{37}-octadecanethiol on gold (dODT/Au) and, of the surfactants studied, the homologue tetradecyltrimethylammonium bromide (C_{14}TAB) is most similar to the CTAB considered here. For an aqueous solution of C_{14}TAB at

the dODT/Au interface, the surfactant chains are orientated towards the hydrophobic solid, and the polar head groups towards the aqueous phase.[27(a),(b)] A quantitative comparison of the ratio S_{d+} / S_{r+} is not possible, since the spectra from monolayers on gold contain contributions from both χ_{xxz} and χ_{zzz}. The wide range of surfactants studied at the solid-water interface, however, indicate substantial variation in conformational disorder with S_{d+} / S_{r+} ranging from 0.2 for dodecanol to 3.9 for dodecylpyridinium chloride. For C_{14}TAB near the cmc, the value of $S_{d+} / S_r = 3.2$ lies near the top of this range. The absence of mixing between the surfactant and the self-assembled monolayer militates against an upright conformation in the surfactant chains.

8.7 Conclusion

As detailed in chapter 7, a new experimental approach has been developed for the acquisition of sum-frequency spectra from the bulk oil-water interface. The key features of this approach are the stabilisation of a thin oil film between a sapphire prism and an aqueous phase, and the use of total internal reflection to enhance the total signal and discriminate against signals from other interfaces in the system. Even with an oil film only 50 μm thick, there is significant attenuation of the IR laser within the oil and careful correction of the SF spectra is required.

With this new methodology, I have obtained the first SF vibrational spectra of surfactant monolayers at an alkane-water interface. At low concentrations, the model system of CTAB/hexadecane showed the expected features in the C–H stretching region, characteristic of a conformationally disordered monolayer. As the bulk concentration approached the cmc, the spectra changed to one characteristic of a more ordered, upright conformation. Ellipsometric measurements supported this

conclusion. This qualitative structural change is not observed in analogous monolayers at the a-w interface, CCl_4-water interface, or in surfactant solutions in contact with a hydrophobic solid surface. Mixed monolayers of CTAB and alkanes at the a-w interface do have a propensity to form ordered upright phases (as do pure alkanes at their interface with air[21(a),28]). This propensity is reflected in a more upright orientation in the fluid interfacial phases studied in this chapter.

This chapter begins to address the question of how the structure of surfactant monolayers at the oil-water differs from that at the air-water or solid-water interface, and points to the importance of mixing of the oil and surfactant in determining the structure. Clearly, these studies will need to be extended to a range of other surfactants and oils to build a complete picture, but the work I describe here does signpost the road ahead. The methodology I describe is generally applicable to surfactants (even those with appreciable solubility in the oil phase) and to various oils, provided that one or other can be obtained in deuterated form. Certain refinements to the methodology would be desirable, such as effective thermostatting and more durable prism coatings.

References

(1) MacPhail, R. A.; Strauss, H. L.; Snyder, R. G.; Elliger, C. A. *J. Phys. Chem.* **1984**, *88*, 334.

(2) Ward, R. N.; Duffy, D. C.; Davies, P. B.; Bain, C. D. *J. Phys. Chem.* **1994**, *98*, 8536.

(3) Bell, G. R.; Bain. C. D.; Ward, R. N. *J. Chem. Soc. Faraday Trans.* **1996**, *92*, 515.

(4) Knock, M. M.; Bain, C. D. *Langmuir* **2000**, *16*, 2857.

(5) (a) Szyszkowski, B. *Z. Phys. Chem.* **1908**, *64*, 385. (b) Prosser, A. J.; Franses, E. I. *Colloids and Surfaces A: Physicochem. Eng. Aspects* **2001**, *178*, 1.

(6) Ward, R. N.; Duffy, D. C.; Davies, P. B.; Bain, C. D. *J. Phys. Chem.* **1994**, *98*, 8536.

(7) Duffy, D. C.; Davies, P. B.; Creeth, A. M. *Langmuir* **1995**, *11*, 2931.

(8) Turner, Hannah J. *Surfactants at the Oil / Water Interface*, Part II Thesis, Trinity College, Oxford, June 2002.

(9) Casson, B. D.; Bain, C. D. *Langmuir* **1997**, *13*, 5465.

(10) Atkins, P. *Physical Chemistry,* 3rd Ed., Oxford University Press: Oxford, 1986, chapter 24.

(11) Lu, J.; Simister, E.; Thomas, R. K. T.; Penfold, J. *J. Phys. Chem.* **1993**, *97*, 6024.

(12) *Handbook of Chemistry and Physics*, 64th Ed. CRC Press, Boca Raton, Fl., 1984, p D-246.

(13) Meunier, J.; *J. Physique*, **1987**, *48*, 1819.

(14) Lu, J. R.; Thomas, R. K.; Penfold, J. *Adv. Colloid Interface Sci.* **2000**, *84*, 143.

(15) (a) Lu, J. R.; Lee, E. M.; Thomas, R. K. *Acta Crystallogr., Sect. A: Fundam. Crystallogr.* **1996**, *A52(1)*, 11. (b) Lu, J. R.; Li, Z. X.; Smallwood, J.; Thomas, R. K.; Penfold, J. *J. Phys. Chem.* **1995**, *99*, 8233. (c) Lu, J. R.; Hromadova, M.; Simister, E. A.; Thomas, R. K.; Penfold, J. *J. Phys. Chem.* **1994**, *98*, 11519. (d) Lu, J. R.; Hromadova, M.; Simister, E.; Thomas, R. K.; Penfold, J. *Physica B* **1994**, *198*, 120.

(16) Manning-Benson, S.; Parker, S. R. W.; Bain, C. D.; Darton, R. C.; Penfold, J. *Langmuir* **1998**, *14*, 990.

(17) (a) Lei, Q.; Knock, M. M.; Bain, C. D. unpublished results (b) McKenna, C. E.; Knock, M. M.; Bain, C. D. *Langmuir* **2000**, *16*, 5853.

(18) Lu, J. R.; Thomas, R. K.; Aveyard, R.; Binks, B. P.; Cooper, P.; Fletcher, P. D. I.; Sokolowski, A.; Penfold, J. *J. Phys. Chem.* **1992**, *96*, 10971.

(19) Lu, J. R.; Thomas, R. K.; Binks, B. P.; Fletcher, P. D. I.; Penfold, J. *J. Phys. Chem.* **1995**, *99*, 4113.

(20) Conboy, J. C.; Daschbach, J. L.; Richmond, G. L. *J. Phys. Chem.* **1994**, *98*, 9688.

(21) (a) Ocko, B. M.; Wu, X. Z.; Sirota, E. B.; Gang, O.; Deutsch, M. *Physical Review E* **1997**, *55 (3)*, 3164. (b) Colussi, A. J.; Hoffmann, M. R.; Tang, Y. *Langmuir* **2000**, *16 (12)*, 5213.

(22) Birdi, K. S. *Colloids and Surfaces A: Physicochem. and Eng. Aspects* **1997**, *123-124*, 543.

(23) Conboy, J. C.; Daschbach, J. L.; Richmond, G. L. *J. Phys. Chem.* **1994**, *98*, 9688.

(24) Richmond, G. L. *Analytical Chem. News & Features* **1997**, 536A-543A.

(25) (a) Messmer, M. C.; Conboy, J. C.; Richmond, G. L. *J. Am. Chem. Soc.* **1995**, *117*, 8039. (b) Conboy, J. C.; Messmer, M. C.; Richmond, G. L. *J. Phys. Chem.* **1996**, *100*, 7617. (c) Conboy, J. C.; Messmer, M. C.; Richmond, G. L. *Langmuir* **1998**, *14*, 6722. (d) Conboy, J. C.; Messmer, M. C.; Richmond, G. L. *J. Phys. Chem. B* **1997**, *101*, 6724. (e) Walker, R. A.; Conboy, J. C.; Richmond, G. L. *Langmuir* **1997**, *13*, 3070.

(26) Miranda, P. B. and Shen, Y. R. *J. Phys. Chem. B* **1999**, *103*, 3292.

(27) (a) Ward, R. N.; Duffy, D. C.; Davies, P. B.; Bain, C. D. *J. Phys. Chem.* **1994**, *98 (34)*, 8356. (b) Ward, R. N.; Davies, P. B.; Bain, C. D. *J. Phys. Chem.* **1993**, *97*, 7141. (c) Bain, C. D. *J. Chem. Soc. Faraday Trans.* **1995**, *91 (9)*, 1281.

(28) (a) Sefler, G. A.; Du, Q.; Miranda, P. B.; Shen, Y. R. *Chem. Phys. Lett.* **1995**, *235*, 347. (b) Pfohl, T.; Beaglehole, D.; Riegler, H. *Chem. Phys. Lett.* **1996**, *260*, 82.

CHAPTER 9

Conclusion

Chapter 9: Conclusion

9.1 Monolayers at the Air-Water and Oil-Water Interfaces

Monolayers of the cationic surfactant hexadecyltrimethylammonium bromide (CTAB) were studied in three different interfacial environments: pure CTAB at the air-water interface, CTAB in mixed monolayers with alkanes at the air-water interface, and pure CTAB at the interface between hexadecane and water. Of these environments, the air-water interface is best understood, followed by mixed monolayers at the air-water interface, and then by surfactant monolayers at the oil-water interface.

The scarcity of information on the molecular structure of surfactant monolayers at the oil-water interface is regrettable since surfactants are often used to bridge the interface between oil and water. This thesis addresses the technical challenges that have hindered the application of most surface-sensitive techniques to the oil-water interface. Through the design of an appropriate experimental setup, sum-frequency vibrational spectroscopy has been applied, for the first time, to study surfactant monolayers at the macroscopic oil-water interface. In this thesis, the choice of CTAB as the surfactant was based upon the large amount of structural information available for CTAB at the air-water interface, which serves as an invaluable standard of comparison for experiments at the oil-water interface. My design of the SFS oil-water setup enables future experiments to continue for a wide range of surfactants and oils.

At the air-water interface, the effect of the bromide counterion on CTAB monolayers was investigated through comparison with analogous CTA^+ surfactants employing chloride, fluoride, and iodide counterions. The effect of added electrolyte was also evaluated for surfactants with bromide, chloride, and fluoride counterions in

the presence of KBr, KCl, and KF, respectively. Adding 0.1 M salt reduces the cmc but appears to have little effect on the limiting area per molecule attained at the cmc, which increases from 44 $Å^2$ for CTAB to 65 $Å^2$ for CTAC and ca. 94 $Å^2$ for CTAF. The principal effect of the counterion is to change the efficiency and effectiveness of the surfactant (both decreasing in order $Br^- > Cl^- > F^-$). My results from ellipsometry and SFS indicate that the structure of the CTAX monolayer is independent of counterion for the same area per molecule.

9.2 Effect of Oil on the Conformation of Surfactant Monolayers

Much research has investigated the structure of surfactant monolayers at the air-water interface. Although air is a sufficiently hydrophobic environment to retain the hydrocarbon chains of surfactants adsorbed at the air-water interface, air is not the environment in which many surfactants are commonly found. A long-standing effort to characterise the structure of surfactant monolayers at the oil-water interface has had quite limited success, with techniques often relying upon volatile organic solvents to substitute for the oil phase, or requiring the environment of an emulsion. This thesis presents the first sum-frequency vibrational spectra from surfactant monolayers adsorbed at the oil-water interface.

The method described in this thesis for acquisition of SF vibrational spectra of monolayers at the oil-water interface represents a significant breakthrough in the molecular characterisation of surfactant monolayers adsorbed at this interface. Application of this experimental method to a range of surfactants and oils will contribute greatly to our understanding of the structure-function relationship for surfactants in their common environment between water and oil.

Spectra of CTAB monolayers at the air-water and oil-water interfaces have been compared to identify differences in the conformational order and structure of the two monolayers. Results for mixed monolayers of CTAB and tetradecane, which undergo a first-order surface-freezing phase transition (at a temperature above the bulk melting point of tetradecane) as the temperature is lowered, suggest that the addition of alkanes to surfactant monolayers serves to increase conformational order within the mixed monolayer as compared to the monolayer of pure surfactant. Such phase changes observed in soluble surfactant monolayers at the surface of a bulk solution are a remarkable feature of interfacial thermodynamics, and motivate research to identify whether surfactant monolayers between bulk oil and water undergo similar ordering transitions.

Comparison of CTAB monolayers of the same surface excess at the air-water and hexadecane-water interfaces indicates that for bulk concentrations approaching the cmc, CTAB monolayers at the oil-water interface are substantially more ordered, with hydrocarbon chains exhibiting fewer gauche defects and having a more upright orientation with respect to the interfacial plane. Ellipsometric measurements support this conclusion. This qualitative structural change is not observed in analogous monolayers at the air-water interface, CCl_4-water interface, or in surfactant solutions in contact with a hydrophobic solid surface. I suspect that this ordering is caused by the close proximity of the system to a phase transition. We have noted through other experiments employing ellipsometry and surface tensiometry that a phase transition does not actually take place for CTAB at the bulk water-hexadecane interface. At low concentrations, however, CTAB monolayers at the oil-water interface had spectra characteristic of a conformationally disordered monolayer. Spectra from CTAB at the

air-water and oil-water interfaces at lower bulk CTAB concentrations are quite similar in their indication of conformational disorder.

Studies that substitute carbon tetrachloride for alkanes do not investigate the effect of the alkane on interfacial ordering of the surfactant (and alkane) hydrocarbon chains. Carbon tetrachloride is thus a poor model hydrocarbon, since it screens interactions between the surfactant chains, effectively eliminating the fascinating 2D thermodynamics that take place when the alkane and surfactant chains are allowed to arrange themselves according to best-fit packing parameters.

9.3 Implications for Future Research

The efficiency of this method could be improved through the development of a more stable hydrophobic, oleophilic coating for the sapphire prism used to achieve total-internal reflection at the oil-water interface. The current coating method is effective but inefficient, as the coating process must be repeated frequently and does not have a 100% coating success rate for each silanisation reaction. As the method involves the use of piranha solution prior to each coating, repeating the coating process regularly (i.e. every other day) over the course of a D.Phil. involves a fair amount of personal risk. With improvements to the procedure for durably hydrophobing the sapphire prism, spectra from a wider range of surfactant/oil systems should be obtained more easily. The base of the existing setup can be modified to accept a pumped-liquid-circulating thermostatted sample well, such that temperature-controlled phase transitions in surfactant monolayers at the oil-water interface could be observed through sum-frequency spectroscopy.

This thesis addresses the structural differences between surfactant monolayers at the air-water and oil-water interfaces, and highlights the importance of mixing between the oil and the surfactant on the structure of the interfacial monolayer. To understand surfactant monolayers at the oil-water interface better, these experiments should be extended to other combinations of surfactant and oil. The design of the sum-frequency oil-water experiment allows for the study of further combinations of oil and surfactant. Combinations that seem readily accessible and relevant to systems we have studied already as mixed monolayers at the air-water interface, include CTAB + tetradecane, pentadecane, heptadecane, and octadecane, phospholipids, non-ionics, and sodium dodecyl sulphate with alkanes. Naturally, other hydrocarbons could be investigated provided their optical properties do not differ widely from those of non-volatile liquid alkanes. I am partial to first continuing the CTAB + alkane experiment since investigation of other alkane chain lengths will elucidate the packing parameters that control the existence and conditions of a phase transition within the monolayer.

Clearly, binary systems of one surfactant and one alkane represent a theoretical ideal that is rarely replicated in real applications of surfactants at the oil-water interface. Complex mixtures of surfactants and of oils present new theoretical challenges that are beyond the scope of this thesis. Further experiments on binary systems will clarify the parameters that control order within the surfactant monolayer adsorbed at the interface between oil and water. This understanding will provide insight into more complex systems, and can guide the selection of experiments to address the role of complexity in surfactant behaviour at the oil-water interface.